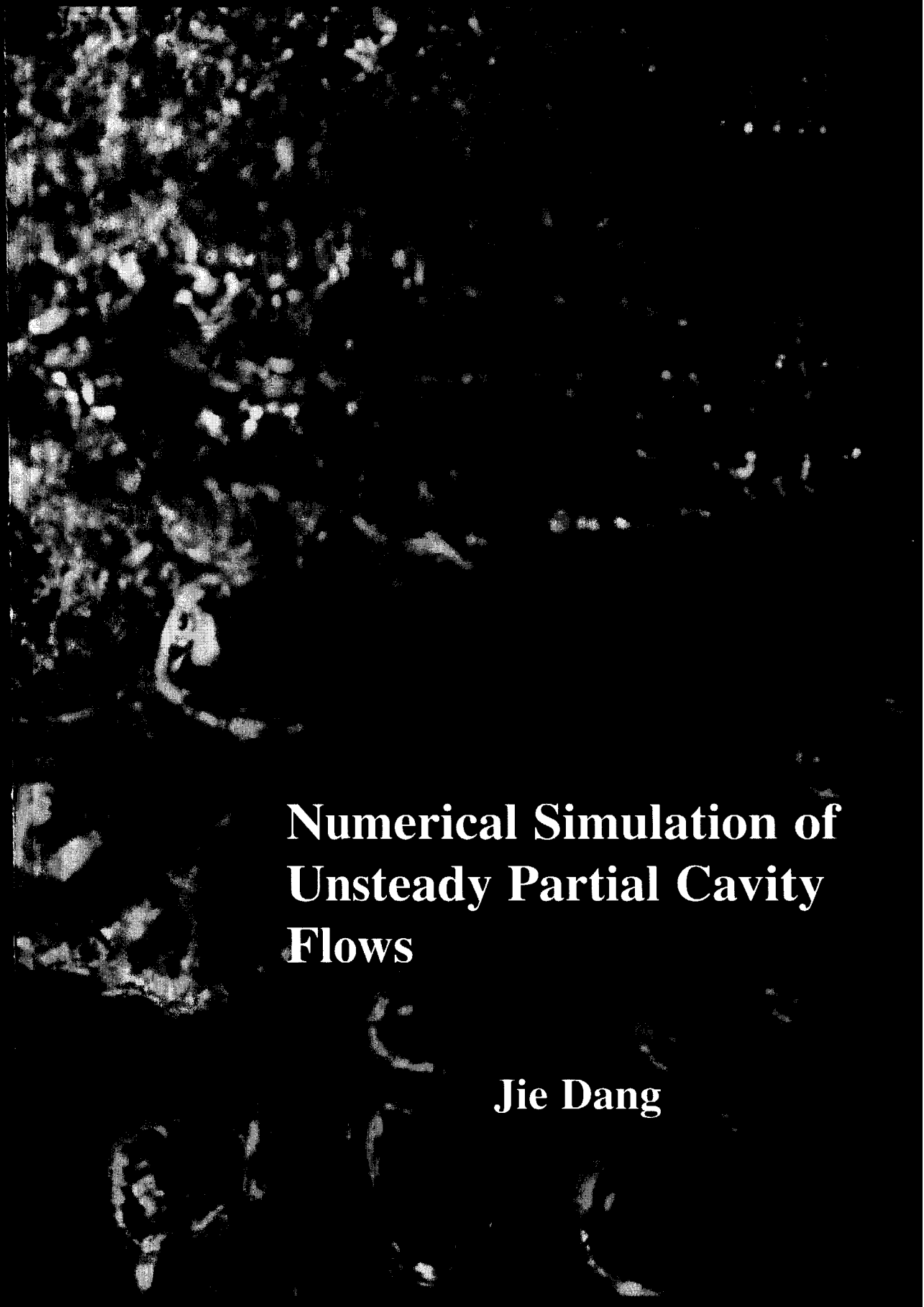

Numerical Simulation of Unsteady Partial Cavity Flows

Jie Dang

TR 3665 S

Stellingen

Behorende bij het proefschrift
'Numerical Simulation of Unsteady Partial Cavity Flows'
van Jie Dang

1. The flow on the cavity surface reflects at the cavity closure line. The reflected flow forms the re-entrant jet that determines the topological structure of the cavity.

2. A non-linear method, as developed in this thesis, predicts the unsteady cavity motion including phase differences both for the cavity length and for the cavity thickness. The cavity surface is 'dancing' instead of simply 'blowing' up and shrinking like a balloon.

3. Cavitation phenomena are chaotic, but not all the chaotic results from numerical simulations represent cavitation.

4. Whatever type of cavitation the customers expect, an expert on cavitation can always generate it in a cavitation tunnel. Before accepting the test results, it is necessary to check carefully the test conditions and the way the test is conducted.

5. Since the scale effect is so strong in a cavitation inception test, full-scale calculations are sometimes better than model tests.

6. The first impression is very often the most correct impression. Further evaluation reflects more or less your preferences.

7. 三人行，必有我師焉，擇其善者而從之，擇其不善者而改之。(Confucianism: Among every three persons, there is always one who can be my teacher. Choose his better ideas to follow and choose his worse ideas to discard.)

8. 學而不思則罔，思而不學則殆。(Confucianism: Learning without thinking is confusing while thinking without learning is exhausting.)

9. Life is a continuous learning experience.

10. Do not miss the train that comes sharp on time, because the next train may be considerably delayed or never come.

3668
753706
TR 3665

Numerical Simulation of Unsteady Partial Cavity Flows

Proefschrift

ter verkrijging van de graad van doctor
aan de Technische Universiteit Delft,
op gezag van de Rector Magnificus
prof. ir. K. F. Wakker,
voorzitter van het College voor Promoties,
in het openbaar te verdedigen
op maandag 19 maart 2001 te 13:30 uur

door

Jie DANG

Chinese MSc diploma in Naval Hydrodynamics
aan de Graduate School
van het China Ship Scientific Research Center.
geboren te Huangshi, CHINA

Dit Proefschrift is goedgekeurd door de promotor:
Prof. Dr. Ir. G. Kuiper

Samenstelling promotiecommissie:

Rector Magnificus, Voorzitter	
Prof. Dr. Ir. G. Kuiper	Technische Universiteit Delft, Promotor
Prof. Dr. Ir. H. W. M. Hoeijmakers	Universiteit Twente
Prof. Dr. Ir. A. J. Hermans	Technische Universiteit Delft
Prof. Dr. Ir. J. Pinkster	Technische Universiteit Delft
Prof. Ir. A. Aalbers	Technische Universiteit Delft
Ir. J. Th. Ligtelijn	Lips B. V.

ISBN 90-9014505-2
Copyright © 2001 by J. DANG, MARIN, Wageningen. All rights reserved.

Acknowledgment

The present research started from early 1997 and lasted for four years, aiming at developing a practical numerical method for predicting unsteady sheet cavity flows on lifting bodies, like propeller blades. It was a follow up work of Dr. H. J. de Koning Gans at Technical University Delft (TU Delft). The research was carried out mainly at Maritime Research Institute Netherlands (MARIN). The computations were done at a Cray C90 at the Academic Computing Services Amsterdam (SARA) under the financial support of the National Computing Facilities Foundation of the Netherlands (NCF). The experiments were carried out in the cavitation tunnel of Technical University Delft.

MARIN supported this research throughout the whole period. Without this support, the research could not be achieved in the present form of a thesis. Therefore, I gratefully acknowledge MARIN for providing this support.

I am very much indebted to my promoter Prof. dr. G. Kuiper for his supervising on the research. His support, guidance and encouragement made it possible for me to finish this thesis. The discussions with him were always interesting, and his constructive remarks could always clean up the cloud I had around cavitation and make it possible for me to see the essence.

I would like to express my great thanks to dr. H. J. de Koning Gans and ir. J. Bosschers for their discussions and contributions to the present work. We had many detailed discussions on the panel method, which gave me a very clear picture and a deep understanding of this method.

I would like to thank Prof. A. J. Hermans, Prof. H. W. M. Hoeijmakers, dr. H. C. Raven and dr. M. Hoekstra for their instructions on the panel method, on numerical simulation of free surface flows and on the vectorization of the code in a supercomputer. I have learnt a lot from the discussions with them.

My thanks should extend to ir. H. C. J. van Wijngaarden for his reading and his comments on my earliest work on two-dimensional simulations; to ir. M. X. van Rijsbergen who let me to try the cavity flow calculation for strut profiles which made me confident about the present method; and to Mr. H. Bijleveld and Ms. L. Bijtelaar for their conducting the experiments in Delft.

I enjoyed very much the time and the fun I had together with my roommates during these four years at MARIN. They were Mr. C. Ji, dr. P. J. F. Berkvens, ir. M. Kiel, dr. Z. Zhou, ir. J. Westhuis, Mr. B. Mazzi, drs. A. Ballast and ir. A. Boorsma.

Cycling in the wood of Wageningen, laying on the beach of Schiermonnikoog, exploring the castles along River Rhine, I enjoyed so much the life together with Ah Xue and Tengteng in these years. Their everlasting love adds bright colors to my thesis writing.

J. Dang *December, 2000*

Nomenclature

AR	aspect ratio
B	Bernoulli constant
C	chord length
C_D	drag coefficient
$C_{i,j,k}$	polynomial expansion coefficients
C_L	lift coefficient
$C(t)$	a closed curve in the fluid
C_p	pressure coefficient
C_V	cavity volume coefficient
D	diameter of propeller, drag
$D^{ic}_{ip,jp}$	dipole influence coefficients
$\mathbf{F}$	volume external force acting on the fluid
F_r	Froude number
$G(\tilde{\mathbf{x}};\mathbf{x})$	Green function, $\mathbf{x} \in \Omega$ and $\tilde{\mathbf{x}} \in \partial\Omega$
I_μ	influence coefficient from the dipole
I_σ	influence coefficient from the source
$I(m,n,p)$	integrals defined by equation (3.48)
J	Jacobian
J	$= \dfrac{V}{nD}$ advance coefficient of propeller
K	$= \dfrac{\omega C}{2V_0}$ reduced frequency
L	lift
L_∞	reference length
$N(m,n,p)$	integrals defined by equation (3.35)
N_G	highest order of the geometry expansion
N_J	highest order of the Jacobian expansion
N_{cav}	chordwide number of panels on the cavity
N_d	panel index of the detachment point
N_{down}	chordwise number of panels on the back of the profile
N_e	number of panel edges or panel index at cavity end
N_μ	highest order of the dipole expansion
N_σ	highest order of the source expansion
NI	total number of panels in main flow direction
NJ	total number of panels in cross flow direction
$O-XYZ$	space fixed inertial coordinate system
S_B	body surface
S_C	cavity surface
S_J	re-entrant jet cross section surface
S_W	wake surface of lifting body
$S^{ic}_{ip,jp}$	source influence coefficients
V_∞	reference velocity like ship speed V_s

$\overline{V}$	cavity volume
$\mathbf{V}$	fluid velocity in $O-XYZ$
$\mathbf{V}_0$	translational velocity of $o-xyz$ system
$\mathbf{V}_r$	relative velocity of fluid with respect to $o-xyz$ system
$\mathbf{V}_{r0}$	$=\mathbf{V}_W-\mathbf{V}_0-\Omega_0\times\mathbf{x}$ relative inflow
$\mathbf{V}_W$	space-fixed existing flow (non-uniform wake)
V_C	the velocity on the cavity surface
$W^{ic}_{ip,jp}$	dipole influence coefficients of the wake
$\mathbf{X}$	$=(X,Y,Z)^T$ position vector in $O-XYZ$
$\mathbf{X}_C$	$=(X_C,Y_C,Z_C)^T$ position vector of the cavity surface in $O-XYZ$
$dS_{\tilde{\mathbf{x}}}$	integral area element on the boundary
$\mathbf{e}_1,\mathbf{e}_2,\mathbf{e}_3$	base vectors on the surface
f	camber of profile
g	gravity acceleration
h	Landau symbol for the panel size or re-entrant jet thickness
ip,jp	panel index in (s_1,s_2) direction respectively
ir,jr	relative panel index
l	cavity length
ℓ	vector along a closed curve $C(t)$
$\mathbf{n}$	$=(x_x,n_y,n_z)^T$ unit normal vector on the surface
n	rotational speed of propellers (rps)
$o-xyz$	body-fixed non-inertial coordinate system
p	pressure
p_v	vapor pressure
p_∞	reference pressure
$\tilde{p}(\varphi)$	pressure induced by disturbance potential
$\mathbf{q}$	$=(x_C,y_C,z_C,\varphi)^T$ solution vector
$\mathbf{r}$	distance vector pointing from $\tilde{\mathbf{x}}$ to $\mathbf{x}$
s_1,s_2	body-fitted curvilinear coordinates
$\tilde{s}_i$	normalized curve length on the cavity (from 0 to 1)
t	time or thickness
u_1,u_2,u_3	local Cartesian disturbance velocity components
$\mathbf{v}$	disturbance velocity
$\mathbf{v}_g$	grid velocity of the cavity surface
$\mathbf{x}$	$=(x,y,z)^T$ position vector in $o-xyz$
$\mathbf{x}_g$	$=(x_g,y_g,z_g)^T$ grid position vector in $o-xyz$
x_d	the coordinate of the detachment point
x_e	the coordinate of the cavity end
$\mathbf{x}_C$	$=(x_C,y_C,z_C)^T$ position vector of the cavity surface in $o-xyz$

Γ	circulation around a closed curve C
Γ_d	detachment line of a 3-D cavity
Δt	time step
Φ	potential of volume force $\mathbf{F}$
Ω	flow domain
Ω_0	rotational speed of $o-xyz$ system
α	angle of attack
γ	strength of vortex
ϵ	artificial disturbance
η	cavity thickness
$\theta(\mathbf{x})$	interior angle of the boundary at point $\mathbf{x}$
$\mu_{ip,jp}$	normal dipole strength
ν	kinematic viscosity of fluid
ρ	fluid mass density
σ	cavitation number
$\sigma_{ip,jp}$	source strength
σ_n	rotational cavitation number
τ_2	$=\mathbf{e}_3 \times \mathbf{e}_1$
ϕ	potential of velocity $\mathbf{V}$
ϕ_W	potential of velocity $\mathbf{V}_W$
φ	potential of the disturbance velocity $\mathbf{v}$
φ_n	$=\dfrac{\partial \varphi}{\partial n}$
ω	circular velocity of the gust
$\dfrac{D}{Dt}$	material derivative in $O-XYZ$
$\dfrac{\mathbf{d}}{\mathbf{d}t}$	material derivative in $o-xyz$
$\partial\Omega$	boundary of domain Ω
∇	nabla operator

Contents

1 Introduction **1**
- 1.1 Physical phenomenon 1
- 1.2 Numerical simulation 6
  - 1.2.1 Hodograph technique 7
  - 1.2.2 Linear theory 8
  - 1.2.3 Non-linear theory 9
  - 1.2.4 Viscous and other method 10
- 1.3 Objectives and outline of the thesis 11

2 Mathematical Formulation **15**
- 2.1 Description of the problem 15
- 2.2 Mathematical model 17
- 2.3 Dynamic equations in moving coordinates 20
- 2.4 Boundary conditions 22
  - 2.4.1 Body surface 22
  - 2.4.2 Cavity surface 23
  - 2.4.3 Re-entrant jet surface 24
  - 2.4.4 Other conditions 25
- 2.5 Solving strategies 29
  - 2.5.1 Cavity surface updating 29
  - 2.5.2 Spatial problem 31
  - 2.5.3 Initial condition 31

3 Panel Method **33**
- 3.1 Introduction 33
- 3.2 Green's identity 35
- 3.3 Description of the geometry and solution 38
  - 3.3.1 The geometry 38
  - 3.3.2 The solution 41
- 3.4 Analytical calculation of influence coefficient 42
- 3.5 Discussion 46

3.5.1 Consistence 46
3.5.2 Convergence 48
3.5.3 Hyperboloidal panels 49

4 Time Stepping **53**
4.1 Introduction 53
4.2 Lagrangian method 54
4.2.1 Explicit method 56
4.2.2 Implicit method 58
4.3 Euler method 58
4.4 Stability 60
4.5 Alternative Euler method 64

5 Numerical Algorithms **67**
5.1 Introduction 67
5.2 System of equations 68
5.2.1 Unsteady flow 69
5.2.2 Steady flow 70
5.3 Cavity planform search 72
5.4 Cavity model and grid update 75
5.5 Detachment of sheet cavity 78
5.6 Wake shape 84
5.6.1 Theory 85
5.6.2 Implementation 85
5.6.3 A test case 88
5.7 Kutta condition 89
5.7.1 Classical Kutta conditions 92
5.7.2 Discussions 95
5.7.3 Unsteady Kutta condition 96
5.7.4 Effect of Kutta conditions on cavity flows 99
5.8 Time derivative of potential 100

6 Steady Cavity Flows **103**
6.1 Two-dimensional section flows 103
6.1.1 Formulation of the problem 104
6.1.2 Boundary conditions 106
6.1.3 Iteration scheme for the cavity surface 107
6.1.4 Cavity volume and hydrodynamic forces 108
6.1.5 Numerical Implementation 109
6.1.6 Results and Discussion 110
6.1.7 Summary 125
6.2 Three-dimensional hydrofoil flows 126
6.2.1 Formulation and discretization 127

6.2.2 Convergence tests and numerical verification 129
6.2.3 3-D results 132
6.2.4 Streamline and re-entrant jet direction 134
6.2.5 Comparison with experimental data 136
6.2.6 Summary 140
6.3 Propeller flows 140

7 Unsteady Cavity Flows **147**
7.1 Hydrofoil flows 151
7.1.1 Two dimensional cavity flows 151
7.1.2 Three-dimensional cavity flows 166
7.2 Propeller flows 171
7.3 Conclusions 176

8 Experiment and Validation **179**
8.1 Experiment Setups 180
8.1.1 The tunnel 180
8.1.2 The twisted hydrofoil 181
8.1.3 Procedure and Photographing 182
8.2 Experimental Results 183
8.3 Comparisons 185

9 Conclusions and Recommendations **189**
9.1 Concluding remarks 190
9.2 Recommendations 192

A Polynomial Coefficients **205**

B Two-dimensional Results **207**

C Experimental Results **209**

Chapter 1

Introduction

Cavitation is a very complicated phenomenon involving phase change, surface tension, turbulence, non-equilibrium thermodynamic effects, etc. Cavitation is unsteady in nature and occurs over a wide range of time and length scales. The development of advanced cavitation simulation tools should not override the physical nature of cavitation. It is essential to understand the behavior of cavitation and develop a numerical simulation method that incorporates the most important phenomena in detail, as much as possible. Section 1.1 describes the basic physical phenomena of cavitation. Emphasis is on various types of cavitation and their behavior on propeller blades. Section 1.2 reviews the development of cavitation simulation and discusses the most recent methods. The research objectives of this thesis are outlined in Section 1.3.

1.1 Physical phenomenon

Cavitation is a flow phenomenon that occurs when liquid changes phase to vapor and results in a visible vapor region (called a bubble or a cavity) in the fluid due to dynamic pressure reduction at essentially constant temperature, like the temperature of river or sea water. Cavitation is different from boiling – the most common phase change phenomenon that we observe in our daily life. Boiling involves also phase change but occurs when the liquid temperature is raised to the *boiling-point* at atmospheric pressure. Growth of a cavity occurs at a slow rate when dissolved gases diffuse into the cavity or when the liquid temperature rises or drops. But the growth of a cavity will be *explosive* if it is primarily the result of vaporization into the cavity (Knapp *et al.* (1970)). When these vaporous bubbles or cavities travel to a high-pressure region or when the

ambient static pressure is increased by some means, the growth process will reverse. The vapor will condense into liquid at a very high rate. The cavity then collapses and eventually disappears. This *implosive* process can be very violent, which results in detrimental effects like erosion, vibration, excessive noise, etc.

Cavitation occurs under three basic conditions: 1) The presence of a low pressure, which should be lower than a critical value, or simply speaking, lower than the vapor pressure p_v. The non-dimensional parameter to scale this low pressure is the cavitation number σ, defined in the inflow as,

$$\sigma = \frac{p_\infty - p_v}{\frac{1}{2}\rho V_\infty^2}, \tag{1.1}$$

where p_∞ is the static pressure of the inflow, p_v is the vapor pressure, ρ is the fluid density and V_∞ is the velocity of the flow; 2) The presence of nuclei, which are tiny bubbles of microscopic size and filled with vapor or gases from e.g. microorganisms or some other sources from the nature. Nuclei are measured in nuclei population spectrum (N/cm^3) or by nuclei number density spectrum (Gates (1977)) based on nuclei sizes; and 3) The duration of time during which the nuclei are exposed to the low pressure.

The cavitation number measures the vulnerability of the flow to cavitation. The higher the cavitation number, the less likely cavitation is to occur; the lower it is, the more likely. Nuclei are always needed for cavitation since 'pure water' can withstand very high tension (Blake (1949)) and cavitation never occurs in this kind of water. Gaseous nuclei form the impurity in the liquid that reduce the tensile strength of the liquid. Different tensile strengths in different cavitation test facilities gives different cavitation inception results for the same test. Enough duration of exposure to low pressure is also important. It enables the nuclei to grow up to visible sizes. If one of the three conditions is different, the cavitation phenomena can be totally different. This is one of the essences of 'scale effects'. Other influences are e.g. turbulence, viscous effects through the Reynolds number, diffusion, etc.

Cavitation occurs in a broad variety of hydrodynamic devices, such as marine propellers, hydrofoils, pumps, water turbines of electric power generators and even in the liner of the cylinders of a diesel engine. Cavitation degrades the performance of these devices in many aspects. E.g. 1) Excessive cavitation reduces the efficiency or affects the rotation rate of a propeller or reduces a head of a pump. 2) Certain types of cavitation (bubble and cloud) damage the structure of these devices by erosion. This can sometimes be so violent that it causes disastrous damage to the structure of a pump within only a few months of operation or to a ship propeller after a single voyage. 3) Periodic (sheet or cloud) cavitation causes a periodic volume change of the cavity, which eventually causes pressure fluctuations on nearby structures (ship hulls). Cavitation nearly always results in a strong noise emission into the water.

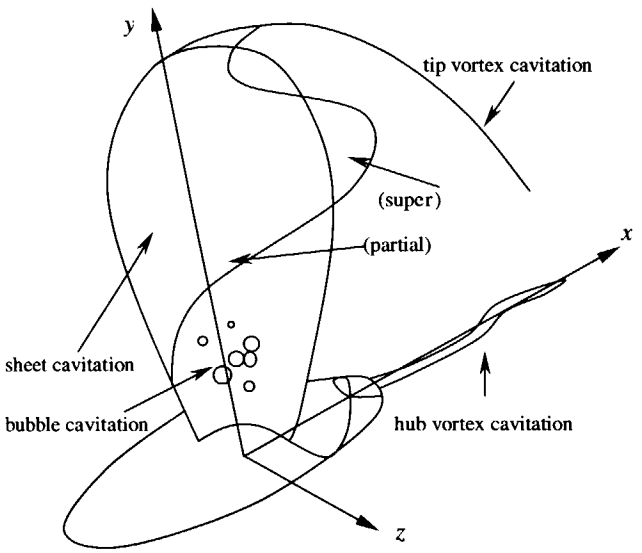

Figure 1.1: Schematics of the various cavitation on propeller blade.

Cavitation occurs in different forms. It can be fixed to body or fixed to the fluid; It occurs in the liquid or at the surface of immersed bodies; It can shape as a group of perfect spheres (bubbles) or as a single sheet. The surface of a sheet cavity can be very smooth and transparent, or very frothy and opaque. As widely accepted by researchers, cavitation on marine propeller blades are organized into the following categories,

1. Bubble cavitation;
2. Sheet cavitation;
3. Tip and hub vortex cavitation;
4. Cloud cavitation,

as schematized in Figure 1.1.

Bubble cavitation occurs when nuclei travel into a low-pressure region, expand explosively into visible bubbles in this region, and collaps implosively when subsequently they travel into a high-pressure region. This kind of cavitation has a relatively less influence on hydrodynamic forces and efficiency of propellers, but generates strong noise emission and erosion when it is close to the surface of the propeller blades. Sheet (fixed or attached) cavitation is fixed relatively to the body, mostly a foil or propeller blade. It starts normally from

the leading edge, where the flow is separated, and forms a pocket of vapor. Over the entire length of the sheet cavity, the cavity surface is always concave towards the blade surface (Ronald (1989)). Because of this, the cavity must eventually close on the blade surface (partial cavity) or close somewhere downstream with other cavity surfaces (super cavity). The end of the sheet cavity is normally unsteady. It either breaks into a lot of small bubbles, which is very local and non-periodic, or it induces large-scale cavity shedding periodically. Both of these different processes eventually form the cloud cavitation further downstream, but the periodic shedding generates large-sized cloud cavitation. Vortex cavitation happens when nuclei are trapped into the core of a vortex, where the pressure is low, and grow into longitudinal bubbles. When these bubbles merge with each other, they eventually form a hollow long spiral tube, which can extend stably over a considerable distance downstream. A vortex cavity will finally collapse when the vortex is dispersed or dissipated by viscosity and therefore the pressure in the core is no longer low enough. This collapse could be also very violent and generate very strong noise emission, but not erosive because it normally occurs far downstream of the propeller blades. However it is possible that erosion damage occurs on rudders.

Sheet cavity closure controls the behavior of a sheet cavitation. When sheet cavity occurs on propeller blades, it starts normally from the leading edge as a smooth transparent film. This sheet may remain smooth and transparent to the end of the cavity if the flow reattaches the blade surface as *laminar reattachment.* But this sheet may become frothy if the cavity surface flow becomes turbulent. This is called *turbulent reattachment.*

When a reentrant jet forms at the end of a cavity, it forms a reverse flow with a speed as high as the free stream velocity at the cavity surface (Furness & Hutton (1975)), and moves into the cavity between the underside of the cavity and the blade surface. If this reentrant jet moves upstream and eventually impinges on the cavity surface near the cavity detachment point, the sheet cavity will break and a large portion of the cavity will be shed into the wake of the cavity and form a large-scale cloud cavity. This cavitation is highly periodic, as shown by De Lange (1996) in Figure 1.2a. It is found that the average shedding frequency, in terms of Strouhal number, is relatively independent of the cavitation number (Ronald (1989), Avellan *et al.* (1989), Le *et al.* (1993)). When there is a turbulent reattachment at the end of a cavity, the end of cavity becomes a bubbly mixture in the cavity wake that is as thick as the maximum cavity height and locates at the maximum thickness point of the sheet cavity (Laberteaux (1998)).

The highly periodic shedding of the cloud cavity, as a result of the impinging of the reentrant jet on the cavity surface (Figure 1.2a) (which is always tried to be avoided by propeller and hydrofoil designers), can be prevented by changing the shape of the hydrofoil or the propeller blade. As a consequence,

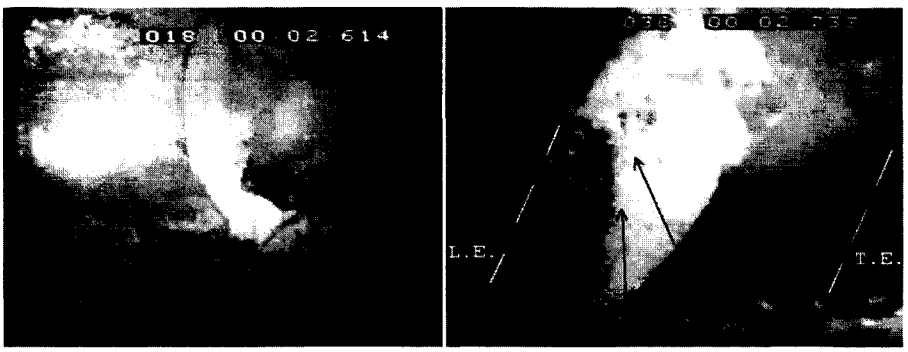

Figure 1.2: a) (left) Convex shape of the closure line in case of a local break-off sequence: NACA 16-009, $\alpha = 3°$, $\sigma = 1.39$, $U = 6.9m/s$. b) (right) Top view of the 3-dimensional cavity and jet layer on the swept wing. The black arrows sketch the direction of the re-entrant jet. De Lange (1996).

the topology of the cavity can be changed completely (see Figure 1.2b). Figure 1.2 shows two cavitating hydrofoils with the same profile, but one is swept and one is not. Experiments show totally different topologies of these cavities. When the reentrant jet shifts its direction from towards the leading edge to a direction along the span, the cavity surface will no longer reached by the jet, and therefore the cavity will not be broken and no periodic cloud cavity sheds at the end of the sheet cavity. De Lange (1996) called this a 'reflection' of the flow at the end of a three-dimensional hydrofoil. This kind of flow reflection is also very often found on propeller blade. Figure 1.3 shows a typical sheet cavity on a conventional propeller blade (Kuiper (1981)). In this picture, the reentrant jet underneath the cavity at the cavity end can be clearly seen from $0.25r/R$ up to $0.7r/R$. Within this region, laminar reattachment of the cavity at the end is observed and no cloud cavity is shedding. But the liquid entering the cavity by the reentrant jet can not stay inside the cavity forever and it must find an exit. For the present situation, instead of impinging on the cavity at the leading edge at the same radius, the reentrant jet flows in radial direction and finally leaves the cavity at about $0.7r/R$ to $0.8r/R$ radii. Around this region, cloud cavity shedding together with the the jet is seen. From $0.8r/R$ up to the tip, the cavity has a cloudy closure. Some cloud cavities are shedding locally from the end of the cavity. But this shedding is not highly periodic.

The topology of a sheet cavity is strongly related to the blade loading in radial direction and thus to the pressure distribution on the propeller blades. The relative velocity between the propeller blades and the liquid is very high at the outer radii and relatively low at the inner radii. This velocity gradient

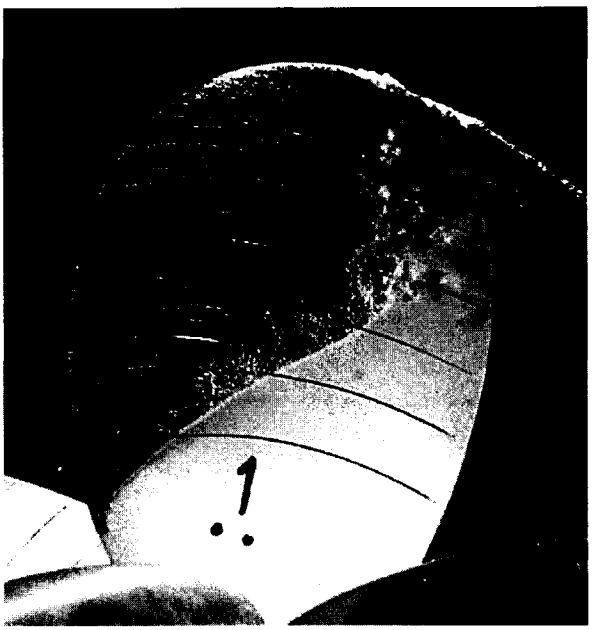

Figure 1.3: Cavitation Observation in the Cavitation Tunnel on Propeller S at $J = 0.4$. ($Re_n = 1.78 \times 10^6$, $\sigma_n = 1.3$, without tunnel wall correction), Kuiper (1981).

makes the cavity on the propeller blades highly three-dimensional and makes that the reentrant jet at the cavity closure flows in radial direction instead of in chord direction. This is true even when the propeller blades are not skewed. Introducing blade skew will move the exit of the reentrant jet from, e.g. $0.7r/R$ for this case, to the propeller tip. Finally the reentrant jet enters the tip vortex cavitation. Therefore over the entire blade surface, no cloud cavitation is shedding, which is important for preventing erosion and noise radiation.

More detailed discussions on the structure and the reentrant jet exit on both model propellers and full scale propellers can be found in the papers of Kuiper (1994) and Van der Meulen & Wijnant (1990).

1.2 Numerical simulation

Research on cavitation has already a very long history. Cavitation phenomena have been recognized since Euler (1754) found that cavitation occurred in high-

speed water flow during his study on water turbines. In 1873, Reynolds recognized cavitation as the cause of the 'racing' of a ship propeller that is loaded above a torque threshold. The first time when the word *cavitation* appeared in literature was as early as 1895 in a paper by Barnaby & Parsons (Ronald (1989)). In the early stage of cavitation research, people focused mainly on experimental investigation to try to understand the cavitation phenomena, such as cavitation inception; cavitation erosion; scale effect; nuclei influence; roughness effect, etc. In recent years, experimental research is still pursued on all of the above aspects, but much more in detail. As to the research on the sheet cavity flow, much attention has been paid to the detachment point (Arakeri (1975), Franc & Michel (1985), Shen & Peterson (1980)), but less attention has been paid to its closure region. Experimental observation of the closure region of a fixed cavity has been continued recently by researchers who are trying to understand the physical mechanism behind the phenomena (Furness & Hutton (1975), Avellan *et al.* (1989), Kubota *et al.* (1989), Le *et al.* (1993), Laberteaux & Ceccio (1997)). Various physical appearances at the cavity end like a vapor core, a horseshoe vortex or a cloud of bubbles have been found. But more experimental investigations are still needed (ITTC (1999)). Nevertheless, it has been widely accepted that the reentrant jet is directly responsible for the generation of large-scale cloud cavitation at the end of a sheet cavity.

According to the 22^{nd} ITTC special committee survey on computational methods for propeller cavitation, numerical simulation of cavity flow on propeller blades is still limited to sheet cavity flows, no matter whether a lifting-surface method, a boundary-element method or a method based on models like Euler, RANS or a two-phase flow model is used (ITTC (1999)). A few methods have been developed for bubble or tip vortex cavitation. No method has ever been tried yet for the simulation of cloud cavitation on propeller blades.

1.2.1 Hodograph technique

The theoretical simulation of sheet cavity flow started more than a century ago when Helmholtz (1868) and Kirchhoff (1869) established the free streamline theory by using conformal mapping techniques, or the hodograph technique (Wu (1972)). The first cavity flow problem was solved for bluff bodies at zero cavitation number with a Riabouchinsky image model (Riabouchinsky (1921)) and the reentrant jet model (Efros (1946)), and later extended to the flat plate at incidence (Kutznetsov and Terentev (1967)) and to the wedge (Cox & Clayden (1958)) at zero cavitation number. The hodograph technique is a non-linear method. It can be used for cavitating flows around simple geometries like bluff bodies and flat plates, but not for arbitrary lifting or non-lifting bodies like hydrofoils or propeller blades. And hence, it is nothing useful for practical use in engineering. A detailed description of the hodograph technique can be found in Birkhoff & Zarantonello (1957). A good review has been provided by

Wu (1972).

1.2.2 Linear theory

The great breakthrough on cavity flow simulation was made by Tulin (1953) when he applied the linear theory to the problem of a supercavitating symmetric section at zero angle of attack and zero cavitation number. This method was latter extended by himself to supercavitating flows around a flat plate at incidence and at any cavitation number (Tulin (1964)). Extensions of this linear theory for super cavitating flow at any cavitation number to arbitrary bodies were contributed by a lot of excellent researchers like Wu (1956), Geurst (1960), Fabula (1962), and Chen (1962). A similar technique for partial cavitation was first obtained by Acosta (1955) and Geurst (1959) independently. The camber influence on partial cavity flow has been incorporated later on in their linear method (Geurst & Verbrugh (1959)) and the thickness influence was added by Wade (1967). But linear theory for partial cavity flow about hydrofoils predicts that the cavity extent and volume will increase when the thickness of the hydrofoil is increased. This contradicts the experimental observations that when the thickness is increased, the leading edge radius is increased and as a result the cavity extent and volume is decreasing. This is because the small perturbation assumption of the linear theory is not valid at the leading edge where the perturbation velocity is of the same order as the free stream velocity. Tulin & Hsu (1980) developed the short cavity theory by considering the cavitating flow as a small perturbation to the nonlinear fully wetted flow (2-Dimensional or 3-Dimensional), which predicts a correct thickness effect on cavitation. Kinnas (1991) recently corrected the linear cavity flow theory by applying a leading-edge correction from Lighthill (1951) and incorporated this correction into a propeller cavitation prediction code (Kerwin *et al.* (1986)). Better prediction of the cavity extent for cavitating propellers were reported (Kinnas (1992)).

Three-dimensional flow application of the two-dimensional linearized cavity flow theory was limited to hydrofoils or propeller blades under the assumption of high aspect ratio. Asymptotic expansion with matching of the inner and outer solutions was normally adopted in these methods. Leehey (1971) introduced a theory for supercavitating hydrofoils of finite span. Uhlman (1978) also developed a similar method for partially cavitating hydrofoils of finite span. But the propeller blades are never shaped as a high aspect ratio foil. Hence, the applicability of this theory to propeller blades is questionable.

The use of digital computers and numerical methods brought cavity flow simulation into a new era. Golden (1975) repeated the solution of the cavity flow of a flat plate (Geurst (1959)) but in a purely numerical way. After that, numerical methods based on linear cavity flow theory have been quickly extended to three-dimensional flow problems. Jiang & Leehey (1977) used the

lifting surface theory to solve the problem of a supercavitating hydrofoil of finite span. Discrete vortex and source distributions were used to formulate the equations. A chordwise cavity closure condition for each strip was enforced, which is exact for a symmetric hydrofoil but not for arbitrarily shaped foils like propeller blades. Even so, this method was extended to solve the problem of an unsteady, cavitating marine propeller by Lee (1979).

Van Houten (1983) calculated the unsteady cavity flow on a high aspect ratio hydrofoil by matching the outer lifting-line solution with the inner linearized cavity flow solution. He succeeded to calculate the slow growth and rapid collapse of the cavity in one cycle of gust variation. He predicted the cyclic variation of the cavity length to decrease as the frequency increases.

1.2.3 Non-linear theory

The drawback of the linear theory for unsteady sheet cavity flow is that the dynamic motion of the cavity is not predicted, since the boundary condition is not satisfied at the real cavity surface. This dynamic motion may give contributions to the higher harmonics of the pressure fluctuations. Stern & Vorus (1983) developed a nonlinear method which divides the cavity flow problem into a three-dimensional outer flow problem and a two-dimensional inner flow problem. In his inner problem, the cavity is modeled by a semi-ellipse on a plane surface and the dynamic boundary condition at the cavity surface is satisfied at the cavity surface in a least-squares sense. The advantage of this method is that the three-dimensional outer flow problem remains fully nonlinear, and hence it can be used for extreme geometry like propellers. Also, the dynamic motion of the cavity is simulated more or less correctly. Stern (1989) compared his results with the experimental results of Shen & Peterson (1978). But the predicted cavity lengths were significantly less than those observed in both steady and unsteady flows.

The big leap to nonlinear cavity flow simulation on arbitrary lifting bodies started as a boundary-integral method (a boundary-element method or panel method) was used. Pioneering work was done by Uhlman (1987) who solved the partial cavity flow on two-dimensional hydrofoils with a cavity termination wall model. In his method, the cavity surface is iterated until both kinematic and dynamic boundary conditions at the cavity surface are satisfied. A cavity termination wall model is used at the end of the sheet cavity. Compared to other linear and nonlinear method, his method correctly predicts the influence of the foil thickness on cavity extent and volume. Similar work was also done by Yamaguchi & Kato (1983), Kinnas & Fine (1991) and recently by Dang & Kuiper (1998*b*).

Pellone & Rowe (1981) calculated the supercavitating flow on a three-dimensional hydrofoil with free surface by a velocity-based method. Peallat & Pellone (1996) extended the same velocity-based panel method to the three-

dimensional partial cavity flow. Systematic research on non-linear simulation of partial and super sheet cavity flow by using potential based panel methods for three-dimensional hydrofoils and propeller blades has been performed at MIT in the last decade (Fine & Kinnas (1993), Kinnas & Fine (1993), Kinnas & Fine (1992), Kinnas *et al.* (1994), Kinnas (1998)). Similar work was also done at the same time by Kim *et al.* (1994) and Kim & Lee (1996). Recently, reentrant jet modeling of the partial cavity termination was simulated for three-dimensional hydrofoils by Dang & Kuiper (1998*a*).

1.2.4 Viscous and other method

Another important development that is prevailing recently is the cavity simulation method based on Euler or RANS, together with two-phase flow equations. High quality solution with large mesh sizes is considered to be required for this simulation especially close to the cavitating region. This claims large computer resources both in memory and speed. Up to now, no method has ever really succeeded to calculate cavitation on propeller blades. As classified by 22nd ITTC (1999) special committee, this method can be grouped into four categories: 1) Interface tracking methods; 2) Two-phase flow methods; 3) Discrete bubbles methods and 4) volume-of-fluid methods.

Deshpande *et al.* (1994) predicted cavity flow on two-dimensional cascades and isolated hydrofoils by using an Euler solver based on artificial-compressibility and a pseudo-time stepping technique. A cubic profile that merges smoothly with the cavity interface and approaches the body surface tangentially is used at the cavity end. The length of this profile is empirically chosen to be three times the cavity thickness at the end. Based on the same cavity model, Deshpande *et al.* (1993) used a Navier-Stokes solver to solve the same partial cavity flows on 2-D foils. He concluded that the comparison with their Euler analysis shows that the presence of viscous effects has little impact on the cavitating region. Chen & Heister (1994) also solved the Navier-Stokes equations but without taking into account the turbulent fluctuations. An empirical cavity end model is also enforced by assuming a circular connection with the body surface when the cavity thickness is reduced to half of its maximum value. Dupont & Avellan (1991) successfully calculated the partial cavity flow at the leading edge of a NACA 0009 profile by using a RANS code with a two-equation $k-\epsilon$ turbulence model. This method was extended lately to a propeller-liked twisted hydrofoil (Hirschi *et al.* (1998)) and cavitation on a pump impeller (Hirschi *et al.* (1997)).

Interface tracking methods have their own limitations in cavitation simulation because it is usually hard to simulate vortex and cloud cavitation due to difficulties to track interfaces of this kind of cavities and to generate three-dimensional meshes for them. Two-phase flow methods seem more promising. At present, this is still in its infancy and only used for sheet cavitation on

simple geometries. Kubota *et al.* (1989) used a variable density Navier-Stokes solver coupled with a microscopic model for the bubbles to predict the unsteady formation of cloud cavitation on a hydrofoil. This model treats the cavity as a local homogeneous cluster of spherical bubbles. The local void fraction is calculated by the local bubble sizes at each point. However, the local void fraction can exceed unity in some situations. Merkle (1998) proposed a mixed model that simulates both vapor and liquid simultaneously. In his method, mass can exchange on the cavity surface from one phase to the other by means of a rate-limited process. The author claims that this method is more robust than single-phase model.

Another approach to cavitation simulation is to treat the cavitation flow as a single-phase flow by assuming a pseudo-density equation of state while using a compressible Euler or RANS code. People working in this field include Delannoy & Kueny (1990), Hoeijmakers *et al.* (1998), Merkle (1998), Song & He (1998), etc. The single-phase flow model has the potential to solve more complicated cavity flow problems like tip vortex and cloud cavitation. These models have the advantage that an explicit model is not needed for the downstream closure of the cavity. However, a pseudo-density has to be used. In the result, the fluid flows across the interface into the cavity, and becomes supersonic when the density drops quickly. This contradicts the experiments, since nobody has ever observed supersonic flow inside a cavity. A good review of these methods can be found in 22^{nd} ITTC (1999) report of the Specialist Committee on Computational Methods for Propeller Cavitation.

1.3 Objectives and outline of the thesis

Cavitation on ship propeller blades is a major source of noise and vibrations. In order to prevent excessive noise and vibrations, either cavitation has to be eliminated entirely or its behavior has to be controlled. Since for reasons of efficiency the propeller always operates in the wake of the ship hull, which is highly non-uniform, cavitation can generally not be avoided. The increasing speed and power installed in ships nowadays make the problems worse. It is therefore important to control the dynamic behavior of cavitation.

Cavitation simulation methods based on Euler and RANS equations are advancing very quickly in recent years but are still in a maturing stage. Most of these methods are still limited to two-dimensional foil flows. The mathematical and numerical details employed in those methods are rather diverse. It means that the explorations are still under way. Stability, robustness, convergence and computational speed are major issues that must be clarified. Using these methods to predict propeller cavitation is still restricted to steady flow, where the propeller is considered to operate in a circumferentially averaged wake.

Boundary Element Methods (BEM) (panel methods) have become practical

tools for both the analysis and design of marine propellers, hydrofoils, pumps and ship appendages. Remarkable progress in numerical algorithms has been achieved in terms of accuracy and efficiency. In the last decade, BEM methods have been successfully extended to sheet cavity flow on propellers. Extension to viscosity dominated flow like tip and hub vortex cavitation will remain difficult however. Applications show that the BEM is a stable and efficient tool for sheet cavity flow prediction on propellers. But further improvement to the detachment and closure of the cavity has to be made, since they have a strong influence on the topology and, in turn, on the stability of the sheet cavity. On the other hand, the linearized method has failed to predict the cavity dynamics in non-uniform ship wakes, which is thought to be important for higher harmonic components of the exciting forces. A fully non-linear simulation, especially at the cavity end, is hence in high demand.

The present thesis presents a general non-linear theory for unsteady partial sheet cavity flows, under the assumption of incompressible and inviscid flow. A potential based panel method is used to solve the spatial problem of the Laplace equation at each time step. The alternative Eulerian method is used for the evolution of the cavity surface. Bernoulli integration of Euler equation is used to update the potential at the cavity surface. At the end of the cavity, a reentrant jet cavity model is used. With this kind of fully nonlinear method, a better prediction of the cavity volume, which in turn results in a better prediction of pressure fluctuation and noise, can be expected. Emphases are given on the simulation of the re-entrant jet, the explanation of the topology of the cavity, the stability of sheet cavities and the dynamics of cavity in a gust.

In Chapter 2, the cavity flow problem considered in the present research is described first. The equations that describe the fully non-linear problem are then derived according to the fundamental conservation laws. Boundary and initial conditions for solving this problem are discussed. Equations for the evolution of the cavity surface and updating of the Dirichlet boundary condition on the cavity surface are formulated. A solving strategy is discussed.

A higher-order panel method, based on an analytical calculation of the influence coefficients, is formulated in Chapter 3 for solving the spatial problem governed by Laplace equation in each time step. The way to describe the geometry and solution by using polynomial expansions is given. The influence of the reference panel and its shape on the convergence of the method is discussed.

Chapter 4 describes the time-stepping technique for the present unsteady flow calculation. Both Lagrangian and Eulerian methods are discussed and addressed by test cases. An alternative Eulerian method is chosen for the present method. The evolution and the motion of the cavity surface mesh are discussed.

Besides the major numerical methods discussed in Chapter 3 and 4, other numerical techniques are given and verified in Chapter 5. The numerical treat-

ment of the system of equations is discussed first with application of different Kutta conditions and the cavity detachment condition. The implicit and explicit Kutta conditions, the cavity detachment condition, the planform search method, the evolution of the cavity surface, the propeller wake shape and the treatment of the time derivatives of the potential and their effect on the cavity flows are all discussed in detail in this chapter.

Numerical results for two-dimensional and three-dimensional hydrofoils and propellers are presented in Chapter 6 for steady flow conditions. Comparisons are presented for results of two-dimensional cavity flows and results of the present method and other linear and non-linear methods. For sectional and simple hydrofoil cavity flows, validation is carried out by using available experimental results. The re-entrant jet thickness and its direction in three-dimensional flow are successfully predicted. The calculated results of the cavity extent on the *S Propeller* at two different conditions agree well with the experiments.

Unsteady flow calculation of both 2-D and 3-D hydrofoil and propeller cavity flows are presented in Charpter 7. 2-D flow calculations are carried out by using a 3-D hydrofoil with very large aspect ratio. The variation of the cavity thickness in a cycle of a vertical gust is found to be out of phase for different positions along the chord. Three-dimensional flow calculation of a hydrofoil with an aspect ratio of 2 shows the phase different of the cavity length variation between the cavity at the tip and the cavity at the mid-span can be as large as 90°. The main dynamics movement of the sheet cavity flow on the blade of a *S Propeller* in a sharp wake is captured by the present simulation.

A benchmark test is now being carried out in the cavitation tunnel of Technical University Delft on a twisted transparent hydrofoil. A stationary sheet cavity is generated on this hydrofoil and the cavity thickness is expected to be measured. The re-entrant jet can be observed due to the transparency of the foil. Some preliminary results have been obtained and compared with results of the present calculations in Chapter 8. Good agreement is found.

A discussion on the present method and a future perspective on cavity flow calculations is given in Chapter 9.

Chapter 2

Mathematical Formulation

A general description of our present problem is given at the beginning of this chapter. The mathematical formulation of the fully non-linear unsteady partial cavity flow on multiple bodies, which are moving together, are derived from the fundamental conservation laws of fluid dynamics. Governing equations, initial conditions and boundary conditions are listed. The strategies for solving this fully non-linear problem are discussed at the end of this chapter.

2.1 Description of the problem

Let us consider a general case that one or more bodies are moving in the same manner in the fluid. Examples are a propeller with propeller blades and hub (see Figure 1.1), and a hydrofoil system that consists of the hydrofoils, the hub and the strut (see Figure 2.1). Those moving bodies can be either lifting bodies (like the propeller blades and the hydrofoils) or non-lifting bodies (like the hub and the strut). For lifting bodies, relatively thin wakes that contain concentrated vorticity are attached to their trailing edges.

When the ambient pressure is low enough, cavitation will occur on some part of these bodies' surfaces. Cavitation can occur on lifting bodies such as the propeller blades and the hydrofoils, as well as on a non-lifting body like the strut surface (Figure 2.1). Since bubble and cloud cavitation involve very complicated physical phenomena, they are still not easy to simulate. Here we deal only with flows with partial sheet cavities.

We define two Cartesian coordinate systems. One is the space-fixed inertial system $O - XYZ$ and the other is the body-fixed moving coordinate system $o - xyz$, which is a non-inertial system as shown in Figure 2.1. The position vectors in these two systems are denoted as $\mathbf{X} = (X, Y, Z)^T$ and $\mathbf{x} = (x, y, z)^T$,

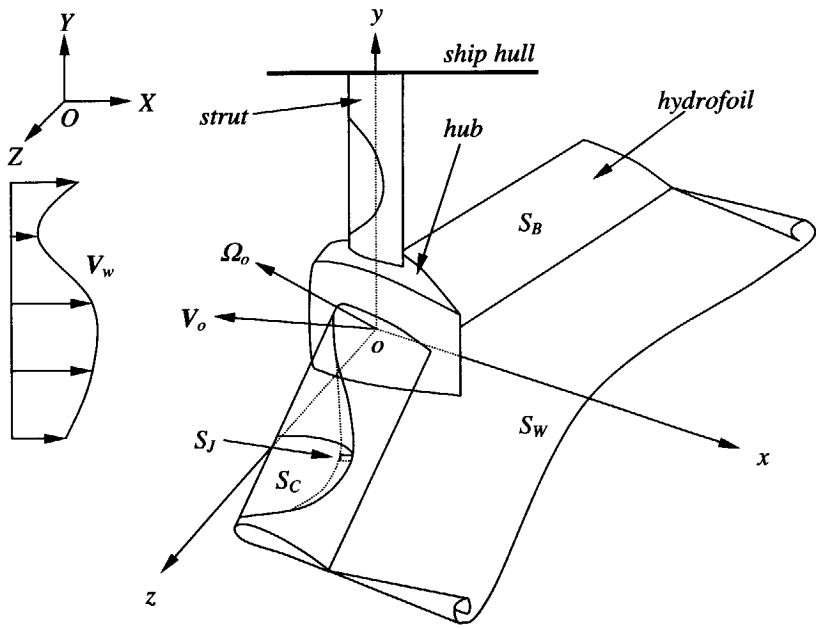

Figure 2.1: Schematics of the general problem by a hydrofoil system.

respectively. The body-fixed system is moving together with the bodies at a translational velocity of $\mathbf{V}_0$ and it is rotating, at the same time, around its origin at a rotational speed of Ω_0. The translational and rotational movement of this system is considered to be constant in the present problem, without accelerations.

When these bodies are moving in the fluid, they encounter a space-fixed existing flow — $\mathbf{V}_W$ in the fluid domain Ω, which extends to infinity. This space-fixed flow field can be thought of as the wake generated by a ship hull or a gust such as the underwater current.

As discussed in the previous chapter, the re-entrant jet at the end of a sheet cavity can flow into the cavity and impinge on the cavity surface near the leading edge. This complicated phenomenon of impinging is still hard to tackle by numerical simulations and hence will not be considered here.

In the present method, we cut the re-entrant jet off at a certain place in the cavity and introduce a special boundary along this cutting-off. We call this artificial boundary 'the re-entrant jet cross-section surface', denoted by S_J in Figure 2.1(see also Figure 6.1 for details). So, S_J consists of the vertical connection between the foil surface and the cavity. Then the entire

flow field is bounded by the boundary $\partial\Omega$ of the domain Ω, which consists of the boundary of the body surfaces S_B, the boundary of the cavity surfaces S_C and the boundary of the re-entrant jet cross section surfaces S_J.

2.2 Mathematical model

In the space-fixed Cartesian coordinate system $O-XYZ$, we denote the absolute velocity as $\mathbf{V} = (U, V, W)^T$. By assuming that the fluid is incompressible, the conservation law of mass requires the following continuity equation to be satisfied,

$$\nabla \cdot \mathbf{V} = 0. \tag{2.1}$$

If the unit volume forces acting on the fluid particles are $\mathbf{F}$ and they have a potential Φ, then this force can be written as the gradient of this potential as $\mathbf{F} = -\nabla\Phi$. The conservation law of momentum is expressed by the Navier-Stokes equation, which can be written in the following vector form,

$$\frac{D\mathbf{V}}{Dt} = -\nabla(\Phi + \frac{p}{\rho}) + \nu\nabla^2\mathbf{V}, \tag{2.2}$$

where $\frac{D}{Dt}$ denotes the material derivative with respect to the time t; p is the static pressure; ρ is the fluid mass density and ν is the kinematic viscosity of the fluid. At high Reynolds numbers, the viscous effects are confined within the thin boundary layers on the body surfaces, as well as on the cavity surfaces, or within the thin wake sheet S_W as shown in Figure 2.1. The fluid in the region outside these thin layers can be treated as inviscid fluid. For a homogeneous inviscid fluid, the Navier-Stokes equation is simplified into the following Euler equation,

$$\frac{D\mathbf{V}}{Dt} = -\nabla(\Phi + \frac{p}{\rho}). \tag{2.3}$$

In most engineering problems, the volume force consists of only the gravity force. Considering that the gravity is in the negative direction along the Y coordinate of the space-fixed system, the volume force potential is then written into the following form,

$$\Phi = gY, \tag{2.4}$$

where g is the gravity acceleration.

Assume that the flow is irrotational at some initial time $t = t_0$, so that,

$$\nabla \times \mathbf{V}(\mathbf{X}; t_0) = 0. \tag{2.5}$$

By taking the curl of the Euler equation, we obtain the following relation for the vorticity in the fluid at any time t,

$$\frac{D}{Dt}(\nabla \times \mathbf{V}) = (\nabla \times \mathbf{V}) \cdot \nabla \mathbf{V}. \tag{2.6}$$

This equation infers that, if no vorticity is transferred into the fluid domain, the initial irrotational flow will remain irrotational in the subsequent time.

Since the flow can be irrotational at any time for our present unsteady problem, if we have assumed it to be irrotational at one time in history, a time dependent velocity potential $\phi(\mathbf{X}; t)$ can be introduced to describe the flow velocity at any time, and,

$$\mathbf{V} = -\nabla\phi. \tag{2.7}$$

Substituting equation (2.7) into the continuity equation (2.1), we obtain the Laplace equation for this potential,

$$\nabla^2\phi = 0. \tag{2.8}$$

This is the governing equation of our present problem.

The solution of the Laplace equation, subject to certain boundary conditions (Dirichlet or Neumann type), yields the potential in the entire flow field. By using equation (2.7), the velocity distribution $\mathbf{V}$ throughout the entire fluid field is then obtained. The interesting observations are that the Laplace equation is a purely kinematic equation (it can be solved in either inertial or non-inertial frame of reference) and it does not include the time derivatives. The time dependency is introduced through its time-dependent boundary conditions.

The dynamics of the fluid flow is governed by Euler equation (2.3), which can be integrated over space, under the assumption of velocity potential as,

$$-\frac{\partial\phi}{\partial t} + \frac{1}{2}|\nabla\phi|^2 + gY + \frac{p}{\rho} = B(t) \tag{2.9}$$

where $B(t)$ is an arbitrary function of time, which has the same value for any point in the fluid field at a certain time. This function can be omitted without affecting the velocity field, or determined by choosing a reference point in the fluid at which the pressure and velocity potential are known. Equation (2.9) is called Bernoulli equation.

It should be noted that this Bernoulli equation is only valid in the inertial system, since it is the integration of the Euler equation (2.3) in this inertial system. The Bernoulli equation in the non-inertial coordinate system will be discussed in the following section.

We consider now the velocity generated by the moving bodies as a disturbance to an existing velocity field of $\mathbf{V}_W$ that is considered to be also a

potential flow. And further, we suppose this velocity field $\mathbf{V}_W$ to be steady in space, i.e., its potential is not a function of time. If we denote the disturbance velocity by $\mathbf{v}(\mathbf{X}, t)$, the potential can be divided, according to the following formula, into two parts,

$$\phi(\mathbf{X}; t) = \phi_W(\mathbf{X}) + \varphi(\mathbf{X}; t), \tag{2.10}$$

where ϕ_W is the velocity potential in the fluid domain for the existing velocity field with $\mathbf{V}_W = -\nabla\phi_W$, and φ is the disturbance velocity potential with $\mathbf{v} = -\nabla\varphi$. We note here again that ϕ_W is only a function of $\mathbf{X}$.

By choosing a point as the reference in the far field at which the disturbance velocity $\mathbf{v} = 0$, and denoting the static pressure at $Y = 0$ as p_∞ (for instance, the pressure upstream of the propeller shaft), we obtain the following equation that links the pressure at any field point to this reference point.

$$-\frac{\partial\phi}{\partial t} + \frac{1}{2}|\nabla\phi|^2 + gY + \frac{p}{\rho} = \frac{1}{2}(\mathbf{V}_W)^2 + \frac{p_\infty}{\rho} \tag{2.11}$$

Here we used that the partial time derivative of the existing flow field

$$\frac{\partial\phi_W}{\partial t} = 0. \tag{2.12}$$

Substituting equation (2.10) into equation (2.8) and (2.11), we get the following Laplace equation and Bernoulli equation for the disturbance velocity potential φ as,

$$\nabla^2\varphi = 0, \tag{2.13}$$

and,

$$-\frac{2}{V_\infty^2}\frac{\partial\varphi}{\partial t} + \frac{|\nabla\varphi - \mathbf{V}_W|^2 - |\mathbf{V}_W|^2}{V_\infty^2} + \frac{2}{{F_r}^2}\frac{Y}{L_\infty} = -C_p, \tag{2.14}$$

where L_∞ is the reference length, which could be the propeller diameter or the hydrofoil chord length; F_r and C_p are the Froude number and the pressure coefficient, respectively defined by the following formulas as,

$$F_r = \frac{V_\infty}{\sqrt{gL_\infty}}, \tag{2.15}$$

and,

$$C_p = \frac{p - p_\infty}{\frac{1}{2}\rho V_\infty^2}. \tag{2.16}$$

The elliptic problem of equation (2.13) can be solved if continuous boundary conditions (Dirichlet, Neumann or mixed type) are given on all boundaries of the flow domain. If the domain boundary $\partial\Omega$ is piecewise smooth, a solution exists for this problem. Since a constant does not contribute to the space derivatives of the potential, a unique solution for the velocity field can be obtained by equation (2.7) and (2.10).

Equation (2.14) gives an expression for the pressure in the flow domain in terms of the derivatives of the disturbance potential, with respect to both space and time. Then the pressure distribution throughout the entire fluid domain can be calculated accordingly.

Since the potential $\phi_W(\mathbf{X})$ is not time dependent in the space-fixed coordinates, it disappears from the term of the partial time derivative of the Bernoulli equation (2.14). This equation is easy to deal with in the sense that it is in the inertial frame of reference and it relates the pressure only to the disturbance potential. And also, the velocity potential ϕ_W is not explicitly seen in this equation, and hence it is not needed to be explicitly prescribed. But in some cases, equations in non-inertial frame of reference are even simpler and easier to be handled. The dynamic equations and its integration in the moving coordinates will be discussed in the following section.

2.3 Dynamic equations in moving coordinates

In many engineering applications, it is easier to treat the flow problem in a body-fixed coordinate system than in a space-fixed coordinate system, because the geometry of the bodies is always given in the body-fixed coordinates. For instance, the geometry of a propeller is described by pitch, chord length, skew, rake, etc. of the blades in a propeller-fixed coordinate system. Furthermore, it is easier to evaluate the space derivatives of the potential in this body-fixed coordinates.

For a propeller problem e.g., due to the rotation of the propeller around its shaft, this frame of reference is non-inertial. The continuity equation, which is reduced to the Laplace equation under the assumption of the existance of a velocity potential, is still valid in this non-inertial coordinate system, but the dynamic equation must be re-written. According to the theory of dynamics, the momentum equation (Euler equation) can be written as,

$$\frac{\mathbf{dV}}{\mathbf{dt}} + \Omega_0 \times \mathbf{V} = -\nabla(\Phi + \frac{p}{\rho}) \tag{2.17}$$

where $\frac{\mathbf{d}}{\mathbf{dt}}$ denotes the material derivative with respect to the moving coordinate system of $o - xyz$.

Integrating the above equation over space, the Bernoulli equation is obtained (Lamb (1945)) as,

$$-\frac{\partial\phi}{\partial t}+\frac{1}{2}|\mathbf{V}_0+\nabla\phi|^2+gY+\frac{p}{\rho}-\Omega_0\cdot(\nabla\phi\times\mathbf{x})=B(t). \tag{2.18}$$

We can carry out the same potential flow linear decomposition (similar to equation (2.10)) as in the following,

$$\phi(\mathbf{x};t)=\phi_W(\mathbf{x};t)+\varphi(\mathbf{x};t). \tag{2.19}$$

But the difference between equation (2.10) and (2.19) is that the potential ϕ_W in equation (2.19) becomes time dependent in the moving coordinates.

Substituting equation (2.19) in equation (2.8), we obtain the Laplace equation as,

$$\nabla^2\varphi=0, \tag{2.20}$$

which keeps the same form as equation (2.13).

Now we choose the same reference point as we discussed in the last section and make the Bernoulli constant $B(t)$ equal for the point of reference and the point in concern. We obtain the following simple form for the pressure coefficient in the moving coordinates,

$$-\frac{2}{V_\infty^2}\frac{\partial\varphi}{\partial t}+\frac{|\mathbf{V}_r|^2}{V_\infty^2}-\frac{|\mathbf{V}_0+\Omega_0\times\mathbf{x}-\mathbf{V}_W|^2}{V_\infty^2}+\frac{2}{F_r^2}\frac{Y(\mathbf{x};t)}{L_\infty}=-C_p, \tag{2.21}$$

where we have defined a relative velocity $\mathbf{V}_r$ with respect to the moving coordinates $o-xyz$ as,

$$\begin{aligned}\mathbf{V}_r&=-\nabla\phi-\mathbf{V}_0-\Omega_0\times\mathbf{x}\\&=\mathbf{V}_{r0}-\nabla\varphi,\end{aligned} \tag{2.22}$$

where $\mathbf{V}_{r0}=\mathbf{V}_W-\mathbf{V}_0-\Omega_0\times\mathbf{x}$ is the relative inflow and the second and the fifth terms in equation (2.18) on the left hand side are combined into the second term in equation (2.21).

It is interesting that the time partial derivative of the existing potential ϕ_W in the moving coordinates appears on both side of the equation, and hence cancels. Finally it does not appear explicitly in the above equation. When we evaluate the pressure on the body or the cavity surfaces, we need only to evaluate the partial time derivative of the disturbance potential φ.

For the case when a propeller operates in an oncoming uniform flow field, without inclination of the shaft, and when the advance velocity $\mathbf{V}_0$ is also

along the shaft, the relative flow field in the propeller-fixed coordinates can be considered as steady flow. If gravity is neglected, the above Bernoulli equation is then reduced to the following form,

$$\frac{|\mathbf{V}_r|^2}{V_\infty^2} - \frac{|\mathbf{V}_0 + \Omega_0 \times \mathbf{x} - \mathbf{V}_W|^2}{V_\infty^2} = -C_p, \tag{2.23}$$

This is the equation that we usually employ to calculate the pressure distribution on the propeller blades for open water operation.

2.4 Boundary conditions

In the present non-linear problem, three different boundaries can be distinguished. The most obvious ones are the body surfaces S_B and the cavity surfaces S_C. The re-entrant jet cross section surface S_J is also one of the boundaries. Depending on the type of the problem, the influence of a tunnel wall and its inlet and outlet surfaces can be also included (see Chapter 8). Boundary conditions for these different boundaries can be different and will be discussed in the following sub-sections.

2.4.1 Body surface

The condition that is always used in potential flow theory on the body surface and the tunnel wall is that of impermeability. On a space-fixed surface, like a tunnel wall, the normal component of the total velocity should be zero,

$$\frac{\partial \phi}{\partial n} = \frac{\partial \varphi}{\partial n} - \mathbf{V}_W \cdot \mathbf{n} = -\mathbf{V} \cdot \mathbf{n} = 0, \quad \text{on} \quad S_B, \tag{2.24}$$

where $\mathbf{n}$ denotes the unit normal vector on the body surface, pointing from the boundary surface into the fluid.

On moving bodies such as the wetted part of the propeller blades, the hydrofoil, the hub and the strut, the normal velocity of the fluid coincides with the velocity of the body motion in that direction,

$$\frac{\partial \varphi}{\partial n} = \mathbf{V}_W \cdot \mathbf{n} - (\mathbf{V}_0 + \Omega_0 \times \mathbf{x}) \cdot \mathbf{n} = \mathbf{V}_{r0} \cdot \mathbf{n}. \tag{2.25}$$

These are the time-dependent momentary boundary conditions, or called Neumann boundary conditions, which are valid both for inertial and non-inertial systems.

2.4.2 Cavity surface

The pressure inside of a sheet cavity has been measured by some experimentalists in their previous research (e.g. Shen & Peterson (1978)). It has been shown that the pressure is nearly constant for both steady and unsteady cavity flows, and it is close to the vapor pressure of the water. Pressure fluctuation is only found at the closure region of the cavity, where the cavity is no longer a smooth sheet and cavity clouds are formed. In our present simulation, we assume that the pressure inside the cavity is constant and equals the vapor pressure p_v. Then we can write the dynamic boundary condition on the cavity surface as,

$$p = p_v, \quad \text{on} \quad S_C. \tag{2.26}$$

Substituting this equation in both equation (2.14) and (2.21), we obtain the dynamic boundary conditions in the space-fixed coordinates as,

$$-\frac{2}{V_\infty^2}\frac{\partial \varphi}{\partial t} + \frac{|\nabla\varphi - \mathbf{V}_W|^2 - |\mathbf{V}_W|^2}{V_\infty^2} + \frac{2}{F_r}\frac{Y}{L_\infty} = \sigma, \tag{2.27}$$

and in the body-fixed coordinates as,

$$-\frac{2}{V_\infty^2}\frac{\partial \varphi}{\partial t} + \frac{|\mathbf{V}_r|^2}{V_\infty^2} - \frac{|\mathbf{V}_0 + \Omega_0 \times \mathbf{x} - \mathbf{V}_W|^2}{V_\infty^2} + \frac{2}{F_r^2}\frac{Y(\mathbf{x};t)}{L_\infty} = \sigma, \tag{2.28}$$

respectively. Here the cavitation number is defined by equation (1.1).

Since the position of the cavity surface is not known *a priori* and it is also a part of the solution itself, more than one boundary condition is needed. Besides the dynamic boundary condition on the cavity surface that we derived in the last paragraph, a kinematic boundary condition can be also enforced, which defines the evolution of the cavity surface with time.

There are two different ways to describe the kinematic boundary condition: the Lagrangian method and the Euler method. The observation of the particles on the cavity surface shows that the fluid particles on the cavity surface always remain on the cavity surface. To describe the cavity surface by tracing the fluid particles on the surface leads us to the following Lagrangian kinematic boundary equations,

$$\frac{D\mathbf{X}_C}{Dt} = \mathbf{V} = -\nabla\phi = \mathbf{V}_W - \nabla\varphi, \quad \text{on} \quad S_C, \tag{2.29}$$

where $\mathbf{X}_C$ denotes the position vector of the cavity surface in the space-fixed coordinates. Its counterpart equation, formulated in the body-fixed coordinates, reads,

$$\frac{\mathbf{dx}_C}{\mathbf{d}t} = (\mathbf{V}_W - \mathbf{V}_0 - \Omega_0 \times \mathbf{x}) - \nabla\varphi, \tag{2.30}$$

where $\mathbf{x}_C$ denotes the position vector of the cavity surface in the frame of reference $o - xyz$.

If we have a cavity surface which is defined by the equation,

$$S_C(X, Y, Z; t) = 0, \tag{2.31}$$

in the $O - XYZ$ coordinate system, or defined by,

$$S_C(x, y, z; t) = 0, \tag{2.32}$$

in the $o - xyz$ system, then at any time, the velocity of the particles perpendicular to these surface must be equal to the normal velocity of the surface,

$$\frac{DS_C(X, Y, Z; t)}{Dt} = 0, \tag{2.33}$$

or,

$$\frac{\mathbf{d}S_C(x, y, z; t)}{\mathbf{d}t} = 0. \tag{2.34}$$

These are the Eulerian descriptions of the kinematic boundary condition.

2.4.3 Re-entrant jet surface

Because the re-entrant jet cross section surface is the cut-off of the real re-entrant jet in the present method, it is then an artificial surface. There is no special kinematic boundary condition on this surface that is physically required. The only requirement on this surface is the dynamic boundary condition. If the viscous effects in the re-entrant jet is neglected, the dynamic condition states that the pressure in the jet should also be the same as the pressure on the cavity surface as well as in the cavity, and hence the vapor pressure,

$$p = p_v \quad \text{on} \quad S_J. \tag{2.35}$$

In Chapter 6, we will see that this dynamic boundary condition can be reduced into a simple kinematic boundary condition in the steady flow situation for both two-dimensional and three-dimensional flow problems. In two-dimensional steady flow, it can even be reduced to a Neumann boundary condition that states that the velocity normal to the jet surface is a constant and its value must be the same as the velocity on the cavity surface but pointing into the boundary, through which the fluid flows outside of the fluid domain. Further numerical experiments will show that this artificial boundary has very limited impact on the solution of the cavity flow (including the shape of the cavity). Here, we did not take into account the impinging of the re-entrant jet on the cavity surface.

However, in three-dimensional with a steady cavity flow, the velocity of fluid going through the cut-off of the jet is not necessarily equal to the cavity velocity because of the strong secondary cross-flow. In the most extreme case, the velocity on the jet cross section can be tangential to its surface. If this happens, the artificial surface will be a natural interface between the fluid and the vapor, and no re-entrant jet can be expected to flow upstream and impinge on the cavity surface close to the detachment point. So, a general kinematic condition can not be derived.

2.4.4 Other conditions

Besides the boundary conditions we have discussed in the previous sub-sections for the cavity surface, the body surface and the re-entrant jet surface, we have other important conditions that must be enforced to ensure the problem to be well-posed and the solution unique. These conditions include the detachment condition, the reattachment condition, the kinematic and dynamic conditions for the wake, etc.

Detachment condition

In the potential flow theory for cavity flows, a so-called *smooth separation* condition is normally used. It is also called Brillouin-Villat condition. This condition states that the curvature of the free streamlines is finite at the separation point, and for smooth bodies, this curvature should be equal to the curvature of the body at the detachment point.

Instead of using this condition, an alternative weaker condition, which states that the cavity surface should be tangential to the body surface, can be used. It is written as,

$$\mathbf{n}_{cavity} = \mathbf{n}_{body} \quad \text{at} \quad \Gamma_d, \tag{2.36}$$

where, Γ_d denotes the detachment line. Practical treatment of the detachment condition and its influence on the solution will be discussed in detail in Chapter 5.

Reattachment condition

At the re-attachment point of the cavity, if the free streamline is going to touch the body surface at a non-zero angle, a stagnation point forms. Then a contradiction occurs. On the one hand, the pressure at this point should be the same as the pressure on the cavity surface. Or, in other words, the pressure at this point remains as low as p_v according to Bernoulli's equation. But on the other hand, the pressure should be as high as the pressure at a stagnation

point. This contradiction requires that the streamlines on the cavity must be tangent to the body surface (but the cavity surface itself doesn't have to be).

In three-dimensional flow, the flow can turn into the cross direction and hence the cavity surface can re-attach with the body surface at any angle. In unsteady cavity flows, the reattachment point is moving, and the speed of the movement can be so high that the cavity surface may reattach to the body surface with any angle but still keep the same pressure as that in the cavity.

But in two-dimensional steady flow, tangential re-attachment is the only possible re-attachment. There are two ways the cavity can reattach to the surface in this case, as shown in Figure 2.2.

Figure 2.2: Schematics of the possible topology for reattachment for 2-dimensional steady cavity flow. a) tangential with body surface but travels upstream; b) tangential with body surface but travels downstream.

It has been stated by Ronald (1989) and proven by De Koning Gans (1994) that the cavity surface must be concave toward the body surface (the guide surface). The illustration of Figure 2.2(b) has a convex shaped cavity close to the reattachment point, and hence it does not occur in reality. Figure 2.2(a), where the flow enters the cavity as a re-entrant jet, is the only possible reattachment. So, we state that the re-entrant jet is always needed for a 2-dimensional steady cavity flow.

Wake and Kutta condition

In potential flow theory, the vortex shear layer behind a lifting body is thought to be confined within a sheet without thickness, which we call the wake sheet. The flow is separated by the sheet and the fluid velocity on its two sides can be different. But this sheet can never be split into two sheets and it carries no force. This leads to the following kinematic and dynamic conditions,

$$\frac{\partial \phi}{\partial n_W^u} = \frac{\partial \phi}{\partial n_W^l}, \tag{2.37}$$

and,

$$p_W^u = p_W^l, \tag{2.38}$$

for the sheet, respectively. Here, $\mathbf{n}_W$ denotes the unit normal vector on the wake surface; p_W the pressure on the wake; and the superscript u and l represent the upper and lower sides of the wake sheet, respectively.

Equation (2.37) tells us that the wake sheet will stay stationary in space if the flow is steady, and the wake sheet will move but not split if the flow is unsteady.

Notice that equation (2.38) is not only applicable to the wake but also to its edges, including the trailing edge of the lifting bodies, where the wake surface starts. When this condition is applied at the trailing edge, we call it the Kutta condition,

$$p^u_{T.E.} = p^l_{T.E.}. \tag{2.39}$$

The implementation of the conditions and the influence of the wake shape and Kutta condition on the cavity prediction will be discussed more in detail in Chapter 5.

Vorticity conservation

Choosing an arbitrary closed curve $C(t)$ in the flow field, which is moving with the flow, we can calculate the circulation Γ of the flow associated with this curve, which is equal to the flux of vorticity through the surface of which $C(t)$ is the boundary contour. Notice that the curve itself can change shape with time in the flow.

$$\Gamma = \int_{C(t)} \mathbf{V} \cdot d\ell, \tag{2.40}$$

where, $d\ell$ is the element of the closed curve $C(t)$.

By taking the derivative of the above equation with respect to time t, we obtain,

$$\frac{D\Gamma}{Dt} = \int_{C(t)} \frac{D\mathbf{V}}{Dt} \cdot d\ell + \int_{C(t)} \mathbf{V} \cdot [(d\ell \cdot \nabla)\mathbf{V}] \tag{2.41}$$

where the first term measures the rate of change of the velocity and the second measures the rate of change of the element $d\ell$ of the curve $C(t)$.

Substituting equation (2.2) in the first term of equation (2.41), we have,

$$\begin{aligned}\frac{D\Gamma}{Dt} &= \nu\int_{C(t)}(\nabla^2\mathbf{V})\cdot d\ell + \int_{C(t)}\mathbf{V}\cdot[(d\ell\cdot\nabla)\mathbf{V}] - \int_{C(t)}\nabla\left(\Phi+\frac{p}{\rho}\right)\cdot d\ell \\ &= \nu\int_{C(t)}(\nabla^2\mathbf{V})\cdot d\ell + \int_{C(t)}d\ell\cdot\nabla\left[\frac{1}{2}V^2-\Phi-\frac{p}{\rho}\right] \\ &= \nu\int_{C(t)}(\nabla^2\mathbf{V})\cdot d\ell.\end{aligned} \tag{2.42}$$

This equation tells us that the circulation around a closed curve, which is moving with the fluid, can only change through viscous diffusion.

For high-Reynolds number flow, or potential flow as in the present problem, the circulation around any closed curve is conserved,

$$\frac{D\Gamma}{Dt} = 0. \tag{2.43}$$

This is Kelvin's circulation theorem. The shedding of the vorticity at the trailing edge of the lifting bodies must satisfy this theorem, whether it is 2-Dimensional or 3-Dimensional, steady or unsteady flow.

Quiescent condition at infinity

The spatial gradient of the disturbance potential φ, as it is defined, should vanish at infinity,

$$\nabla\varphi \to 0 \quad \text{when} \quad \mathbf{x}\to\infty. \tag{2.44}$$

This is automatically garanteed by using Green's Function for the solution of Laplace's equation. And more over, if the source singularity distribution on the surfaces are limited, the disturbance potential itself is pre-assumed to be zero at infinity even if there is no condition requiring for a fixed potential value at a certain position in the flow field,

$$\varphi \to 0 \quad \text{when} \quad \mathbf{x}\to\infty. \tag{2.45}$$

For the dynamic quiescent condition at infinity, it requires that the pressure induced by the disturbance potential should also vanish at infinity,

$$\tilde{p}(\varphi) \to 0 \quad \text{as} \quad \mathbf{x}\to\infty, \tag{2.46}$$

where $\tilde{p}(\varphi)$ is the component of the pressure caused by the disturbance velocity field.

2.5 Solving strategies

The equations that we have discussed in section 2.1 through 2.4 form the equation set which describes the present problem both in the flow field and the boundaries. This set of equations forms a hyperbolic system which describes the motion of the cavity surface in space with respect to time. It can be viewed and hence treated in different ways. The most natural way to treat this problem is to view it as an elliptic problem with time-dependent boundary conditions. So, at a certain time, the problem can be solved as a spatial problem for given boundary conditions. Subsequently the boundary condition is updated to a new time level and the spatial problem can be solved again at this new time level, and so forth. This is the so-called *method of line approach.*

In the spatial problem, the governing equation for the disturbance potential φ is the Laplace equation (2.13) or (2.20). It is a linear equation and looks very simple and can be solved easily. But the solution of this equation can become very complicated due to its time-dependent and fully non-linear boundary conditions. The problem can become extremely hard to solve when the boundary itself is part of the solution and moving with time, like the boundary of the wave and cavity surfaces. The nonlinearity of the present problem certainly originates from the boundary and its motion.

Some of these equations on the boundary are easy to be handled and implemented in the calculation, like the boundary condition of equation (2.24) and (2.25) on the wetted part of the bodies. But some of them are not that easy to be treated, like the equations on the cavity surface, (2.27), (2.28).

The updating of the spatial boundary-value problem includes both the updating of the boundary conditions and the boundary position. The updating of the Neumann boundary condition on the wetted body surface with time is trivial, since the boundary position does not have to be updated. The updating of the Dirichlet boundary condition on the cavity surface needs some additional equations. This will be discussed in the following sections.

2.5.1 Cavity surface updating

In order to show the general idea of the cavity surface updating, here we take the Lagrangian method as an example. Detailed discussion about its numerical stability and convergence will be given in Chapter 4.

As we trace the cavity surface by following the particles on the cavity surface using the Lagrangian method (equation (2.29) and (2.30)), the updating of the Dirichlet boundary condition on the cavity surface can be done in a similar way.

We view the potential φ as a property of a particle. Then we have the following material derivatives of the potential to describe its variation in space

for both space-fixed and the body-fixed frame of referencec,

$$\frac{D\varphi}{Dt} = \frac{\partial\varphi}{\partial t} + \mathbf{V}\cdot\nabla\varphi, \quad \text{on} \quad S_C, \tag{2.47}$$

and,

$$\frac{\mathbf{d}\varphi}{\mathbf{d}t} = \frac{\partial\varphi}{\partial t} + \mathbf{V}_r\cdot\nabla\varphi, \quad \text{on} \quad S_C, \tag{2.48}$$

respectively, where $\mathbf{V}$ and $\mathbf{V}_r$ are the velocity of the particles in the recpective frames of reference.

Taking the equation for the body-fixed coordinates as an example, the equations for the updating of the cavity surface consists of,

$$\frac{\mathbf{d}\mathbf{x}_C}{\mathbf{d}t} = (\mathbf{V}_W - \mathbf{V}_0 - \Omega_0\times\mathbf{x}) - \nabla\varphi, \tag{2.49}$$

and,

$$\frac{\mathbf{d}\varphi}{\mathbf{d}t} = \frac{\partial\varphi}{\partial t} + \mathbf{V}_r\cdot\nabla\varphi, \quad \text{on} \quad S_C, \tag{2.50}$$

where the partial time deriviative of the potential is given by Bernoulli equation (2.21), re-written here as,

$$\frac{\partial\varphi}{\partial t} = \frac{|\mathbf{V}_r|^2}{2} - \frac{|\mathbf{V}_0+\Omega_0\times\mathbf{x}-\mathbf{V}_W|^2}{2} - \frac{V_\infty^2}{2}\sigma + \frac{Y(\mathbf{x};t)}{F_r^2}\frac{V_\infty^2}{L_\infty}. \tag{2.51}$$

If we introduce a new variable vector $\mathbf{q}$ (solution vector) that consists of the cavity surface position vector $\mathbf{x}_C$ and the potential φ as $\mathbf{q} = (x_C, y_C, z_C, \varphi)^T$, we can combine equation (2.49), (2.50) together into the following ordinary differential equation,

$$\frac{\mathbf{d}\mathbf{q}}{\mathbf{d}t} = \mathbf{f}(\mathbf{q},t) \tag{2.52}$$

where the function $\mathbf{f}$ consists of the right-hand side of equation (2.49) and (2.50), which are known from the spatial solution of the potential φ and from the surface position.

Then the update of the cavity surface and its boundary condition is calculated by solving the ordinary differential equation (2.52) in time. The numerical algorithm for solving this equation, and also for the alternative method like the Neumann method, will be discussed in detail in Chapter 4.

2.5.2 Spatial problem

Solving the spatial problem governed by Laplace's equation can be achieved in different ways. When we think about the numerical method for this problem, we immediately find, that the finite-difference method, finite-volume method, finite-element method and boundary-integral method are all available.

All of these methods are well developed in the last few decades. No one is superior to the other in the sense of efficiency and accuracy of the solver. Nowadays when people are using these methods to solve a practical problem, much work has to be done for generating the grid of a specific complicated geometry. Comparing to other methods, the boundary-integral method needs only a surface grid rather than a volume grid and hence grid generation for this method costs relatively less. For a complex geometry like a propeller blade, the boundary-integral method has been successful both in efficiency and accuracy. Hence, the boundary-integral method based on point collocation will be used in the present research.

The boundary-integral method is not new and it has been used in different fields. The basic theory is Green's theorem. Using this theory, the spatial solution of the potential φ can be written as the integral of its boundary values in the following way,

$$\varphi(\mathbf{x};t) = \int_{\partial\Omega} \left[\frac{\partial\varphi(\tilde{\mathbf{x}};t)}{\partial n_{\tilde{\mathbf{x}}}} G(\tilde{\mathbf{x}};\mathbf{x}) - \varphi(\tilde{\mathbf{x}};t) \frac{\partial G(\tilde{\mathbf{x}};\mathbf{x})}{\partial n_{\tilde{\mathbf{x}}}} \right] dS_{\tilde{\mathbf{x}}}, \tag{2.53}$$

where $G(\tilde{\mathbf{x}};\mathbf{x})$ is the Green function and $\tilde{\mathbf{x}} \in \partial\Omega$.

Details of the theory and its application to the present method will be discussed in the next chapter.

2.5.3 Initial condition

Because our present problem is a hyperbolic problem, an initial condition must be given. When we solve the problem with the method of line approach that is based on solving Laplace's equation, the solution depends on the time-dependent boundary conditions. Then, an accurate solution of the cavity flow at time $t = t_0$ must be obtained.

The well-posedness of a hyperbolic problem requires that at time $t \geq 0$ a solution $\mathbf{q}(t)$ exists, which is unique and continuously depends on the initial condition and the boundary conditions.

Since the solution depends on the initial condition, in order to render our present problem well-posed, a good initial condition should be given.

In our calculation, we start always from the steady flow state, and then march in time to reach the final unsteady state. The fully non-linear steady calculation of cavity flow will be treated first in the following chapters and their results will be given in details and validated in Chapter 6.

Chapter 3

Panel Method

The boundary integral equations for the potential theory of cavity flows are given in this chapter. A potential based panel method with higher-order geometry and singularity descriptions is discussed. The lower-order panel method based on hyperboloidal panels is implemented and used in the present research. The perspectives on using the higher-order panel method in cavity flows are made.

3.1 Introduction

With the advent of the fast electronic computers in the 1950's, boundary integral method (such as panel method) was introduced in various fields for solving potential problems, such as aerodynamics, elastostatics, acoustics, etc. (Hess (1990)). Since the application of the boundary element methods to marine propellers with a velocity based method (Hess & Valarezo (1985)) and potential based method (Lee *et al.* (1994)), remarkable progress has been made for prediction accuracy and computational efficiency. For fully wetted propeller flow, panel methods can, at the present time, handle very complicated geometry like propeller hubs, highly-skewed blades (Kinnas & Hsin (1992)), propeller ducts (Kerwin *et al.* (1987)) and rolling-up wake (Pyo (1995)). Panel methods can also handle difficult flow conditions such as off-design operating condition. Comparative calculations of propeller flow by panels method have been carried out for steady operating condition by 19^{th} ITTC Propulsion Committee and for unsteady operating condition by 22^{nd} ITTC Propulsion Committee. Results show that the panel method can not only predict the total forces (K_T, K_Q) accurately, but also predict the pressure distribution on the blade surface reasonably well.

With respect to the velocity-based panel method, the potential-based panel

method reduces the computational effort for the influence coefficient calculations and the memory by two third at least. So, the potential based panel method is now the mainstream of the panel methods used for propeller performance predictions. Another advantage of the potential based panel method is that it is easier to be extended to the sheet cavitation prediction of propellers, because the dynamic boundary condition is easier enforced on the cavity surface by prescribing the potential than by prescribing the velocity. Most of these potential based panel methods are using hyperboloidal quadrilateral panels with constant source and constant normal-dipole distributions, as proposed by Morino & Kuo (1974). The analytical formulas for the influence coefficient, derived by Morino, are exact for the dipole, but approximate for the source distribution.

The advantage of the constant singularity panel method is its simplicity and the relative ease of its implementation. The main drawbacks are the grid dependence of the solution and the large number of panels that are usually needed for complex geometry and hydrodynamics, such as the flow around the cavity end.

The use of a large number of panels leads to an increased computation costs for solving the system equations. The leading edge of a lifting body, such as a hydrofoil, and the cavity end where the re-entrant jet turns direction by 180° are two examples where both high local geometry curvature and steep change of the surface velocity and pressure occur. For unsteady fully wetted flow, influence coefficients normally don't need to be re-evaluated for each time step, but for fully non-linear cavity flows, the influence coefficients must be re-evaluated. Calculation efficiency has to be taken into account in our present simulation.

As the effort to achieve equivalent accuracy and grid independent solution for a smaller number of panels, the higher-order panel methods have been proposed. Hess (1979) found that the high-order method is superior to the constant panel method for the interior flow with an example of the flow through a duct of varying cross-section. Johnson & Rubbert (1975) concluded that the higher-order method is insensitive to the panel distributions by a case of random discretization of the surface.

In the analytical calculation of the influence coefficients for the higher-order panel method, two different methods are used. One carries out the integration based on a physical reference plane which is the projection of the original curved surface on its surface tangential plane through the collocation point (Romate (1989)). The other method calculates the coefficients based on a body-fitted curvilinear coordinates (see De Koning Gans (1994), Maniar (1995)).

In the present investigation for the prediction of sheet cavity flows, both the lower-order panel method, based on hyperboloidal panels with constant singularity distribution, and the higher-order panel method, based on the body-fitted

curvilinear coordinates, are implemented. The details about the description of the geometry and the solution, and the calculation of the influence coefficients for the higher-order panel method are discussed in the following sections. A comprehensive review on panel method in general can be found in Romate (1989).

3.2 Green's identity

Before describing the details of the panel method, the boundary integral equations for the potential theory are discussed briefly first, assuming that the reader is familiar with most of the concepts. The elements of potential theory and the boundary integral methods can be found in many textbooks on fluid dynamics. Rigorous mathematical treatments of the potential theory are also available in the publications like Courant & Hilbert (1962). Since there are so many different ways to use these integral equations, the choice of the integral equations for our present cavity flow problem is the main discussion in the section.

Our present concern is the solution of the Laplace equation of (2.13) or (2.20),

$$\nabla^2\varphi(\mathbf{x};t) = 0 \quad \mathbf{x} \text{ in } \Omega, \tag{3.1}$$

subject to the boundary conditions, either in Dirichlet or in Neumann format,

$$B(\varphi, \frac{\partial\varphi}{\partial n}, \tilde{\mathbf{x}}) = 0 \quad \tilde{\mathbf{x}} \text{ on } \partial\Omega, \tag{3.2}$$

where, Ω is the fluid field of our concern which is assumed to be singly-connected, and $\partial\Omega$ is the boundary. It is assumed that the potential φ and its spatial derivatives are finite and continuous at all points, except for some possible points on the boundary, where a non-smooth junction of two smooth surfaces may occur. So, the solution depends highly on the boundary shape and the boundary conditions. When the potential or its derivatives are given on all of the boundaries, there is a unique solution in the fluid field and the solution can be expressed as an integral over the boundaries.

If we apply Green's theorem to this fluid field and assume that one of the field is $\varphi(\mathbf{x};t)$ of our solution and the other is the Green's function of,

$$G(\tilde{\mathbf{x}};\mathbf{x}) = -\frac{1}{4\pi r} \quad \text{for 3D space,} \tag{3.3}$$

and,

$$G(\tilde{\mathbf{x}};\mathbf{x}) = \frac{1}{2\pi}\ln(r) \quad \text{for 2D space,} \tag{3.4}$$

where $\tilde{x}$ is the position vector of a point on the boundary, $\mathbf{x}$ is a point in the field and $r = |\mathbf{r}| = |\mathbf{x} - \tilde{\mathbf{x}}|$.

When the point $\mathbf{x}$ is in the fluid field, the Green's function becomes singular at this point. By excluding this singularity with the small spherical neighborhood of this point $\mathbf{x}$, the boundary integral can be calculated analytically. The Green theorem becomes,

$$\varphi(\mathbf{x};t) = \int_{\partial\Omega} \left[\frac{\partial\varphi(\tilde{\mathbf{x}};t)}{\partial n_{\tilde{\mathbf{x}}}} G(\tilde{\mathbf{x}};\mathbf{x}) - \varphi(\tilde{\mathbf{x}};t) \frac{\partial G(\tilde{\mathbf{x}};\mathbf{x})}{\partial n_{\tilde{\mathbf{x}}}} \right] dS_{\tilde{\mathbf{x}}}. \tag{3.5}$$

Taking the spatial gradient of the above identity, we obtain the following equation for the velocity field as,

$$\nabla_{\mathbf{x}}\varphi(\mathbf{x};t) = \int_{\partial\Omega} \left[\frac{\partial\varphi(\tilde{\mathbf{x}};t)}{\partial n_{\tilde{\mathbf{x}}}} \nabla_{\mathbf{x}} G(\tilde{\mathbf{x}};\mathbf{x}) - \varphi(\tilde{\mathbf{x}};t) \nabla_{\mathbf{x}} \left(\frac{\partial G(\tilde{\mathbf{x}};\mathbf{x})}{\partial n_{\tilde{\mathbf{x}}}} \right) \right] dS_{\tilde{\mathbf{x}}}, \tag{3.6}$$

where the gradient $\nabla_{\mathbf{x}}$ denotes the operation with respect to the field point $\mathbf{x}$.

When the field point is on the boundary $\partial\Omega$, the above equations can be derived in a similar way and become into the following form,

$$\frac{\theta(\mathbf{x})}{4\pi}\varphi(\mathbf{x};t) = \oint_{\partial\Omega} \left[\frac{\partial\varphi(\tilde{\mathbf{x}};t)}{\partial n_{\tilde{\mathbf{x}}}} G(\tilde{\mathbf{x}};\mathbf{x}) - \varphi(\tilde{\mathbf{x}};t) \frac{\partial G(\tilde{\mathbf{x}};\mathbf{x})}{\partial n_{\tilde{\mathbf{x}}}} \right] dS_{\tilde{\mathbf{x}}}, \tag{3.7}$$

$$\frac{\theta(\mathbf{x})}{4\pi}\nabla_{\mathbf{x}}\varphi(\mathbf{x};t) = \oint_{\partial\Omega} \left[\frac{\partial\varphi(\tilde{\mathbf{x}};t)}{\partial n_{\tilde{\mathbf{x}}}} \nabla_{\mathbf{x}} G(\tilde{\mathbf{x}};\mathbf{x}) - \varphi(\tilde{\mathbf{x}};t) \nabla_{\mathbf{x}} \left(\frac{\partial G(\tilde{\mathbf{x}};\mathbf{x})}{\partial n_{\tilde{\mathbf{x}}}} \right) \right] dS_{\tilde{\mathbf{x}}}, \tag{3.8}$$

where, $\oint$ is the finite part of the integral and $\theta(\mathbf{x})$ is the interior angle of the boundary $\partial\Omega$ at point $\mathbf{x}$. For a smooth boundary at $\mathbf{x}$, $\theta(\mathbf{x}) = 2\pi$.

If the boundary values of both the potential and its derivatives are known, the potential and the velocity throughout the whole flow field can be calculated through equation (3.5) and (3.6). If only one of the potentials or the potential derivatives are known, the other can be always obtained by using either equation (3.7) or (3.8). The uniqueness of the solution has been discussed intensively by Romate (1989). It is concluded that, for external flow problem with mixed boundary conditions like our present cavity flow problem, the above two equations always give unique solution.

If we apply equation (3.7) onto the body surface where the impermeable boundary condition (2.25) (Neumann boundary condition) is enforced, then we obtain the following Fredholm integral equation of the second kind for the potential $\varphi(\mathbf{x};t)$,

$$\frac{\theta(\mathbf{x})}{4\pi}\varphi(\mathbf{x};t) + \oint_{\partial\Omega}\left[\varphi(\tilde{\mathbf{x}};t)\frac{\partial G(\tilde{\mathbf{x}};\mathbf{x})}{\partial n_{\tilde{\mathbf{x}}}}\right] dS_{\tilde{\mathbf{x}}} = \oint_{\partial\Omega}\left[\frac{\partial\varphi(\tilde{\mathbf{x}};t)}{\partial n_{\tilde{\mathbf{x}}}}G(\tilde{\mathbf{x}};\mathbf{x})\right] dS_{\tilde{\mathbf{x}}}, \tag{3.9}$$

where the right-hand side is known.

If we apply equation (3.7) on the cavity surface where the potential is prescribed by the solution of equation (2.48) (Dirichlet boundary condition), then we obtain the following Fredholm integral equation of the first kind for the potential derivatives $\partial\varphi(\mathbf{x};t)/\partial n_{\tilde{\mathbf{x}}}$,

$$\oint_{\partial\Omega}\left[\frac{\partial\varphi(\tilde{\mathbf{x}};t)}{\partial n_{\tilde{\mathbf{x}}}}G(\tilde{\mathbf{x}};\mathbf{x})\right] dS_{\tilde{\mathbf{x}}} = \frac{\theta(\mathbf{x})}{4\pi}\varphi(\mathbf{x};t) + \oint_{\partial\Omega}\left[\varphi(\tilde{\mathbf{x}};t)\frac{\partial G(\tilde{\mathbf{x}};\mathbf{x})}{\partial n_{\tilde{\mathbf{x}}}}\right] dS_{\tilde{\mathbf{x}}}, \tag{3.10}$$

where the right-hand side is known.

Fredholm equations of the first kind will generate a matrix which is ill-conditioned because it has no large entries on the main diagonal. If all of the equations are Fredholm equations of the first kind, it has been found that this kind of system of equations may cause severe numerical instability. To improve the condition, we can take an inner product of equation (3.8) with the surface normal unit vector $n_{\mathbf{x}}$ at $\mathbf{x}$ and move the potential integral term to the right hand side, then we obtain a Fredholm equation of the second kind for the potential derivative as,

$$\frac{\theta(\mathbf{x})}{4\pi}\frac{\partial\varphi(\mathbf{x};t)}{\partial n_{\mathbf{x}}} - \oint_{\partial\Omega}\left[\frac{\partial\varphi(\tilde{\mathbf{x}};t)}{\partial n_{\tilde{\mathbf{x}}}}\frac{\partial G(\tilde{\mathbf{x}};\mathbf{x})}{\partial n_{\mathbf{x}}}\right] dS_{\tilde{\mathbf{x}}} = -\oint_{\partial\Omega}\left[\varphi(\tilde{\mathbf{x}};t)\frac{\partial^2 G(\tilde{\mathbf{x}};\mathbf{x})}{\partial n_{\tilde{\mathbf{x}}}\partial n_{\mathbf{x}}}\right] dS_{\tilde{\mathbf{x}}}. \tag{3.11}$$

It will be a perfect combination by using equation (3.9) on the body surface and using equation (3.11) on the cavity surface, respectively, since both of these two integral equations are Fredholm equations of the second kind. In this situation, the system matrix will be diagonally dominant. An iterative method, like the conjugate gradient method, can then be used, and solving the equations can be more efficient and economic.

But on the other hand, using equation (3.11) results in more effort for the evaluation of the influence coefficients, which have to be computed as vector variables. The evaluation of these influence coefficients is much more expensive (roughly about three times more expensive) than that of equation (3.9). For our present three-dimensional fully non-linear simulation, we always have to re-evaluate the influence coefficients when the cavity shape is changing in time

(or within a time step when an iterative method is used). This makes the above combination extremely expensive and hence practically prohibitive.

For lifting bodies, a Kutta condition, which results in the required circulation around the bodies, is always needed and must be enforced at the trailing edge. When an implicit Kutta condition (Morino condition) is used, the original diagonal dominant matrix will be destroyed (more or less). But the application of the panel method for a complex geometry like highly skewed propellers did not show any numerical instability (Kerwin *et al.* (1987), Hoshino (1989)). And furthermore, the continuity requirement of the potential at the cavity detachment point (which will be discussed in section 4.5 and given in equation e.g. (6.5) and (6.26)) will also affect this diagonal dominance. Successful application of the Green's Identity of equation (3.7) to both the body surface and the free surface in wave calculation (Romate (1989)) and cavity calculation (Kinnas & Fine (1993), Dang & Kuiper (1998*a*)) shows that partially using a Fredholm equation of the first kind will not result in numerical instability. And also, it forms a system of equations that is the cheapest for the evaluation of the influence coefficients.

So, we chose the combination of equation (3.9) and (3.10) for our present investigation.

3.3 Description of the geometry and solution

3.3.1 The geometry

The hydrodynamic devices that are designed nowadays turn out to be very sophisticated and complicated in order to meet certain design requirements. The surface geometry of these devices is far more complicated than can be described analytically by simple mathematical formulas. A marine propeller consists of, at least, a few blades and a hub. For one blade, the surface is very smooth, but the blade width, the thickness, the pitch and the skew can vary along the radius. To express the geometry using surface gridding is not in our present scope. In the following sections, ways are discussed to re-construct the surface locally with mathematical formulas based on the given position of discrete grid points on the surface.

In general, it is difficult to find a global mathematical expression for a complicated surface. For the usage of a panel method, a local mathematical expression of the geometry suffices.

The surface is first discretized into smooth patches. All the patches are assumed to be connected smoothly and re-construct the original geometry. We call these patches 'panels'. Here we discuss only quadrilateral panels forming a structured grid. Given panel index in two directions as ip and jp, then a panel is uniquely identified by its index pair (ip, jp). We define a surface-fitted

curvilinear coordinate system (corresponding to these indices) as s_1 and s_2. For the later use, the third coordinate is along the normal direction. It is denoted as s_3. Suppose the position of a point on the surface is described by its position vector $\mathbf{x}(s_1, s_2)$, then the position vector can be written into a Taylor expansion around the panel center (ip, jp) (normally at $(s_1, s_2) = (0, 0)$) as,

$$\mathbf{x}_{ip,jp}(s_1, s_2) = \sum_{i=0}^{N} \sum_{j=0}^{N-i} \mathbf{a}_{i,j} \ {s_1}^i \ {s_2}^j \tag{3.12}$$

where N is the order of the expansion, and subscripts ip, jp emphasize that this expansion is only valid for panel ip, jp. Note that there is no restriction on the choice of the body-fitted coordinates (say, no need to be orthogonal) except that the above expression gives the correct geometry that connects with all its neighbor panels with the degree of smoothness desired.

Once the coefficients $\mathbf{a}_{i,j}$ are obtained, the geometry of the panel is defined. For a certain order of expansion, the coefficients are not unique, they depend on the numerical scheme. Different schemes give different coefficients. A good scheme should give the best approximation of the original geometry with fast convergence of the expansion and should make a smooth connection between panels.

Consider an arbitrary scalar one-dimensional function $f_{ip}(s_1)$ on panel ip, (here we take s_1 as the variable), the following Taylor expansion will be valid both for s_1 and s_2 curvilinear coordinate on the body surface.

$$f_{ip}(s_1) = \sum_{i=0}^{N} a_i^{(N)} {s_1}^i = \sum_{i=0}^{N} \left[\frac{1}{i!} \frac{\partial^i}{\partial {s_1}^i} f_{ip}(s_1) \right]_{s_1=0} {s_1}^i, \tag{3.13}$$

where N denotes the order of the expansion. Because the coefficient a_i depend on the order, we use a superscript (N). Subscript ip means that this expansion is only applicable for panel ip. The coefficients of this expansion $a_i^{(N)}$ are given in Appendix A. According to equation (A.6), these coefficients depend on the function values at the panel center and at the neighboring panel centers. It can be written as,

$$a_i^{(N)} = \left[\frac{1}{i!} \frac{\partial^i}{\partial {s_1}^i} f_{ip}(s_1) \right]_{s_1=0} = \sum_{k=1}^{N_k(N)} C_k^{N_k(N)} f_{ip+ir(k)} \tag{3.14}$$

where, N_k is the number of supports of the spline, which depends on the order of the expansion. Details of the expansion can be found in Appendix A. The

increment $ir(k)$ is the relative index of the supporters. So, we can write the expansion as,

$$f_{ip}(s_1) = \sum_{i=0}^{N} \left[\frac{1}{i!} \frac{\partial^i}{\partial {s_1}^i} f_{ip}(s_1) \right]_{s_1=0} {s_1}^i = \sum_{i=0}^{N} \left(\sum_{k=1}^{N_k(N)} C_k^{(N)} f_{ip+ir(k)} \right) {s_1}^i. \tag{3.15}$$

Applying the above formula to the s_2 direction for a function $g_{jp}(s_2)$ at panel jp, we obtain the similar expansion,

$$g_{jp}(s_2) = \sum_{j=0}^{N} \left[\frac{1}{j!} \frac{\partial^j}{\partial {s_1}^j} g_{jp}(s_2) \right]_{s_2=0} {s_2}^j = \sum_{j=0}^{N} \left(\sum_{l=1}^{N_l(N)} C_l^{(N)} g_{jp+ir(l)} \right) {s_2}^j, \tag{3.16}$$

where $jr(l)$ is also the relative index but in jp direction.

For a two-dimensional function, like the geometry position vector, we need construct the two-dimensional Taylor expansions. We can do this sequentially in two directions. If we expand it in s_2 direction first, we have,

$$\begin{aligned} \mathbf{x}_{ip,jp}(s_1, s_2) &= \sum_{i=0}^{N} \sum_{j=0}^{N-i} \mathbf{a}_{i,j} {s_1}^i {s_2}^j \\ &= \sum_{i=0}^{N} \sum_{j=0}^{N-i} \left[\frac{1}{i!j!} \frac{\partial^{i+j}}{\partial {s_1}^i \partial {s_2}^j} \mathbf{x}_{ip,jp}(s_1, s_2) \right]_{s_1=0, s_2=0} {s_1}^i {s_2}^j \\ &= \sum_{i=0}^{N} \left[\frac{1}{i!} \frac{\partial^i}{\partial {s_1}^i} \left(\sum_{j=0}^{N-i} \frac{1}{j!} \frac{\partial^j}{\partial {s_2}^j} \mathbf{x}_{ip,jp}(s_1, s_2)|_{s_2=0} {s_2}^j \right) \right]_{s_1=0} {s_1}^i. \end{aligned} \tag{3.17}$$

Substituting equation (3.15) and (3.16) sequentially into the above expansion, we obtain,

$$\mathbf{x}_{ip,jp}(s_1, s_2) = \sum_{i=0}^{N} \sum_{j=0}^{N-i} \left(\sum_{k=1}^{N_k(N)} \sum_{l=1}^{N_l(N-i)} C_k^{(N)} C_l^{(N-i)} \mathbf{x}_{ip+ir(k),jp+jr(l)} \right) {s_1}^i {s_2}^j \tag{3.18}$$

If we expand along s_1 first, then we obtain a similar expansion as,

$$\mathbf{x}_{ip,jp}(s_1, s_2) = \sum_{j=0}^{N} \sum_{i=0}^{N-j} \left(\sum_{l=1}^{N_l(N)} \sum_{k=1}^{N_k(N-j)} C_l^{(N)} C_k^{(N-j)} \mathbf{x}_{ip+ir(k),jp+jr(l)} \right) {s_1}^i {s_2}^j \tag{3.19}$$

Since the expansion is symmetrical in s_1 and s_2, the position vector $\mathbf{x}(s_1, s_2)$ can then be expanded into the following combined form,

$$\mathbf{x}_{ip,jp}(s_1, s_2) = \sum_{i=0}^{N} \sum_{j=0}^{N-i} \left(\sum_{k=1}^{N_k(N-j)} \sum_{l=1}^{N_l(N-i)} C_k^{(N-j)} C_l^{(N-i)} \mathbf{x}_{ip+ir(k),jp+jr(l)} \right) {s_1}^i {s_2}^j. \quad (3.20)$$

Equation (3.20) tells us that the local geometry expansion depends on the central point of the panel itself and the other central points of the neighboring panels. These kind of local function molecules are discussed extensively by De Koning Gans (1994) for the panels in the central part of the surface as well as for the panels close to the edges.

It should be pointed out that, since the molecule passes through the central points (collocation points) of the panel only, there is no guarantee from the present method on the connection of panels along their edges. Practical usage shows that the gaps between panels are reducing quickly as the expansion order increases. Some examples will be shown in the following paragraphs.

If we combine the summations in the bracket of equation (3.20) into one summation, and rearrange the relative index ir and jr. We can have a more compact form as,

$$\mathbf{x}_{ip,jp}(s_1, s_2) = \sum_{i=0}^{N} \sum_{j=0}^{N-i} \sum_{k=1}^{Num_cf} C_{i,j,k} \quad \mathbf{x}_{ip+ir(k),jp+jr(k)} {s_1}^i {s_2}^j \quad (3.21)$$

where Num_cf is the total number of the supports for this two-dimensional molecule, and ir, jr are not the same as in equation (3.20).

3.3.2 The solution

The expansion of the solution is expressed in the same way as the expansion of the geometry. The difference is that the central-point function values are known when the geometry is given, but the central-point function values of the solution are not known, i.e., they are part of the solution.

For a mixed problem where part of the surface is prescribed with potential and the other part is prescribed with the potential derivatives, the expansion should be done for both. As we discussed previously for the geometry expansion, the solution expansion applies to a certain panel and hence it is a local expansion, instead of a global prescription. So, the following expression should be used for each panel, e.g. for panel indexed ip, jp,

$$\sigma_{ip,jp}(s_1, s_2) = \sum_{k=1}^{Num_cf} \sum_{i=0}^{N} \sum_{j=0}^{N-i} C_{i,j,k}^{\sigma} \sigma_{ip+ir(k),jp+jr(k)} {s_1}^i {s_2}^j, \quad (3.22)$$

$$\mu_{ip,jp}(s_1,s_2) = \sum_{k=1}^{Num_cf} \sum_{i=0}^{N} \sum_{j=0}^{N-i} C^{\mu}_{i,j,k} \mu_{ip+ir(k),jp+jr(k)} {s_1}^i {s_2}^j, \tag{3.23}$$

where, for simplicity of notation, we call the potential on the surface the normal dipole μ and the potential normal derivative the source σ. We will use either μ and σ, or φ and $\dfrac{\partial \varphi}{\partial n}$ alternatively, but they are identical throughout the rest of the thesis.

Upon solving the problem, the solution can be re-constructed by the following expansions on each panel as,

$$\sigma_{ip,jp}(s_1,s_2) = \sum_{i=0}^{N} \sum_{j=0}^{N-i} C^{\sigma}_{i,j} {s_1}^i {s_2}^j, \tag{3.24}$$

$$\mu_{ip,jp}(s_1,s_2) = \sum_{i=0}^{N} \sum_{j=0}^{N-i} C^{\mu}_{i,j} {s_1}^i {s_2}^j, \tag{3.25}$$

where the coefficients are calculated by the following equations,

$$C^{\sigma}_{i,j} = \sum_{k=1}^{Num_cf} C^{\sigma}_{i,j,k} \sigma_{ip+ir(k),jp+jr(k)}, \tag{3.26}$$

$$C^{\mu}_{i,j} = \sum_{k=1}^{Num_cf} C^{\mu}_{i,j,k} \mu_{ip+ir(k),jp+jr(k)}. \tag{3.27}$$

3.4 Analytical calculation of influence coefficient

The influence coefficient can be computed numerically or analytically. Since analytical calculation has higher accuracy and efficiency, it is discussed in this section in detail.

Basically, the coefficients can be calculated either in the physical space (x, y, z) or in the computational space (s_1, s_2). When the coefficients are calculated in the physical space, a local coordinate system has to be established at each panel center and the panel geometry is expressed in this coordinate system. Normally a tangential reference plane is chosen, which passes through the central point of the panel and it takes the shape of the projection of the panel on the plane. When the curvature of the panel is not too large, the difference between the curved panel and the reference flat panel is small. The detailed formulation is given by Hess (1972) for the velocity and Romate (1988) for the potential.

Since the computational space is a rectangular space, the evaluation of the integrals in this space is much simpler. After we expanded both the geometry and the solution in the computational space, we can adopt the method based on the surface (s_1, s_2) coordinates. The details about the evaluation of the integral are given by De Koning Gans (1994) and Maniar (1995). For the sake of completeness, the method of De Koning Gans (1994) is briefly repeated below. Some discussions on this method are given in section 3.5.

From equation (3.9), we need to evaluate two integrals. When we use the Green function of equation (3.3) for calculations in three dimensions, these two integrals can be written as,

$$I_\mu = \frac{1}{4\pi} \oint_{\partial\Omega} [-\varphi(\tilde{\mathbf{x}};t)\ \ \mathbf{n}_{\tilde{\mathbf{x}}} \cdot \mathbf{r}(\tilde{\mathbf{x}},\mathbf{x})] \frac{1}{r^3(\tilde{\mathbf{x}},\mathbf{x})} dS_{\tilde{\mathbf{x}}},$$

$$= \frac{1}{4\pi} \int\int_{\partial\Omega} [-\mu(s_1,s_2)\ \ \mathbf{n}_{\tilde{\mathbf{x}}}(s_1,s_2) \cdot \mathbf{r}(s_1,s_2)\ J] \frac{1}{r^3(s_1,s_2)} ds_1 ds_2, \qquad (3.28)$$

and,

$$I_\sigma = \frac{1}{4\pi} \oint_{\partial\Omega} \left[-\frac{\partial\varphi(\tilde{\mathbf{x}};t)}{\partial n_{\tilde{\mathbf{x}}}}\right] \frac{1}{r(\tilde{\mathbf{x}},\mathbf{x})} dS_{\tilde{\mathbf{x}}}.$$

$$= \frac{1}{4\pi} \int\int_{\partial\Omega} [-\sigma(s_1,s_2)\ J] \frac{1}{r(s_1,s_2)} ds_1 ds_2, \qquad (3.29)$$

where $\mathbf{n}_{\tilde{\mathbf{x}}}$ is the surface normal unit vector and J is the Jacobian. They are given in the following sub-sections.

The base vector on the surface and the Jacobian

The tangential base vectors on the surface along s_1 and s_2 directions are the first derivatives of the position vector from equation (3.12),

$$\mathbf{e}_1 = \frac{\partial\mathbf{x}}{\partial s_1} / |\frac{\partial\mathbf{x}}{\partial s_1}| = \mathbf{x}_{1,0}/|\mathbf{x}_{1,0}|, \qquad (3.30)$$

and,

$$\mathbf{e}_2 = \frac{\partial\mathbf{x}}{\partial s_2} / |\frac{\partial\mathbf{x}}{\partial s_2}| = \mathbf{x}_{0,1}/|\mathbf{x}_{0,1}|, \qquad (3.31)$$

and the unit normal vector is the cross product of this two vectors,

$$\mathbf{e}_3 = \mathbf{e}_1 \times \mathbf{e}_2. \qquad (3.32)$$

The Jacobian is the norm of the normal vector. It can be written as,

$$J = |\mathbf{x}_{1,0} \times \mathbf{x}_{0,1}|, \tag{3.33}$$

and the surface unit vector $\mathbf{n}_{\tilde{\mathbf{x}}}$ is then,

$$\mathbf{n}_{\tilde{\mathbf{x}}} = \mathbf{e}_3. \tag{3.34}$$

Once the geometry is expanded into equation (3.12), the expansion of the base vectors and the Jacobian can be derived. Substitute all the polynomial expansions of equation (3.22), (3.23), (3.33) and (3.34) into the brackets of equation (3.28) and (3.29), re-arrange and re-organize by multiplication and summation between polynomial expansions, we encounter the following basic integral for both the normal dipole and the source influence coefficients,

$$N(m,n,p) = \int\int \frac{{s_1}^m {s_2}^n}{r^p} ds_1 ds_2 \quad p = 1,3 \;\; m,n = 0,1,2,\cdots,N_h, \tag{3.35}$$

where, N_h is the highest order of the expansion.

The near field

In the near field, the variation of the distance between the collocation point and the point on the curved panel surface must be evaluated accurately. But generally, the integral can not be evaluated analytically on arbitrarily curved panel. A reference panel is always needed, on which all the integrals are expressed by analytical formulas.

Here we use $\mathbf{x}_{col}$ to denote the collocation point, then we have the distance in the following form,

$$\mathbf{r}(s_1, s_2) = \mathbf{r}_{col} - \mathbf{x}(s_1, s_2), \tag{3.36}$$

or in the polynomial expansion form as,

$$\mathbf{r} = \sum_{i=0}^{N} \sum_{j=0}^{N-i} \mathbf{r}_{i,j} {s_1}^i {s_2}^j. \tag{3.37}$$

We can define the distance as,

$$r = \sqrt{\mathbf{r} \cdot \mathbf{r}} = \sqrt{\sum_{i=0}^{N} \sum_{j=0}^{N-i} a_{i,j} {s_1}^i {s_2}^j}, \tag{3.38}$$

where, $a_{i,j}$ is the coefficient after the multiplication of the series of $\mathbf{r}$ from equation (3.37).

Suppose we find a reference surface $\mathbf{x}_{ref}$, on which the integrals can be evaluated analytically. We denote the distance from the collocation point to the reference surface as $\mathbf{r}_{ref}$, then,

$$\mathbf{r}_{ref} = \mathbf{x}_{col} - \mathbf{x}_{ref}(s_1, s_2), \tag{3.39}$$

and the distance between the reference surface and the collocation point can be expanded as well,

$$r_{ref} = \sqrt{\sum_{i=0}^{N_{ref}} \sum_{j=0}^{N_{ref}-i} \tilde{a}_{i,j} {s_1}^i {s_2}^j}, \tag{3.40}$$

where N_{ref} is the highest order of the expansion.

Now we can make the following re-arrangement,

$$\frac{1}{r^p} = \left(1 + \frac{r^2 - r_{ref}^2}{r_{ref}^2}\right)^{-\frac{p}{2}} \frac{1}{r_{ref}^p}. \tag{3.41}$$

Here we assume that the reference surface is very close to the curved panel surface and that the difference between the true surface and the reference surface is very small.

$$\alpha = r^2 - r_{ref}^2 << r_{ref}^2. \tag{3.42}$$

If the above inequality is true, the following expansion will be convergent,

$$\left(1 + \frac{r^2 - r_{ref}^2}{r_{ref}^2}\right)^{-\frac{p}{2}} = \sum_{k=0}^{N_p} C_k \left(\frac{\alpha^k}{r_{ref}^{2k}}\right) \tag{3.43}$$

where,

$$C_k = (-1)^k \frac{\frac{p}{2}(\frac{p}{2}+1)\cdots(\frac{p}{2}+k-1)}{k!}. \tag{3.44}$$

Substitute (3.41) and (3.43) into equation (3.35), the integral (3.35) becomes,

$$N(m,n,p) = \sum_{k=0}^{N_p} C_k \int\int \frac{\alpha^k {s_1}^m {s_2}^n}{r_{ref}^{p+2k}} ds_1 ds_2. \tag{3.45}$$

Let us expand α^k into a series as well,

$$\alpha^k = \sum_{i=0}^{N_\alpha} \sum_{j=0}^{i} \alpha_{i-j,j}^{(k)} {s_1}^{i-j} {s_2}^j. \tag{3.46}$$

Then Equation (3.45) becomes,

$$N(m,n,p) = \sum_{k=0}^{N_p} C_k \left\{ \sum_{i=0}^{N_\alpha} \sum_{j=0}^{i} \alpha_{i-j,j}^{(k)} \int\int \frac{{s_1}^{m+i-j} {s_2}^{n+j}}{r_{ref}^{p+2k}} ds_1 ds_2 \right\}$$

$$= I(m,n,p) + \sum_{k=1}^{N_\alpha} C_k \left\{ \sum_{i=0}^{N_\alpha} \sum_{j=0}^{i} \alpha_{i-j,j}^{(k)} I(m+i-j, n+j, p+2k) \right\} \qquad (3.47)$$

where, we introduced a new integral $I(m,n,p)$ as,

$$I(m,n,p) = \int\int \frac{{s_1}^m {s_2}^n}{r_{ref}^p} ds_1 ds_2 \qquad m,n = 0,1,2,\cdots \qquad p = 1,3,5,\cdots \qquad (3.48)$$

The integral $I(m,n,p)$ can be easily evaluated by analytical method. The detailed formulation is given by De Koning Gans (1994).

3.5 Discussion

The calculation of the near field influence coefficients is essentially important when the higher-order panel method is used. The formulation involved in the previous sections contains a lot of polynomial expansions and their multiplication and summations. Consistence of calculation and convergence of expansions must be analyzed.

The consistence of the panel method with the physics and the convergence of the numerical modeling as a whole are supposed to be true and will not be discussed in the following paragraphs. For an extreme geometry like a propeller blade, these are still not very clear and remain un-solved, because they involve those difficulties in detailed modeling of the wake, the Kutta condition, the tip and the joint of the blade with the hub. These are out of our present scope.

3.5.1 Consistence

The basic idea of the present higher order method is based on the series expansion of all the functions in the body-fitted curvilinear coordinates. The main expansions involved in the calculation of the near-field coefficients are equation (3.22), (3.23) for the solution, equation (3.12) for the geometry, equation (3.33) and (3.34) for the base vectors and the Jacobian, and equation (3.37) for the distance. In order to make the calculation consistent with each other, each part of the above equations must be analyzed.

Now we use Landau symbol with parameter h (the size of the panel) as the order to investigate the orders of the expansions (in equation (3.28) and (3.29)),

which must be made in order to achieve a certain order for the global integrals. The orders of the expansions of the variables used in the above equations are listed in the following:

The panel size

$$\Delta s_1 = O(h) \tag{3.49}$$

$$\Delta s_2 = O(h) \tag{3.50}$$

The singularity distributions

$$\sigma = O(1) + O(h) + O(h^2) + \cdots + O(h^{N_\sigma}) \tag{3.51}$$

$$\mu = O(1) + O(h) + O(h^2) + \cdots + O(h^{N_\mu}) \tag{3.52}$$

The geometry and the distance

$$\mathbf{x} = O(1) + O(h) + O(h^2) + \cdots + O(h^{N_G}) \tag{3.53}$$

$$\mathbf{n}_\mathbf{x} = O(1) + O(h) + O(h^2) + \cdots + O(h^{N_G}) \tag{3.54}$$

$$J = O(h) + O(h^2) + \cdots + O(h^{N_G}) \tag{3.55}$$

For the near-field calculation, the order of the distance is the same as the size of the panel, hence they are one order higher than the position vector $\mathbf{x}$.

$$\mathbf{r} = O(h) + O(h^2) + \cdots + O(h^{N_G}) \tag{3.56}$$

$$r = O(h) + O(h^2) + \cdots + O(h^{N_G}) \tag{3.57}$$

Combining the above analysis with equation (3.28) and (3.29), we obtain the following consistence table (Table 3.1) for the singularity distribution and the geometry expansion, which achieves the same global order for the boundary integral equations.

It is obvious that the geometry expansion should be always one order higher than the global order. With this one order higher expansion of the geometry, the Jacobian can be the same order as the global order. The source expansion keeps the same order as the global order but the dipole should be also one order higher than the global order. For the consistence of the expansion for the velocity, see De Koning Gans (1994).

Table 3.1: Consistence requirement for potential based higher-order panel method.

Global order N	Geometry N_G	Jacobian N_J	Source N_σ	dipole N_μ
$O(h)$	$O(h^2)$	$O(h)$	$O(h)$	$O(h^2)$
$O(h^2)$	$O(h^3)$	$O(h^2)$	$O(h^2)$	$O(h^3)$
...	...	...	...	...
$O(h^N)$	$O(h^{N+1})$	$O(h^N)$	$O(h^N)$	$O(h^{N+1})$

3.5.2 Convergence

The convergence analysis here focuses only on the convergence of expansion (3.43), which is based on the difference of the distance square between the original curved panel and the reference panel. For the others, the convergence property is guaranteed by the Taylor expansion where s_1 and s_2 are in the order of h.

The condition for the convergence of the expansion is equation (3.42), which states that the distance difference should be much smaller than the distance itself. But if we print out the coefficients of expansion (3.43) C_k for $p = 1$ (the source) and $p = 3$ (the dipole), we obtain the following table.

Table 3.2: Series expansion coefficients of equation (3.43).

	$p = 1$	$p = 3$
C_0	1.0	1.0
C_1	-0.5	-1.5
C_2	0.375	1.875
C_3	-0.3125	-2.1875
...	...	...

It indicates that the coefficients are not convergence. The convergence of the series expansion can be only guaranteed if α is very small. This is true for most panels on the surface, but not true when the panel is topologically triangular or close to triangular, as shown in Figure 3.1.

In this situation, α in equation (3.43) can be of the same order in magnitude as the distance $\mathbf{r}$ or $\mathbf{r}_{ref}$. The problem is caused by the choice of the reference plane. When we choose the flat plane, we obtain always a parallelogram that is too far away from a triangular shaped panel. A typical picture, which shows these parallelograms for a propeller blade-liked circular disk at the tip, is given

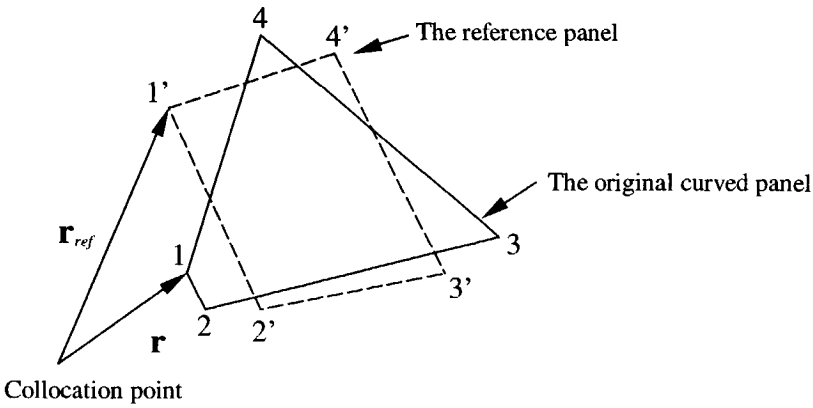

Figure 3.1: Schematics of the topological triangular or close to triangular panel and its flat reference panel.

in Figure 3.2. For the last strip along the chord at the tip, no convergent solution can be expected from equation (3.43).

When this happens, subdivision of the panel for the integral (but not to increase the total number of panels for the global problem) has to be used. Or for some panels, the quadratic terms or some part of them can be included in the reference panel. This has been discussed by Mazzi (1999) and implemented in *Delprop* (De Koning Gans (1994)).

3.5.3 Hyperboloidal panels

Hyperboloidal quadrilateral panels with constant singularity distribution have been widely used in propeller calculations, both for fully wetted and cavity flows (Hoshino (1989), Hoshino (1994)). Obviously, the advantage of using this method is that the formulation and implementation of this method is relatively simple and the code based on this method is easily optimized for certain computers. On a vector computer, the code can be fully vectorized and runs very efficiently and hence the cost for the evaluation of the influence coefficients is very low.

According to the previous consistency analysis, this hyperboloidal panel method with constant singularity distributions, both for sources and normal dipoles, are mathematically not consistent. But due to this higher order term (the cross term $\mathbf{x}_{1,1}s_1s_2$) in the geometry, the discretized body surface is fully covered with panels that have no gaps between them. The panels can represent the original surface nicely, however note that the connections between panels

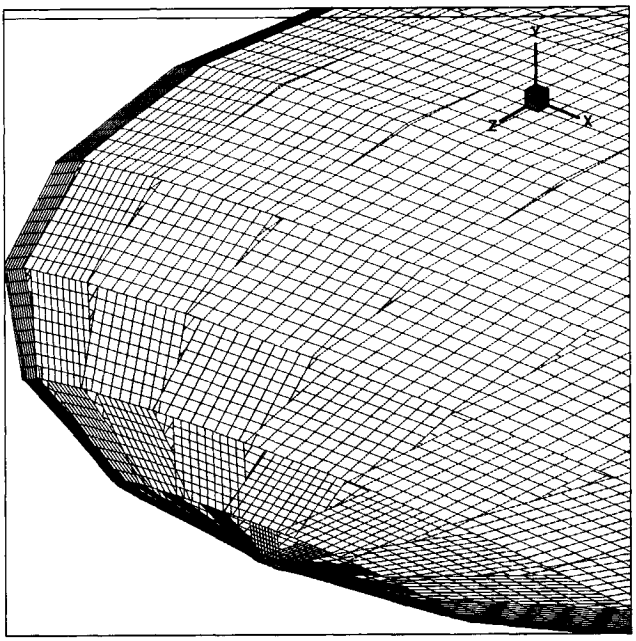

Figure 3.2: Flat reference plane for a propeller blade-liked circular disk at the tip.

are straight lines. These well-connected panels eliminate the problem we had with the triangular panels, which we have discussed in the previous section.

The formulation of the influence coefficients from a hyperboloidal panel was first derived by Morino & Kuo (1974). More discussions can be found in Hoshino (1989). The potential influence coefficient from the constant normal dipole can be exactly evaluated by the following formula,

$$I_\mu = \frac{1}{4\pi} \sum_{i=1}^{N_e} (-1)^i \tan^{-1} \left(\frac{(\mathbf{r}_i \times \mathbf{e}_1) \cdot (\mathbf{r}_i \times \mathbf{e}_2)}{|\mathbf{r}_i| \mathbf{r}_i \cdot (\mathbf{e}_1 \times \mathbf{e}_2)} \right) \tag{3.58}$$

where, N_e is the number of edges and $N_e = 4$ for quadrilateral panels. The potential influence coefficient from the constant source can be approximately evaluated by the following equation by neglecting some curvature influence

terms,

$$I_\sigma = \frac{1}{4\pi}\sum_{i=1}^{N_e}(-1)^i \left\{ \frac{(\mathbf{r}_i \times \mathbf{e}_1)\cdot\mathbf{n}}{|\mathbf{e}_1|} \sinh^{-1}\left(\frac{\mathbf{r}_i\cdot\mathbf{e}_1}{|\mathbf{r}_i\times\mathbf{e}_1|}\right) - \frac{(\mathbf{r}_i \times \mathbf{e}_2)\cdot\mathbf{n}}{|\mathbf{e}_2|} \sinh^{-1}\left(\frac{\mathbf{r}_i\cdot\mathbf{e}_2}{|\mathbf{r}_i\times\mathbf{e}_2|}\right) -(\mathbf{r}_i\cdot\mathbf{n})\tan^{-1}\left(\frac{(\mathbf{r}_i\times\mathbf{e}_1)\cdot(\mathbf{r}_i\times\mathbf{e}_2)}{|\mathbf{r}_i|\mathbf{r}_i\cdot(\mathbf{e}_1\times\mathbf{e}_2)}\right)\right\}, \quad (3.59)$$

where, $\mathbf{n}$ is the unit normal vector on the surface and its value is simply taken as $\frac{\mathbf{e}_1\times\mathbf{e}_2}{|\mathbf{e}_1\times\mathbf{e}_2|}$ at the central point of the panel.

Due to its simplicity, it is also implemented and used in our present research and for the calculations in the coming chapters.

Chapter 4

Time Stepping

Time stepping methods based on Lagrangian and Eulerian descriptions, with explicit and implicit schemes, are discussed. Linear stability analysis has been applied to these schemes and marginal stablility has been found on the cavity surface. Problems have been shown along the boundaries of the cavity — the detachment and the closure. A more stable alternative Euler method is proposed.

4.1 Introduction

The governing equations for linear and nonlinear cavity flows are the same — the Laplace equation. There is no difference to solve this boundary value problem in both methods, as far as the boundary conditions are properly given.

But solving the fully non-linear unsteady cavity flow problem is much more difficult than solving its linear version. Laplace's equation is an elliptic partial differential equation. The difficulties in solving Laplace's equation come from its complicated boundary conditions. On one hand, these boundary conditions can be time dependent. On the other hand, it can be highly non-linear so that the linearization of these conditions is sometimes not possible. Moreover, when these non-linear conditions are going to be enforced on moving boundaries, such as the cavity surface, the problem becomes extremely complicated and hard to solve.

In the linear method, all the boundaries are fixed, no matter they are body surfaces or cavity surfaces. Instead of applying the boundary conditions on the real cavity and body surfaces, these boundary conditions are satisfied on a simple reference plane, like the nose-tail line of a hydrofoil section (Geurst (1959)). Improved linear method can apply the boundary conditions on the camber line, which is then curved (Geurst & Verbrugh (1959)). The most novel

linear method (it is also called nonlinear or quasi-nonlinear method) applies the impermeable boundary condition on the real body surface, but applies the dynamic boundary condition for the cavity on the body surface beneath the cavity (Kinnas & Fine (1993), Kim *et al.* (1994)).

While in the fully non-linear method, the cavity surface itself is part of the solution and must be determined before the kinematic and dynamic boundary conditions can be enforced on it.

The dynamic boundary condition (2.27) or (2.28) links the disturbance potential φ with the pressure p_v on the cavity surface through the prescribed cavitation number σ. If this equation can be solved in advance at a certain time t, the disturbance potential φ on the cavity surface can then be prescribed for this time level. When on some part of the boundary the potential condition (Dirichlet condition from equation (2.27) or (2.28)) are prescribed and on the other part of the boundary the normal derivatives of the potential (Neumann condition from equation (2.24) or (2.25)) are prescribed, Laplace's equation can then be solved on this time level t. The potential and velocity field throughout the entire fluid domain are obtained.

But solving the dynamic boundary condition of equation (2.27) or (2.28) in advance to obtain the potential on the cavity surface for the new time step is practically not possible, because it needs information about the potential and its derivatives on the cavity surface at the new time step. This leads to the requirement of the spatial solution of the Laplace equation in the new time step too. Obviously this solution can not be found, since the new cavity surface position is not known *a priori* for the new time step.

A possible way is to use some kind of implicit scheme to link two time levels through the dynamic boundary condition, and solve the spatial problem in two levels simultaneously. This, at least, doubles the number of variables of the problem and increases the computation effort to a large extent, and hence is too expensive.

An efficient, accurate and stable time stepping method for the cavity surface evolution will be explored for the present calculation. The fixed wetted body surface has shown not to be a problem in the calculation, and hence omitted from this chapter. We focus, in the following discussion, only on the method of time stepping for the cavity surface.

4.2 Lagrangian method

For any variable $\mathbf{q}(x, y, z; t)$, vector or scalar, the following total derivative can be defined,

$$\frac{\mathbf{dq}}{\mathbf{dt}} = \frac{\partial \mathbf{q}}{\partial t} + (\mathbf{v} \cdot \nabla)\mathbf{q}, \tag{4.1}$$

where the first term is called the local time derivative and the second term is the convective time derivative. When the velocity $\mathbf{v}$ is the particle velocity of the fluid, we call this derivative $\frac{\mathbf{d}}{\mathbf{d}t}$ the *material derivative.*

If we trace the cavity surface according to the particles on it and update the particle properties, like the potential, according to the above equation at the same time, we call this method a Lagrangian method.

Substitute equation (2.51) into equation (2.48), we obtain the Lagrangian description of the present problem, together with (2.49) for the cavity surface, as,

$$\frac{\mathbf{d}\varphi}{\mathbf{d}t} = \frac{\mathbf{V}_r^2}{2} - \frac{(\mathbf{V}_0 + \Omega_0 \times \mathbf{x} - \mathbf{V}_W)^2}{2} - \frac{V_\infty^2}{2}\sigma + \mathbf{V}_r \cdot \nabla\varphi, \tag{4.2}$$

$$\frac{\mathbf{d}\mathbf{x}_C}{\mathbf{d}t} = (\mathbf{V}_W - \mathbf{V}_0 - \Omega_0 \times \mathbf{x}) - \nabla\varphi, \tag{4.3}$$

where the gravity term is neglected. Solving these equations with respect to time, we can update the cavity surface as well as the potential together. Then the solution can be stepped in time.

But solving these purely Lagrangian equations has revealed difficulties for cavity flows, because cavity flow problems often show rapidly varying flow quantities. If the cavity surface grid is updated according to the speed of the fluid particles, the grid will break from the detachment point immediately and move downstream. Then either new grid points have to be generated at the detachment point or very small time steps have to be used. When the time step is too small, the method becomes impractical.

Fortunately, when we use potential theory, the shear stress on the boundary surface is neglected. From the kinematic point of view, the tangential movement of the particle is not required by any boundary condition and hence has no effect on the cavity movement. In other words, it does not affect the evolution of the cavity surface. The movement of the cavity surface is purely controlled by the normal component of the particle velocity. Then, the kinematic boundary condition (equation (4.3)) can be modified to,

$$\frac{\mathbf{d}\mathbf{x}_C}{\mathbf{d}t} \cdot \mathbf{n} = [(\mathbf{V}_W - \mathbf{V}_0 - \Omega_0 \times \mathbf{x}) - \nabla\varphi] \cdot \mathbf{n}. \tag{4.4}$$

Hence the grid updating of the cavity surface can be done using the normal velocity only.

Let us define a grid velocity $\mathbf{v}_g$ as,

$$\mathbf{v}_g = \frac{\mathbf{d}\mathbf{x}_g}{\mathbf{d}t} = \left(\frac{\mathbf{d}\mathbf{x}_C}{\mathbf{d}t} \cdot \mathbf{n}\right)\mathbf{n}, \tag{4.5}$$

$\mathbf{x}_g$ is the grid position vector and $\mathbf{x}_g = (x_g, y_g, z_g)^T$.

Now, we obtain the modified Lagrangian method, in which the grid and the potential follow the artificial particles on the cavity surface with velocity $\mathbf{v}_g$,

$$\frac{\mathbf{dx}_g}{\mathbf{d}t} = \left[(\mathbf{V}_W - \mathbf{V}_0 - \Omega_0 \times \mathbf{x}) \cdot \mathbf{n} - \frac{\partial \varphi}{\partial n}\right] \mathbf{n}, \tag{4.6}$$

and,

$$\frac{\mathbf{d}\varphi}{\mathbf{d}t} = \frac{\mathbf{V}_r^2}{2} - \frac{(\mathbf{V}_0 + \Omega_0 \times \mathbf{x} - \mathbf{V}_W)^2}{2} - \frac{V_\infty^2}{2}\sigma + \mathbf{v}_g \cdot \nabla\varphi. \tag{4.7}$$

The equation for the potential φ keeps the same form because it is the total derivative following the artificial particles on the grid.

Combining equation (4.6) and (4.7), we obtain the following ordinary differential equation (ODE),

$$\frac{\mathbf{dq}}{\mathbf{d}t} = \mathbf{f}(\mathbf{q}; t), \tag{4.8}$$

where $\mathbf{q} = (x_g, y_g, z_g, \varphi)^T$ is the vector variable and function $\mathbf{f}(\mathbf{q}, t)$ consists of the right-hand side of equation (4.6) and (4.7). If the right-hand side function $\mathbf{f}(\mathbf{q}, t)$ can be evaluated, then we can march $\mathbf{q}$ explicitly in time by solving this ordinary differential equation in time.

4.2.1 Explicit method

There are two distinctive ways to solve this system of ordinary differential equations explicitly, the Taylor method and the Runge-Kutta method.

The Taylor method estimates the values of the numerical solution $\mathbf{q}_{t+\Delta t}$ in the new time step by using the first and higher derivatives of the solution at the old time level t,

$$\mathbf{q}_{t+\Delta t} = \mathbf{q}_t + \sum_{i=1}^{m} \frac{1}{i!} \left.\frac{\partial^i \mathbf{q}}{\partial t^i}\right|_t (\Delta t)^i$$

$$= \mathbf{q}_t + \mathbf{f}(\mathbf{q}; t)\Delta t + \sum_{i=2}^{m} \frac{1}{i!} \left.\frac{\partial^i \mathbf{q}}{\partial t^i}\right|_t (\Delta t)^i. \tag{4.9}$$

The accuracy and stability of this method depends on its order m. When a higher-order is used, the higher-order time derivatives of $\mathbf{q}$ have to be evaluated. Evaluation of the higher order derivatives (of the cavity surface and potential) by numerical differentiation is not always possible, or it is possible but very inaccurate. So, this method is not favorable for the present application.

Because the Runge-Kutta method needs only to evaluate the first-order derivative of the solution, it can be used in the present calculation. The general algorithm of the Runge-Kutta method is written as,

$$\mathbf{q}_{t+\Delta t} = \mathbf{q}_t + \sum_{j=1}^{m} \gamma_j \mathbf{k}_j \Delta t \tag{4.10}$$

where,

$$\mathbf{k}_j = \mathbf{f}(\mathbf{q} + \Delta t \sum_{i=1}^{m} \beta_{ji} \mathbf{k}_i; t + \alpha_j \Delta t) \quad j = 1, 2, \cdots, m, \tag{4.11}$$

where α, β and γ are constants and their values depend on the order of the method. The disadvantage of this method is that the first derivatives have to be evaluated four times if a 4th-order 4-stage Runge-Kutta method is used. It means that the spatial problem has to be solved four times by the panel method within each time step. Since the evaluation of the influence coefficients is the most expensive part of the panel method, it makes the Runge-Kutta method quite expensive too.

Besides, this explicit method is only marginal stable. The stability region is small and depends on the order. The Runge-Kutta 4th-order 4-stage method has a relatively large stability region, but it still limits the time step extremely. A stability analysis of this method for cavity flow calculation is given by De Koning Gans (1994). The estimated time step is given in the following formula,

$$\Delta t \leq \varepsilon \frac{\Delta s}{2v} \tag{4.12}$$

where Δs is the panel size and v is the local velocity. He concluded that a practical value for ε is less than 0.25. It means that the fluid particles have to pass one grid interval in more than one step. If we look at Figure 6.2 and notice how many panels are used in order to resolve the details of the cavity closure, then we realize that a tremendous number of time steps is needed for unsteady flow calculations.

It has been found by many people that the normal evolution of the cavity is relatively easy to be fulfilled, but the longitudinal development of the cavity is more difficult. Figure 6.5 and 6.6 in Chapter 6 will show how difficult it is for the cavity to evolve in longitudinal direction.

The other reason for noy choosing explicit methods is the consistency problem. In order to gain numerical stability, a higher-order stepping method must be used, for instance, fourth-order Runge-Kutta method. But on the other hand, the order of panel method is not as high as fourth-order. They are not consistent with each other. And the lower accuracy of the evaluation of the

right-hand side of equation (4.8) will deteriorate the stability region of the higher-order Runge-Kutta method.

Detailed discussions on the stability region for the explicit method can be found in De Koning Gans (1994) and Romate (1989).

4.2.2 Implicit method

As we have discussed at the beginning of this chapter an implicit method needs to solve these two time steps simultaneously and hence it is not practical because the cavity surface position is not known at the new time step. But an iterative implicit method is still possible, which builds up the relation between the two time levels by an implicit scheme, iteratively updating both the cavity surface and the potential on it until the implicit scheme is satisfied. This method can be very expensive, but the efficiency is gained by using large time steps allowed due to its stability.

Implicit methods have been thought to be unconditionally stable for any arbitrary time step. This is true if we are dealing with only an unbounded cavity surface. But as the cavity surface is normally bounded and restricted in a small region, the instability can be introduced from the boundary of the cavity.

De Lange (1996) has used a second-order implicit method based on $t + \frac{1}{2}\Delta t$ time level. The total derivatives for the cavity position and the potential (equation (4.8)) are given by the following scheme,

$$\mathbf{q}_{ip}^{n}|_{t} = \mathbf{q}_{ip}|_{t-\Delta t} + \frac{\Delta t}{2}\left[\mathbf{f}(\mathbf{q}_{ip}^{n-1}; t) + \mathbf{f}(\mathbf{q}_{ip}; t - \Delta t)\right], \tag{4.13}$$

where, ip is the panel index in the two-dimensional case and superscript n denotes the iteration steps at time step t.

Some results have been obtained. But numerical tests show that the method sometimes fails for certain calculation conditions. So, limited results have been presented. Some numerical instability is believed to transmit from the boundary to the central part of the cavity and hence spoils the calculation completely.

4.3 Euler method

Another method to describe the evolution of the cavity surface is the Euler method. This method has been used widely for solving wave problems (e.g. Cheng & Lu (1986) and De St Isaacson (1982)). Similar work for cavity flows was not found by the author in the literature.

We use the same body-fitted curvilinear coordinates (s_1, s_2, s_3) as we used in Section 3.3. Based on this body-fitted coordinates, we define the cavity with

a thickness of $s_3 = \eta(s_1, s_2; t)$, and hence,

$$S_C(s_1, s_2, s_3; t) = s_3 - \eta(s_1, s_2; t) = 0. \tag{4.14}$$

The Euler kinematic boundary condition (2.34) becomes,

$$-\frac{\partial \eta}{\partial t} + \mathbf{V}_r \cdot \nabla \left[s_3 - \eta(s_1, s_2; t) \right] = 0. \tag{4.15}$$

Working out the surface metric tensor for the curvilinear coordinates, the second term on the left-hand side of equation (4.15) can be written as a function of the co-variant differentiations $\frac{\partial \eta}{\partial s_1}$ and $\frac{\partial \eta}{\partial s_2}$, and equation (4.15) becomes,

$$\frac{\partial \eta}{\partial t} = \left(\mathbf{V}_{r0} \cdot \mathbf{n} - \frac{\partial \varphi}{\partial n} \right) - A \frac{\partial \eta}{\partial s_1} - B \frac{\partial \eta}{\partial s_2}, \tag{4.16}$$

where,

$$A = (\mathbf{V}_{r0} \cdot \mathbf{e}_1 + u_1) - \frac{\mathbf{e}_1 \cdot \mathbf{e_2}}{\mathbf{e_2} \cdot \tau_2} (\mathbf{V}_{r0} \cdot \tau_2 + u_2), \tag{4.17}$$

$$B = \frac{1}{\mathbf{e_2} \cdot \tau_2} (\mathbf{V}_{r0} \cdot \tau_2 + u_2), \tag{4.18}$$

with τ_2 perpendicular to both $\mathbf{e}_1$ and $\mathbf{e}_3$ and $\tau_2 = \mathbf{e}_3 \times \mathbf{e}_1$, u_1 and u_2 denote the contra-variant components of the disturbance velocity in the local Cartesian coordinates $(\mathbf{e}_1, \tau_2, \mathbf{e}_3)$ and $\mathbf{v} = (u_1, u_2, u_3)^T$. The local Cartesian velocities of the disturbance can be also expressed as a function of their co-variant velocities in,

$$u_1 = -\frac{\partial \varphi}{\partial s_1}, \tag{4.19}$$

$$u_2 = \frac{-\partial \varphi / \partial s_2 + (\mathbf{e}_1 \cdot \mathbf{e}_2) \partial \varphi / \partial s_1}{\mathbf{e}_2 \cdot \tau_2}, \tag{4.20}$$

$$u_3 = -\frac{\partial \varphi}{\partial n}. \tag{4.21}$$

When the spatial problem is solved, the co-variant velocity of the disturbance can be easily evaluated by the surface numerical differentiation of the potential and hence the right-hand side of equation (4.16) is known. Then the cavity surface can be stepped into the new time by explicit or implicit method, as we have discussed in the last section.

The drawback of the present Euler method is that the cavity thickness is defined in the body fixed coordinate, so that it cannot be used to predict the re-entrant jet where the cavity thickness becomes bi-valued.

Note that equation (4.16) is not only valid when the curvilinear coordinates are defined on the body surface but also valid when the coordinates are defined on the cavity surface. Then η in equation (4.16) denotes the additional cavity thickness based on these coordinates. With this idea, the re-entrant jet can still be calculated.

In this situation, the cavity surface, in the frame of reference of the curvilinear coordinates (s_1, s_2, s_3), is fixed in space and hence the temporal differentiation $\frac{\partial \varphi}{\partial t}$ represents the local change of the potential with respect to the grid points. Then the potential on the cavity surface can be stepped in time according to equation (2.51), which can be re-written into,

$$\frac{\partial \varphi}{\partial t} = \frac{\mathbf{V}_r{}^2}{2} - \frac{\mathbf{V}_{r0}{}^2}{2} - \frac{V_\infty{}^2}{2}\sigma, \tag{4.22}$$

where $\mathbf{V}_r$ is a function of the co-variant velocity $\frac{\partial \varphi}{\partial s_1}$ and $\frac{\partial \varphi}{\partial s_2}$, which can be evaluated.

In order to gain stability in the time stepping, an implicit method for updating both η from equation (4.16) and the potential φ from equation (4.22) was implemented according to the scheme of equation (4.13) for the unsteady cavity flows over a three-dimensional rectangular hydrofoil with very high aspect ratio ($AR = 500$) in vertical gust.

But it appears that this scheme is very stable for the cavity surface but tooth-like ($2\Delta s$) wiggles are propagating into the central part of the cavity from the detachment and the closure of the cavity, where the curvature is high and the evaluation of the co-variant velocity components is relatively inaccurate. After few cycles of the gust, the cavity surface blows up and the calculation has to stop. The calculated potential φ and its normal derivative φ_n just before the cavity blows up is plotted in Figure 4.1 and 4.2.

Because the potential φ on the cavity surface is prescribed but the potential derivative φ_n is calculated by the panel method, the wiggles in Figure 4.2 are the consequence of the wiggles in Figure 4.1, where the potential is determined by equation (4.22). It appears that this system is very sensitive to the smoothness of the prescribed potential on the cavity. The small wiggles in the potential will generate large wiggles in potential derivatives. The large wiggles in the potential derivatives finally generate large wiggles in the cavity thickness through equation (4.16). Then the cavity surface will blow up after several cycles of calculation.

4.4 Stability

A simple stability analysis of the present time stepping method is carried out in this section. The interior part of the cavity is analyzed first and the boundary

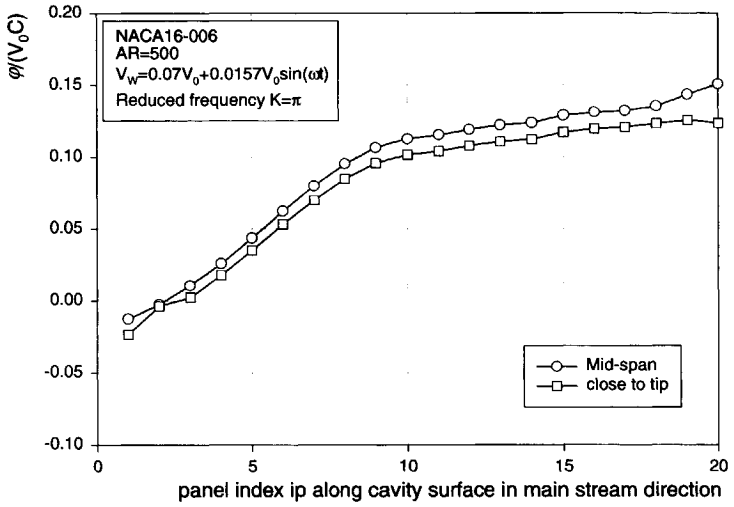

Figure 4.1: The wiggles of the disturbance potential on the cavity surface by using an implicit iterative algorithm. (NACA 16-006, AR=500, vertical gust $V_W = 0.07V_0 + 0.0157V_0 \sin \omega t$), time step $\Delta(\omega t) = 0.2\pi$.

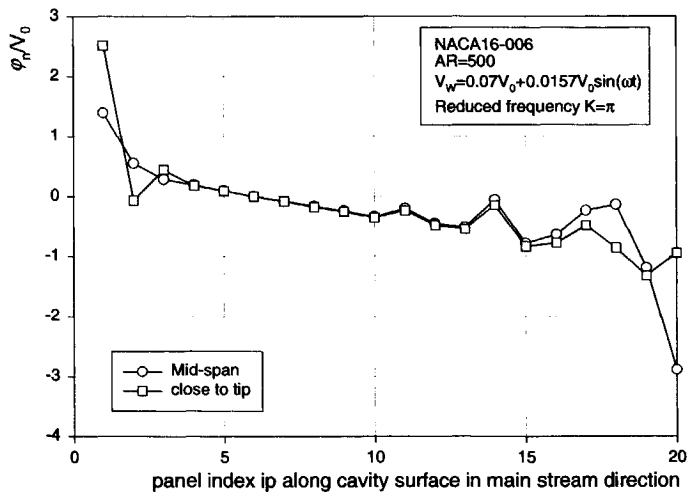

Figure 4.2: The wiggles in the normal derivative of the potential on the cavity surface by using implicit iterative algorithm. (NACA 16-006, AR=500, vertical gust $V_W = 0.07V_0 + 0.0157V_0 \sin \omega t$), time step $\Delta(\omega t) = 0.2\pi$.

of the cavity is then discussed at the end of this section.

Here we will apply Von Neumann stability analysis to equation (4.8) by linearizing the non-linear problem. We introduce a disturbance vector ϵ to the solution vector $\mathbf{q}$ and analyze the growth of the disturbance in space with time. Equation (4.8) is then written as,

$$\frac{\mathbf{dq}}{\mathbf{d}t} + \frac{\mathbf{d}\epsilon}{\mathbf{d}t} = \mathbf{f}(\mathbf{q} + \epsilon; t). \tag{4.23}$$

Substituting equation (4.6) and (4.7) into the above equations, we have the following equations for the disturbance ϵ and the solution $\mathbf{q}$,

$$\frac{\mathbf{d}(\mathbf{x}_g + \epsilon_\mathbf{x})}{\mathbf{d}t} = \left[\mathbf{V}_{r0} \cdot (\mathbf{n} + \epsilon_n) - \frac{\partial(\varphi + \epsilon_\varphi)}{\partial n}\right] \mathbf{n}, \tag{4.24}$$

where the disturbance consists of two parts and $\epsilon = (\epsilon_\mathbf{x}, \epsilon_\varphi)^T$, and ϵ_n is the disturbance to the unit normal vector on the cavity surface due to $\epsilon_\mathbf{x}$. According to the definition of the cavity thickness, we have $\eta = (\mathbf{x}_g - \mathbf{x}_B) \cdot \mathbf{n}$. Note that $\frac{d\mathbf{x}_B}{dt} = 0$, the above equation can be then written as,

$$\frac{d(\eta + \epsilon_\eta)}{dt} = \mathbf{V}_{r0} \cdot (\mathbf{n} + \epsilon_n) - \frac{\partial(\varphi + \epsilon_\varphi)}{\partial n}, \tag{4.25}$$

where $\epsilon_\eta = \epsilon_\mathbf{x} \cdot \mathbf{n}$. And for the potential, we have,

$$\frac{\mathbf{d}(\varphi + \epsilon_\varphi)}{\mathbf{d}t} = \frac{\mathbf{V}_{r0}{}^2}{2} - \mathbf{V}_{r0} \cdot \nabla(\varphi + \epsilon_\varphi) + \frac{\nabla(\varphi + \epsilon_\varphi)^2}{2} - \frac{\mathbf{V}_{r0}}{2} - \frac{V_\infty^2}{2}\sigma + \mathbf{V}_g \cdot \nabla(\varphi + \epsilon_\varphi). \tag{4.26}$$

Subtracting equation (4.6) and (4.7) from equation (4.25) and (4.26) respectively, and neglecting the non-linear higher order terms, the evolution of the errors in the cavity surface is governed by,

$$\frac{d\epsilon_\eta}{dt} \approx -V_{r0} \cos\alpha \frac{\partial \epsilon_\eta}{\partial s} - \frac{\partial \epsilon_\varphi}{\partial n}, \tag{4.27}$$

$$\frac{d\epsilon_\varphi}{dt} \approx -(V_r)_s \frac{\partial \epsilon_\varphi}{\partial s}, \tag{4.28}$$

where s and n are tangential and normal direction of the cavity surface, $(V_r)_s$ denotes the tangential component of the total relative velocity and α is the angle between $\mathbf{V}_{r0}$ and s.

Now we assume a two-dimensional disturbance with the following form, which is harmonic on the cavity surface but decays in the normal direction toward the fluid ($n > 0$) for the potential,

$$\begin{pmatrix} \epsilon_\eta \\ \epsilon_\varphi \end{pmatrix} = e^{\omega t} \begin{pmatrix} e^{iks} \epsilon_{\eta 0} \\ e^{iks - |k|n} \epsilon_{\varphi 0} \end{pmatrix}, \tag{4.29}$$

and then we can observe the evolution of the disturbance by the value of ω. If this value has a non-positive real part of ω, the disturbance will not grow and the problem is stable.

Here we choose central difference schemes for the tangential derivatives on the right-hand sides of equation (4.27) and (4.28), while the normal derivative on the right-hand side of equation (4.27) is assumed to be exact. Applying this numerical discretization on the cavity surface (where $n = 0$) to equation (4.27) and (4.28), we obtain,

$$\omega \begin{pmatrix} \epsilon_{\eta 0} \\ \epsilon_{\varphi 0} \end{pmatrix} = \begin{bmatrix} -iV_{r0}\cos\alpha \sin(k\Delta s)/(\Delta s) & |k| \\ 0 & -i(V_r)_s \sin(k\Delta s)/(\Delta s) \end{bmatrix} \begin{pmatrix} \epsilon_{\eta 0} \\ \epsilon_{\varphi 0} \end{pmatrix}, \quad (4.30)$$

where Δs is the panel size.

The matrix in this equation has the following eigenvalues,

$$\lambda_{1,2} = \frac{i}{2}\left\{-[V_{r0}\cos\alpha + (V_r)_s]\sin(k\Delta s)/(\Delta s) \pm \sqrt{[V_{r0}\cos\alpha - (V_r)_s]^2 \sin^2(k\Delta s)/(\Delta s)^2 + 4|k|}\right\}. \quad (4.31)$$

They are purely imaginary. That means there is no positive eigenvalue and the disturbance will not grow. So, the problem is ***marginally stable.***

The same analysis can be applied to the Euler method of equation (4.16) and (4.22) and, without giving details, the same conclusion can be drawn.

As for the stability of the problem for the cavity surface close to the corners (detachment and re-attachment), the situation is too complicated to carry out the same analysis. The examples from the previous section illustrate that the wiggles can start from the edges and propagate into the interior part of the cavity. Since the scheme for the interior part is stable, it implies that once the wiggles are prevented from the edges, the scheme can give stable solution.

One of the tools we can use is a filter, a smoother, to smooth out all of the wiggles, but the drawback is that the high curvature and the formation of the re-entrant jet might also be smoothed out and no details of the flow can be predicted.

The alternative is to find a new scheme that itself is acting as a smoother. This idea leads us to the proposal of an alternative Euler method in the following section.

4.5 Alternative Euler method

Let us consider equation (4.16) and (4.22) again, the evaluation of the spatial derivatives of the potential and the cavity thickness are all on the right-hand side of the equations, but the time derivatives are on the left-hand side. The integration with respect to time does not act as a natural smoother in space for the potential, neither for the cavity thickness.

Since the propeller cavitation and the hydrofoil cavitation in the gust has a cyclic behavior, we can reverse equation (4.16) and (4.22) by solving the right-hand side of these two equations for the potential and the cavity thickness under the estimated time derivatives of the left-hand side of the equations from the previous cycle.

With this idea, equation (4.16) becomes,

$$A\frac{\partial \eta}{\partial s_1} + B\frac{\partial \eta}{\partial s_2} = -\frac{\partial \eta}{\partial t} + \left(\mathbf{V}_{r0}\cdot\mathbf{n} - \frac{\partial \varphi}{\partial n}\right), \tag{4.32}$$

and equation (4.22) becomes,

$$\frac{\mathbf{V}_r{}^2}{2} = \frac{\partial \varphi}{\partial t} + \frac{\mathbf{V}_{r0}{}^2}{2} + \frac{V_\infty{}^2}{2}\sigma. \tag{4.33}$$

According to equation (2.22), $V_r{}^2$ can be written as,

$$V_r{}^2 = (\mathbf{V}_{r0}\cdot\mathbf{e}_1 + u_1)^2 + (\mathbf{V}_{r0}\cdot\tau_2 + u_2)^2 + (\mathbf{V}_{r0}\cdot\mathbf{n} - \frac{\partial \varphi}{\partial n})^2. \tag{4.34}$$

Substitute this equation into equation (4.33) and after rearrange it, we obtain,

$$\frac{\partial \varphi}{\partial s_1} = -u_1 = \sqrt{2\frac{\partial \varphi}{\partial t} + V_{r0}{}^2 + V_\infty{}^2\sigma - (\mathbf{V}_{r0}\cdot\tau_2 + u_2)^2 - (\mathbf{V}_{r0}\cdot\mathbf{n} - \frac{\partial \varphi}{\partial n})^2} - \mathbf{V}_{r0}\cdot\mathbf{e}_1. \tag{4.35}$$

When the cross-flow is relatively small (which is true for the hydrofoil with high aspect ratio, but not for the flow on the propeller blade close to the tip), the potential on the cavity surface can be simply calculated by the following integration,

$$\varphi = \varphi_0 + \int_0^{s_1} \left[\sqrt{2\frac{\partial \varphi}{\partial t} + V_{r0}{}^2 + V_\infty{}^2\sigma - (\mathbf{V}_{r0}\cdot\tau_2 + u_2)^2 - (\mathbf{V}_{r0}\cdot\mathbf{n} - \frac{\partial \varphi}{\partial n})^2} - \mathbf{V}_{r0}\cdot\mathbf{e}_1\right] ds_1, \tag{4.36}$$

where φ_0 is the potential at the detachment of the cavity where $s_1 = 0$. Equation (4.36) guarantees that the potential is continuous at the detachment, but

it prescribes only the value relative to the value at the detachment φ_0 that still has to be determined by the panel method. This makes some change in the system of equations and hence we call it the continuity condition of cavity detachment.

The advantages of using equation (4.36) are:

1. The integration of equation (4.36) guarantees the prescribed potential on the cavity surface to be smooth and no wiggles will be introduced by numerical differentiation formula.

2. Equation (4.36) links the potential on the cavity surface with the potential at the detachment point (on the body surface). This guarantees the continuity and smoothness of the potential at the edge of the cavity and prevents wiggles originating from the edges.

When the prescribed potential is smooth enough, the calculated potential derivatives $\partial\varphi/\partial n$ will be smooth as well. The wiggles in Figure 4.2 disappear. Based on this smooth $\partial\varphi/\partial n$, equation (4.32) can be solved by a recursive method starting from the detachment point where the cavity thickness $\eta = 0$ and a smooth cavity surface can be obtained.

A similar procedure was followed by Kinnas & Fine (1992) and Kim & Lee (1996), who show stable and smooth results.

Chapter 5

Numerical Algorithms

Besides the numerical algorithms discussed in the previous chapters for the panel method and time stepping, other numerical implementations for the present nonlinear method are presented in this chapter, with detailed algorithms for each problem. Emphasis is on the numerical accuracy. Cavity planform search, grid update, detachment position and the cavity-body intersection are discussed. Other highly-related numerical problems for panel method and cavity flows, like Kutta condition and wake alignment, are also addressed with numerical tests. Concerns are focussed on the influence of these numerical algorithms on cavity flows.

5.1 Introduction

When a cavity surface is introduced in panel methods, the numerical algorithms for solving the problem become more complicated than the calculation for fully wetted flows. The system of equations for the boundary-value problem has to be rearranged due to both the Kutta condition at the trailing edge of a lifting body and the continuity condition (equation (4.36)) at the cavity detachment point. Different Kutta and cavity detachment conditions result in different systems of equations.

Both for the steady and the unsteady cavity flow problem, we need to guess an initial cavity shape before we can start the surface iteration or the time stepping. The natural way of starting a calculation is to start from the body surface where the cavity is expected. Searching for a possible cavity area has been found important since a good choice will save calculation time and reduce the possibility of errors that might be brought into the subsequent calculations and contaminate the whole result.

Furthermore, the cavity flow problem is a pressure sensitive problem both in the sense of physics and in the sense of numerical simulations. Kutta condition, wake shape, tip flow, grid arrangement and vortex shedding at the trailing edge have been found to have strong influence on the pressure distribution on the lifting bodies, and as a result, having a strong effects on cavitation. A good method with better prediction of pressure on the surface can expect to give a better prediction of cavitation too. Morino's Kutta condition satisfies the vorticity conservation law of Kelvin, but it does not guarantee an equal pressure at both sides of the trailing edge. However, the pressure Kutta condition gives sometimes *peculiar* pressure peaks at the trailing edge for a complex geometry and Kelvin's theorem is violated in some implementations. And for unsteady flows, the wake shape and the shedding vortex strength also have strong effects on the amplitude of the pressure peak and hence strong influence on the cavitation too.

All of these issues will be discussed in this chapter by elaborating relevant details for each numerical algorithm. Some numerical tests for these algorithms are also given in the following.

5.2 System of equations

As we have discussed in Section 3.2, using the Green's identity of equation (3.9) for both body boundary and cavity boundary will save tremendous computation time and memory for the evaluation of the influence coefficients. This kind of mixed problem will generate both Fredholm equations of the first and the second kind. Free surface wave and cavity flow applications of this method have not shown any problem when mixing Fredholm equations of the first and of the second kind. Since the Kutta condition and the continuity condition of the potential at the detachment point (equation (4.36)) will change the matrix too, it is impossible to keep the matrix strictly diagonally dominant, even in case of a fully wetted flow.

The present method is designed such that it can cope with more than one smooth surfaces, with or without cavity attached. Each surface can be either a lifting or a non-lifting body. For convenience of discussion in the following, we take a simple case of only one smooth cavitating surface with lift as an example.

We discretize the body surface with a structured network of panels so that we have NI_B panels streamwise (chordwise) and NJ panels crosswise (spanwise). The cavity is assumed to detach from the body surface at the NI_D^{th} panel from the leading edge of the streamwise strips. Similarly, the network of the panels on the cavity is also structured with the same panels in the cross direction as that on the body surface, but with different panels in the main stream direction. We denote the number of the panels in the main stream

direction on the cavity as NI_C. The collocation point has been chosen to be at the center of each panel, which is denoted as ic.

After we have calculated the integrals of equation (3.35) by the analytical method described in Section 3.4 or 3.5.4, we can substitute them into equation (3.28) and (3.29). For a certain collocation point ic, where $\mathbf{x} = \mathbf{x}_{ic}$, after re-organizing the coefficients, Green's identity can be discretized into the following system of linear equations with the sources and dipoles as the unknowns at the collocation points,

$$\sum_{ip=1}^{NI}\sum_{jp=1}^{NJ} D_{ip,jp}^{ic}\varphi_{ip,jp} = \sum_{ip=1}^{NI}\sum_{jp=1}^{NJ} S_{ip,jp}^{ic}\sigma_{ip,jp}, \tag{5.1}$$

where NI denotes either NI_B or NI_C, $D_{ip,jp}^{ic}$ are the re-organized dipole influence coefficients including the term $\dfrac{\theta(\mathbf{x})}{4\pi}\varphi(\mathbf{x};t)$ in the left-hand side of equation (3.9), and $S_{ip,jp}^{ic}$ are the re-organized source influence coefficients. We use σ instead of $\dfrac{\partial\varphi}{\partial n}$ for the sake of the notation simplification.

When the body is a lifting body, a wake surface is introduced and the normal dipole singularities are also distributed on the wake surface. We keep the same number of panels NJ for the wake too, but we used different number of panels NI_W in the main stream direction. Then the system of equations becomes,

$$\sum_{ip=1}^{NI}\sum_{jp=1}^{NJ} D_{ip,jp}^{ic}\varphi_{ip,jp} + \sum_{ip=1}^{NI_W}\sum_{jp=1}^{NJ} W_{ip,jp}^{ic}\varphi_{w\ ip,jp} = \sum_{ip=1}^{NI}\sum_{jp=1}^{NJ} S_{ip,jp}^{ic}\sigma_{ip,jp}, \tag{5.2}$$

where $W_{ip,jp}^{ic}$ are wake dipole influence coefficients and $\varphi_{w\ ip,jp}$ are the dipole strengths on the wake surface.

5.2.1 Unsteady flow

For the unsteady lifting-surface problem, whatever method is used for the Kutta condition (Morino's or pressure Kutta condition, which will be discussed in the following sections), the dipole strengths on the first spanwise row in the wake are unknowns and they are related to the dipole strengths on the body surface at the trailing edge (Morino's method) or they are determined in an iterative way (pressure method). The rest of the dipoles in the wake are known from the previous time steps. Then we can split the wake term in the previous equations into two parts as,

$$\sum_{jp=1}^{NJ} W_{1,jp}^{ic}\varphi_{w\ 1,jp} + \sum_{ip=2}^{NI_W}\sum_{jp=1}^{NJ} W_{ip,jp}^{ic}\varphi_{w\ ip,jp},$$

where the first part is unknown and the second part is known.

As we have discussed in the Chapter 4 about the alternative method for time stepping, the dipole strength on the cavity surface is obtained by integrating the velocity along the main stream direction, but it is a function of the potential φ_0 at the detachment point. For the cavity surface, the dipole term in equation (5.2) can be split as well by,

$$\varphi = \varphi_0 + \tilde{\varphi} \tag{5.3}$$

into two parts,

$$\sum_{ip=1}^{NI}\sum_{jp=1}^{NJ} D^{ic}_{ip,jp}\varphi_0 + \sum_{ip=1}^{NI}\sum_{jp=1}^{NJ} D^{ic}_{ip,jp}\tilde{\varphi}_{ip,jp},$$

where the first part is unknown and the second part is known.

Now we can apply equation (5.2) both to the body surface and the cavity surface. By moving the unknowns to the left-hand side and the knowns to the right-hand side, we obtain the following system of equations for solving the mixed unsteady cavity flow problem with Morino's Kutta condition as,

$$\begin{aligned}
&\sum_{ip=1}^{NI_B}\sum_{jp=1}^{NJ} D^{ic}_{ip,jp}\varphi_{ip,jp} - \sum_{ip=1}^{NI_C}\sum_{jp=1}^{NJ} S^{ic}_{ip,jp}\sigma_{ip,jp} \\
&\qquad + \sum_{ip=1}^{NI_C}\sum_{jp=1}^{NJ} D^{ic}_{ip,jp}\varphi_0 + \sum_{jp=1}^{NJ} W^{ic}_{1,jp}\varphi_{w\,1,jp} \\
&\quad = \sum_{ip=1}^{NI_B}\sum_{jp=1}^{NJ} S^{ic}_{ip,jp}\sigma_{ip,jp} - \sum_{ip=1}^{NI_C}\sum_{jp=1}^{NJ} D^{ic}_{ip,jp}\tilde{\varphi}_{ip,jp} \\
&\qquad - \sum_{ip=2}^{NI_W}\sum_{jp=1}^{NJ} W^{ic}_{ip,jp}\varphi_{w\,ip,jp},
\end{aligned} \tag{5.4}$$

where the first dipole strength in the wake is related to the unknowns on the body surface by Morino Kutta condition, and hence it is on the left (the fourth term). Once the pressure Kutta condition is going to be enforced, this term will be on the right-hand side as a known term, but its value will be determined by an outer iteration scheme.

5.2.2 Steady flow

For steady cavity flow, if the Morino's Kutta condition is used, all the wake dipoles are unknowns and related to the dipole strength on the body surface,

which is then moved to the left-hand side of the equations. The system of equations becomes,

$$\sum_{ip=1}^{NI_B}\sum_{jp=1}^{NJ} D^{ic}_{ip,jp}\varphi_{ip,jp} - \sum_{ip=1}^{NI_C}\sum_{jp=1}^{NJ} S^{ic}_{ip,jp}\sigma_{ip,jp} + \sum_{ip=1}^{NI_C}\sum_{jp=1}^{NJ} D^{ic}_{ip,jp}\varphi_0 + \sum_{ip=1}^{NI_W}\sum_{jp=1}^{NJ} W^{ic}_{ip,jp}\varphi_{w\ ip,jp} = \sum_{ip=1}^{NI_B}\sum_{jp=1}^{NJ} S^{ic}_{ip,jp}\sigma_{ip,jp} - \sum_{ip=1}^{NI_C}\sum_{jp=1}^{NJ} D^{ic}_{ip,jp}\tilde{\varphi}_{ip,jp}. \quad (5.5)$$

But if the pressure Kutta iteration is going to be used, the system of equations has to be rearranged as,

$$\sum_{ip=1}^{NI_B}\sum_{jp=1}^{NJ} D^{ic}_{ip,jp}\varphi_{ip,jp} - \sum_{ip=1}^{NI_C}\sum_{jp=1}^{NJ} S^{ic}_{ip,jp}\sigma_{ip,jp} + \sum_{ip=1}^{NI_C}\sum_{jp=1}^{NJ} D^{ic}_{ip,jp}\varphi_0 + \sum_{ip=2}^{NI_W}\sum_{jp=1}^{NJ} W^{ic}_{ip,jp}\varphi_{w\ ip,jp} = \sum_{ip=1}^{NI_B}\sum_{jp=1}^{NJ} S^{ic}_{ip,jp}\sigma_{ip,jp} - \sum_{ip=1}^{NI_C}\sum_{jp=1}^{NJ} D^{ic}_{ip,jp}\tilde{\varphi}_{ip,jp} - \sum_{jp=1}^{NJ} W^{ic}_{1,jp}\varphi_{w\ 1,jp}, \quad (5.6)$$

where, except for the first panel in the wake, the others are on the left. It is due to the reason that Kelvin's Theorem (equation (2.43)) must be fulfilled, which means that the rest of the wake should satisfy Morino's Kutta condition and the first panel is used as an artificial device to make the pressure equal. More discussions about this will be given in the section of this chapter on Kutta conditions.

But whatever system of equations is used, we can always write it into the following compact matrix form as,

$$\begin{pmatrix} \mathbf{D}_{BB} & -\mathbf{S}_{BC} \\ \mathbf{D}_{CB} & -\mathbf{S}_{CC} \end{pmatrix} \begin{pmatrix} \varphi_{\mathbf{B}} \\ \sigma_{\mathbf{C}} \end{pmatrix} = \begin{pmatrix} \mathbf{S}_{BB} & -\mathbf{D}_{BC} \\ \mathbf{S}_{CB} & -\mathbf{D}_{CC} \end{pmatrix} \begin{pmatrix} \sigma_{\mathbf{B}} \\ \tilde{\varphi}_{\mathbf{C}} \end{pmatrix}, \quad (5.7)$$

where, the subscript B and C denotes the body surface and the cavity surface, respectively. However they include terms from the wake and φ_0.

Since the right-hand side of the system of equations is known, we can write it in the following form as a system of linear equations for the unknowns $\mathbf{v}$,

$$\mathbf{A}\,\mathbf{v} = \mathbf{b}. \tag{5.8}$$

where,

$$\mathbf{v} = \begin{pmatrix} \varphi_{\mathbf{B}} \\ \sigma_{\mathbf{C}} \end{pmatrix}.$$

Solving this equation, we obtain the potential distribution on the body surface and the normal derivatives of the potential on the cavity surface. The wake dipole strength is hence obtained.

It should be noted that, for a purely nonlinear method, the influence coefficients in the matrix $\mathbf{A}$ of equation (5.8) have to be re-evaluated in each iteration or time step since the cavity shape is changing with either the surface iteration or the time iteration. This makes the present method relatively more expensive than the linear method. On the other hand, the coefficients are not needed to be re-calculated if a linear method with some special techniques is used, such as the so-called split-panel method proposed by Kinnas & Fine (1993). If the cavity planform is moving with time, even when a linear method is used, the influence coefficients have to be re-evaluated.

Matrix $\mathbf{A}$ is a full matrix. And due to the use of the Fredholm equation of the first kind for the cavity surface, this matrix is no longer diagonally dominant. The third and fourth terms on the left-hand side of equation (5.4) make it even worse. A conventional iterative method can not give a convergent result for this system of equations. Even if the congrate-conjugate method is used, the speed of the convergence doesn't show much advantage on calculation efficiency. So, an L-U method is used in the present calculations.

5.3 Cavity planform search

Strictly speaking, there is no need to search for the planform (the area the cavity covers) in the fully non-linear cavity flow theory. The cavity surface evolves iteratively and the planform of the cavity is determined accordingly. But the first good guess will speed up the whole calculation and reduce the risk of instability that may happen when the first guess is too far away from the final result.

Another reason of searching the planform in the fully non-linear theory is that, comparing to its evolution in the normal direction, the evolution of the cavity shape in longitudinal direction is very slow, especially when the first guess is a too short cavity. Numerical experiments on two-dimensional cavity flow show that hundreds of iteration steps are needed to achieve the convergence

(as shown in Figure 6.5 and 6.6). But this is prohibitive for three-dimensional cavity flow calculations.

The basic idea of searching the cavity planform is to apply the cavity boundary condition on the body surface beneath the guessed cavity and then predict only once the cavity shape to find the intersection of the cavity with the body and determine the new guess of the cavity planform as shown in the **1st search** of Figure 5.1, where we chose a NACA 16-006 section with an aspect ratio of 2 as an example. The angle of attack is 4° and the cavitation number is 0.5. First, we choose the cavity planform as an equal length cavity with $l/chord = 0.8$. After one calculation of the cavity, the basic shape of the cavity is obtained as shown in this figure with zero cavity length at the tip where the load is zero. By applying the boundary conditions on the new planform again (but not on the last predicted cavity surface), a new cavity shape and its intersection can be found, as shown by the **2nd search** in Figure 5.1. We can make some more searching until a converged result is reached. But normally, three searches are enough.

This scheme has been found to be stable even for the cavity flow on a propeller blade close to the tip, where other methods might fail. But it may be somewhat slower than the Newton-Raphson method that we will discuss in the following. The disadvantage of this method is that we have to start with a very long guess of the cavity length to make sure that there is an intersection between the cavity and the body surface.

The other cavity planform searching method, which is thought to be more general and faster, is proposed by Kinnas & Fine (1993) with a Newton-Raphson (secant method) scheme. After the calculation of the cavity shape according to the alternative Euler method, the cavity thickness at the guessed cavity end is obtained. This value can be positive (if the cavity does not intersect with the body surface) or negative (if the cavity end intersects the body surface). Let us denote this thickness as $\eta_{end} = (\eta_1, \eta_2, \cdots, \eta_{N_{T.E.}})^T$, where $N_{T.E.}$ is the number of the trailing edge panel, then the scheme reads,

$$\mathbf{l}^{k+1} = -\mathbf{J}^{-1}{\eta_{end}}^k + \mathbf{l}^k, \tag{5.9}$$

where $\mathbf{l} = (l_1, l_2, \cdots, l_{N_{T.E.}})^T$ denote the cavity length, the supercript k denotes the iteration step and $\mathbf{J}$ is the Jacobian,

$$J_{ij} = \frac{\partial \eta_i}{\partial l_j} \quad i, j = 1, 2, \cdots, N_{T.E.}. \tag{5.10}$$

If we would like to renew the Jacobian in each iteration step, it will take us at least $N_{T.E.}$ full calculations. It makes this method prohibitively expensive and hence impractical. But for some simple geometry like a rectangular hydrofoil, a local scalar Newton-Raphson method for a single strip can be used which converges very fast.

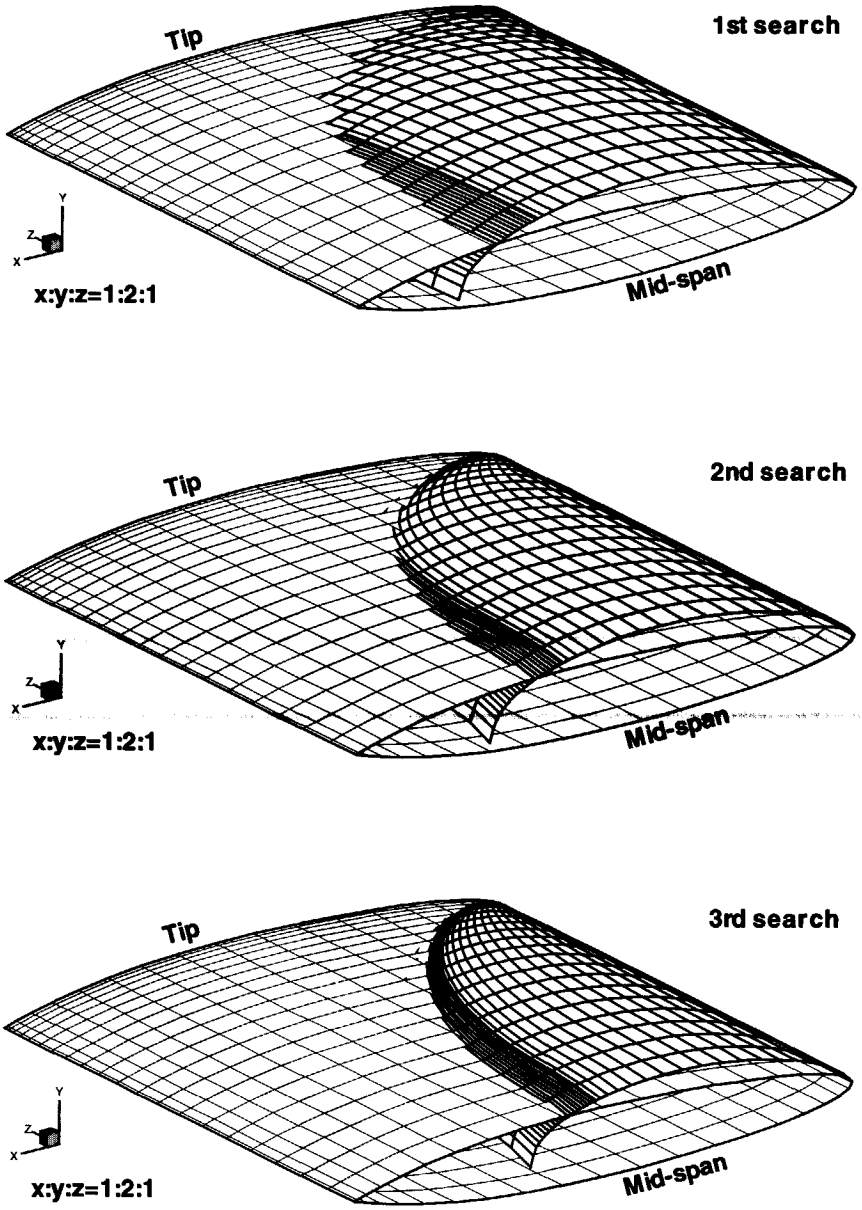

Figure 5.1: Planform searching procedure on a rectangular hydrofoil. (NACA 16-006, aspect ratio AR=2, angle of attack $\alpha = 4^o$, cavitation number $\sigma = 0.5$).

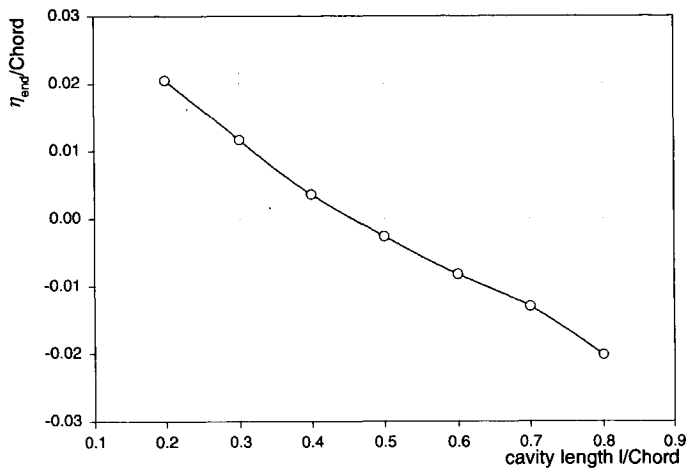

Figure 5.2: The cavity end thickness on a rectangular hydrofoil. (NACA 16-006, aspect ratio AR=500, angle of attack $\alpha = 4^o$, cavitation number $\sigma = 1.0$).

In order to evaluate the Jacobian, a two-point finite-difference scheme is used. That means we must give a perturbation to the cavity length and then calculate the cavity thickness at the end again. An example of the relation between the chosen cavity length and its calculated thickness at the end is shown in Figure 5.2. Here the hydrofoil is a rectangular one with a very high aspect ratio. Since this variation of the end thickness, with respect to the cavity length, is almost linear, the choice of the amount of perturbation is relatively insignificant and the two-point difference scheme can be accurate enough.

The disadvantage of this method is that it may become very inaccurate for propeller cavity flows, because the neglected off-diagonal terms in the Jacobian can be very important for the case where three-dimensional effects are strong. Furthermore, the variation of the cavity end thickness with respect to the length in the propeller case is no longer linear or close to linear anymore. Newton-Raphson method may lead to an unexpected result, like a zigzag cavity end, which finally induces instability in the further non-linear iteration.

For an extreme geometry, the local scalar Newton-Raphson method is therefore not recommended.

5.4 Cavity model and grid update

As we have discussed in Section 2.4.4 with Figure 2.2 that the cavity end, in the present frame of the inviscid potential flow theory, can be only tangential

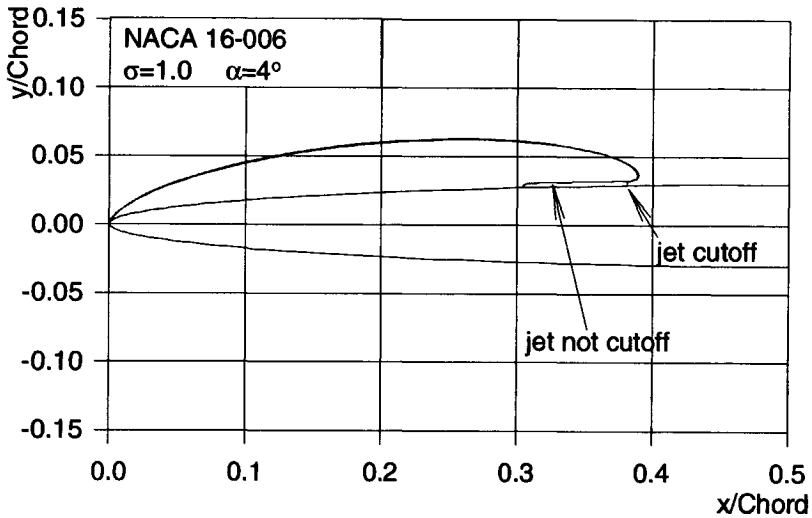

Figure 5.3: Comparison of the cavity shapes with and without jet section.

to the body surface with fluid moving upstream into the cavity. This kind of cavity model is called re-entrant jet cavity closure model, which is thought to be the most physical and mathematically consistent model. Furness & Hutton (1975) have filmed the process of the re-entrant jet formation by high-speed cinaphotography. From the speed of the film, the velocity of the re-entrant jet was measured. The measurement shows that the maximum speed of the re-entrant jet is close to the freestream velocity.

De Lange (1996) succeeded to simulate this re-entrant jet. But his calculation has to stop when the re-entrant jet touches the cavity surface. In order to avoid this, we decided to cutoff the re-entrant jet and prescribe a boundary condition at this cut-off to make the flow pass through it. We call this a re-entrant jet model and it will be discussed in Chapter 6.

We succeeded to use this model for two-dimensional cavity flow. To investigate the influence of the re-entrant jet velocity on the cavity volume and length, the flow around NACA 16-006 at an angle of attack 4° is calculated and shown in Figure 5.3. In order to make sure that this cut-off will give the same results as that of De Lange (1996)'s model, we calculated also the flow with a free re-entrant jet. It is also plotted in Figure 5.3. They are very close.

The free jet here means that we did not use the jet cut-off boundary and the jet is not cut-off. So, with the iteration continuing, the jet evolves automatically. Figure 5.3 shows that when the free jet is developed long enough, these two methods give exactly the same result.

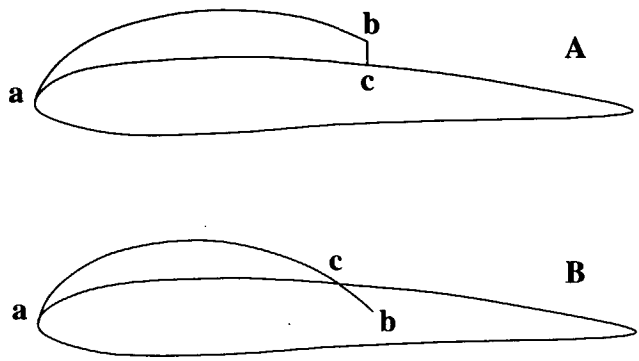

Figure 5.4: Schematics of the intersection between cavity surface and the solid body surface.

This result suggests that the jet boundary is not really needed. It can be easily described in the two-dimensional situation, however it can be hard to describe it in a three-dimensional situation. So this model is not used in our three-dimensional calculations.

To give as much freedom as possible to the evolution of the cavity surface and the re-entrant jet in three-dimensional flow, we decided to apply the exact dynamic and kinematic boundary conditions up to the last panel at the cavity closure and let the end of the cavity evolve by itself.

We reduced our restrictions at the end of the cavity to the minimum by using only two treatments as shown in Figure 5.4.

1. When the cavity end is above the body surface, the end of the cavity is simply connected with the body surface with a vertical surface that is thought to be the continuity of the original cavity surface, as shown in Figure 5.4A. The cavity surface has to be re-paneled according to the arc length from a to c in this figure.

2. When the cavity end intersects the body surface, these part inside of the body is simply truncated, and the cavity surface is re-paneled also according to the arc length from a to c in Figure 5.4B.

We use a fixed form of panel distribution on the cavity from the detachment point to the reattachment point, as given in equations (6.21) to (6.24) later on. This means that after each iteration, the cavity surface has to be re-paneled and the panel size is varying along the cavity surface all the time.

In order to find the intersection of the cavity surface with the body surface, the paneling of the cavity surface is chordwise based. This means that the

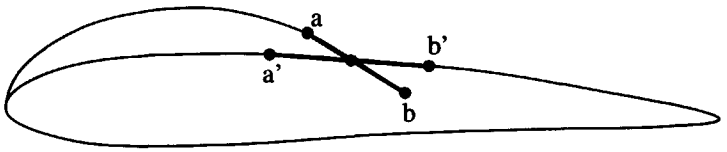

Figure 5.5: Schematics of the intersection between cavity surface and the solid body surface.

cavity panels are always just above the panels that on the same strip of the body from which the cavity surface detaches at its leading edge. This does not always guarantee that the panel edges intersect as shown in Figure 5.5. The panels on the body surface are fixed ($a'b'$ panel in Figure 5.5), but the cavity surface (ab line) is modified to be on the same surface as line $a'b'$ by a movement in the direction of $(\vec{a'b'} \times \vec{ab})$.

For the panel that has straight edges, the edge can be written into the following parametric formulas as straight lines (as shown in Figure 5.5),

$$\begin{aligned} \mathbf{x}' &= \mathbf{x}_{a'} + (\mathbf{x}_{b'} - \mathbf{x}_{a'})\lambda_1 \quad (0 \le \lambda_1 \le 1) \\ \mathbf{x} &= \mathbf{x}_a + (\mathbf{x}_b - \mathbf{x}_a)\lambda_2 \quad (0 \le \lambda_2 \le 1). \end{aligned} \tag{5.11}$$

At the intersection point, these two equations are equal and we have,

$$\mathbf{x}_{a'} + (\mathbf{x}_{b'} - \mathbf{x}_{a'})\lambda_1 = \mathbf{x}_a + (\mathbf{x}_b - \mathbf{x}_a)\lambda_2. \tag{5.12}$$

It consists of three equations with only two unknowns λ_1 and λ_2. This system is over-determined and a least-square approach has to be used to find the value of λ_1 and λ_2. Since the calculated intersection by these two formulae might be slightly different due to numerical truncation errors, an average value is used,

$$\mathbf{x}_{inter} = \frac{\mathbf{x}(\lambda_1) + \mathbf{x}'(\lambda_2)}{2}, \tag{5.13}$$

where, $\mathbf{x}_{inter}$ denotes the position vector of the intersection.

5.5 Detachment of sheet cavity

The detachment point of a cavity from the solid body is also called the position of cavitation separation. Bodies with sharp corners possess a cavitation separation point which is known to be located at this sharp corner and hence it is given *a priori* for our present method. But for smooth bodies, a smooth separation condition, as we have given in equation (2.36), is usually used.

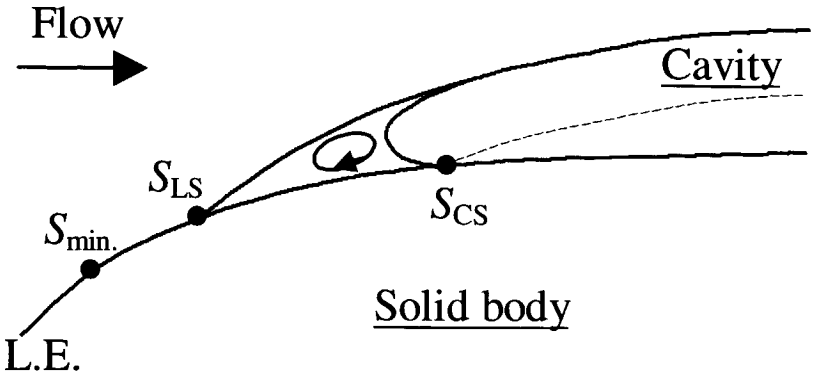

Figure 5.6: Schematics of the separation point of the cavity on a smooth solid body.

But it was observed that the experimentally-found position of cavitation separation lies considerably downstream from that predicted by smooth separation. This leads us to assess the present smooth separation condition and its influence on the predicted cavity length and volume.

Arakeri (1975) observed the smooth cavitation separation on two different headforms and found two different kinds of separations: the viscous laminar separation and the nucleate separation. He concluded that the position of nucleate cavitation separation is predicted quite accurately by the smooth separation condition. But for the viscous laminar cavitation separation, the predicted position by smooth separation condition does not given accurate results. A similar observation and conclusion was later given by Franc & Michel (1985) for the case of cavitating hydrofoils.

A schematics of the observation at the separation point of the cavity is given in Figure 5.6. The minimum pressure point is denoted by $s_{min.}$ in this figure. The laminar separation point s_{LS} is known to be close to the maximum negative pressure gradient point downstream of the minimum pressure peak $s_{min.}$, where subscript LS denotes laminar separation. The cavitation separation point is observed well downstream of the laminar separation point as shown at s_{CS}, where CS means the cavitation separation. The area between s_{LS} and s_{CS} is called a *dead water* region. Within this region, there is a local circulation of the fluid in the direction as shown by the arrow in the figure.

But the observation of Arakeri (1975) shows that cavitation bubbles are first observed to originate within the reattachment portion of the separation region in the non-cavitating laminar boundary layer. With reduction in the cavitation

number, a considerable portion of the separated flow region is observed to be filled by cavitation bubbles, and, with further reduction of the cavitation number, almost all of the separation region is occupied by the attached smooth cavity. Accompanied with this process is that the laminar separation position is also observed to move upstream and close to the minimum pressure position $s_{min.}$.

Since the present numerical simulation of cavity flow deals only with fully developed sheet cavity flows, due to the existence of the cavity, the laminar separation of the boundary layer before the cavity separation point can be roughly set to the minimum pressure point $s_{min.}$ with acceptable errors.

On the other hand, the round nose of the cavity at the separation point as observed is believed to be the effect of the surface tension, which is neglected in the present method. Therefore, we could not predict a cavity with round nose. If we still set the cavity separation point at s_{CS} as observed, the cavity shape is predicted as shown in the dashed line in Figure 5.6. It does not give a correct prediction. A reasonable choice of the detachment point of the cavity for the present method might be the laminar separation point s_{LS}, which is close to the minimum pressure peak point $s_{min.}$ as we argued before. It then means that we take the triangular part of the dead water in front of the cavity as part of the cavity.

Kinnas *et al.* (1994) investigated the influence of the detachment point on the predicted cavity flow. They fixed the cavity length and calculated the corresponding cavitation numbers. Rowe & Blottiaux (1993) predicted the influence of the detachment point on the geometry of the cavity and the pressure distribution on the foil surface. In the following, we will show the influence of the cavity separation point on the cavity shape and the cavity length too. The sensitivity for different profiles and the relation between the pressure distribution and the cavity shape are also discussed.

We took NACA 16 series section as an example. The angle of attack is set at 4° because it is a typical situation of a section on a propeller blade. We chose four different thicknesses for the investigation, $t/C = 0.06, 0.09, 0.12$ and 0.15. The cavitation number is chosen to be $\sigma = 0.87513$. At this cavitation number the cavity length is approximately 50% of the foil chord length.

All the calculation have been obtained with 100 panels for the wetted part of the foil, 100 panels for the cavity surface and 10 panels for the re-entrant jet surface.

The influence of the detachment point on the cavity length is surprisingly large as shown in Figure 5.7. For all four sections, it is found that there is a special detachment point for each section, for which the predicted cavity length reaches its maximum. For the thin section (NACA 16-006), this point is at the leading edge. With the increase of the foil thickness, this point moves downstream.

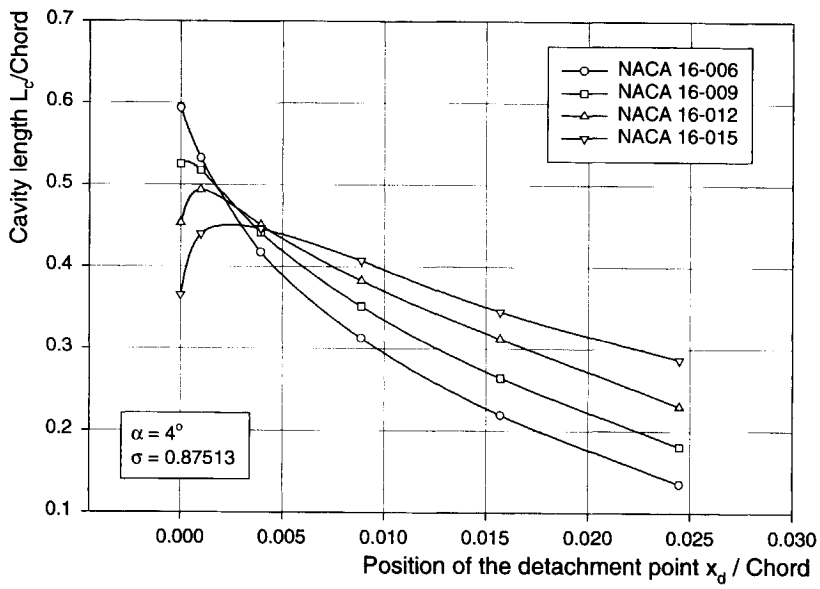

Figure 5.7: Influence of the detachment position on the cavity length. (NACA 16 series, $\alpha = 4°$, $\sigma = 0.87513$)

The sensitivity of the cavity length to the detachment point is much higher for the thin section (NACA 16-006) than for the thick section (NACA 16-015). This makes the present research easier since the thin sections (e.g. NACA 16-006) has normally a cavitation separation at the leading edge, which avoids the strong influence of the detachment point. For a thick foil (e.g. NACA 16-015), the laminar separation point strongly depends on Reynolds number, but a small error in the estimation of the separation point does not affect the predicted cavity length and volume too much.

This effect can be expressed more precisely in term of the pressure distribution. When the suction peak and the gradient is very high, the cavity is sensitive to its detachment point. When the suction peak and its gradient is lower, the cavity is relative insensitive to the detachment point.

If we compare the position of the detachment point, for which the cavity has a maximum length, with the pressure distribution of the fully wetted flow around the nose (Figure 5.8), we will notice that the cavity reaches the maximum when the detachment point is around the minimum pressure point. At the same time, the cavity shape at the nose of the foil shows that the detachment is smooth only when the detachment point is at the minimum pressure

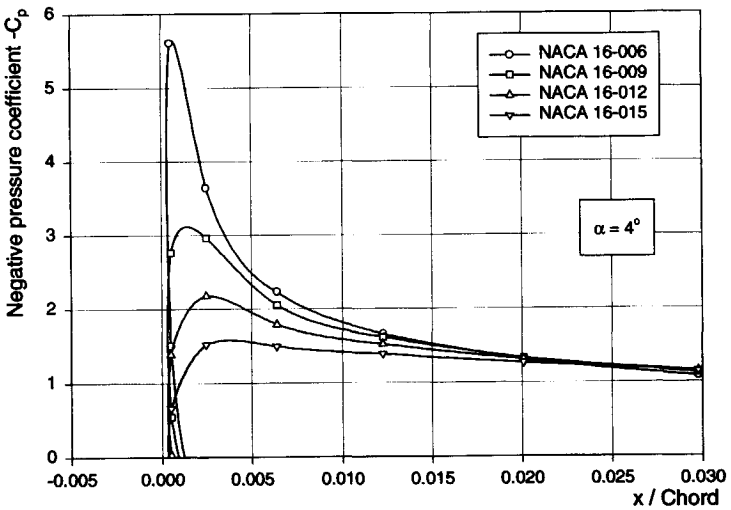

Figure 5.8: Pressure distribution at the nose of NACA 16 series.

point (Figure 5.9). If the detachment point is chosen in front of this point, the predicted cavity surface intersects the solid surface. This is contradictory to reality.

On the other hand, if the detachment point is chosen at a location downstream of the minimum pressure point, the cavity detaches from the solid surface at nonzero angle. Then a stagnation point is expected at this point, which is also impossible in reality.

The most applicable and maybe the most correct location to choose the detachment point in the present simulation is still at the minimum pressure point of the fully wetted flow.

It should be pointed out that, the outer surface from s_{LS} to s_{CS} of the boundary layer is treated in the present method as cavity surface and a cavity pressure p_c is enforced on this part of the surface in the calculation. An error can be expected due to this, but the error will not be too large because the pressure in the *dead water* should be a constant and close its environment, the cavity.

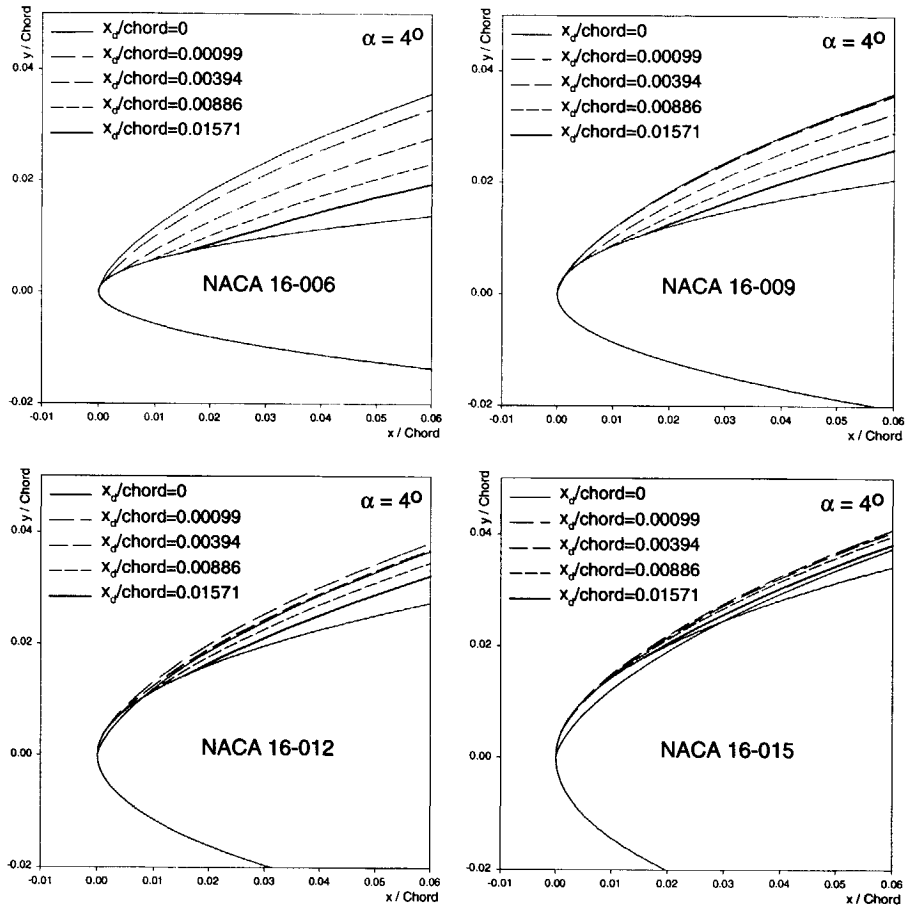

Figure 5.9: Detachment of the cavity from the foil surface at different positions. (NACA 16 series, $\sigma = 0.87513$, $\alpha = 4°$)

5.6 Wake shape

Hydrodynamic modeling of the wake geometry of a propeller is one of the important problems in propeller theory. It has been found that the influence of the wake geometry on the predicted hydrodynamic forces on the propeller can be higher than 4% for a heavily loaded conventional propeller (Moulijn & Kuiper (1995)), comparing to the wake geometry determined by mean blade geometric pitch. For highly skewed propellers, this effect is believed to be higher. A calculation for the highly skewed propeller DTMB 4661 at $J = 0.8$ (design $J = 1.038$) shows that the influence of the wake alignment on both the thrust and torque is as high as about 4.5% (Kinnas & Pyo (1997)), comparing to the original wake used in their program. Since the cavity flow is a sensitive phenomenon reflecting severely in the surface pressure distribution, a similar level of influence on the cavity flow, volume and length of the cavity, can be expected.

The treatment of the wake alignment started from the application of lifting line-theory to both the propeller prediction and the propeller design. At that stage the wake shape is normally chosen as a constant pitch on helical lines at constant radius. This is expected to give a good approximation of the wake geometry under the assumption that the propeller is well designed and close to the optimal efficiency condition, for which the wake has a constant pitch in the far-field wake (Burrill (1947)). Practically, this pitch is chosen to be the blade mean geometrical pitch.

A sophisticated empirical wake model was suggested by Kerwin & Lee (1978). They assumed that all the trailing vortices would roll-up into the tip vortices for each blade and a single hub vortex at a certain contracted point in the wake. The far-field wake is treated as constant pitch helical lines. This model later has been revised by partially alignment of the wake pitch for the transition wake with the calculated velocity in the wake, but the wake sheet roll-up is ignored (Greeley & Kerwin (1982)). The radial position of the wake is restrained to a certain radius, only the pitch is aligned in this method. In stead of aligning the transition wake, Hoshino (1991) aligned the far-field wake and interpolate the transition wake with a linear method connecting the blade trailing edge and the far-field wake.

A full alignment of a marine propeller wake according to the flow velocity was carried out by Maitre & Rowe (1991) using a panel method. A similar method was also used by Takinaci (1996) accounting for the viscous effect at the trailing edge. A quantitative analysis of the effect of wake alignment on the induced velocity and on the loading distribution on the propeller is given by Moulijn & Kuiper (1995). A more sophisticated method based on a higher-order panel method is provided by Pyo (1995).

Up to today, all of these method are for steady flows. Unsteady wake alignment is now tried for two-dimensional flows but no method has been available

for unsteady three-dimensional wake alignment, due to its high cost. In most unsteady flows, the wake is considered to be fixed as the aligned wake in the circumferentially averaged inflow.

Other wake alignment theory based on potential panel method can be found in Johnson & Rubbert (1975) and Hoeijmakers (1989).

5.6.1 Theory

According to the boundary condition of equation (2.38), there should be no pressure jump across the wake sheet. In other words, the wake sheet cannot carry any force. According to the Kutta-Joukowsky law, the force $\mathbf{F}$ acting on a vortex segment ds in the wake sheet is given in the following equation,

$$d\mathbf{F} = \rho \mathbf{V} \times \gamma ds, \tag{5.14}$$

where, γ is the vector of the vortex and $\mathbf{V}$ is the total velocity. Then the pressure jump Δp across the sheet can be written as,

$$\Delta p = \rho \mathbf{V} \times \gamma. \tag{5.15}$$

Because the velocity $\mathbf{V}$ and the vorticity γ are generally not zero, they have to be co-parallel or anti-parallel to avoid a pressure jump across the sheet,

$$\mathbf{V} \times \gamma = 0. \tag{5.16}$$

Whatever lower-order or higher-order panel method is used, the vorticity is assumed to keep the same value streamwise on the sheet to satisfy Kelvin's theorem. In other words, the vorticity vector γ is presumed to be in the streamwise direction, i.e. approximately along the chordwise grid lines. In order to fulfill the requirement of equation (5.16), the grid line has to be aligned with the local velocity.

5.6.2 Implementation

The local velocity can be calculated by equation (2.7). A method based on the hyperboloidal quadrilateral panel method with constant singularity distributions has been used in the present investigation. The induced velocity from the surface normal dipole and the source distributions is calculated by the spatial derivation of equation (3.86) and (3.87). The velocity is evaluated at the nodal point of the grid. The self-induced velocity from the edge (passing through the nodal point) is neglected.

It has been shown by Pyo (1995) that lower-order panel method with the simple Euler method,

$$\mathbf{x}_{ip,jp} = \mathbf{x}_{ip-1,jp} + \mathbf{V}_{ip-1,jp}\Delta t \quad \text{for every } jp, \tag{5.17}$$

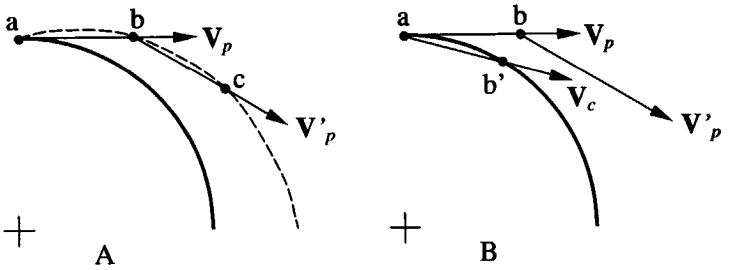

Figure 5.10: Euler method (A) and prediction-correction method (B) for the wake alignment in the circular moving flow.

for the wake alignment does not lead to convergent result, where Δt is the time interval when the fluid particle travels from grid point $ip-1$ to ip. This is true when coarse grid is used.

The problem of using Euler's method is shown in Figure 5.10(A), where the fluid particle follows the velocity $\mathbf{V}_p$ from point a to b, and it travels further in the next time step according to velocity $\mathbf{V}'_p$ from point b to point c. Even if the velocity field is a solid-body rotation field, like the uniform inflow towards a propeller, the trace of the particle will follow a divergent path as shown in the dashed line in Figure 5.10(A). This divergent effect is not retrievable by increasing the number of panels. A method based on Euler formula will never predict the contraction of the wake. This is why Moulijn & Kuiper (1995) concluded that the application of the cylinder coordinates is necessary to get a converged result. Using cylinder coordinates however will loose generality and limit its applications to other lifting problems.

This problem can be simply avoided by using a prediction-correction method, where the prediction is given by Euler's formula,

$$\tilde{\mathbf{x}}_{ip,jp} = \mathbf{x}^{n-1}_{ip-1,jp} + \mathbf{V}(\mathbf{x}^{n-1}_{ip-1,jp}) \cdot \Delta t \quad \text{for every } jp, \tag{5.18}$$

and the correction is given by,

$$\mathbf{x}^{n}_{ip,jp} = \mathbf{x}^{n-1}_{ip-1,jp} + \frac{1}{2}(\mathbf{V}(\mathbf{x}^{n-1}_{ip-1,jp}) + \mathbf{V}(\tilde{\mathbf{x}}_{ip,jp})) \cdot \Delta t \quad \text{for every } jp, \tag{5.19}$$

where the superscript n means the iteration steps. An illustration is given in Figure 5.10B where the subscript p denotes the prediction and the c denotes the correction. Instead of from point a to b, fluid particle will move from point a to b', which stays on the circle in the uniform inflow.

A strategy to speed up the roll-up of the wake has been discussed by Pyo (1995) and a similar method has been developed in the present method. The

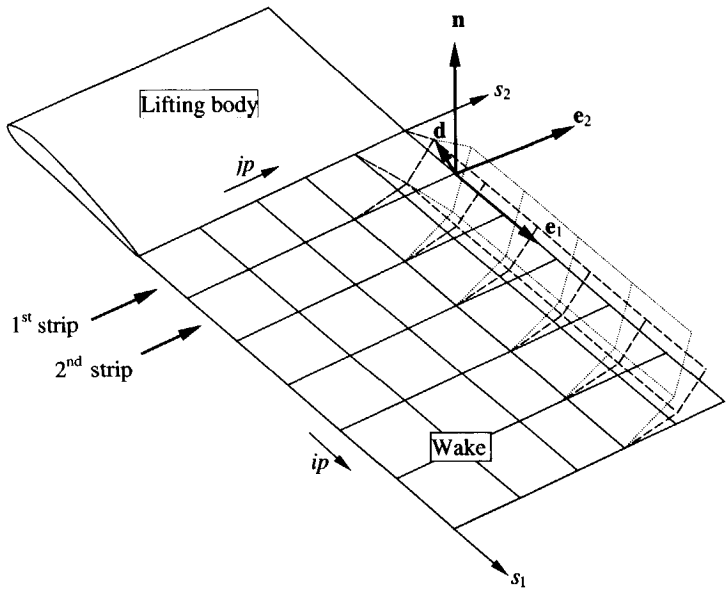

Figure 5.11: Schematics of the effective wake rolling-up procedure, downstream of a lifting body.

roll-up of the wake is done spanwise, strip by strip, as illustrated in Figure 5.11. The observation of a particle on the wake sheet shows:

1. The particle remains on the wake sheet surface and its travelling direction determines the whole wake downstream of it.

2. The neighboring panels of the particle have the strongest influence on the induced velocity at this particle and hence determine its moving direction.

which suggest us to update all the geometry downstream of the present strip immediately as shown in Figure 5.11.

As we have used in the curvilinear higher-order panel method, a local Cartesian surface coordinate system is set up at every nodal point, where $\mathbf{n}$ is the unit normal vector and $\mathbf{e}_2$ is perpendicular to $\mathbf{n}$ and $\mathbf{e}_1$ as shown in Figure 5.11. As soon as the displacement of the grid point (ip, jp) is calculated according to the prediction-correction method,

$$\mathbf{d} = \mathbf{x}^n_{ip,jp} - \mathbf{x}^{n-1}_{ip,jp}, \tag{5.20}$$

it is decomposed into the components along $\mathbf{e}_1$, $\mathbf{e}_2$ and $\mathbf{n}$ and preserved for the subsequent strips. The displacement of the subsequent grid points is de-

termined by this preserved components and applied in its local Cartesian coordinates. After the alignment of the first strip, the whole wake is shown as the dashed line in Figure 5.11. Applying the same technique to the second strip, the wake geometry becomes as shown by the dotted line in the same figure. This is done until the last strip of the wake.

5.6.3 A test case

It has been found that this technique gives a very quick convergence of the wake shape. A test case is shown in figure 5.12 for Propeller 4119 (Jessup (1989)) in uniform inflow at an advance coefficient of $J = 0.833$. The initial wake is determined by the uniform onset flow. It is shown that the present prediction-correction method gives a perfect circular shape for the initial wake (Figure 5.12(a)) and the pitch of the wake is a constant along both the shaft and radial directions. After one iteration, the wake pitch shows variation along the radial direction and it is already very close to the converged wake shape. Practically, three iterations are generally enough.

It should be noted that the roll-up of the vortex sheet into the tip and hub vortex cores is an endless procedure. To resolve the details of the core requires tremendous amount of panels and hence is generally not practical. This detailed core shape has found to have almost no effect on the pressure distribution and loading of the propeller. Hence it is not of interest in the present work. The judgement of the convergence of the wake is simple by its global shape and its induced velocity on the propeller blade.

A top view from the blade tip to the root for the aligned wake is shown in Figure 5.13. Generally speaking, at the design condition, the empirical method which determines the wake pitch as the averaged direction of the upper surface and lower surface at the blade trailing edge is correct for the wake at most radial positions, except the radius close to the tip, where the wake leaves the trailing edge at a large angle to the nose-tail line. The waviness of the wake lines at the last radius is caused by the roll-up of the tip vortices.

The aligned wake improves the prediction of the thrust and torque acting on the propeller in a wide range of advance coefficients J, independent of empirical ways of choosing the wake, which in most situations are propeller geometry dependent. More consistent results can be expected by using the wake relaxation. But due to the complication of this problem, the influence of the wake alignment on the cavitation prediction within the present theory is not investigated in detail in the present research. The discussion about its influence on fully wetted flows and the loading on propeller blades can be found in Pyo (1995), Maitre & Rowe (1991), Takinaci (1996), etc.

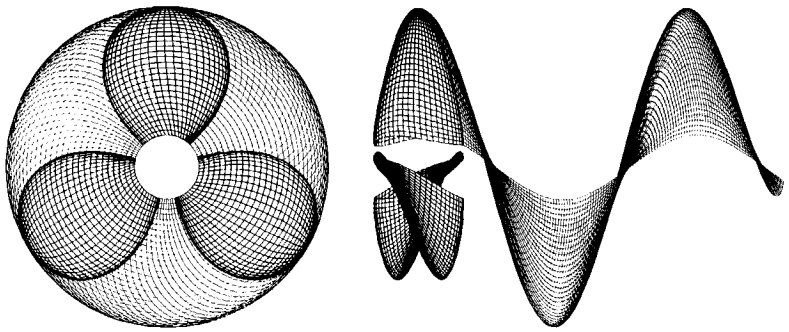

(a) Initial wake

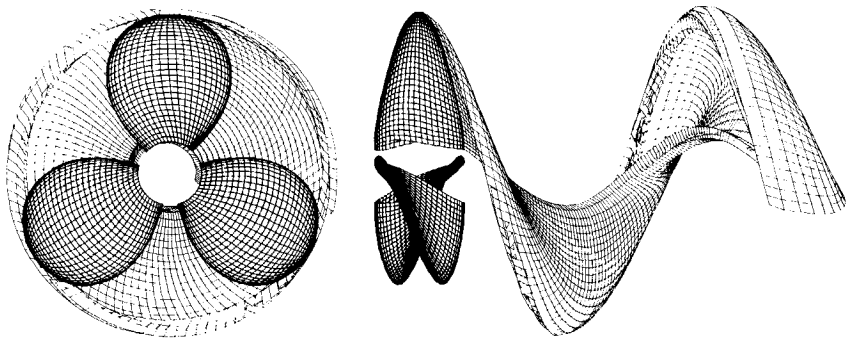

(b) After 1st iteration

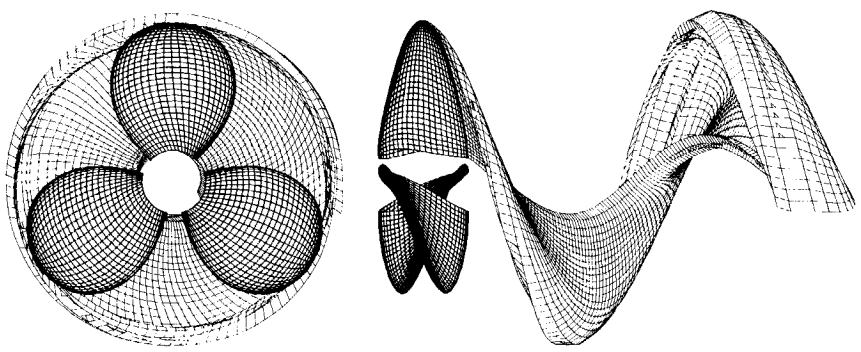

(c) After 2nd iteration

Figure 5.12: Wake alignment procedure for Propeller 4119 at design point $J = 0.833$. 30×50 panels are used on the blade surface, 30×120 are used on the wake. (Only one of the three wake sheets is shown.)

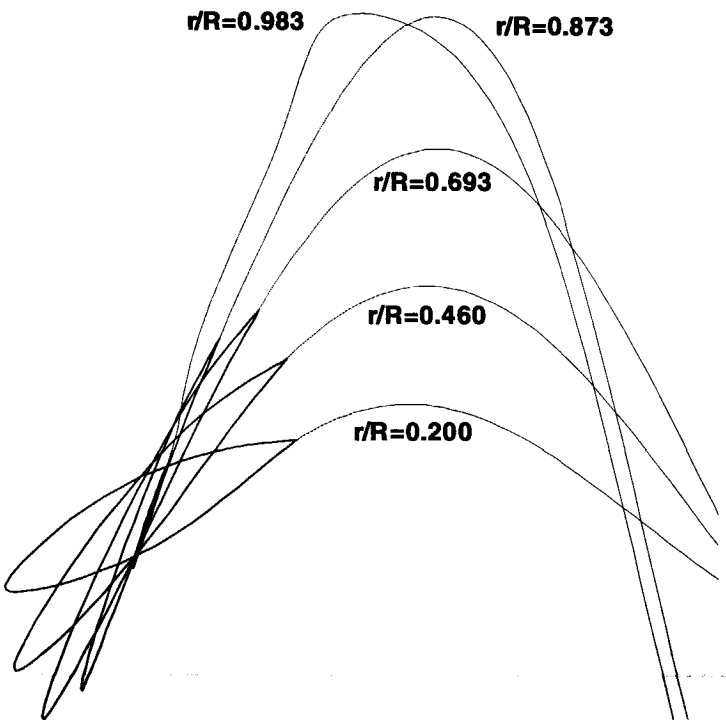

Figure 5.13: Top view (from the tip to the root) of blade sections and their aligned wake at selected radius for Propeller 4119 at $J = 0.833$.

5.7 Kutta condition

The flow around the trailing edge of a lifting body is very complicated, which involves viscous effects, boundary layer development, flow separation, and vortex forming and shedding. Solving the full Navier-Stokes equations for such a problem with the present numerical method and computer is still not practical. It is found that, for un-separated flows, the trailing edge plays a crucial role in controlling the entire flow field around lifting bodies. Although methods based on interacting boundary-layer theory (Crighton (1985)) are well developed and practically used in recent years to tackle the trailing edge problem, potential flow theories with a Kutta condition at the trailing edge, still remain the main stream of engineering methods.

The Kutta condition at the sharp trailing edge of lifting bodies, in the frame work of invicid flow, has been proposed in the beginning of the last century. The initial idea is to fix the undetermined value of the bound circulation around

a lifting body by removing the velocity singularity at the trailing edge, or in other words, to make the velocity at the trailing edge finite. Later on, this Kutta condition was extended to unsteady flow as stated: the change of the bound circulation should make the stagnation streamline to be an extension of either one of the tangents of the body surface at the trailing edge. These are the classical Kutta conditions for both steady and unsteady flows. A logical reasoning on this classic condition has been given recently by Polling & Telionis (1986) for both steady and unsteady flows. It is concluded from the paper that these conditions are equivalent to requiring a zero loading at the trailing edge, as given by equation (2.39).

Many experiments have been done to validate this statement of the Kutta condition and the range of its applicability. But no consistent pattern has emerged yet (McCroskey (1982)). In unsteady flow, the situation is even worse and the trailing edge flow is poorly understood, physically and mathematically. Visualization experiments of Ohashi & Ishikawa (1972) found that the Kutta condition is valid for all their test conditions. But Polling & Telionis (1986) stated from their results that the classical unsteady Kutta condition is clearly not valid and the experiments show that the loading at the trailing edge is not always zero too, due to the abrupt high curvature of the shedding vortex sheet at the trailing edge. In the other word, the very near wake sheet after the trailing edge can withstand vertical forces. The same phenomenon has also been found by Fleeter (1979).

All the experiments suggest that the Kutta condition is still valid for flows when the reduced frequency is low. It is believed that there is a critical number for the reduced frequency, above which the Kutta condition is no longer applicable.

As for the value of the critical number, different experiments conclude differently. Polling & Telionis (1986)'s results showed that when the reduced frequency is higher than 2 and when the amplitude of the gust is not small, the Kutta condition fails, whereas Fleeter (1979) concluded that the zero-loading condition prevailed up to a value of 7 for the reduced frequency on a flat plate but not for a highly cambered blade.

On the other hand, Polling & Telionis (1986)'s measurement with LDV in the near wake downstream of the trailing edge tells us also show that the loading difference can only sustain up to 3% of the chord length, but never more. Since in numerical simulation, a Kutta condition has been widely recognized and should be applied at least for the situation at a low reduced frequency for the angle of attack is not sufficient to cause trailing edge separation, we are encouraged to use the pressure Kutta condition, as given in equation (2.39), for propeller flow problems, including cavitating propellers.

5.7.1 Classical Kutta conditions

Mathematical statements of the Kutta condition for potential based panel method are diverse, but two statements are widely used. One says that the potential jump at the trailing edge should be equal to the dipole strength on the free wake surface, it is known as the *Implicit Kutta Condition* or called Morino's Kutta condition,

$$\varphi_w = \varphi^u - \varphi^l, \tag{5.21}$$

where, superscript u and l denotes upper and lower surface, respectively. The other states that the pressure jump at the trailing edge should be zero. In other words, the loading at the trailing edge should be zero. We call it zero-loading condition. This is known as the *Explicit Kutta Condition* or pressure Kutta condition.

When we apply the Bernoulli equation (2.21) to the trailing edge at both the upper and the lower side and enforce equal pressure, we obtain the following formula to guarantee a zero-loading,

$$\frac{\partial(\varphi^u - \varphi^l)}{\partial t} = \frac{1}{2}(V_r^{u2} - V_r^{l2}). \tag{5.22}$$

This equation is certainly a different condition than the previous Morino one for unsteady flow, because it contains the contribution of the time derivative of the potential and hence can really guarantee the pressure equality. On the other hand, Morino's condition is obviously not valid for unsteady flow.

But in the steady flow case, the pressure Kutta condition can be simplified into the following velocity equality condition,

$$|V_r^u| = |V_r^l|, \tag{5.23}$$

which is eventually nothing more than the Morino's Kutta condition in two dimensions, but still differs for three-dimensional flows. A simple proof is given in the following.

Consider a three-dimensional hydrofoil with a trailing edge which is not perpendicular to the main stream direction, but at an angle of θ, as shown in Figure 5.14. Morino's Kutta condition guarantees that there is no concentrated vortex along the trailing edge in l_2 direction. This means that the velocity components in l_1 direction on both side are equal,

$$(V_r^u)_{l_1} = (V_r^l)_{l_1}. \tag{5.24}$$

The velocity component in l_2 direction can be evaluated in the following way. We choose two points at the trailing edge, marked 1 and 2, which are very close

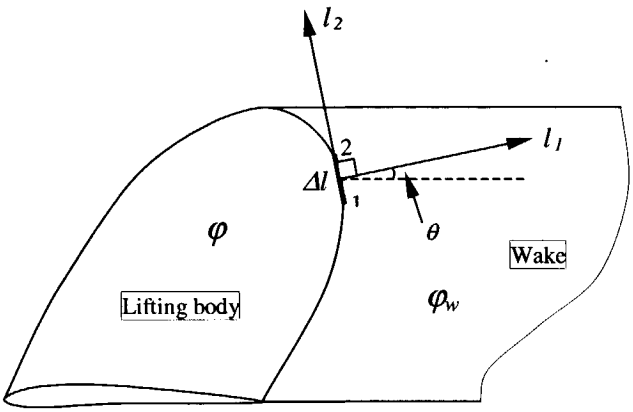

Figure 5.14: Schematics of the Morino's Kutta condition.

to each other. The potentials at these two points are different for the upper surface and the lower surface. We can write the two velocities as,

$$(V_r^u)_{l_2} = \frac{\varphi_2^u - \varphi_1^u}{\Delta l_2}, \quad (V_r^l)_{l_2} = \frac{\varphi_2^l - \varphi_1^l}{\Delta l_2}. \tag{5.25}$$

Upon subtracting them, then,

$$(V_r^u)_{l_2} - (V_r^l)_{l_2} = \frac{\varphi_{w2} - \varphi_{w1}}{\Delta l_2}. \tag{5.26}$$

Because the dipole strength on the wake is equal to the circulation around the section which differs for different span positions, then the right hand side of the above equation is not zero in general. It means that the total velocities on the upper surface and on the lower surface are generally different at the trailing edge. So, the pressure is different too.

Using the pressure Kutta equation (5.22) directly is not easy due to its nonlinearity. Davi *et al.* (1997) suggested an algorithm based on higher-order panel method, but most of the others are using an iterative method (Kerwin *et al.* (1987), Hoshino (1994), Bose (1994), Kinnas & Hsin (1992)). Whatever methods they are using, these methods are all found quite time consuming.

Kinnas & Hsin (1992) state that the circulation around the foil is iterated until the pressure is equal at the trailing edge, but Hoshino (1994) states that the potential jump at the first panel in the wake is iterated, until the jumps are zero. But the essence behind it is the same. That is: iterating the dipole strength at the first panel of the wake (or the whole strength in one strip for steady flow) until the pressures on the upper and lower body surface are equal at the trailing edge.

We denote the pressure difference at the trailing edge as,

$$\Delta p_m = p_m^u - p_m^l, \tag{5.27}$$

where subscript $m = 1, 2, \cdots, M_{TE}$, M_{TE} is the total number of trailing edge panels. Our objective is to make,

$$\Delta p_m = 0 \quad \text{for} \quad m = 1, \cdots, M_{TE}. \tag{5.28}$$

If we can find the derivative matrix (Jacobian) $\mathbf{J}$ which relates the pressure difference with the dipole strength at the first panel in the wake as,

$$\mathbf{J} = \frac{\partial(\Delta p_m)}{\partial(\varphi_w^{TE}{}_m)}, \tag{5.29}$$

then we can use a Newton-Raphson iterative procedure to achieve equal pressure by changing the strength of the first dipole in the wake,

$$\varphi_w^{TE(n+1)} = \varphi_w^{TE(n)} - \mathbf{J}^{-1}\Delta\mathbf{p}^{(n)}, \tag{5.30}$$

where, $\Delta\mathbf{p} = (\Delta p_1, \Delta p_2, \cdots, \Delta p_{M_{TE}})^T$, $\varphi_w^{TE} = (\varphi_w^{TE}{}_1, \varphi_w^{TE}{}_2, \cdots, \varphi_w^{TE}{}_{M_{TE}})^T$, and the superscript n denotes the iteration step.

The Jacobian is simply calculated by given a small perturbation to the initial guess of the dipole strength at the first wake panel as $(1+\epsilon)\varphi_w^{TE}{}_i$. Solving the complete problem again and obtain the pressure difference after this perturbation from the initial value as $\Delta p_j{}^\epsilon$, then the elements in the Jacobian can be evaluated by the following difference scheme,

$$J_{ij} = \frac{\Delta p_j{}^\epsilon - \Delta p_j}{\epsilon\varphi_w^{TE}{}_i}, \tag{5.31}$$

where, $i, j = 1, 2, \cdots, M_{TE}$. It is obvious that M_{TE} times of completely solving the whole problem has to be done before the Jacobian is obtained. This makes the present algorithm very expensive. But fortunately, it is found both in steady and unsteady flow calculations that the Jacobian has not to be re-evaluated in every iteration or time stepping. Once it is formed, it can be used throughout the whole calculation.

But sometimes it happens that the evaluation of the Jacobian fails. This occurs when the dipole strength in the wake is zero or close to zero. An example is the unloaded tip propeller, where the dipole strength in the wake can be very small. An evaluation of the Jacobian based on the perturbation of this small value will not give a correct searching direction for the Newton-Raphson method, which eventually make the iteration divergent. This can easily be

improved by using an absolute value of the perturbation, instead of using the relative ones. Then the Jacobian can be evaluated by,

$$J_{ij} = \frac{\Delta p_j{}^{\epsilon} - \Delta p_j}{\varphi_{pert}}, \tag{5.32}$$

where,

$$\varphi_{pert} = (\max_{i=1,M_{TE}} \varphi_w^{TE}{}_i) \times \epsilon.$$

5.7.2 Discussions

Until now, the mathematical consistency of the present method for the flow at the trailing edge is still not clear. Numerical experiments show that the equal pressure condition and Kelvin's law cannot be satisfied at the same time, even if very dense panel distributions are used at the trailing edge and even if the wake alignment is applied at the same time, so that the numerical model shall converge to its mathematical model. This occurs because the details of the trailing edge flows, which involve strong viscous effects, are not modeled in the potential flow theory.

The method by changing the wake strength to obtain equal pressure, as we discussed in the previous section, is actually one of the simplest models for the trailing edge flow. But using this value as the strength of the shedding vortex (Kinnas & Hsin (1992), Hoshino (1994)) violates the Kelvin's theorem of equation (2.43). This value has no physical meaning and should be seen as some kind of *spurious* dipole, which makes the pressure equal by hiding all the numerical errors coming from:

1. the non-accurate simulation of the wake shape and its position,
2. the non-accurate calculation of the influence coefficients by using lower-order panel geometry and lower-order singularity distribution,
3. all those errors that contribute to the velocity difference in s_1 direction in Figure 5.14,
4. etc ...

So, it has no physical meaning. This can be shown in the following simple analysis for a two-dimensional flow.

Taking a two-dimensional sectional flow as an example (Figure 5.15), we can form a rectangular closed path around the section on which we calculate the circulation $\Gamma(t)$. This path is chosen so that it just passes through the trailing edge on the body surface. According to Kelvin's theorem, after a short time Δt, the closed path moves downstream with the fluid to the new location

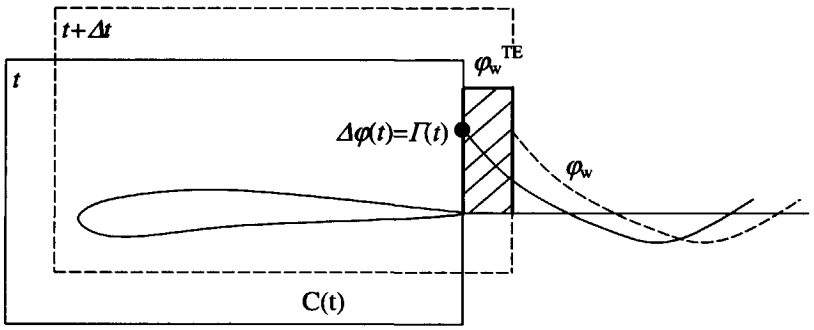

Figure 5.15: Schematic illustration of Kelvin's theorem.

as shown by the dotted path in the figure, but the circulation along the path should keep the same. A spurious dipole of strength φ_w^{TE} (as shown in the shaded area) can be introduced to make the pressure the same at the trailing edge, but it has nothing to do with the shedding of the circulation. Shedding the vortex according to φ_w^{TE} is certainly a mistake. This analysis is also valid for the three-dimensional flows, and also for the steady flows where the dipole strength does not change in the flow direction along the wake.

The drawback of using the first wake dipole as a device to make the pressure the same is that it becomes very non-efficient and even mis-leading for the flows close to the tip of a propeller where the grids are highly distorted. Even for a conventional propeller, if an equal radius grid is used, the panels are skewed so much that l_1 and l_2 become almost parallel with each other, and furthermore parallel to the shedding vortex of the wake. Changing the first dipole strength in the wake equals changing the strength of shedding vortex. The wake vortex has strong influence on the velocity component along l_1 direction but has almost no effect (or very small effect that depends on the angle θ) on the velocity component along l_2 direction (Figure 5.14), which is the key part to make the pressure equal as we have discussed through equation (5.26). When this happens, the solution converges to such a situation that the wake strength φ_w^{TE} becomes very large and the velocity at the trailing edge becomes very large too. Then a low pressure peak at the trailing edge is predicted that is never observed in experiments.

5.7.3 Unsteady Kutta condition

It has been shown by Kinnas & Hsin (1992) that a time-independent Kutta condition needs at least a linear distribution of the singularity in the wake close to the trailing edge. This is investigated and verified in this sub-section,

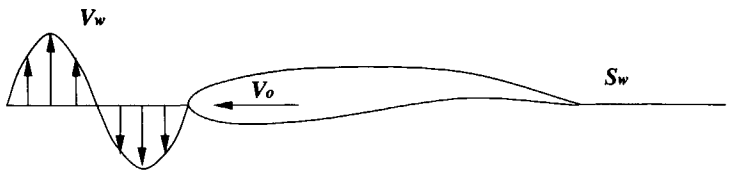

Figure 5.16: A hydrofoil travelling in a sinusoidal vertical gust with a constant speed.

which is essential for our following prediction of the unsteady cavity flow on hydrofoils in a gust.

Numerical tests were carried out for a case where a hydrofoil is traveling into a spatially fixed vertical gust as shown in Figure 5.16. The vertical gust is given as $V_W = \tilde{V} + \Delta V \sin \omega t$, where $\tilde{V}$ is the mean value and ΔV is the amplitude of the gust. The hydrofoil has a rectangular planform so that the panels are non-skewed. The shedding vortices are vertical to the trailing edge so the pressure Kutta iteration can be very efficient. We define a non-dimensional reduced frequency K as,

$$K = \frac{\omega C}{2V_0}, \tag{5.33}$$

where, C is the chord length and V_0 is the forward speed of the foil. In the following calculation, the reduced frequency is chosen to be π, so that the wave length of the gust equals the chord length. When the time step is chosen to be $\Delta(\omega t) = 0.2\pi$, the wake panel size will be 0.1 chord length. The calculated lift variation is shown in Figure 5.17.

A constant singularity distribution on the wake panel is used for the calculation. It is believed that the cross flow is not strong on this rectangular hydrofoil, except for the time derivative of the potential, Morino Kutta condition should be able to given reasonable results. The solid line in this figure is calculated by using Morino's Kutta condition with very short time steps which means very small panels in the wake too. It is found that the result is very close to the result for the pressure Kutta condition (it will be shown in the next section). But when the large time step is used, Morino's Kutta condition fails to control the pressure at the trailing edge and the amplitude of the unsteady lift is reduced to only half of what it should be (as shown by the circles).

The under-estimation of the amplitude cannot be totally corrected even if the pressure Kutta condition is used, where the strength of the shedding vortex is determined by the spurious dipole strength (as shown by the squares in the figure).

This problem can be solved automatically when a higher-order panel method

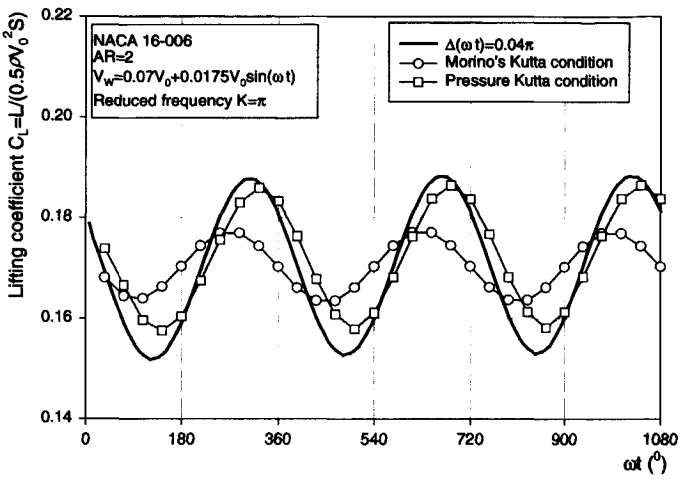

Figure 5.17: Influence of the unsteady wake on the lift force. (rectangular foil with aspect ratio of 2, NACA16-006 section, in sinusoidal gust with reduced frequency $K = \pi$)

is used. For lower-order panel method, a linear or quadratic distribution of the singularity in the first panel of the wake has to be specially implemented. The influence coefficients from this higher-order distribution can be easily calculated by panel subdivision. It does not increase too much computer time but increases the accuracy a lot and makes the calculation independent of the wake paneling. The detailed treatment can be done as shown in Figure 5.18 for a linear or quadratic distribution.

The shedding dipole strength φ_{TE} equals the dipole strength difference at the trailing edge $\varphi^u - \varphi^l$. After a time step Δt, this dipole will travel downstream to the next panel edge, which we denote as φ_{TE+1}. The dipole strength is fitted with a spline to determine its distribution over the first panel. In the subsequent panels, the constant dipole is calculated by the integration of the distributed dipole over the panel as,

$$\varphi_{w1} = \frac{\varphi_{TE} + \varphi_{TE+1}}{2} \tag{5.34}$$

for the linear method, and,

$$\varphi_{w1} = \frac{5}{12}\varphi_{TE} + \frac{8}{12}\varphi_{TE+1} - \frac{1}{12}\varphi_{TE+2} \tag{5.35}$$

for the quadratic method. This method has been found to give a consistent

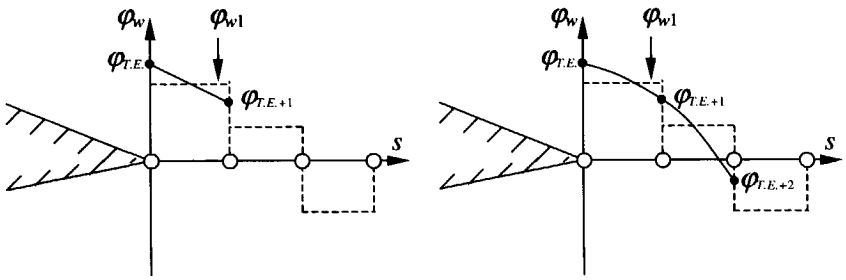

Figure 5.18: Schematics of the wake dipole strength and wake shedding (left: linear; right: quadratic).

and wake independent results. Details of this improvement will be shown in the last section of this chapter.

5.7.4 Effect of Kutta conditions on cavity flows

Kutta conditions can have a big influence on the cavity flows, because different Kutta conditions may result in different loadings, which in turn are directly related to the surface pressure distribution. In case the pressure at the trailing edge is almost equal using Morino Kutta condition, the cavity shape will not change too much when the pressure Kutta condition is enforced. In case the pressure gap at the trailing edge under Morino Kutta condition is not small and the cavity is relatively long, then the predicted cavity shape can be quite different from that predicted using pressure Kutta condition. To show this influence, calculations have been carried out for the S propeller (Kuiper (1981)) at an advance coefficient of $J = 0.4$ and cavitation number of $\sigma_n = 1.7$. The results are shown in Figure 5.19.

For this propeller at this condition, we found that the trailing-edge pressure difference using the Morino Kutta condition is not big for outer radii. But it is quite big for the inner radii. As we expected, the result in Figure 5.19 shows a big difference in the cavity extent for the inner radii.

In general, it can not be stated how much the influence of the Kutta condition can be on the predicted cavity extent and volume. But it will be shown in section 6.4 that the cavity extent predicted using pressure Kutta condition agrees very well with the experiment of open water tests in the Depressurized Towing Tank.

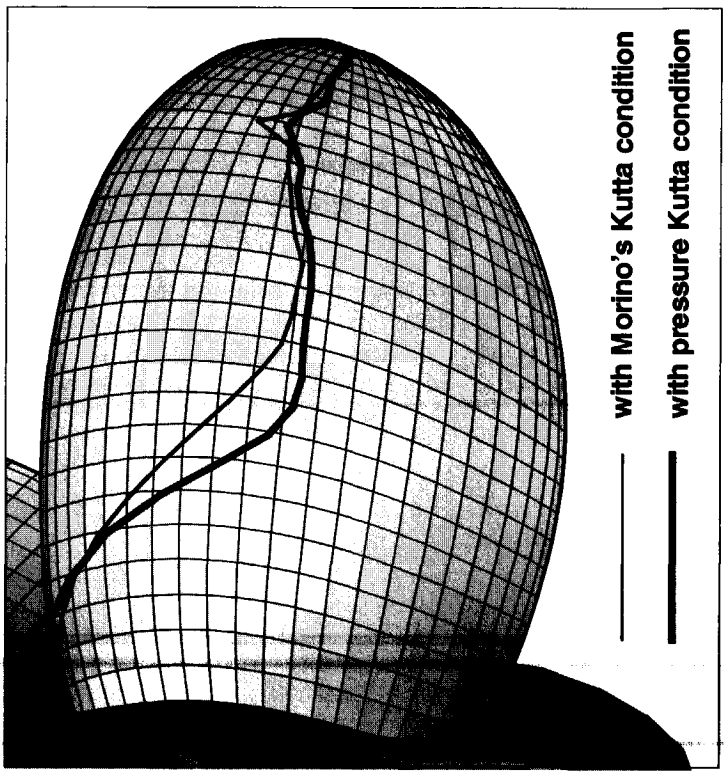

Figure 5.19: Comparison of calculated cavity extent on S-propeller (Kuiper (1981)) using Morino and pressure Kutta conditions. ($J = 0.4$, $\sigma_n = 1.7$)

5.8 Time derivative of potential

In the calculation of the unsteady pressure distribution from the Bernoulli equation (2.14) or (2.21), the partial time derivative of potential $\frac{\partial \varphi}{\partial t}$ plays an important role. For a moving boundary, like the cavity surface, this value is not easily evaluated, it has to be determined iteratively during the solving procedure. This has been discussed in Chapter 4 and we will not repeat it here.

For the solid body surface, when we use body-fixed coordinates, this temporal change of the potential can be evaluated easily by finite-difference scheme that relates the value at the present time with the value at the previous times. But we would like to mention that, generally speaking, the potential itself can be multi-valued without influence on the velocity field. In other words, the

potential at different time steps can include a different constant without influence on the velocity field. To use the above-mentioned finite-difference scheme, at least one point in the flow field must be chosen as which the potential at different time steps fixed.

When a boundary-integral method is used, the unique potential is guaranteed by the Green's function (3.3), which renders the perturbation potential φ zero at infinity for any time level. Kinnas & Hsin (1992) suggested to use a fourth-order backward finite-difference scheme. They concluded that this fourth-order method has been found to produce results that are less sensitive to the number of time steps in one cycle of the unsteady flow than the second-order finite-difference scheme. Hoshino (1994) used third-order scheme for the time derivative term in the pressure Kutta iteration, but a fourth-order central-difference scheme for the evaluation of the pressure on the body surface.

In order to quantitatively evaluate these schemes and their effect on the results, the same test case as we have used in the previous section is used here again. Four different schemes are used — the first-, the second-, the third- and the fourth-order scheme.

The calculated lift coefficients are plotted in Figure 5.20 for the results obtained with Morino's Kutta condition and in Figure 5.21 for the results obtained with the pressure Kutta condition. Solid lines in these figures represent the results obtained by using a very fine grid in the wake. Both figures show that the first-order scheme is not accurate enough and hence should not be used. But the fourth-order scheme does not show to be superior to the second- or third-order scheme as expected. Since the fourth order scheme does not require more computer time, it is used in our present method.

Together with the discussion in the previous section about Kutta condition, we can conclude that Morino's Kutta condition, with a higher-order wake singularity distribution and a higher-order scheme for the time derivative of the potential, can produce the same results as the pressure Kutta condition, at least for a three-dimensional rectangular foil. However Morino's Kutta condition is much cheaper than the pressure Kutta condition. In Chapter 7, where unsteady cavitation flow on a rectangular hydrofoil is calculated, the Morino Kutta condition is used.

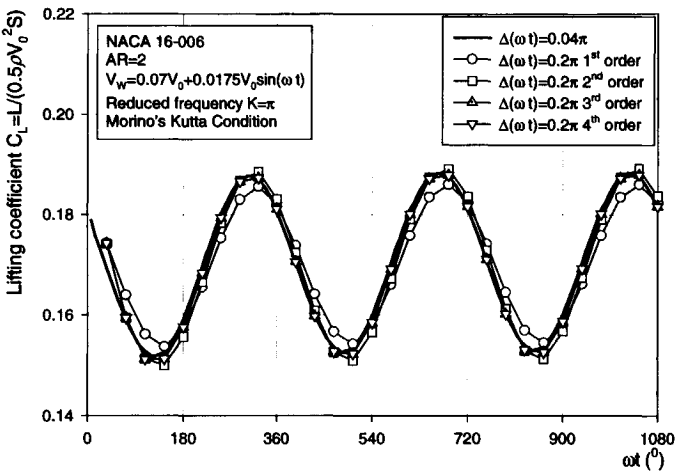

Figure 5.20: Influence of partial time derivative of the potential $\frac{\partial \varphi}{\partial t}$ on the unsteady lift with Morino's Kutta condition. (rectangular foil with aspect ratio of 2, NACA16-006 section, in sinusoidal gust with reduced frequency $K = \pi$)

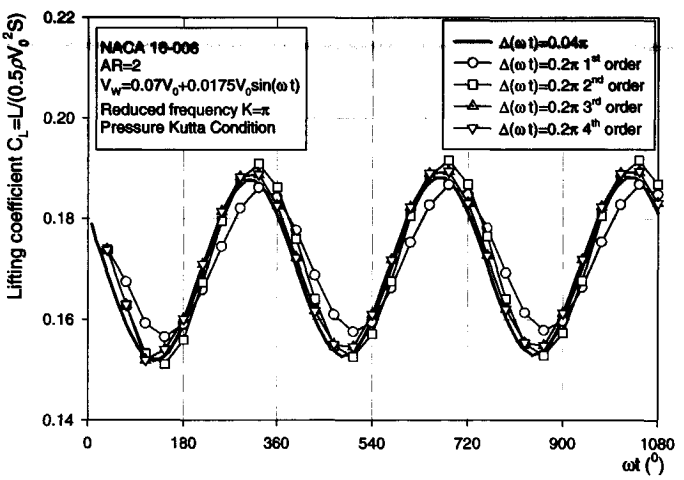

Figure 5.21: Influence of partial time derivative of the potential $\frac{\partial \varphi}{\partial t}$ on the unsteady lift with pressure Kutta condition. (rectangular foil with aspect ratio of 2, NACA16-006 section, in sinusoidal gust with reduced frequency $K = \pi$)

Chapter 6

Steady Cavity Flows

The present nonlinear cavity flow theory is first checked in numerical tests for steady cavity flows. Numerical convergence tests, comparisons with results of other methods, verifications and validations are carried out in this chapter, both for two- and three-dimensional hydrofoil cavitating flows, and for propeller cavitating flows.

6.1 Two-dimensional section flows

Cavitation on a ship propeller is three-dimensional and unsteady. If there is no sharp peak in the wake behind a ship stern, the inflow variations into the propeller have a low frequency, however. Although the blade loading is highly unsteady and has to be calculated as such, it seems acceptable as a first approximation to consider the cavity as quasi-steady. In the years before the 1980's, most attention has been given to two-dimensional cavity flows. Only a few authors have investigated the characteristics of three-dimensional cavity flow at that time (e.g. Leehey (1971)). Some of the three dimensional cavity flow models were based on two-dimensional cavity sectional flows, which matches the inner flow with the outer flow asymptotically. We also start the numerical tests and cavity flow calculations with two-dimensional cavity flows. The results and experience for the two-dimensional cavity flows will be used as guide line for the three-dimensional cavity flow calculations.

Excellent reviews of the research and predicting theories on two-dimensional steady cavity flows have been given by Wu (1972) and Uhlman (1987). The classical linear solution of cavity flow around a hydrofoil by Tulin & Hsu (1980), Wu (1956) and Geurst (1959) has been modified by Kinnas (1991) to predict the leading-edge partial cavity flows. Different from traditional linear meth-

ods, this method predicts the cavity length to decrease with an increase of foil thickness. This is in accordance with experimental observations. A systematic investigation from two-dimensional foils to three-dimensional propeller cavitation has been performed recently at MIT by Kinnas (1992), Kinnas & Fine (1992), Kinnas (1991). A so-called split-panel technique is used to avoid re-paneling of the cavity-foil surface. At the end of the cavity, a simple empirically algebraic expression of the pressure recovery is enforced over a given range of the cavity length in this method. This approach of artificial recovery may influence the final results. Also, the detailed flow structure at the trailing edge of the cavity is ignored and no insight is obtained in its behavior.

In real flow a re-entrant jet will occur, especially in two-dimensional flows. The formation of such a jet determines the shedding of the cloud cavitation and the subsequent generation of noise by the cloud's implosion. And hence the jet influences the volume of the cavity as well. Using the present method, a re-entrant jet model is very easily be implemented for two-dimensional cavity flow since it is easy to define a re-entrant jet cross-section boundary on which the boundary conditions can be applied.

In the following sub-sections, the focus is mainly on the non-linear cavity volume prediction and the re-entrant jet simulation. A separate two-dimensional potential based lower order panel method has been developed. A re-entrant jet cross section is introduced as a boundary of the problem. According to the Bernoulli equation, the original dynamic boundary condition on the jet (2.35) can be simplified into a kinematic boundary condition, which states that the jet velocity should be the same as the free stream velocity on the cavity to keep the same pressure as in the cavity (the vapour presure). So, a normal velocity into the cavity on the jet cross section can be prescribed which equals the free-stream velocity on the cavity surface. Then a Dirichlet dynamic boundary condition can be enforced on the cavity surface, while the Neumann boundary conditions can be enforced both on the jet boundary and on the wetted surface of the foil. Giving an initial shape for the cavity (normally on the body surface), the cavity surface is iterated. The kinematic boundary condition on the cavity surface is satisfied by iterating the cavity length and shape. Upon convergence, both the dynamic and kinematic boundary conditions on the cavity surface are satisfied and a re-entrant jet with a certain thickness evolves automatically.

6.1.1 Formulation of the problem

Taking a cross-section of the hydrofoil of Figure 2.1, we draw a scheme of a sectional flow with a cavity surface in a two-dimensional way as shown in Figure 6.1, which uses the same notation as Figure 2.1 but in more detail. The re-entrant jet in the real flow is generally unsteady, moves upstream and impinges the cavity surface close to the detachment point. But the re-entrant jet can

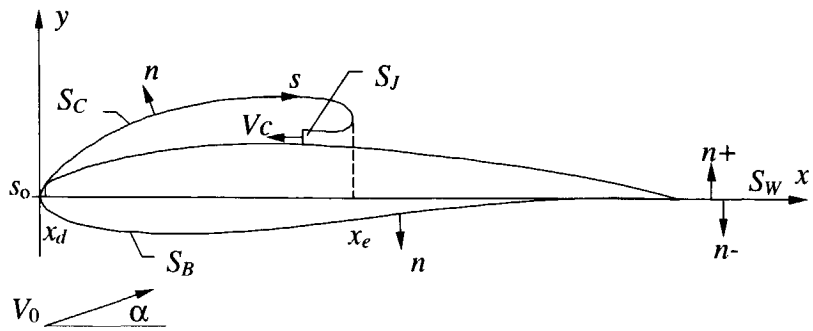

Figure 6.1: Schematics of the cavity-hydrofoil system in two-dimensional flow.

be also steady if there is a velocity component in the third direction along the span. The latter one is the case we are investigating here.

The section is thought to be fixed in space and an inflow V_0 has an angle of incidence α to the nose-tail line of the foil section. A steady partial cavity is formed on the surface of the foil when the ambient pressure is lower than the cavitation inception pressure, which can be taken as the vapor pressure. A re-entrant jet is formed at the end of the cavity and flows inward to the cavity with the same speed as the speed on the cavity surface. The detailed development of the jet in the cavity is not easily simulated. Fortunately this is not important for the steady flow simulation. So we simply cut the re-entrant jet at a certain location. Suppose that the re-entrant jet flows through this cut of the jet (S_J in Figure 6.1) and disappears. Then the flow around the cavity and the foil can be treated as an inviscid fluid flow with a velocity potential function that satisfies Laplace's equation. The solution for the disturbance potential φ can be obtained by Green's identity on this closed boundary. Since the two-dimensional flow field around the foil is not a simple connected zone, a cut (wake surface) has to be introduced to connect the foil trailing edge to the infinity. A boundary condition should also be enforced on this cut.

In two-dimensional problem, a Green's function of equation (3.4) is used and the governing equation can be generally written as,

$$\pi\varphi_p = -\int_S \varphi \left(\frac{\partial}{\partial n} \ln r_{p,q}\right) ds + \int_S \frac{\partial \varphi}{\partial n} (\ln r_{p,q})\, ds \tag{6.1}$$

where, $S = S_B + S_C + S_W + S_J$, p is the collocation point (control point) and both p and q are on the boundary S. The calculation of the influence coefficients is different from the three-dimensional problem as we discussed in Chapter 3.

6.1.2 Boundary conditions

All the boundary conditions we have discussed in Chapter 2 are valid for two-dimensional flows. For the present specific problem, they get the following simple forms.

The kinematic boundary condition on the cavity surface (equation (2.30) and (4.4)) and the kinematic boundary condition on the foil surface (equation (2.25)) become the same. They are combined and simply written as,

$$\frac{\partial \varphi}{\partial n} = \mathbf{V}_0 \cdot \mathbf{n} \qquad \text{on} \quad S_B \quad \text{and} \quad S_C \tag{6.2}$$

where, $\mathbf{n}$ denotes the outward normal unit vector both on the foil surface and on the cavity surface.

In steady two-dimensional cavity flows, the dynamic boundary condition of equation (2.26) is also simplified into a kinematic requirement from equation (2.28), which states that the velocity on the cavity surface should be a constant and,

$$V_C = V_0\sqrt{1+\sigma}, \tag{6.3}$$

where V_C is the freestream velocity on the cavity surface and we choose V_0 as the reference velocity of V_∞.

Taking into account the disturbance velocity $\nabla\varphi$, and defining the same curvilinear coordinates on the cavity surface as in section 3.3.1, so that the detachment point is at $s_1 = 0$, then equation (4.35) is simplified into,

$$\frac{\partial \varphi}{\partial s_1} = -\mathbf{V}_0 \cdot \mathbf{e}_1(s_1) + V_0\sqrt{1+\sigma} \qquad \text{on} \quad S_C. \tag{6.4}$$

Following the same method as the alternative method discussed in section 4.5, the potential on the cavity surface can be prescribed by,

$$\varphi(s_1) = \int_0^{s_1} [V_0\sqrt{1+\sigma} - \mathbf{V}_0 \cdot \mathbf{e}_1(s_1)]ds_1 + \varphi_0 \qquad \text{on} \quad S_C. \tag{6.5}$$

On the jet cross section S_J, the dynamic condition of equation (2.35) can also be simplified into a kinematic requirement,

$$\frac{\partial \varphi}{\partial n} = -V_0\sqrt{1+\sigma} - \mathbf{V}_0 \cdot \mathbf{n} \qquad \text{on} \quad S_J. \tag{6.6}$$

where $\mathbf{n}$ is the normal unit vector on the jet boundary (the cut-off) but pointing into the fluid field.

On the wake surface S_W, the velocity in magnitude is considered to be continuous while the potential has a jump across the wake, but is kept constant along the wake from the trailing edge to infinity. It is expressed in the

perturbation potential as,

$$\frac{\partial \varphi}{\partial n^+} = \frac{\partial \varphi}{\partial n^-} \qquad \text{on} \quad S_W \tag{6.7}$$

$$\Delta\varphi = \varphi_w^+ - \varphi_w^- \qquad \text{on} \quad S_W \tag{6.8}$$

where $\Delta\varphi$ is the potential jump across the wake surface and superscripts + and − denote the variables on the upper and lower surface of the wake, respectively.

Morino's Kutta condition is used in the present investigation since it gives good results in steady two-dimensional flow cases. A pressure Kutta condition is not necessary. The so-called Brillouin-Villat condition can be also enforced at the detachment of the cavity. But at present, the detachment point is treated as an input parameter. The guideline is given in section (5.5).

6.1.3 Iteration scheme for the cavity surface

An estimated cavity length and shape, and a re-entrant jet cross section boundary are first estimated at the beginning of the calculation. The dynamic Dirichlet boundary condition (6.5) is imposed on the cavity surface, and the kinematic Neumann boundary conditions (6.2) and (6.6) are imposed on the wetted part of the foil and on the cross-section surface of the jet. Only the kinematic boundary condition on the cavity surface is not satisfied at this moment. The potential on the wetted part of the foil and on the cross-section of the jet, and the normal derivative of the potential on the cavity surface are calculated by solving equation (6.1). These calculated normal derivatives of the potential on the cavity surface are usually not equal to the value prescribed in equation (6.2). The difference ΔV_n is defined as,

$$\Delta V_n = \frac{\partial \varphi}{\partial n}|_{req.} - \frac{\partial \varphi}{\partial n}|_{cal.} = \mathbf{V}_0 \cdot \mathbf{n} - \frac{\partial \varphi}{\partial n}|_{cal.} \tag{6.9}$$

where the subscripts "req." and "cal." denotes the value prescribed by equation (6.2) and the calculated values respectively.

In two-dimensional flows, the coefficient defined by equation (4.17) is simplified into $A = V_0\sqrt{1+\sigma}$ and equation (4.32) becomes,

$$V_0\sqrt{1+\sigma}\frac{d\eta}{ds_1} = \mathbf{V}_0 \cdot \mathbf{n} - \frac{\partial \varphi}{\partial n}|_{cal.} = \Delta V_n \tag{6.10}$$

and then the cavity thickness η can be determined by the integration,

$$\eta = \int_0^{s_1} \frac{\Delta V_n}{V_0\sqrt{1+\sigma}} ds_1 = \int_0^{s_1} \frac{\Delta V_n}{V_C} ds_1. \tag{6.11}$$

6.1.4 Cavity volume and hydrodynamic forces

The most important parameter of the cavity in the present simulation is its volume. If the cavity thickness is described by $\eta(x)$, then the cavity volume $\overline{V}$ can be obtained by the following integration,

$$\overline{V} = \int_{x_d}^{x_e} \eta(x) dx \tag{6.12}$$

where, x_d denotes the position of the cavity detachment point and x_e denotes the position of the maximum cavity length (see 6.1). The lift L and drag D on the foil section are calculated by integrating the pressure all over the surface as,

$$\begin{aligned} F_x &= -\int p n_y d\ell, \\ F_y &= -\int p n_x d\ell, \end{aligned}$$

and then,

$$\begin{aligned} L &= F_y \cos\alpha - F_x \sin\alpha, \\ D &= F_y \sin\alpha + F_x \cos\alpha. \end{aligned} \tag{6.13}$$

where n_x and n_y are the two components of the outward normal unit vector on the foil surface and $d\ell$ is the line integral element along the surface. The pressure under the cavity, but on the foil surface, is set to p_c in these calculations.

The following non-dimensional parameters are used in the expression of the results in this section.

The pressure coefficient is defined,

$$C_p = \frac{p_0 - p}{\frac{1}{2}\rho {V_0}^2}. \tag{6.14}$$

The lift and drag coefficients are defined as,

$$C_L = \frac{L}{\frac{1}{2}\rho {V_0}^2 C}, \tag{6.15}$$

and,

$$C_D = \frac{D}{\frac{1}{2}\rho {V_0}^2 C}, \tag{6.16}$$

where C is the chord length of the foil.

In the two-dimensional flow case, we also define the following non-dimensional cavity volume coefficient,

$$C_V = \overline{V}/C^2. \tag{6.17}$$

6.1.5 Numerical Implementation

Discrete expression of the problem

The computing time for the two-dimensional flow problem with potential theory is not a key issue nowadays. Instead of using the higher-order panel method, we used the lower-order panel method with constant source and dipole distributions on every panel. When the number of panels is high enough, it should give a result with the same level of accuracy as that of the high-order method and approach the analytic solution.

The details of the discretization of the geometry and the system of equations are not discussed in the following. Only the discretization of equation (6.5) and (6.11) are given.

All of the prescribed dipole strengths on the cavity surface are related to the dipole strength on the panel just ahead of the detachment point of the cavity as described in equation (6.5) by φ_0. Suppose the cavity starts at panel N_d, and ends at panel N_e. For consistency with the panel method, a simple integration of equation (6.5) by mid-point rule is used here,

$$\varphi_i = \sum_{k=N_d}^{i} \left[V_0\sqrt{1+\sigma} - (\mathbf{V}_0 \cdot \mathbf{e}_1)_k\right] \Delta s_k + \varphi_{N_d-1} \qquad i = N_d, \ldots, N_e \tag{6.18}$$

where,

$$\Delta s_k = \frac{1}{2}(l_k + l_{k+1}) \tag{6.19}$$

and l_k is the length of the k^{th} panel and the second term $(\mathbf{V}_0 \cdot \mathbf{e}_1)_k$ in the summation is calculated at the collocation point for panel k.

After solving the system of equations, we obtain the normal derivatives of the potential on the cavity surface. This ΔV_n is evaluated at the collocation point and the cavity thickness is calculated by the same rule as,

$$\eta_i = \sum_{k=N_d}^{i} \frac{(\Delta V_n)_k}{V_C} \Delta s_k \qquad i = N_d, \ldots, N_e. \tag{6.20}$$

At the beginning of each calculation, after the length of the cavity is assumed, a re-entrant jet surface with very small height is firstly taken vertically to the surface at this point and the cavity thickness distribution is assumed to increase from the detachment point to the jet linearly. If the cavity length is under estimated, the cavity will grow very quickly over the jet boundary. If the end of the cavity surface intersects the foil surface, the program simply truncates that part. But if the end of the cavity is above the foil surface, the jet boundary is adjusted to connect this end point vertically to the foil surface. No more restrictions are enforced and the re-entrant jet can evolve automatically, as we have discussed in section 5.4.

Surface paneling

A very fine grid is generally needed to simulate the re-entrant jet at the closure of the cavity where the curvature is very large. At the leading edge and the trailing edge, a fine grid should be also used. It is known that the abrupt change of the panel size for neighboring panels will influence the accuracy of the calculation. A fine grid on the foil surface close to the closure of the cavity is also needed. Our arrangement for the panels is as follows.

On the lower surface of the foil, a cosine distribution of the panel from the leading edge to the trailing edge is used. On the cavity surface, two sets of panels are used. Half of the panels on the cavity surface are used for the last 5% of the arc length on the cavity surface.

$$\tilde{s}_i = 0.95\left(0.5 - 0.5\cos\frac{i-1}{N_{cav}/2}\pi\right) \quad i = 1, 2, \ldots, N_{cav}/2, \tag{6.21}$$

and,

$$\tilde{s}_i = 0.95 + 0.05\frac{i - N_{cav}}{N_{cav}/2}\pi \quad i = N_{cav}/2, \ldots, N_{cav} + 1, \tag{6.22}$$

where, N_{cav} is the total number of panels on the cavity surface and $\tilde{s}$ is the normalized arc length.

For the paneling on the foil surface downstream of the cavity end, a similar distribution is used with fine paneling close to the re-entrant jet.

$$\tilde{s}_i = 0.1\frac{i-1}{N_{down}/2} \quad i = 1, 2, \ldots, N_{down}/2 \tag{6.23}$$

and,

$$\tilde{s}_i = 0.1 + 0.9\left(0.5 - 0.5\cos\frac{i - N_{down}/2}{N_{down}/2}\right) \quad i = N_{down}/2, \ldots, N_{down} + 1, \tag{6.24}$$

where N_{down} is the total number of panels on the back of the foil downstream of the cavity.

Figure 6.2 shows an example of the panel arrangement around the re-entrant jet for this scheme of paneling.

6.1.6 Results and Discussion

Convergence test

At first, we carried out a convergence test for the present method to check the number of panels we need to obtain a convergent result. We took a NACA16-006 section at an angle of attack 4° and a cavitation number of 0.87513 as

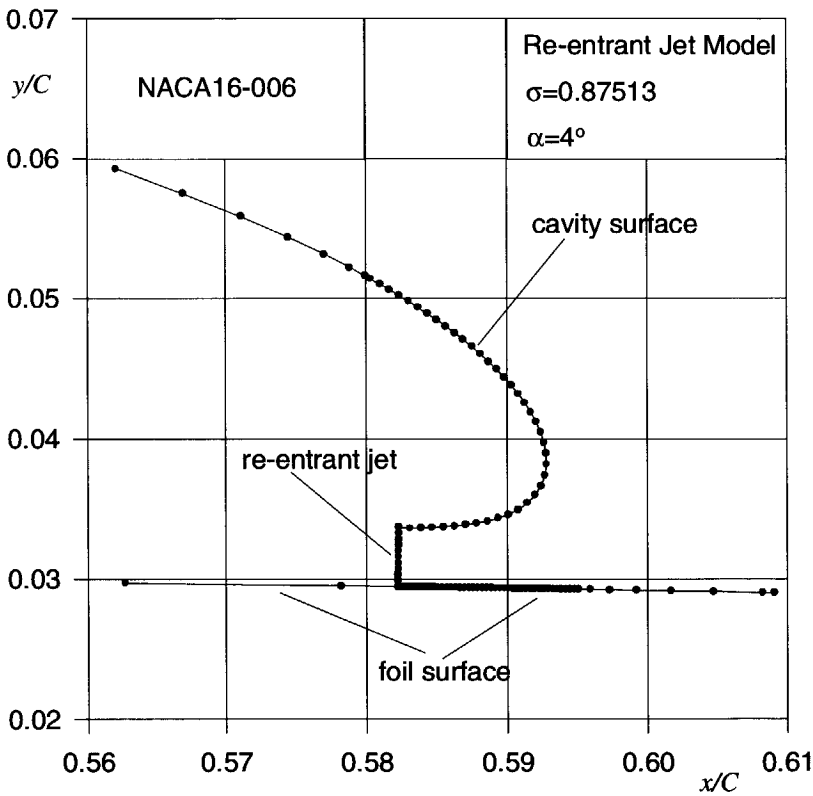

Figure 6.2: Surface paneling around the re-entrant jet surface and the cavity end. (NACA16-006 section at an angle of attack 4°, and cavitation number 0.87513)

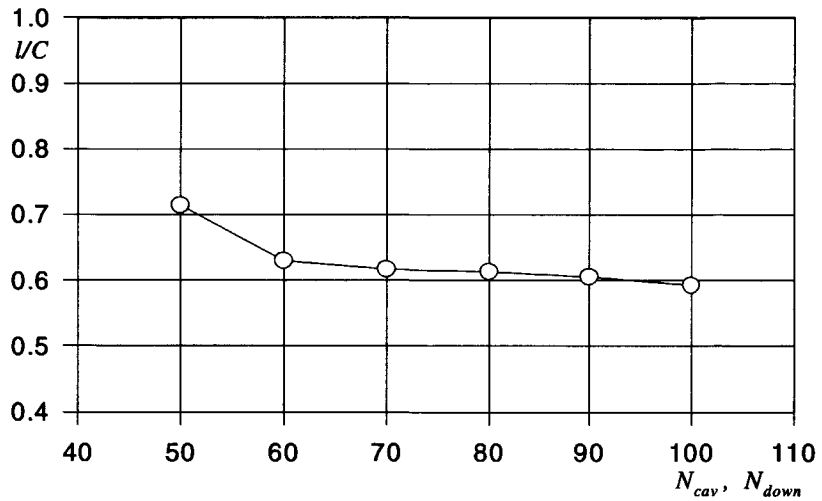

Figure 6.3: Variation of the cavity length with number of panels. (NACA16-006 section at an angle of attack 4°, and cavitation number 0.87513)

a test case. Figure 6.3 shows the change of the calculated cavity length and Figure 6.4 shows the change of the re-entrant jet thickness, with increasing the number of panels.

It is obvious that the solution quickly approaches an asymptotic value with increasing number of panels. When both of the number of panels on the cavity surface and on the foil surface downstream of the cavity is increased to 80, the changes of the cavity length and the re-entrant jet thickness become small. So, 80 panels on the cavity surface and 80 panels on the foil surface downstream of the cavity is sufficient. In the following calculations, we take 100 panels for both surfaces. That means a total of 260 panels (with 50 on the pressure side of the foil and 10 on the jet cross section).

Figure 6.5 and Figure 6.6 show the cavity convergence on the NACA16-006 section at an angle of attack of 4° for two different cavitation numbers, respectively. It is found that the convergence is slow toward the final result. From our experience, although the steps needed for the iteration depend on the initial assumption of the cavity, 100 steps are always needed to achieve a result with a maximum error between the calculated velocity on the cavity surface and the prescribed freestream cavity velocity of less than 1%. The maximum error always occurs at the intersection of the cavity and the re-entrant jet. But on most part of the cavity surface, the tangential velocity converges much faster and the errors are much smaller.

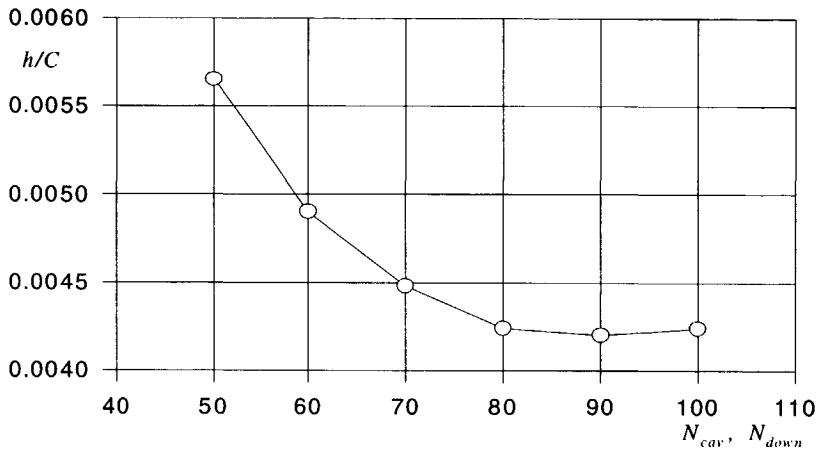

Figure 6.4: Variation of the jet thickness with number of panels. (NACA16-006 section at an angle of attack 4°, and cavitation number 0.87513)

Figure 6.5: Changes of the cavity shape with iteration steps. (NACA 16-006 $\alpha = 4°$, $\sigma = 0.87513$, $l_{initial}/C = 0.37550$, converged $l/C = 0.59279$).

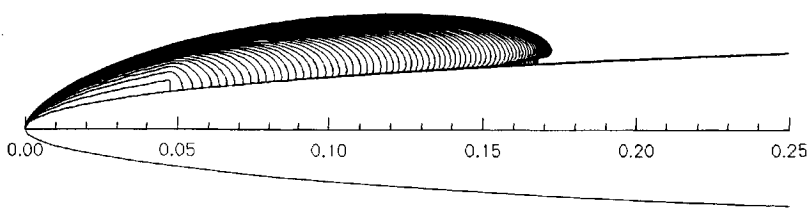

Figure 6.6: Changes of the cavity shape with iteration steps. (NACA 16-006, $\alpha = 4°$, $\sigma = 1.4$).

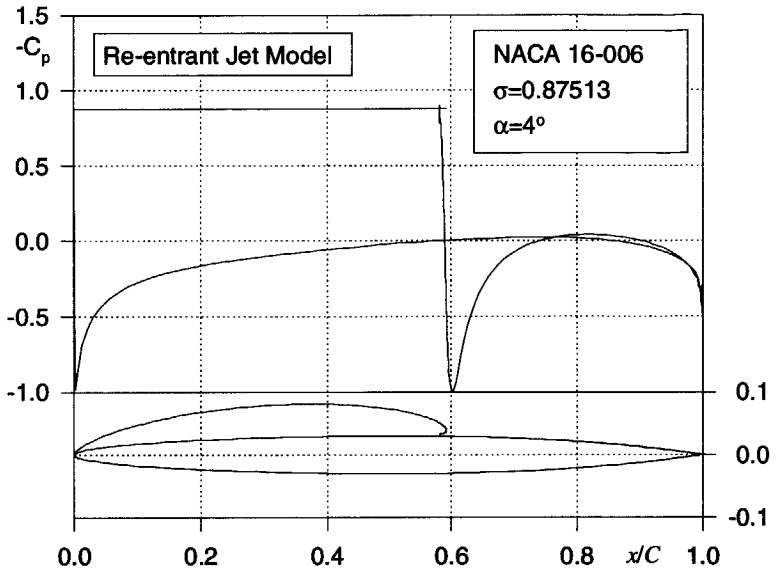

Figure 6.7: Pressure distribution on the cavity and foil surface. (NACA 16-006, $\alpha = 4°$, $\sigma = 0.87513$, re-entrant jet cavity model)

As we have discussed in Section 5.3, the longitudinal growth of the cavity in the iteration is very slow when a short initial guess is used. For three-dimensional cavity flow calculations, this is prohibitive.

The influence of the detachment point on the final cavity volume and cavity length has been investigated in Section 5.5. Since we have not found a good way to calculate the position of the detachment point, detachment is always set at the leading edge for all the calculations in the following paragraphs.

Predictions for NACA16 series

A calculation for the cavity flow with a re-entrant jet on the NACA 16-006 section at an angle of attack of 4° is carried out at a cavitation number of 0.87513. This cavitation number is chosen because the author wanted to make a comparison with the result of Uhlman (1987) cavity termination wall model. The converged shape of the cavity and its re-entrant jet and the final pressure distribution on the cavity and on the wetted part of the foil are presented in Figure 6.7. Details on the re-entrant jet are shown in Figure 6.2 with the panel arrangement.

Figure 6.7 shows that the velocity on the cavity surface equals to the pre-

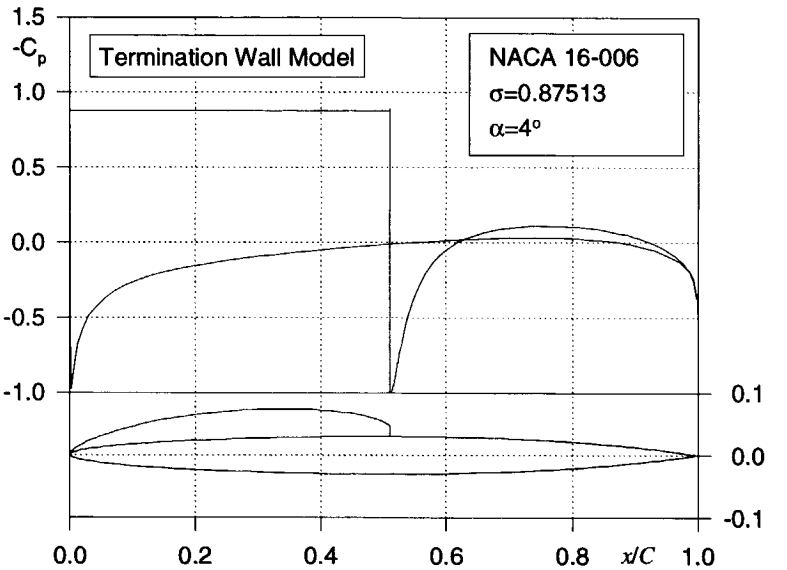

Figure 6.8: Pressure distribution on the cavity and foil surface. (NACA 16-006, $\alpha = 4°$, $\sigma = 0.87513$, termination wall cavity model)

scribed freestream velocity since the pressure equals to the prescibed pressure. It means that both the dynamic boundary condition and the kinematic boundary condition on the cavity surface are very well satisfied. Only at the control point of the last panel on the cavity, the velocity is slightly higher than the freestream velocity, but the relative error is still less than 1%. A stagnation point $C_p = 1$ is clearly visible downstream of the end of the cavity.

The flexibility of the present program makes it very easy to change the kinematic boundary condition on the jet section from equation (6.6) to a non-penetration condition similar to equation (6.2) and find the solution with a cavity termination-wall model. The result is shown in Figures 6.8. A stagnation point is also shown at the corner of the wall. The difference of the predicted cavity shapes by these two cavity models can be clearly seen in Figure 6.9 and Figure 6.10 for two different cavitation numbers. The predicted cavity lengths and volume are about 10% larger than those of the termination-wall model. But for a thicker section (NACA 16-012) however, the predicted cavity length and volume of the re-entrant jet model are smaller than those in the results of the termination-wall model. This will be shown later.

A parametric analysis has been performed for the NACA 16 series with different thickness to chord ratios, to study the relations between the cavity

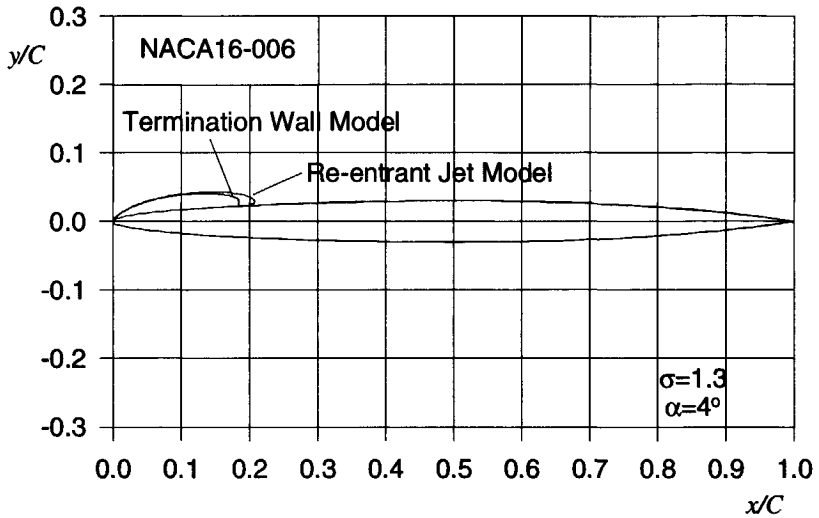

Figure 6.9: Comparison of the cavity shapes for these two different cavity models. (NACA 16-006, $\alpha = 4°$, cavitation number $\sigma = 1.3$).

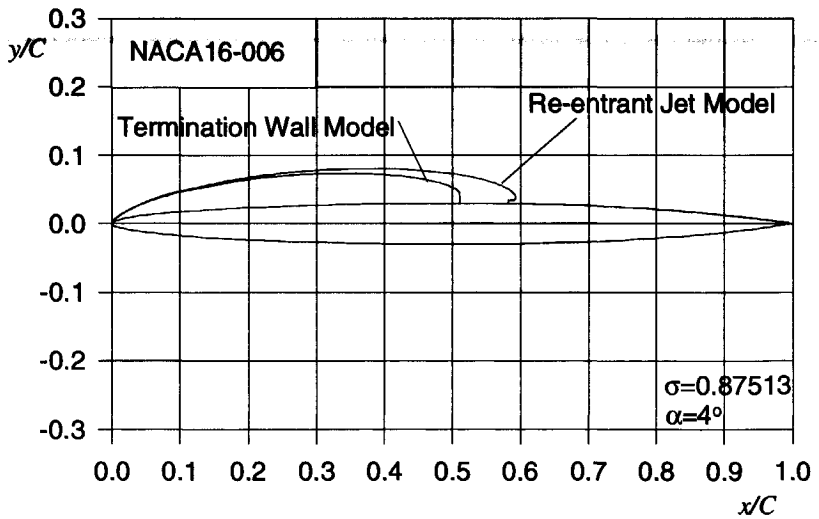

Figure 6.10: Comparison of the cavity shapes for these two different cavity models. (NACA 16-006, $\alpha = 4°$, cavitation number $\sigma = 0.87513$).

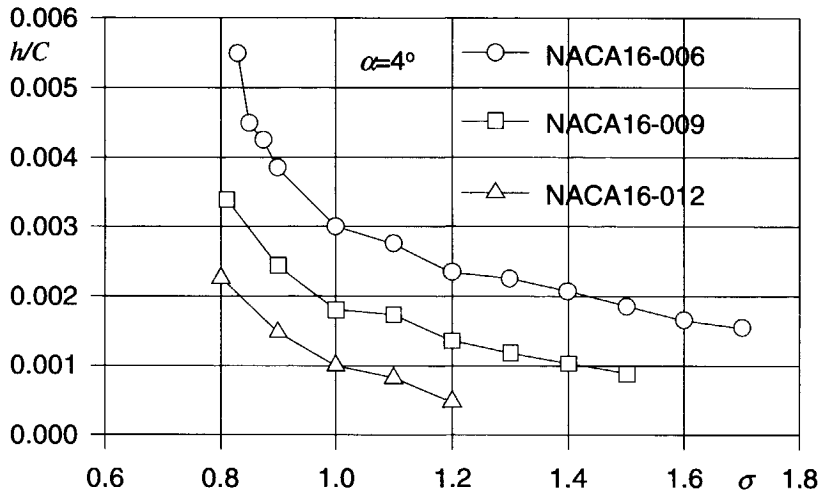

Figure 6.11: Cavity re-entrant jet thickness h/C versus cavitation number σ. (the angle of attack α is 4°)

volume, the cavity length, the cavitation number and the re-entrant jet thickness. All results are listed in Table B.1, Table B.2 and Table B.3 in Appendix B.

The special feature of the present method is the re-entrant jet calculation. Figure 6.11 shows the re-entrant jet thickness versus the cavitation number for three sections. It follows from this figure that the re-entrant jet thickness decreases with increasing cavitation number. Also found is that the re-entrant jet is thicker on a thinner profile.

When we plot the ratio of the re-entrant jet thickness and the maximum cavity thickness against the cavity length, we obtain Figure 6.12. It shows that the re-entrant jet thickness is always a certain fraction of the maximum cavity thickness t_{max}, irrespective of the cavitation number and the profile thickness. This percentage is around 8% to 10%. It is also found that the maximum cavity thickness is also always located at 60% of the total cavity length (Figure 6.13), irrespective of the cavitation number and the profile thickness as well. These characteristics of the re-entrant jet can also be found in Gilbarg & Rock (1946) for the re-entrant jet behind an obstacle.

Comparison with other linear and nonlinear results

In order to assess the difference in the prediction results of the present method and those of other linear methods with thickness correction and nonlinear meth-

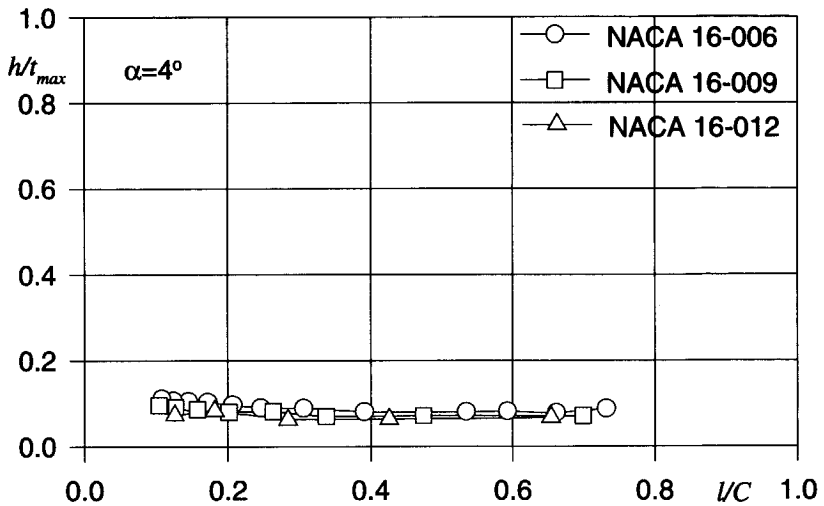

Figure 6.12: The re-entrant jet thickness as fraction of the cavity maximum thickness versus the cavity length. (NACA 16 series, angle of attack $\alpha = 4°$)

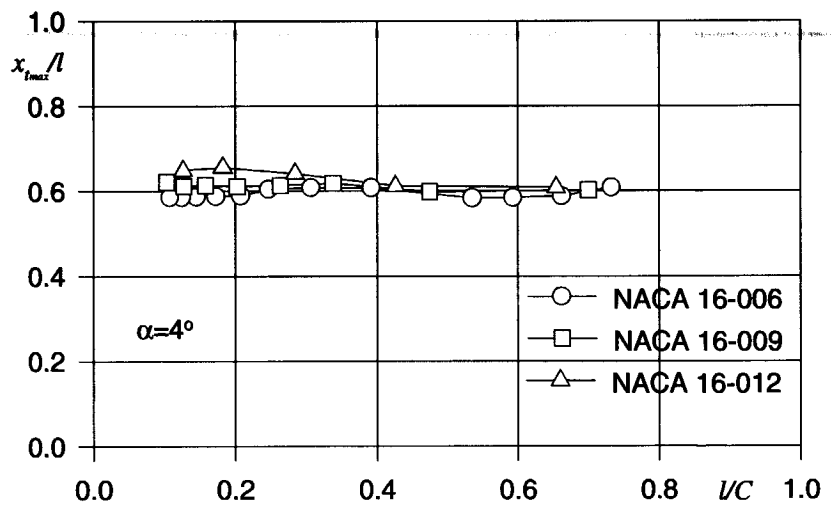

Figure 6.13: The maximum cavity thickness position as fraction of the cavity length. (NACA 16 series, angle of attack $\alpha = 4°$)

Table 6.1: Comparison of different approaches for the same cavity termination wall model.

	Uhlman's Results	Present Results	Relative Differences
Cav. Number σ	0.87513	0.87513	0.00%
Cavity Length l/C	0.5000	0.5100	+2.00%
Cavity Volume C_v	0.01670	0.01794	+7.4%
Lift Coeff. C_L	0.53562	0.51705	-3.5%

ods with termination-wall model, comparisons have been made for NACA 16 series sections at an angle of attack 4° for different cavitation numbers.

Uhlman (1987)'s method is based on velocity. A cavity termination-wall model is employed in his method. The cavity length is prescribed, while a cavitation number is calculated. When the shape of the cavity has converged, the cavitation number was obtained. By assuming the velocity on the jet boundary to be zero in the present method, we can also obtain the solution with a termination wall model. A comparison is shown in Table 6.1. It can be concluded that the results are very close to each other. The cavity length predicted by the present method is 2% longer than the length predicted by Uhlman.

The calculated cavity lengths have also been compared with the results of Uhlman (1987)'s nonlinear method, as shown in Figure 6.14. It is found that the results for NACA16-009 are very close to each other. The cavity predicted by present method is longer for NACA16-006 section but shorter for NACA16-012 section compared to the nonlinear method results by Uhlman (1987). Another comparison has been made of the present results and the linear method results with thickness correction provided also by Uhlman (1987) for his comparison. This is shown in Figure 6.15. The linear method with thickness correction gives very good results compared to the present nonlinear method for NACA16-006 but over-predicts the cavity length for NACA16-012. The present method predicts a decrease of the cavity length with increasing thickness while the linear method predicts an increase. Since the tendency is different, we can say the linear method is not accurate enough even for a cavity flow on a very thin section, especially when the cavity is long.

As for the cavity volume, a comparison is shown in Figure 6.16 between results of the present method and results of the linear method. The tendency that the cavity volume decreases with increasing foil thickness is the same but the results are very different. The linear method seems to over-predict the cavity volume. For NACA16-012 section, the volume predicted by the linear method is twice as large as that predicted by the present method. This

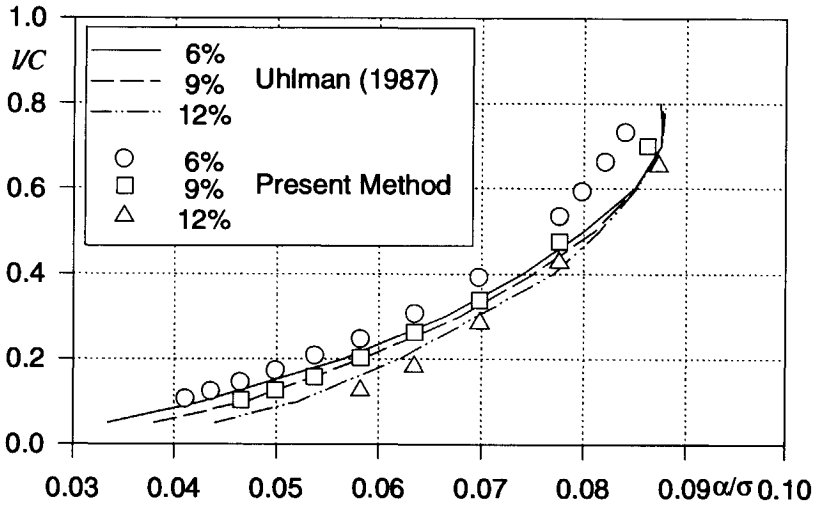

Figure 6.14: Comparison of results of the present method and those of the non-linear method of Uhlman (1987) for NACA 16 series.

emphasizes that for the calculation of pressure fluctuation the linear method is not accurate enough.

Comparison with experimental measurements

In order to validate the present method, the present results are compared with measured results of Shen & Peterson (1978) and Shen & Dimotakis (1989*a*) both for a modified Joukowsky profile and for a NACA 66 (MOD) a=0.8 section. Since the leading edge sheet cavity is very sensitive to the pressure distribution at the suction side of the profile, a careful investigation of the influence of viscosity, boundary-layer separation and wall effects in the experiment should be done before the comparison can be made.

The viscosity has strong effects not only on the cavity flow, but also on the wetted flow (Shen & Dimotakis (1989*b*)). The experimental results show that the lift coefficient of the NACA 66(MOD) a=0.8 section obtained in the experiment is 0.531 at an angle of attack of 3° when the Reynolds number is 3×10^6, while the potential theory predicts 0.626, which is 15% larger than the experiment. Correspondingly, the calculated pressure at the suction side is also lower than the measured one. For the cavity flow, Avellan *et al.* (1989)'s experiment shows that the leading edge cavity on a NACA 0009 symmetric profile at 2.5° incidence is 30% chord length when the water speed is 20 m/s, but 45% chord length when the water speed is 35 m/s.

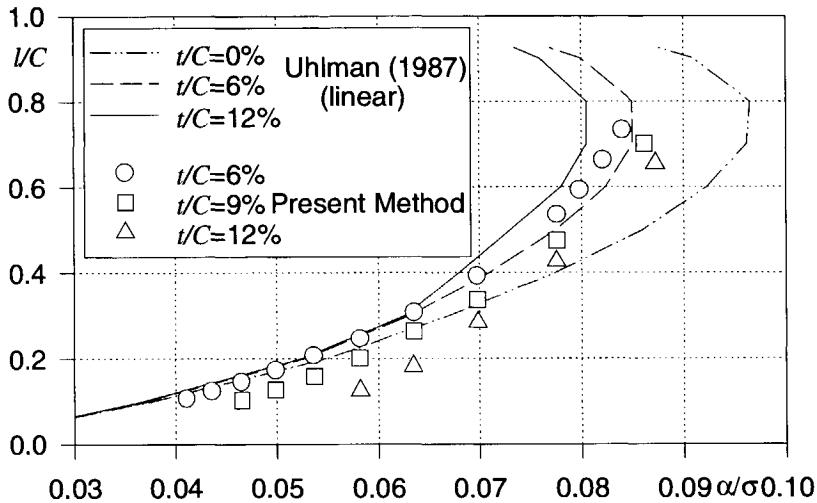

Figure 6.15: Comparison of results of the present method and the results from the linear method provided by Uhlman (1987). (NACA 16 series)

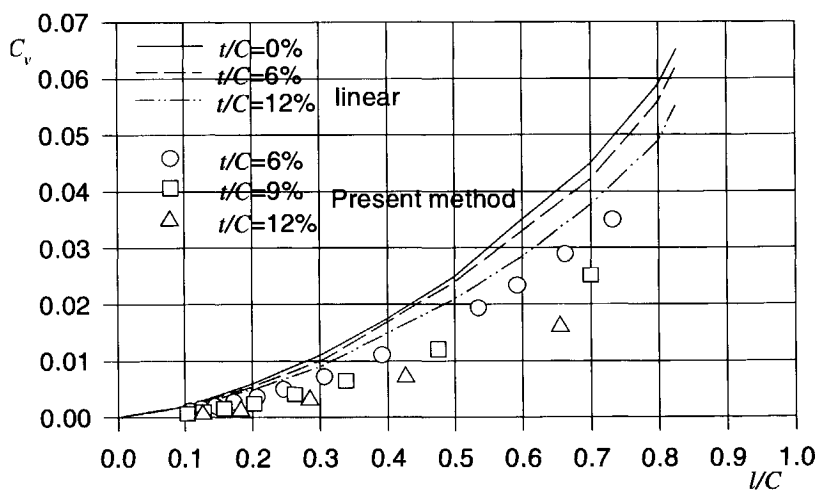

Figure 6.16: Comparison of cavity volume obtained from different methods. ($C_v = volume/C^2$, NACA 16 series).

This may be caused by the differences of the boundary-layer development at the suction side and at the pressure side at different Reynolds numbers. For the NACA 66 (MOD) a=0.8 section, the transition location of the boundary layer is reported to be at 13% of the chord length on the suction side and at 89% of the chord length on the pressure side. At a Reynolds number of 5×10^5, the flow is almost laminar all over the section surface. The section is actually de-cambered and also the effective angle of attack is reduced by the boundary-layer. This de-cambering could be treated accurately by a careful calculation of the boundary-layer development on the section surface. A viscous/inviscid interaction calculation (Kinnas *et al.* (1994)) for a 2-D section has shown this strong effect already. Any comparison based on equal angle of attack or equal lift coefficient does not work. In the equal angle of attack comparison, the potential flow method always over-estimates the cavity length and volume because the negative pressure on the suction side is always over-predicted. But in the equal lifting coefficient comparison by changing the angle of attack only, the potential theory always under-predicts the negative pressure peak at the leading edge.

In the present method a boundary-layer calculation has not been carried out for this comparison because the difference in the pressure distribution may result not only from the boundary-layer flow but also from the blockage of the test section (Deshpande *et al.* (1994)). We think that if the cavity is small, the boundary layer at the suction side of the section is not influenced too much by the cavity, and a comparison could be made on an equivalent section that has the same pressure distribution as measured in the wetted condition.

A simple empirical method like Pinkerton (1936)'s is used. An arbitrary function is used to de-camber the section,

$$\Delta(f/C) = (f/C)_{T.E.} \cdot (1 - (x/C)^2)$$

where $(f/C)_{T.E.}$ is the total de-camber amount at the trailing edge. For this NACA 66(MOD) a=0.8 section, $(f/C)_{T.E.} = -0.009$ gives a good correlation between the experiments and the calculations for pressure distribution, as shown in Figure 6.17.

Based on this de-cambered profile, the calculations are done for three cavitation numbers (0.84, 0.91, and 1.00) at an angle of attack of 4°. The agreement is quite good, as shown in Table 6.2.

In order to estimate, as a first estimate, how strong the viscous effect is, the same section in a condition of $\alpha = 4°$ and $\sigma = 1.0$ is calculated both for the original geometry and for the de-cambered geometry. The results are plotted in Figure 6.18. As expected, the predicted cavity length on the original geometry is 2.5 times as long as that predicted for the de-cambered section.

But this result can not be generalized because it strongly depends on the pressure distribution on the section surface. For a NACA 66 section, which has

Table 6.2: Comparison of the cavity length and the lift coefficient. (NACA 66(MOD) thickness + NACA a=0.8 camber, angle of attack $\alpha = 4°$)

Cavitation Number	Experiment		Calculation	
σ	l/C	C_L	l/C	C_L
1.00	0.20	0.645	0.223	0.619
0.91	0.36	0.670	0.363	0.652
0.84	0.60	0.699	0.610	0.678

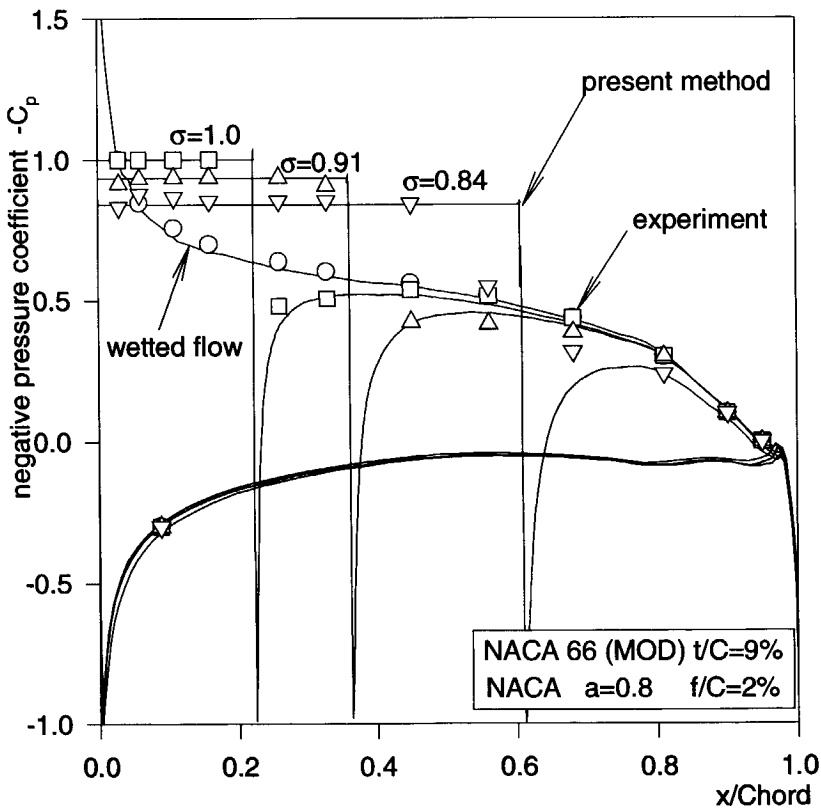

Figure 6.17: Comparison of the pressure distribution for an angle of attack of 4°. (NACA 66(MOD) thickness + NACA a=0.8 camber, the experimental data are from Shen & Dimotakis (1989*a*))

Table 6.3: Comparison of cavity length calculations with experiments. (Modified Joukowsky foil, Shen & Peterson (1978))

α	Experiments	Calculations
3.8°	0.25	0.249
4.3°	0.39	0.395

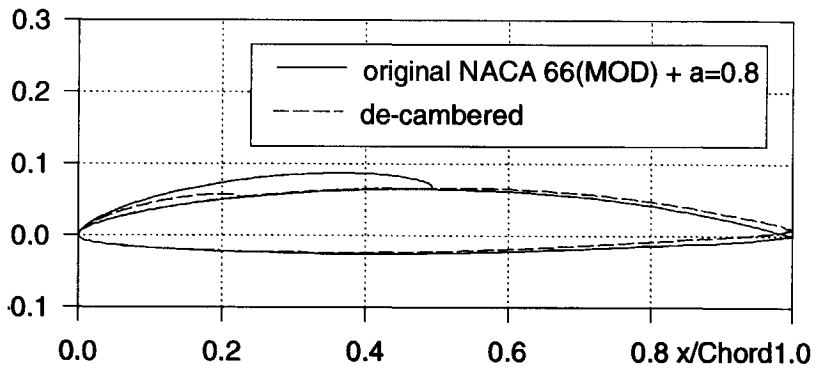

Figure 6.18: Comparison of the cavity shape for the de-cambered and the original section. (NACA 66(MOD) thickness + NACA a=0.8 camber, angle of attack $\alpha = 4°$)

a relative flat pressure distribution (Figure 6.17) over a large part of the suction surface in wetted-flow condition, the cavity length and volume are very sensitive to the pressure. On the other hand, for a section like the modified Joukowsky section (Shen & Peterson (1978)), a de-cambering seems not necessary because the pressure distribution is not so flat on the suction side.

Figure 6.19 shows the pressure distribution calculated by the present potential flow theory and the measured data (Shen & Peterson (1978)) for the modified Joukowsky profile. Since the agreement is quite good and the pressure distribution is not very flat on the suction side of the section, a comparison can be made without viscous correction. The calculated cavity lengths for two different angle of attacks are listed in Table 6.3. The agreement is very satisfactory.

Since no good experimental results are available for the cavity volume, comparison can not be made at present.

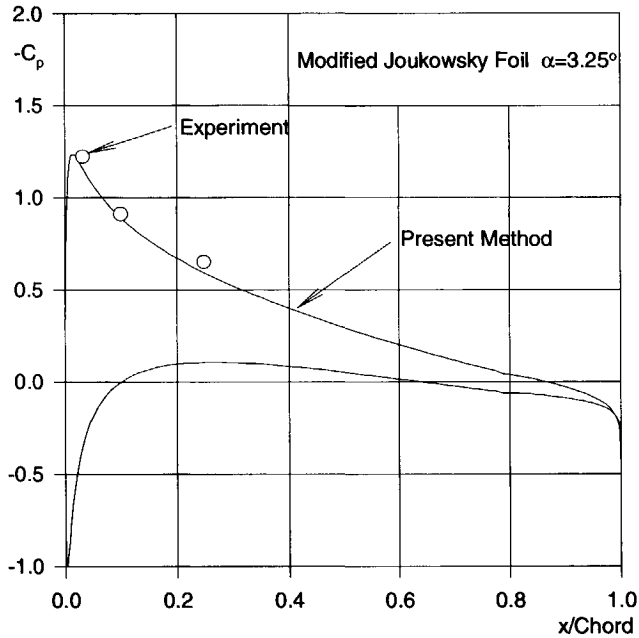

Figure 6.19: Comparison of pressure distribution on the modified Joukowsky profile. (angle of attack $\alpha = 3.25°$, experimental data are from Shen & Peterson (1978))

6.1.7 Summary

The results obtained using a cavity termination wall model in the present method shows a good agreement with results of Uhlman's non-linear termination-wall model. Calculations for NACA 16 series sections with three different thicknesses to chord ratio (6%, 9% and 12%) have been performed. The present results show, like other non-linear methods, that the cavity length decreases with increasing foil thickness.

We have found that the re-entrant jet thickness is always a certain percentage of the cavity maximum thickness, irrespective of the cavitation number, the cavity length and the foil thickness. The location of the maximum cavity thickness for different conditions is also fixed at 60% of the cavity length from the detachment point. This may be of importance for the shedding of the cavity by the re-entrant jet.

The present method is validated by comparing results with experimental data. The comparisons were made by de-cambering the original NACA section

into a modified section in order to take the displacement of the boundary layer on the section surface into account. Three cases (σ=1.00, 0.91, 0.84) have been investigated for this de-cambered section and a good correlation has been found.

In summary, the re-entrant jet modeling with the potential flow theory for two-dimensional cavity flows is a quite stable and convergent method. If the viscous effect could be included in the method, it could provide a rather precise prediction. A benchmark test of the cavity volume for the steady flow condition should be carried out to verify the present theory. A further extension of the method to three-dimensional predictions and unsteady cavity flow around hydrofoils and propeller blades appears feasible.

6.2 Three-dimensional hydrofoil flows

It is important to control the dynamic behavior of cavitation on a propeller blade in order to reduce cavitation induced ship vibrations. As has been shown in previous research (De Lange (1996)), the re-entrant jet at the end of the sheet cavity plays an important role in the instability of the cavity and the formation of cloud cavitation. The surface of a sheet cavity is initially smooth, transparent and stable. In many situations, the sheet cavity surface will distort and break partially into small bubbles at the end of the cavity (20th ITTC Report, 1993). When the angle of attack is increased, a strong re-entrant jet forms at the end of the cavity. When the re-entrant jet touches the cavity surface, the cavity will break up and part of the cavity will be shed and form cloud cavitation in the wake.

A re-entrant jet is always needed to close a 2-dimensional cavity. A steady 3-dimensional cavity flow, however, can have a smooth closure over much of its extent, even when a re-entrant jet is formed. Many observations, both at model and full scale, show that a sheet cavity can be very stable if the re-entrant jet is able to find a good exit (Kuiper (1994)). A typical exit for highly skewed propeller blades is in the cavitating tip vortex. This makes the sheet cavity on the propeller blades quite stable.

Most of the prediction methods for 3-D cavity flow are aiming at the influence of cavitation on the hydrodynamic forces. Only a few methods tried to predict the cavity volume accurately in recent years. At first, methods were developed only for high-aspect-ratio hydrofoils (Leehey (1971) , Furuya (1975), Uhlman (1978)and Van Houten (1983)) by matching the asymptotic expansion of the inner and outer solutions. After having published their 1971 paper, Jiang & Leehey (1977) accomplished a complete 3-D calculation. Because of the difficulty to determine the cavity planform, a closure condition for each individual spanwise strip was used. Recently, nonlinear methods have been developed for arbitrary hydrofoils. Pellone & Rowe (1981) calculated the su-

percavitating flow on a 3-D flow hydrofoil with free surface by a velocity-based panel method. Peallat & Pellone (1996) developed a nonlinear method for the prediction of the partial cavity flow. Systematic research on partial cavity flow using potential-based panel methods for 3-D hydrofoils and propeller blades has been performed at MIT in the last ten years (Kinnas & Fine (1992), Kinnas & Fine (1993), Fine & Kinnas (1993)). A so-called split-panel technique is used to avoid re-paneling of the cavity-foil surface and a fast convergence is achieved in their method.

In order to predict accurately the cavity volume and to analyze the possible influence of the jet on the stability of the cavity, a re-entrant jet model at the cavity end is needed. Calculations of the re-entrant jet formation at the end of a 2-D cavity were first carried out by Furness & Hutton (1975) and recently by De Lange (1996) for arbitrary hydrofoil sections. But 3-D simulations of the re-entrant jet have not been found in the literature. Encouraged by the successful simulation of the re-entrant jet in the 2-D cavity flow, the present method has been extended to the steady 3-D partial cavity flow on arbitrary hydrofoils.

6.2.1 Formulation and discretization

We consider a simple case (see Figure 2.1), where only a three-dimensional hydrofoil is in the flow and fixed in the space, as shown in Figure 6.20. The incoming flow is along the chord direction with an angle of attack α with respect to the hydrofoil. We consider the situation that the cavity starts from the leading edge and a re-entrant jet is formed at the end of the cavity. As we have discussed in Section 5.4, a cut-off of the re-entrant jet is not easy for the three-dimensional case and not really necessary. So, we will let the re-entrant jet develop by itself. The detail of the jet is not our interest. When the cavity surface has converged, the calculation is terminated.

Even if for the purely three-dimensional steady flow, the dynamic boundary condition on the cavity surface can be simplified from equation (2.28) into a kinematic requirement that the velocity on the cavity surface should be a constant and,

$$V_C = V_0\sqrt{1+\sigma}. \tag{6.25}$$

The difference of this equation from equation (6.3) is that this velocity contains components in three directions, including the span direction.

In the present case, equation (4.36) becomes,

$$\varphi = \varphi_0 + \int_0^{s_1} (\sqrt{(1+\sigma)V_0^2 - (\mathbf{V}_0 \cdot \tau_2 + u_2)^2} - \mathbf{V}_0 \cdot \mathbf{e}_1) ds_1 \tag{6.26}$$

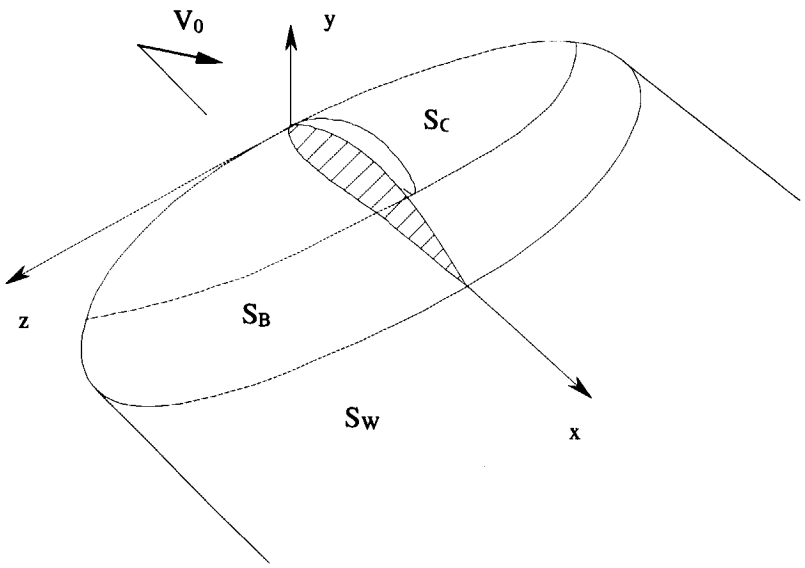

Figure 6.20: Schematics of the 3-D cavity flow of a hydrofoil in uniform oncoming flow.

where the $\left(\mathbf{V}_0 \cdot \mathbf{n} - \dfrac{\partial \varphi}{\partial n}\right)$ term is omitted since it will valish when the calculation is converged.

By using a similar discretization as we used for the two-dimensional flow calculations, the potential on the cavity surface can be determined by the following equation,

$$\varphi_i^n = \sum_{k=1}^{i} (\sqrt{(1+\sigma)V_0^2 - [(\mathbf{V}_0 \cdot \tau_2)_k^n + (u_2)_k^n]^2} - (\mathbf{V}_0 \cdot \mathbf{e}_1)_k^n)\Delta s_k + \varphi_0 \quad (6.27)$$

where n denotes the iteration step, and this equation is applied on each chordwise strip. The potential on the cavity has to be updated after each iteration.

The updating of the cavity surface from an initial guess or the previous iteration is then determined by the following hyperbolic equation,

$$A\frac{\partial \eta}{\partial s_1} + B\frac{\partial \eta}{\partial s_2} = \left(\mathbf{V}_{r0} \cdot \mathbf{n} - \frac{\partial \varphi}{\partial n}\right), \quad (6.28)$$

which is a simplification of equation (4.32). This equation is solved recursively starting from the detachment point, where η is zero.

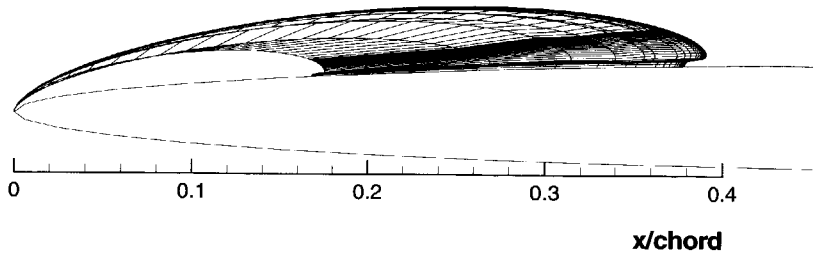

Figure 6.21: The side view of the cavity on a NACA 16-006 rectangular hydrofoil (aspect ratio = 500, angle of attack $\alpha = 4°$ and cavitation number $\sigma = 1.0$).

6.2.2 Convergence tests and numerical verification

A convergence test has been carried out successfully for the 2-D simulation of the cavity flow with a re-entrant jet. Quite a large number of panels is needed in the 2-D flow case to achieve an accurate result.

Here we take a high-aspect-ratio (AR=500) rectangular hydrofoil as an example. The cross-section is NACA 16-006. The intention is to verify our following calculations by our previous two-dimensional calculations. The angle of attack is chosen to be 4 degrees, which is representative for the situation on a propeller blade. In our test the spanwise number of panels is maintained at 20 for the half-span while the chordwise number of panels on the cavity surface is varied from 20 to 50. A side view of this converged cavity shape is given in Figure 6.21. The re-entrant jet is clearly shown for every spanwise station.

Because the hydrofoil has a very high aspect ratio, the cavity length is uniform over the whole span, except for the region very close to the tip. The flow at mid-span can be regarded as a purely 2-D flow in this case. The cavity end and the re-entrant jet are quite similar to the 2-D flow result, as will be illustrated below.

The prediction of the volume of the cavity is important for the prediction of the pressure fluctuations in a cavitating flow. Therefore the cavity volume is used as a criterion to check convergence. Not all the boundary conditions on every cavity panel are satisfied in that case, especially on the last few panels at the cavity end. But the calculations show that the shape of the cavity and its volume converge much faster than the kinematic boundary condition on the cavity surface. Figure 6.22 shows the cavity volume with varying chordwise number of panels on the cavity surface. When the number of panels is increased to 50, convergence is approached. A reasonable result can be expected when the chordwise number of panels is around 50 to 60. The cavity length for the

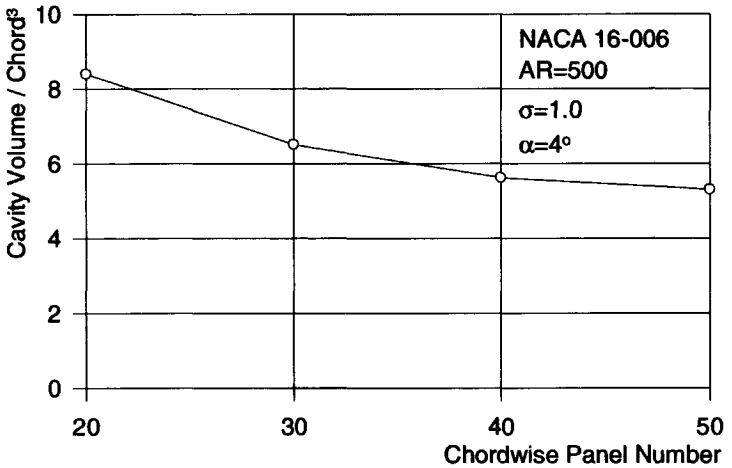

Figure 6.22: Cavity volume as a function of the number of chordwise panels on the cavity surface (NACA 16-006, aspect ratio = 500, angle of attack $\alpha = 4°$ and cavitation number $\sigma = 1.0$).

same calculation is presented in Figure 6.23. This is also compared with the previous 2-D flow result. A satisfactory agreement is found again when the number of panels is 50.

Because we intent to simulate the cavity re-entrant jet, a very fine panelling is applied at the end of the cavity. In the span direction, the panel distribution on the cavity surface follows the same distribution as on the foil surface below the cavity and no special arrangement is needed. But in the chordwise direction, the grid is refined according to the same formulae as given for the two-dimensional case (equation (6.21),(6.22),(6.23) and (6.24)).

The correction of the cavity surface in the iteration steps can not be too large because otherwise a small waviness of the surface will result in a twisted cavity end. So, a relaxation factor between 0.2 to 0.4 is used. The disadvantage of this relaxation factor is that it makes the convergence slower and more iteration steps are needed. Figure 6.24 shows the change of the cavity volume with the number of iteration steps. When the number of iteration steps exceeds 40, the cavity volume does not change any more. The change of the cavity shape after 40 iteration steps is mainly in the re-entrant jet, while the whole upper part of the cavity has already converged.

A verification of the present 3-D cavity flow method is obtained by comparing this prediction for the high-aspect-ratio hydrofoil with the 2-D cavity flow calculations. The cavity shape at midspan calculated by the 3D method

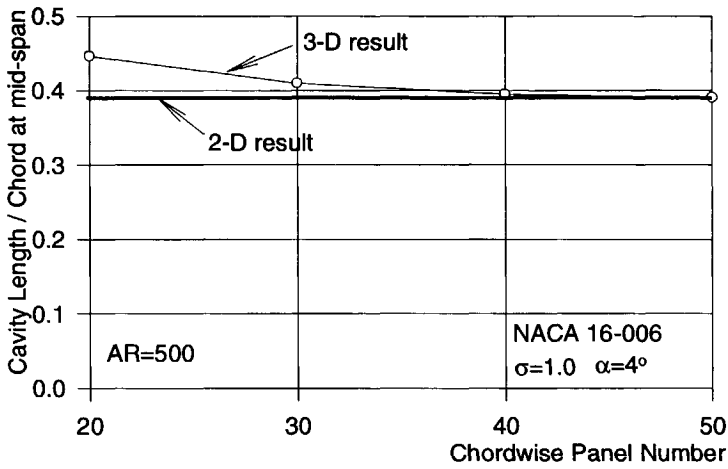

Figure 6.23: Cavity length as a function of the number of chordwise panels on the cavity surface (NACA 16-006, aspect ratio = 500, angle of attack $\alpha = 4°$ and cavitation number $\sigma = 1.0$).

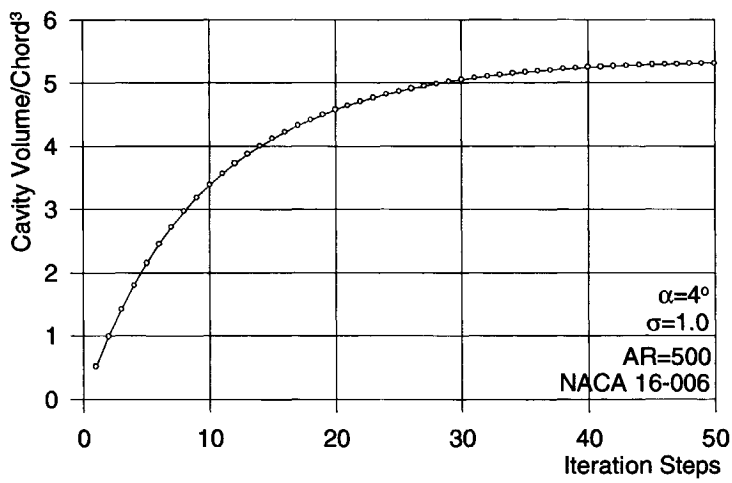

Figure 6.24: Cavity volume as a function of the number of iteration steps (NACA 16-006, aspect ratio = 500, angle of attack $\alpha = 4°$ and cavitation number $\sigma = 1.0$).

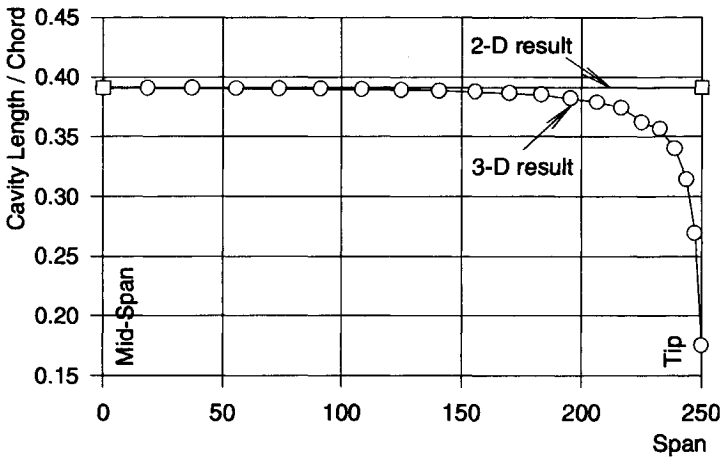

Figure 6.25: Comparison of 2-D flow cavity length with 3-D flow results at midspan (NACA 16-006, aspect ratio = 500, angle of attack $\alpha = 4°$ and cavitation number $\sigma = 1.0$).

should be the same as the 2D result. These comparisons are shown for the cavity length, the cavity cross-sectional area and the re-entrant jet thickness in Figure 6.25, Figure 6.26 and Figure 6.27 respectively. The agreement is quite satisfactory. This is true even for the re-entrant jet. Although the kinematic boundary condition on the jet is not fully satisfied, the calculated jet thickness in 3D is still the same as the result from the 2-D cavity flow calculation: about 9% of the maximum cavity thickness.

6.2.3 3-D results

To show the behavior of 3-D cavity flow and its re-entrant jet on hydrofoils, both a flat rectangular hydrofoil and a twisted rectangular hydrofoil at an angle of attack of 4° have been considered. The aspect ratio of these two hydrofoils are set to 2 in order to provide the geometry and the working condition similar to that of a propeller blade.

For the flat rectangular hydrofoil, the cavitation number is set to 0.5 and the initial cavity length is chosen to be ($l_{initial}/Chord = 0.5$), uniform all over the span.

The result of the cavity and hydrofoil system at a cavitation number of 0.5 is shown in Figure 6.28. In order to show the shape clearly, the y-axis is elongated by a factor of two. Some more calculations for the same hydrofoil at different cavitation numbers have also been carried out. The calculated cavity

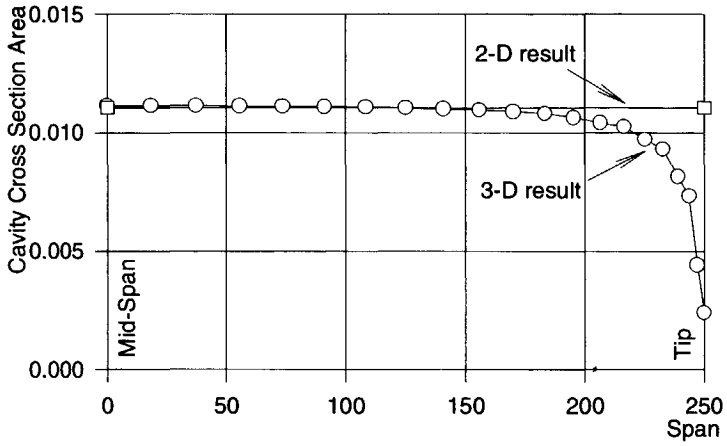

Figure 6.26: Comparison of cavity volume at midspan in 3-D cavity flow calculation with 2-D cavity flow results (NACA 16-006, aspect ratio = 500, angle of attack $\alpha = 4°$ and cavitation number $\sigma = 1.0$).

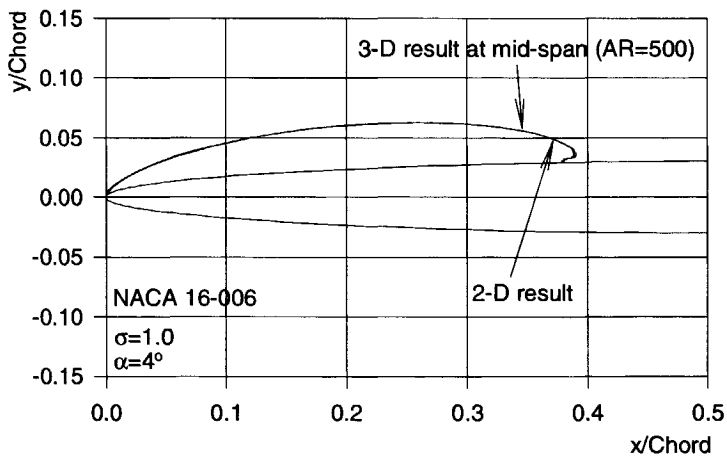

Figure 6.27: Comparison of the cavity shape at midspan (NACA 16-006, aspect ratio = 500, angle of attack $\alpha = 4°$ and cavitation number $\sigma = 1.0$).

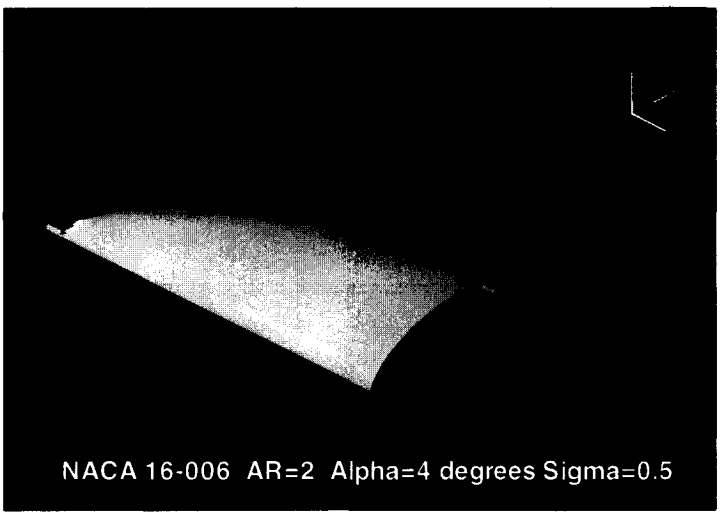

Figure 6.28: The calculated 3-D cavity-hydrofoil system (NACA 16-006, aspect ratio = 2, angle of attack $\alpha = 4°$ and cavitation number $\sigma = 0.5$).

planform at various cavitation numbers is given in Figure 6.29. The cavity shape converges even when the maximum cavity length at mid-span is as long as 0.85. It is well known that in the 2-D flow case the solution is bifurcated when the cavity length is longer than about 3/4 chord length. The cavitation volume predicted for these different cavitation numbers is given in Figure 6.30. It is obvious that the change of the cavity volume with the cavitation number is not linear. The gradient becomes higher when the cavity is longer. Or in other words, when the cavity is very short at the leading edge, the cavity variation is less sensitive to the pressure variation. This is in accordance with experimental observations that the cavity length becomes more variable when it is longer.

6.2.4 Streamline and re-entrant jet direction

Theoretically the re-entrant jet is always needed for a 2-D cavity flow because the cavity must be closed with the same pressure as the pressure on the cavity surface. But in the 3-D cavity flow case, a re-entrant jet is not needed when a strong cross flow exists at the end of the cavity. The flow characteristics around the trailing edge of the cavity end are therefore of interest. Both the experiment of a swept hydrofoil (Figure 2.6 in De Lange (1996)) and the experiment of a conventional propeller (Figure 15 in Kuiper (1994)) show that the re-entrant jet turns away from the flow direction on the cavity surface. It is assumed by

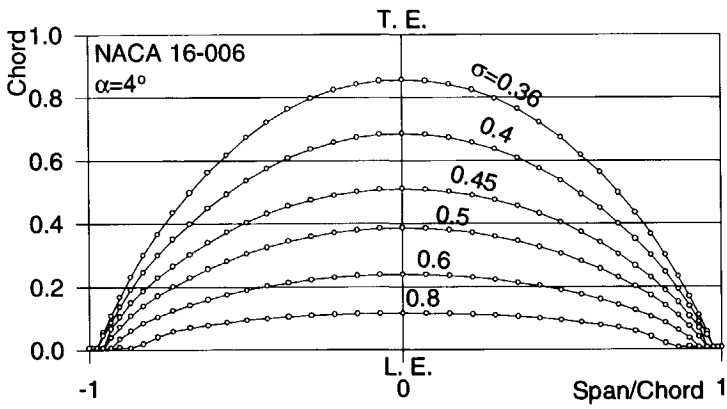

Figure 6.29: The calculated cavity planform for different cavitation numbers (NACA 16-006, aspect ratio = 2, angle of attack $\alpha = 4°$).

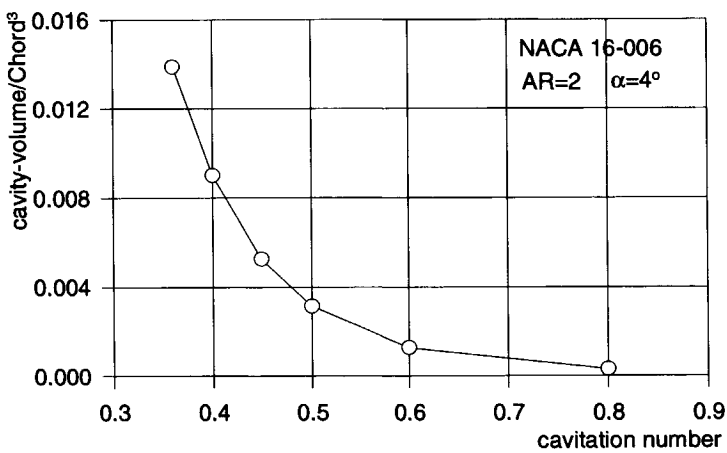

Figure 6.30: The cavity volume at different cavitation numbers (NACA 16-006, aspect ratio = 2, angle of attack $\alpha = 4°$)

De Lange (1996) that the flow is 'reflected' at the end of the cavity, which has been verified by Schöön (2000) in experiments. But no theoretical calculation has been carried out.

In order to understand the characteristics of the flow at the end of the cavity, the streamlines on the cavity surface and in the re-entrant jet are calculated for the hydrofoil in Figure 6.28 of the same conditions. The result is given in Figure 6.31. Also drawn in this figure is the distribution of the negative pressure coefficient on the cavity and foil surface. From the pressure coefficients it is found that a stagnation point is present on the foil surface downstream of the end of the cavity, especially at mid-span. But in the tip region, where the gradient of the cavity length is large, no stagnation pressure is found. From the streamlines in this figure, we find that in that region the flow is almost tangential to the cavity. Consequently re-entrant jet is not found. But in the region close to the mid-span, the flow remains perpendicular to the inflow direction and a re-entrant jet is found. A detail of the flow in the region without stagnation pressure is shown in Figure 6.32. It is quite clear that the flow is indeed "reflected" at the cavity end. That means the angle between the jet and the cavity extent is equal to the angle between the cavity end line and the flow on the cavity. So the cavity can be stable when the spanwise gradient of the cavity extent is large enough. Since the re-entrant jet is cut off in our calculations, prediction of the behavior of the jet internally in the cavity and thus of the occurance of cloud cavitation can not be derived.

6.2.5 Comparison with experimental data

At present good and accurate experimental data on 3-D cavity flow are not available in literature. An example of available data is the experiment conducted at MIT by Kinnas & Fine (1993). Unfortunately there is uncertainty about the angle of attack and the section geometry. But it can still be used to validate our calculations qualitatively. A NACA65a section in the present calculation approximates the cross section of the foil. Its main parameters can be found in Kinnas & Fine (1993). The angle of attack is 6.5°. Only the cavity length has been measured at two different cavitation numbers. No information is available about the cavity volume.

The calculated cavity length along the span is compared with experimental data in Figure 6.33. The calculation shows a very good correlation with the data over most part of the hydrofoil surface. Slight deviations occur at the tip and at midspan. The calculated cavity volume is listed in Table 6.4 and the calculated cavity shapes for several span positions are shown in Figure 6.34 for a cavitation number of 1.084.

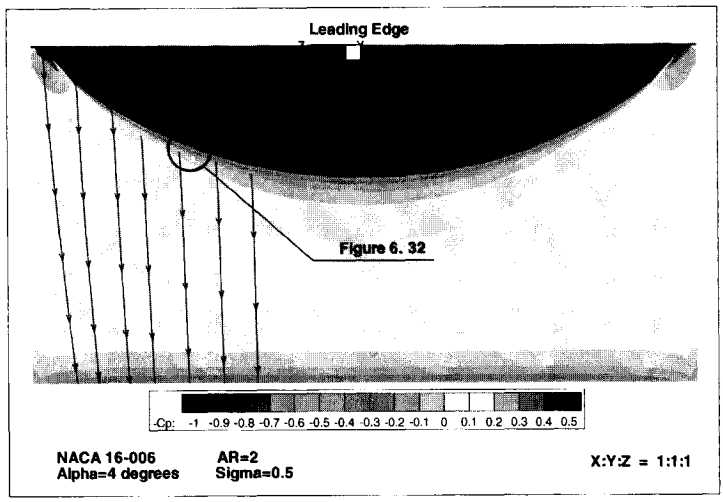

Figure 6.31: Pressure distribution and streamline on the cavity-foil surface(NACA 16-006, aspect ratio = 2, angle of attack $\alpha = 4°$, cavitation number $\sigma = 0.5$).

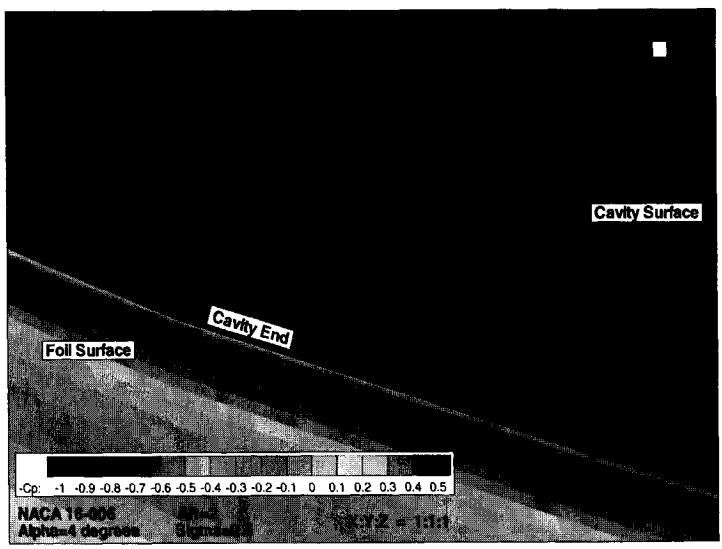

Figure 6.32: The flow 'reflects' at the end of the cavity(NACA 16-006, aspect ratio = 2, angle of attack $\alpha = 4°$, cavitation number $\sigma = 0.5$).

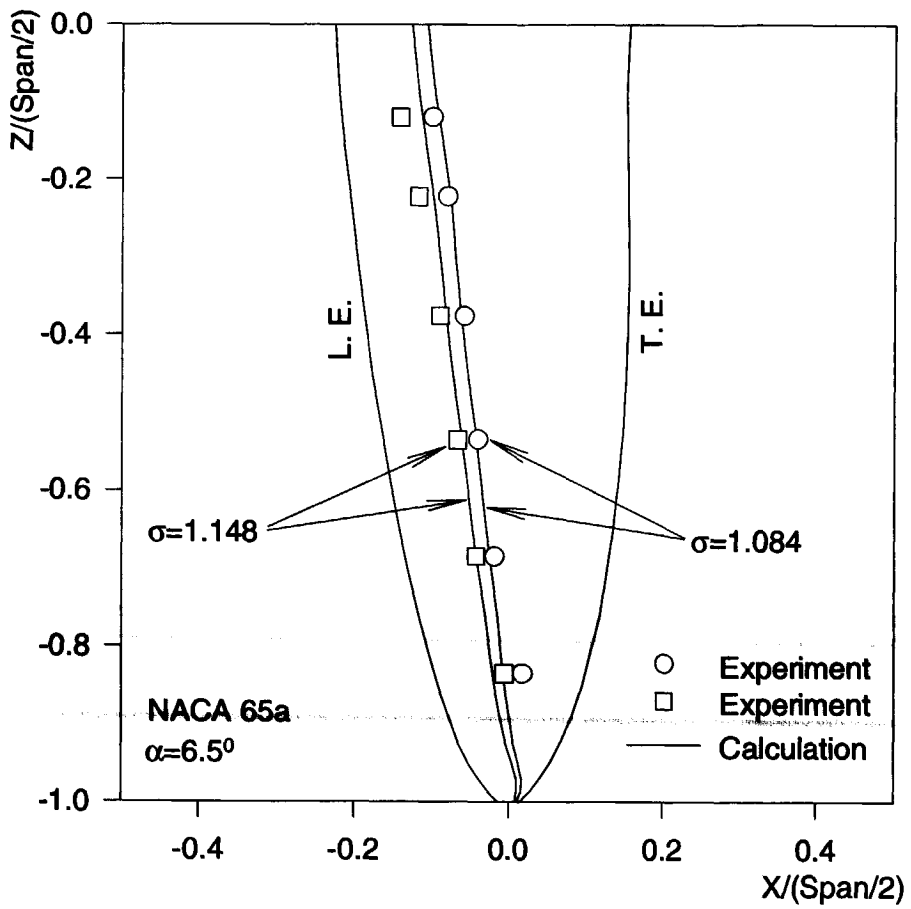

Figure 6.33: Comparison of calculated cavity length with experimental data. (Kinnas & Fine (1993), angle of attack $\alpha = 6.5°$)

Table 6.4: The calculated cavity volume for the three dimensional hydrofoil used by Kinnas & Fine (1993). (cavitation number $\sigma = 1.084$ and 1.148, angle of attack $\alpha = 6.5°$)

Cavitation number	1.084	1.148
$Cavity\ volume/(Span/2)^3$	1.40×10^3	1.04×10^3

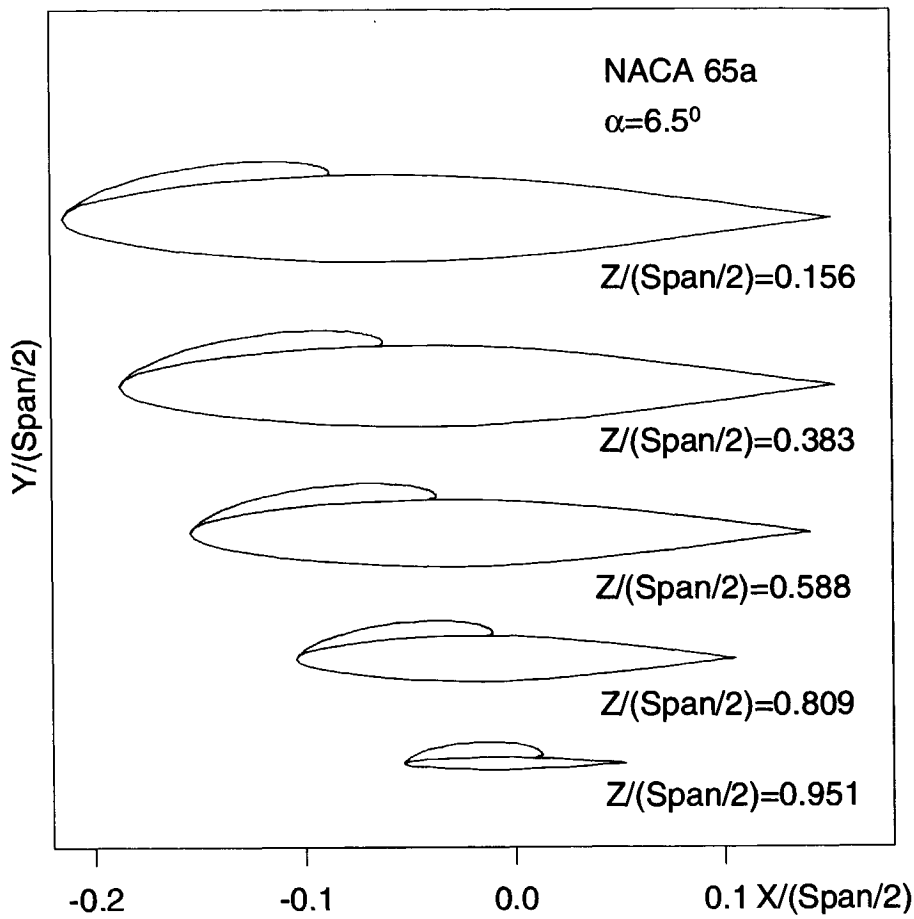

Figure 6.34: Cavity shapes at different spanwise positions. (for the hydrofoil of Kinnas & Fine (1993), angle of attack $\alpha = 6.5°$)

6.2.6 Summary

A three-dimensional cavity re-entrant jet has been simulated. Systematic convergence tests of the present method show that the method is quite stable and convergent. Calculation of the cavity on a high-aspect-ratio hydrofoil shows good agreement with previous non-linear 2-D cavity flow calculations for both cavity length and cavity volume. Some 3-D cavity flow calculations for a flat and a twisted rectangular hydrofoil with NACA 16-006 wing section have been made at different cavitation numbers. The calculated results show that the re-entrant jet is not always needed. In the tip region, the fluid at the end of the cavity flows in a direction tangential to the cavity end. The calculations confirm that the flow on the cavity surface is 'reflected' at the cavity end line when the re-entrant jet exists. A preliminary experimental validation of the present method has been made for a MIT hydrofoil. The present method gives a quite good prediction of the cavity length over the whole span. In order to validate the present method systematically, more experimental data are needed, especially for the cavity shape and volume in 3-D flows.

6.3 Propeller flows

So far, the present method has been verified by numerical tests, like convergence tests. Present results have been and compared with results of other linear and non-linear methods both for two- and three-dimensional flow cases. Some simple validations are given as well for hydrofoils. Although our objective is the prediction of the dynamics of cavitation on propeller blades, tests and validations of the present method for steady propeller flows are essential too, because the previous test cases are relatively simple which do not include aspect of propeller flows like the tip vortices, the skewness and the warp of the blade, the pitch variation, etc. These aspects are essential and make the propeller flows different from hydrofoil flows.

Since the present method has been developed only for leading-edge partial cavity flows, we will take a test case with only leading-edge partial cavity flows on the blades, but it should still cover a wide range of different cavity extents, say from short leading-edge cavitation up to cavities of 80% of the chord.

The most reliable experimental results we have are the results for *Propeller S* from the thesis of Kuiper (1981). This propeller is designed such that a high suction peak at the leading edge will result in boundary-layer separation and lead to a stable sheet cavity from the leading edge. Since the tip region is unloaded, it provides an ideal test case for the partial sheet cavity flow on propeller blades.

The geometry of this propeller can be found in Table A1.3 and Table A1.4 of Kuiper (1981). The experiments were carried out in the depressurized towing

tank at MARIN. The pictures were recorded on 16mm black and white films. The experiments were carried out for two different advanced coefficients $J = 0.4$ and 0.6 and a number of different cavitation numbers σ_n, where we defined,

$$J = \frac{V_p}{nD} \tag{6.29}$$

and,

$$\sigma_n = \frac{p_\infty - p_v}{\frac{1}{2}\rho n^2 D^2} \tag{6.30}$$

with V_p the oncoming velocity to the propeller, D the diameter of the propeller and n the rotational speed.

The basic structure of the cavity on the blade is the same as that observed in the cavitation tunnel (Figure 1.3) for $J = 0.4$. In this case the cavity extent increases from 0 at the root of the propeller to a certain length on the blade. The cavity then remains almost of the same length before it decreases to zero again at the tip, due to the unloading at the tip. A comparison of the present calculation with the experiments for four different cavitation numbers $\sigma_n = 2.2,\ 2.0,\ 1.7,\ 1.5$ is given in Figure 6.35 and Figure 6.36. To minimize the scale effect, only the test results with surface roughness are used. The agreement is quite good.

There is no experimental data on the thickness and volume of the cavity. But the calculations show that the cavities for all the calculated conditions are predicted to be very thin. They are so thin that only when a very fine grid is used at the cavity closure, the details of the re-entrant jet can be resolved. This was not done, since the details of the re-entrant jet have no effect on the cavity extent and volume in the present situation.

It has been concluded by Laberteaux (1998) that the prediction by potential flow theory gives a good correlation with the experiments when the cavity closure is a laminar closure, but overpredicts the cavity extent when the cavity closure is a turbulent closure, because the observation shows that the cavity ended almost at the maximum thickness point. According to our prediction in the two-dimensional cavity flow, the position of the maximum thickness of the cavity is located at 60% of the cavity extent (Figure 6.13). It means that the observed cavity extent can be only 60% of the calculated one. This appears not to be true for our present test case. At the inner radii where the re-entrant jet is clearly seen in the experiment, the potential flow theory gives a very good prediction. At the certain radius, the re-entrant jet impinges on the cavity surface and the closure becomes frothy thereafter. But the potential theory gives still a reasonable good prediction.

Another comparison is carried for a different advance coefficient $J = 0.6$. The pressure peak at the leading edge is not as high as that for $J = 0.4$ and

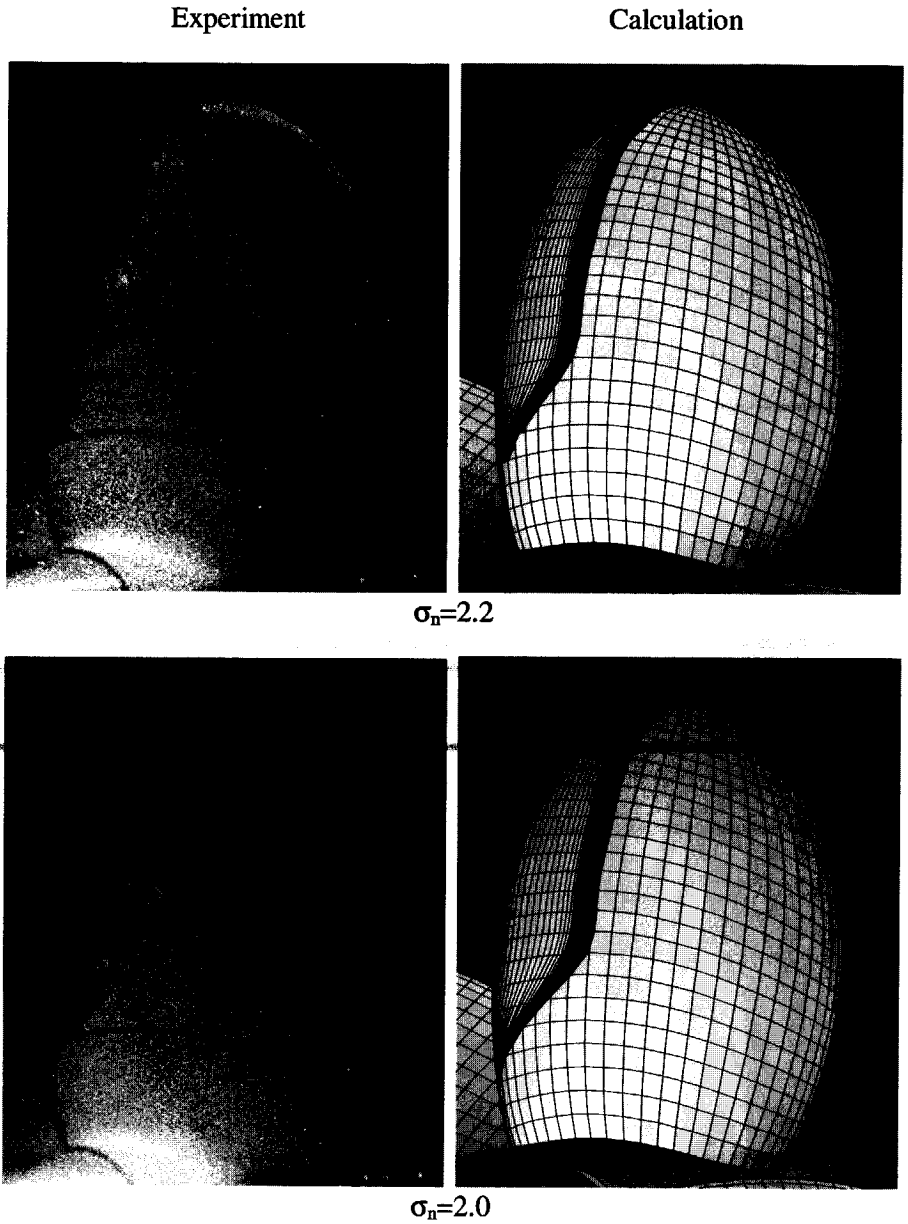

Figure 6.35: Comparison of cavity shape on *S Propeller* at $J = 0.4$, $\sigma_n = 2.2$ and 2.0. Experiments were carried out in the depressurized towing tank with roughness (Kuiper (1981)).

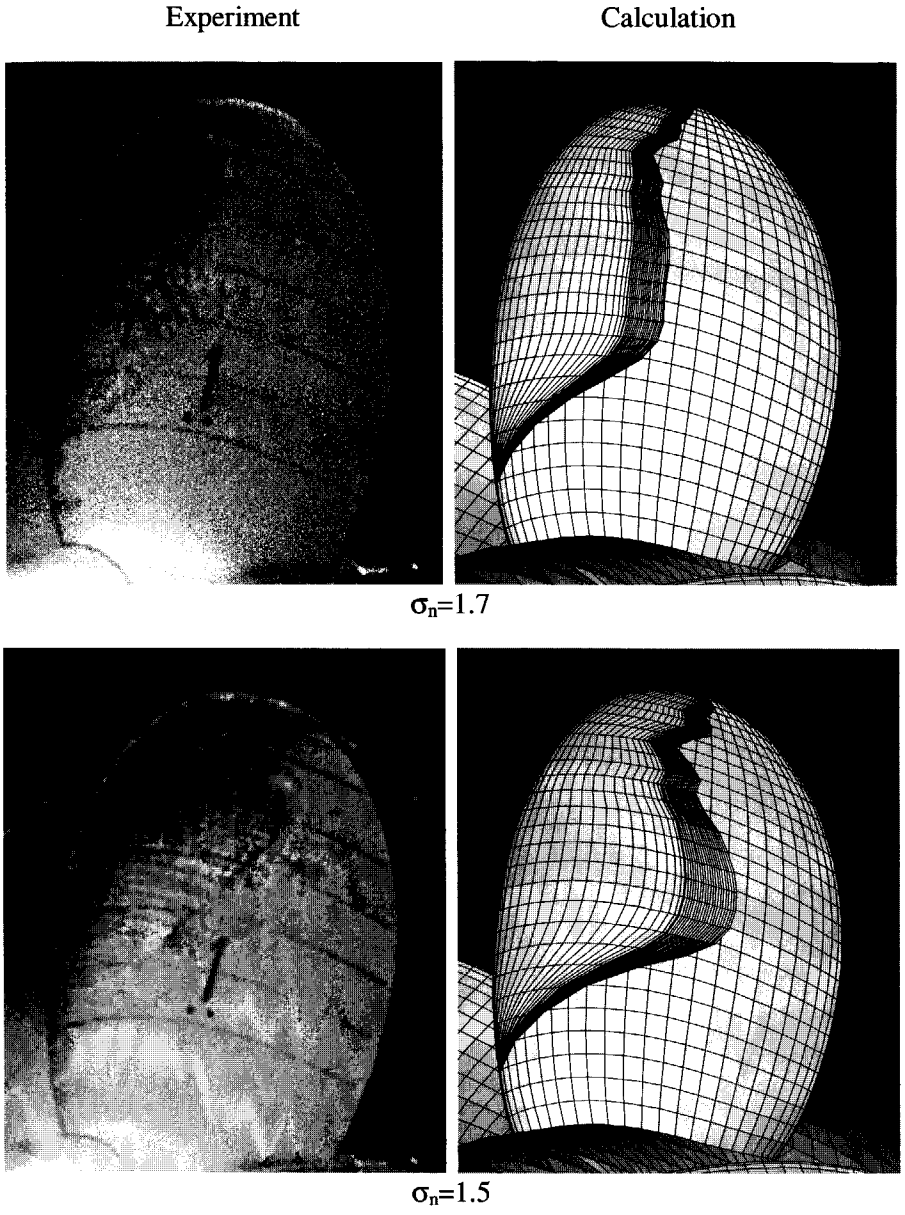

Figure 6.36: Comparison of cavity shape on *S Propeller* at $J = 0.4$, $\sigma_n = 1.7$ and 1.5. Experiments were carried out in the depressurized towing tank with roughness (Kuiper (1981)).

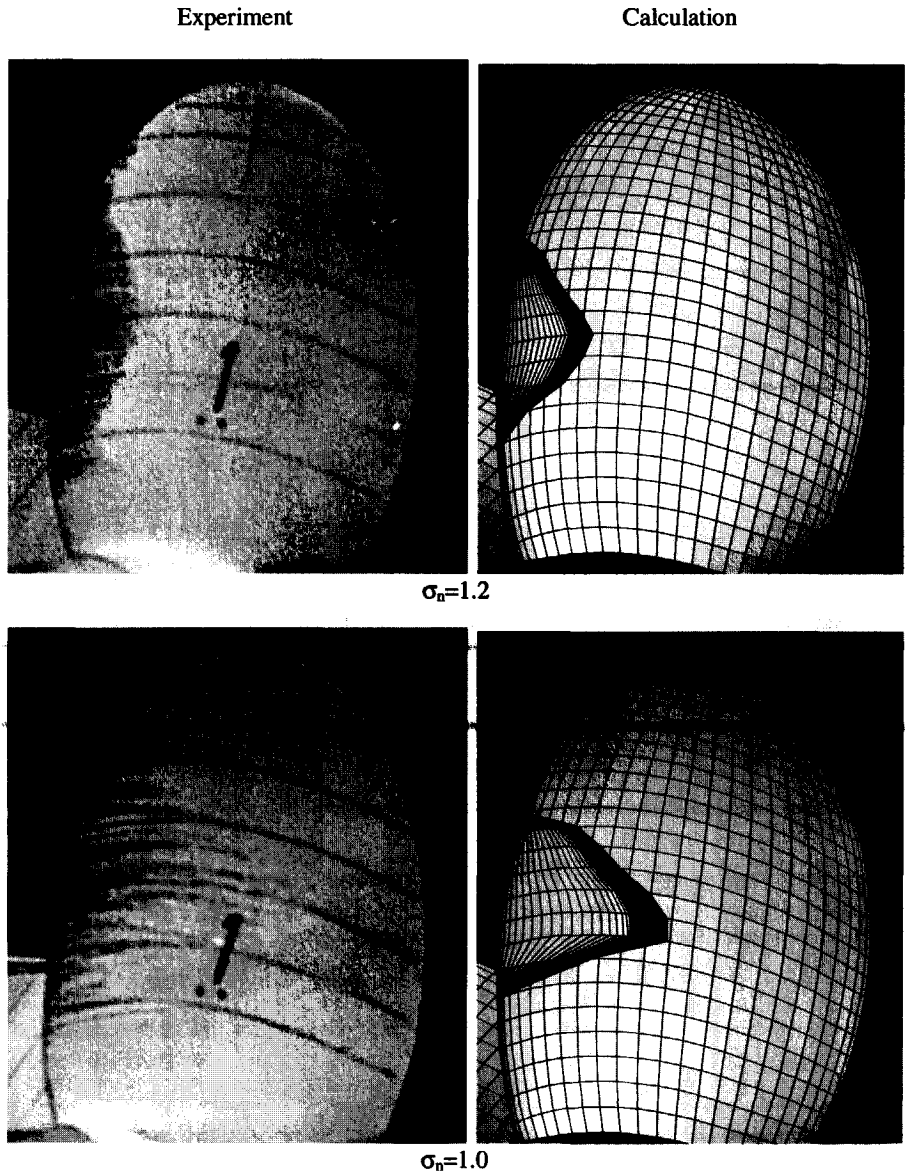

Figure 6.37: Comparison of cavity shape on *S Propeller* at $J = 0.6$, $\sigma_n = 1.2$ and 1.0. Experiments were carried out in the depressurized towing tank with roughness (Kuiper (1981)).

the suction peak exists only in the middle part of the blade span. This gives a very much restricted cavity in the mid span region. The comparison is given in Figure 6.37. The calculation results are reasonable. The difference at the two sides of the cavity maybe due to the roughness at the propeller leading edge in the experiments.

All the calculations in this sub-section have been obtained using 50 chordwise panels and 30 spanwise panels on the blade surface, and 40 chordwise panels on the cavity surface. It has been proven in the previous sections that this number of panels is large enough to provide a grid-converged result.

Chapter 7

Unsteady Cavity Flows

The prediction of unsteady cavity flows occurring on two-dimensional profiles, on three-dimensional hydrofoils and on propeller blades in a non-uniform wake flow is investigated. Emphasis is on the dynamics of the cavity variation and its effect on the pressure fluctuations. Some preliminary features of the unsteady cavity dynamics are predicted. Phase differences of the cavity shape change, in extent and thickness, are found both in chord and in span directions. The main characteristics of the cavity growth and collapse, when the propeller blade is passing through a sharp wake peak, are captured. The present approach proves to be able to predict unsteady cavity flows.

It has been more than three decades that propeller loading has been increasing due to the growth in the size of bulk carriers and fast cargo liners. Even before this time, the ship stern vibration excited by the shaft and hull forces from the non-cavitating propellers had been noticed as an important problem for ship and propeller designers. The appearance of unsteady cavitation on the heavily loaded propeller blades increases the exciting forces up to an order of magnitude in the blade frequency. Generally speaking, the excitation forces generated only by cavitation are 4 to 6 times those from the sum of the blade loading and thickness by non-cavitating propellers (Breslin & Andersen (1994)). Specific features of some cavitating propellers are that the excitation forces of higher blade harmonics (second and third blade frequency) have the same magnitude as that of the blade frequency. This has never been observed for the case of non-cavitating propellers and hence it is believed that the higher harmonics originate from the dynamics of the cavity.

From an integrated point of view of Van Gent (1994), by using the Green's theorem, the pressure generated by a cavitating propeller can be expressed in

the body-fixed moving coordinates $o-xyz$ in the following form,

$$\begin{aligned}\frac{p(\mathbf{x})}{\rho} &= \frac{1}{4\pi}\iint_{\partial\Omega}\frac{p}{\rho}\left(\mathbf{n}\cdot\nabla\frac{1}{r(\tilde{\mathbf{x}},\mathbf{x})}\right)dS_{\tilde{\mathbf{x}}} \\ &- \frac{1}{4\pi}\iint_{\partial\Omega}\frac{1}{r(\tilde{\mathbf{x}},\mathbf{x})}\left(\mathbf{n}\cdot\nabla\frac{p}{\rho}\right)dS_{\tilde{\mathbf{x}}} \\ &- \frac{1}{4\pi}\iiint_{\Omega}\frac{1}{r(\tilde{\mathbf{x}},\mathbf{x})}\left(\nabla^2\frac{p}{\rho}\right)dV_{\tilde{\mathbf{x}}},\end{aligned} \tag{7.1}$$

assuming that the pressure p has continuous derivatives up to the second di-revitives. In equation (7.1), $\mathbf{x}$ is a point in the flow field and it is moving when you are observing it in the body-fixed coordinates, and $\tilde{\mathbf{x}}$ is a point on the boundary for the surface integrals or a point in the flow field for the volume integral.

Notice that the temporal variation of the total potential ϕ depends on the coordinate system, but as a vector, the gradient of the potential is independent of the system of reference. Expressing the material derivative of the potential (following a fluid particle) both in the space-fixed and in the body-fixed coordinates, we have,

$$\frac{D\phi}{Dt} = \frac{\partial\phi(\mathbf{X};t)}{\partial t} + \mathbf{V}\cdot\nabla\phi = \frac{\partial\phi(\mathbf{x};t)}{\partial t} + \mathbf{V}_r\cdot\nabla\phi. \tag{7.2}$$

Then we obtain the relation between the two partial time derivatives of the potential,

$$\begin{aligned}\frac{\partial\phi(\mathbf{X};t)}{\partial t} &= \frac{\partial\phi(\mathbf{x};t)}{\partial t} + (\mathbf{V}_r-\mathbf{V})\cdot\nabla\phi \\ &= \frac{\partial\phi(\mathbf{x};t)}{\partial t} - \mathbf{V}_e\cdot\nabla\phi,\end{aligned} \tag{7.3}$$

where $\mathbf{V}_e = -(\mathbf{V}_r-\mathbf{V}) = \mathbf{V}_0+\Omega_0\times\mathbf{x}$ is the velocity due to the motion of the body-fixed coordinates.

Within the frame of potential flow theory, the pressure on the right-hand side of equation (7.1) can be determined by equation (2.9) in the space-fixed coordinates $O-XYZ$. Substituting equation (7.3) in equation (2.9), the pressure can be expressed as a function of the velocity potential in the body-fixed frame of reference and hence the excitation pressure can be expressed as,

$$\begin{aligned}\frac{p}{\rho} = &- \frac{1}{4\pi}\iint_{\partial\Omega}\left[-\frac{\partial\phi}{\partial t}+\mathbf{V}_e\cdot\nabla\phi+\frac{1}{2}(\nabla\phi)^2\right]\frac{\partial}{\partial n}\left(\frac{1}{r}\right)dS_{\tilde{\mathbf{x}}} \\ &+ \frac{1}{4\pi}\iint_{\partial\Omega}\frac{\partial}{\partial n}\left[-\frac{\partial\phi}{\partial t}+\mathbf{V}_e\cdot\nabla\phi+\frac{1}{2}(\nabla\phi)^2\right]\left(\frac{1}{r}\right)dS_{\tilde{\mathbf{x}}} \\ &- \frac{1}{4\pi}\iiint_{\Omega}\left[\frac{1}{2}(\mathbf{w}\cdot\mathbf{w})-(\mathbf{E}\cdot\mathbf{E})\right]\left(\frac{1}{r}\right)dV_{\tilde{\mathbf{x}}},\end{aligned} \tag{7.4}$$

where $\mathbf{w}$ is the vorticity and $\mathbf{E}$ is the flow deformation tensor.

From equation (7.4) we can distinguish three major contributions to the pressure field. The first term on the right-hand side of equation (7.4) is a "dipole-like" term, which contains mainly the effects of the blade loading and the thickness of a propeller blade. This term decays fast with the distance as $1/r^2$. It is related to the pressure generated by the non-cavitating propellers. The second term is a "source-like" term, which contains mainly the effects of the acceleration of the cavity thickness, the velocity of the cavity thickness and the thickness itself. Comparing to the other terms, the acceleration of the cavity thickness is dominant. Since the decay of this term is as $1/r$, which is slower than that of the dipole term, the contribution of this term to the pressure in the far field is largest. By application of the divergence operator to the Navier-Stokes equation, the third term of equation (7.1) can be re-written into the third term of equation (7.4), which contains the effects of the fluid deformation and the vorticity. These effects are concentrated in the boundary layer or in the shear layer of the wake, which is out of the scope of our present potential flow theory and hence is neglected here.

Because the second term has the largest contribution to the pressure fluctuation and also because it decays much slower than the dipole term, we focus on this term in the following. By taking the partial time derivative of the kinematic boundary condition of equation (4.16) and substituting it in the second term of equation (7.4) for $\dfrac{\partial}{\partial n}\left(-\dfrac{\partial \phi}{\partial t}\right)$ term, the contribution of the second term can be written as,

$$\begin{aligned}
\frac{p_2}{\rho} &= \frac{1}{4\pi}\iint_{S_C} \frac{\partial^2 \eta}{\partial t^2}\left(\frac{1}{r}\right) dS_{\bar{\mathbf{x}}} \\
&+ \frac{1}{4\pi}\iint_{S_C} \frac{\partial}{\partial t}\left[A\frac{\partial \eta}{\partial s_1} + B\frac{\partial \eta}{\partial s_2} - \mathbf{V}_{r0}\cdot\mathbf{n}\right]\left(\frac{1}{r}\right) dS_{\bar{\mathbf{x}}} \qquad (7.5)\\
&+ \frac{1}{4\pi}\iint_{S_C} \frac{\partial}{\partial n}\left[\mathbf{V}_e\cdot\nabla\phi + \frac{1}{2}(\nabla\phi)^2\right]\left(\frac{1}{r}\right) dS_{\bar{\mathbf{x}}},
\end{aligned}$$

where p_2 denotes the contribution of the second term in equation (7.4).

It has been proven by Van Gent (1994) that, using linearization, the second and the third term on the right-hand side of equation (7.5) can be integrated by partial integration and represented as chordwise dipole distributions, generated by the thickness of both the cavity and the foil and by the cavity thickness velocity. The only source-like term is the first term, which we can re-write into,

$$\frac{p_{acc.}}{\rho} = \frac{1}{4\pi}\iint_{S_C} \frac{\partial^2 \eta}{\partial t^2}\left(\frac{1}{r}\right) dS_{\bar{\mathbf{x}}}, \qquad (7.6)$$

where the subscript *acc.* denotes the contribution of the cavity acceleration.

When the observation point is a field point which is sufficiently far from the propeller at $r = R$, the detailed geometry of the propeller and the cavity is no longer important. Then equation (7.6) is simplified into,

$$\frac{p_{acc.}}{\rho} = \frac{1}{4\pi R}\frac{\partial^2}{\partial t^2}\left[\iint_{S_C} \eta dS_{\vec{x}}\right] = \frac{1}{4\pi R}\frac{\partial^2 \overline{V}}{\partial t^2}, \tag{7.7}$$

or,

$$p_{acc.} = \frac{\rho}{4\pi R}\frac{\partial^2 \overline{V}}{\partial t^2}, \tag{7.8}$$

where $\overline{V}$ is the cavity volume.

In summary, we can conclude,

1. The contribution of the cavity acceleration to the pressure excitation comes from the integration of the acceleration of the cavity thickness, which is distributed over the cavitating area, instead of from the total volume of the cavity.

2. When the field point is far away from the unsteady cavity on the propeller blades, only the cavity volume acceleration is important for the prediction of the pressure fluctuations (equation (7.8)), and the detailed information about the cavity shape is not needed. Hence large pressure amplitudes at higher blade frequencies can not be predicted.

3. But when the field point is in the intermediate or near field, the details of the cavity thickness distribution on the blade surface and its acceleration play an important role. Their contribution to the pressure field is expressed as the surface integral given in equation (7.6). Hence the higher blade frequency components can be predicted.

The previous quasi-steady methods of cavity flow prediction are suffering from the fact that cavity dynamics are not really predicted. Only the wake non-uniformity is transferred into a time-dependent pressure field, which then causes the cavity volume change. These methods can supply a reasonable estimate for the lowest frequency of vibration excitation, but not for the higher frequencies. The improved method (Van Gent (1994)) used an unsteady lifting surface code and a two-dimensional dynamic model of the cavity, and hence the dynamics of the cavity were predicted. But the cavity was represented simply by a semi-ellipse, in which the cavity thickness at different chord positions increases or decreases simultaneously and in phase. In this case, equation (7.6) acts like equation (7.8) and hence the higher blade frequency components of the pressure excitation can not be predicted.

The results of the present non-linear method will show that the cavity extent and the thickness variations both in chord and span direction, are generally not in phase. When some parts of the cavity are growing, some other parts are shrinking. During the growth phase of the cavity, the maximum thickness is at the mid-chord of the cavity. But when the cavity reaches its maximum extent, the maximum thickness of the cavity moves toward the end of the cavity. These details of the cavity dynamics are expected to provide enough information to be able to calculate the higher blade frequency of the excitation.

7.1 Hydrofoil flows

7.1.1 Two dimensional cavity flows

Strictly speaking, the simulation of unsteady cavity flows in two-dimensions violates the condition at infinity (see equation (2.46)). This is shown in the following.

Instead of using Green's function of equation (3.3) in the pressure integration of equation (7.1), equation (3.4) is used in two-dimensional flows. Following the same derivation as used in the previous paragraphs, the contribution to the pressure in the far field by the acceleration of the cavity volume is written as,

$$p_{acc.} = -\frac{\rho}{2\pi}\frac{\partial^2 \overline{V}}{\partial t^2}\ln R, \tag{7.9}$$

in stead of equation (7.8).

Due to the logarithmic function, the pressure tends to infinity when $R \to \infty$, which violates the boundary condition at infinity. Hence no calculation is tried for two-dimensional potential flow theory, as we did in section 6.1.

The two exceptions are when the cavity flow is a steady flow or when the cavity is growing or shrinking at a constant speed. For a steady cavity flow, the cavity can be represented by a source at the origin with zero strength and hence satisfy the condition at infinity. For a cavity which is growing or shrinking at a constant speed, the cavity is a source or sink at the origin with a constant strength and hence its contribution to the pressure at infinity is zero as well.

So, the present investigation on two-dimensional cavity flow is carried out for three-dimensional hydrofoils which have very high aspect ratio. We believe that the flow at mid-span will asymptotically approach the two-dimensional cavity flow and reveal some characteristics of the unsteady two-dimensional cavity flow.

Cavity flow in a gust

The present theory is first checked using a rectangular hydrofoil with an aspect ratio of 500. The NACA 16-006 profile is chosen as the cross-section and no camber is applied. The hydrofoil is plane and not twisted along the span.

The hydrofoil is traveling in unbounded fluid at a constant speed V_0. There is a space-fixed vertical gust field V_W in the whole fluid field, which is seen by the hydrofoil-fixed system as,

$$\begin{aligned} V_W &= 0.07V_0 + 0.0157V_0 \sin(\omega t) \\ &= 0.07V_0 + 0.0157V_0 \sin(\frac{2V_0K}{C}t), \end{aligned} \tag{7.10}$$

where K is the reduced frequency of the gust defined by equation (5.33) and ω is the angular frequency. At mid-span the flow is similar but not equivalent to the sectional flow with an angle of attack of 4° to the inflow and with 1° of pitching around its chord center.

Only the cavity details at the central cross-section are taken from the calculations and plotted in the following figures. The details close to the tip are not important for our present two-dimensional flow investigations.

Due to the symmetry of the hydrofoil with respect to the mid-span, only half of the hydrofoil is discretized. On the foil surface, 20 panels are used in the span direction and 24 panels are used in the chord direction. In order to simulate the cavity surface in more detail, 40 panels along the chord are used for the cavity surface.

For the very high aspect ratio hydrofoil a relatively long wake length is needed. In the present case, the wake length is chosen as 8 times the chord length, which requires 20 panels chordwise for $K = \pi/4$, 40 panels for $K = \pi/2$ and 80 panels for $K = \pi$.

One cycle within the cyclic motion of the cavity at mid-span is plotted in Figure 7.1 from **A** to **J**. Also plotted in Figure 7.1 is the relative position of the gust in which the peak and the trough of the gust can be seen. The cavitation number σ is 1.0. The reduced frequency $K = \pi$, which means that the wave length of the gust equals the chord length. This situation is regarded as a very high frequency situation for the propeller flows. Only a sharp peak in the ship wake will generate a gust to the propeller blade that corresponds to this high frequency. The cavity is growing from **A** to **E** in Figure 7.1 and is shrinking from **F** to **J** in this figure. During the growth of the cavity, we can see that the location of the cavity maximum thickness is around 50% of the total length in **A**, and it moves towards the end of the cavity. The thickness of the cavity at the end is building up while the cavity extent is increasing. But a re-entrant jet is not observed in the whole process of cavity growth. When the cavity reaches its maximum extent (**F** in Figure 7.1), the re-entrant jet starts to form. In the early stage of shrinking of the cavity, the re-entrant jet is clearly seen at the

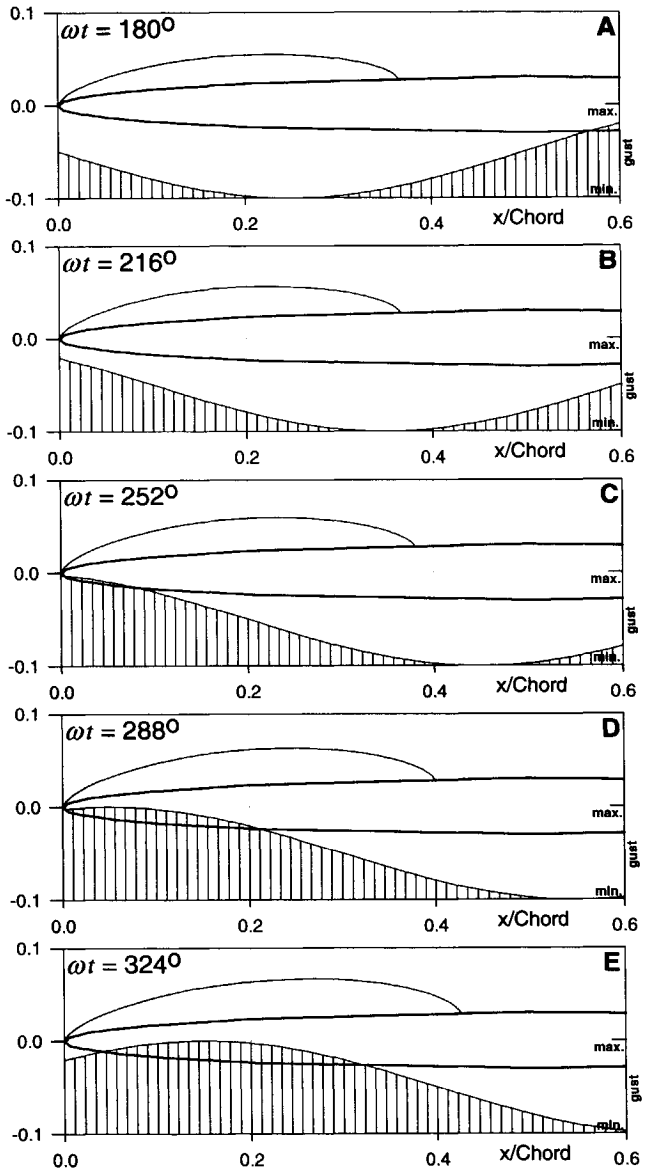

Figure 7.1: Unsteady motion of the cavity on a high aspect ratio hydrofoil travelling in a sinusoidal vertical gust. (Aspect ratio AR=500, NACA16-006 section, vertical gust $V_W = 0.07V_0 + 0.0157V_0 \sin(\omega t)$, reduced frequency $K = \pi$, $\sigma = 1.0$.)

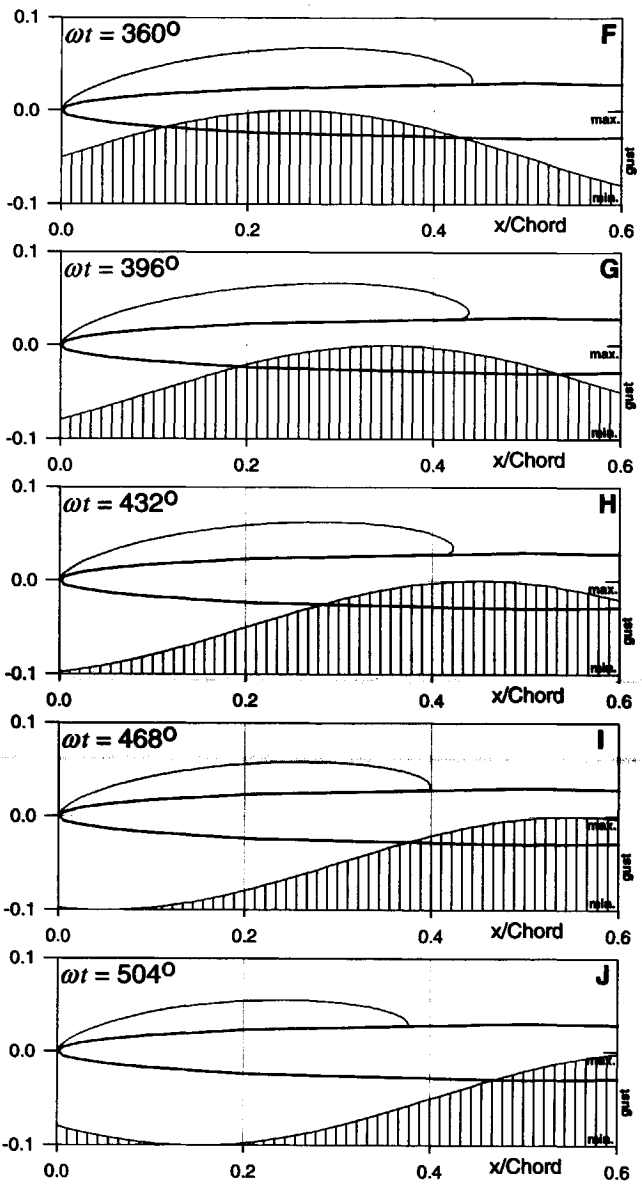

Figure 7.1: (continued) Unsteady motion of the cavity on a high aspect ratio hydrofoil travelling in a sinusoidal vertical gust. (Aspect ratio AR=500, NACA16-006 section, vertical gust $V_W = 0.07V_0 + 0.0157V_0 \sin(\omega t)$, reduced frequency $K = \pi$, $\sigma = 1.0$.)

end of the cavity (**G** in Figure 7.1). The re-entrant jet is present during the whole process of the shrinking (collapsing) of the cavity until the cavity stops shrinking (**J** in Figure 7.1).

The details of the re-entrant jet are not represented with the present numbers of panels. More details about the re-entrant jet can be expected when more panels are used, but the computation time will increase dramatically and hence is not tried at the present research stage. An important feature of this calculation is that the cavity thickness distribution varies during a cycle. This results in a motion of the location of the maximum cavity thickness back and forth. Watching the movie generated by the results in Figure 7.1, we found that the cavity surface looks like '*dancing*' instead of simply '*blowing*' up and shrinking of a balloon.

The variation of the cavity extent, the maximum thickness, the cavity volume and the second time-derivative of the cavity volume with time are plotted in Figure 7.2 to Figure 7.7 for three different reduced frequencies, $K = \pi/4, \pi/2$ and π. The influence of the reduced frequency on the variation of the cavity can be clearly seen.

Figure 7.2 shows that both the cavity length and the maximum cavity thickness have the same characteristics: they grow slowly but collapse slightly faster. The curves themselves are quite close to the sinusoidal curve, which reflects that the response of the cavity variation to the sinusoidal gust is close to linear. But it becomes more and more non-linear as the reduced frequency is increased to $K = \pi/2$ in Figure 7.4 and to $K = \pi$ in Figure 7.6.

The same is true for the variation of the cavity volume with time. The circles in Figure 7.3 represent the variation of the cavity volume with time, which collapses also faster than it grows. Especially the second time derivatives $\partial^2/\partial(\omega t)^2$ shows already strong non-linear response to the gust. This becomes stronger with the increasing reduced frequency in Figure 7.5 and Figure 7.7.

Since the pressure excitation from the unsteady cavity depends on the second time derivative (equation (7.8)), the higher harmonics of the pressure field can be more or less calculated even if we use equation (7.8). This is only because of the non-linear response of the pressure field to the gust.

The analysis of the pressure fluctuations from an unsteady cavity is beyond the scope of the present research and will not be calculated. But the harmonic analysis can be done for the cavity volume to show the capability of the present non-linear cavity flow theory in capturing higher harmonics of the cavity dynamics. This is plotted in Figure 7.8. It is obvious that when the reduced frequency is increased, the variation of the cavity volume with time becomes faster and hence the time derivatives of the volume become much larger. But Figure 7.8(c) shows that the second harmonic becomes larger than its first harmonic in (a) of the same figure, but still smaller than its first harmonic in (c). These harmonics are directly related to the pressure fluctuation through equa-

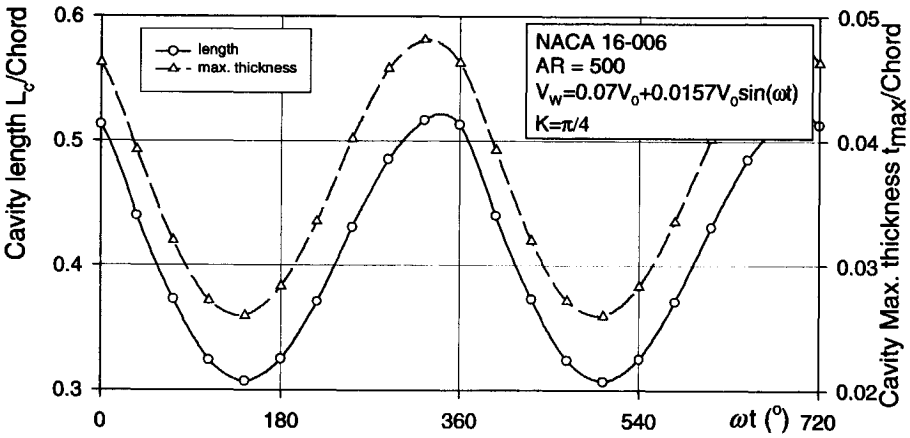

Figure 7.2: Cavity length and maximum thickness variation in time for a high aspect ratio hydrofoil in a sinusoidal vertical gust. (Aspect ratio AR=500, NACA16-006 section, vertical gust $V_W = 0.07V_0 + 0.0157V_0 \sin(\omega t)$, reduced frequency $K = \pi/4$, $\sigma = 1.0$.)

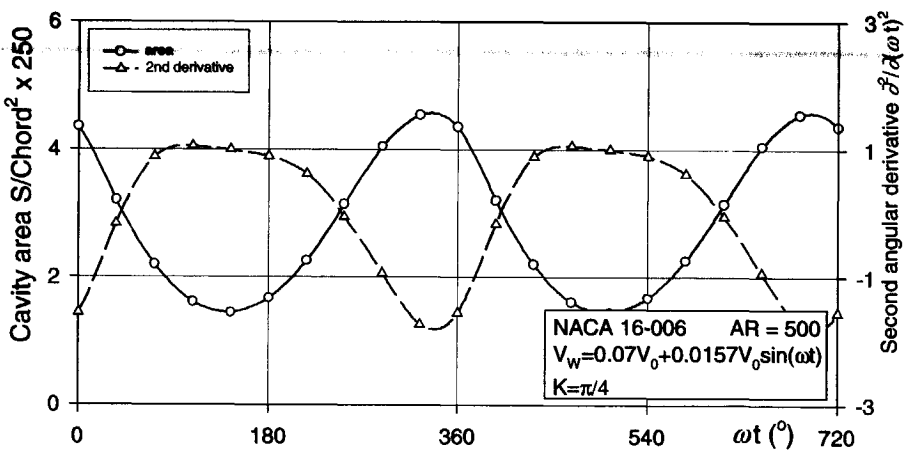

Figure 7.3: Cavity cross-sectional area and its second derivative in time for a high-aspect-ratio hydrofoil in a sinusoidal vertical gust. (Aspect ratio AR=500, NACA16-006 section, vertical gust $V_W = 0.07V_0 + 0.0157V_0 \sin(\omega t)$, reduced frequency $K = \pi/4$, $\sigma = 1.0$.)

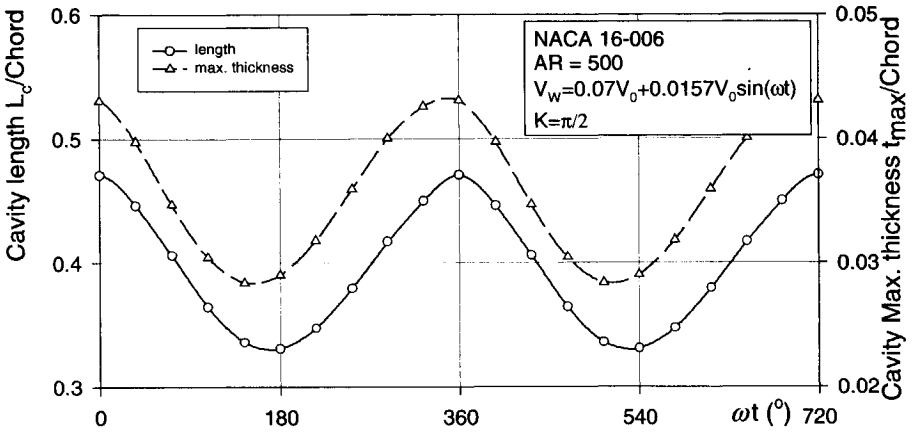

Figure 7.4: Cavity length and maximum thickness variation in time for a high-aspect-ratio hydrofoil in a sinusoidal vertical gust. (Aspect ratio AR=500, NACA16-006 section, vertical gust $V_W = 0.07V_0 + 0.0157V_0 \sin(\omega t)$, reduced frequency $K = \pi/2$, $\sigma = 1.0$.)

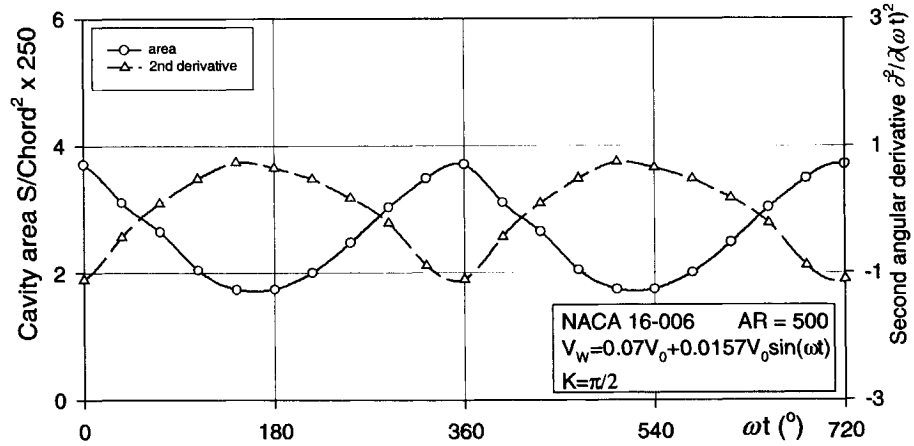

Figure 7.5: Cavity cross-sectional area and its second derivative variation in time for a high-aspect-ratio hydrofoil in a sinusoidal vertical gust. (Aspect ratio AR=500, NACA16-006 section, vertical gust $V_W = 0.07V_0 + 0.0157V_0 \sin(\omega t)$, reduced frequency $K = \pi/2$, $\sigma = 1.0$.)

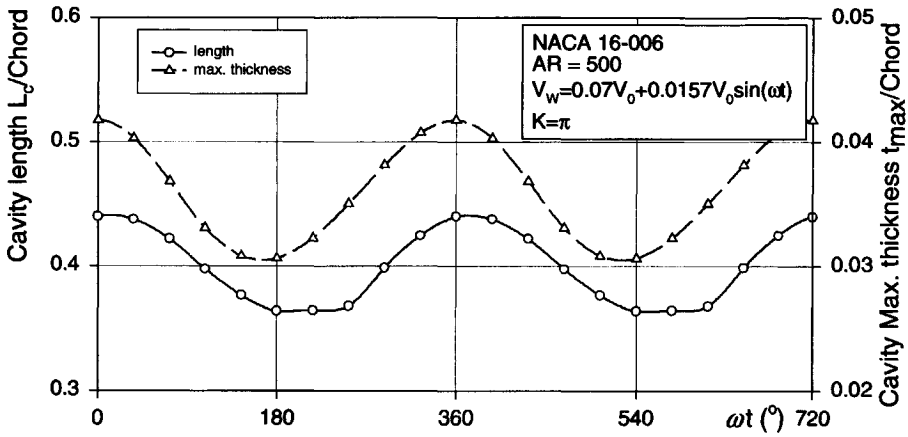

Figure 7.6: Cavity length and maximum thickness variation in time for a high-aspect-ratio hydrofoil in a sinusoidal vertical gust. (Aspect ratio AR=500, NACA16-006 section, vertical gust $V_W = 0.07V_0 + 0.0157V_0 \sin(\omega t)$, reduced frequency $K = \pi$, $\sigma = 1.0$.)

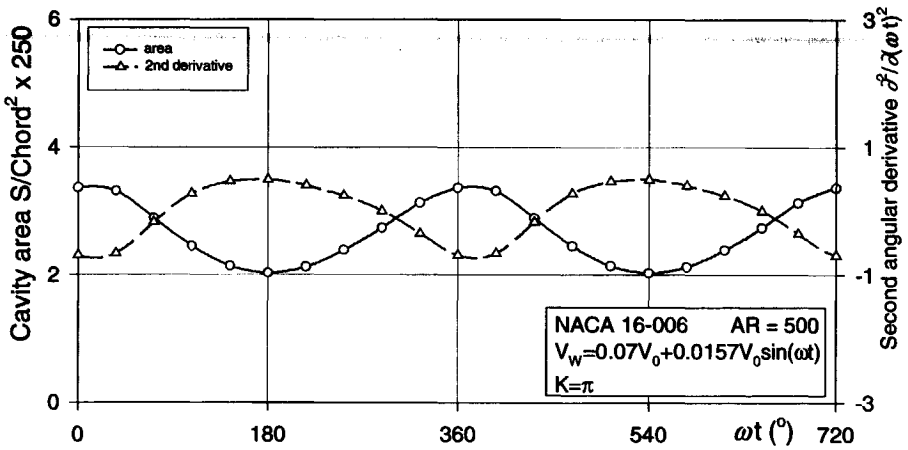

Figure 7.7: Cavity cross-sectional area and its second derivative variation in time for a high-aspect-ratio hydrofoil in a sinusoidal vertical gust. (Aspect ratio AR=500, NACA16-006 section, vertical gust $V_W = 0.07V_0 + 0.0157V_0 \sin(\omega t)$, reduced frequency $K = \pi$, $\sigma = 1.0$.)

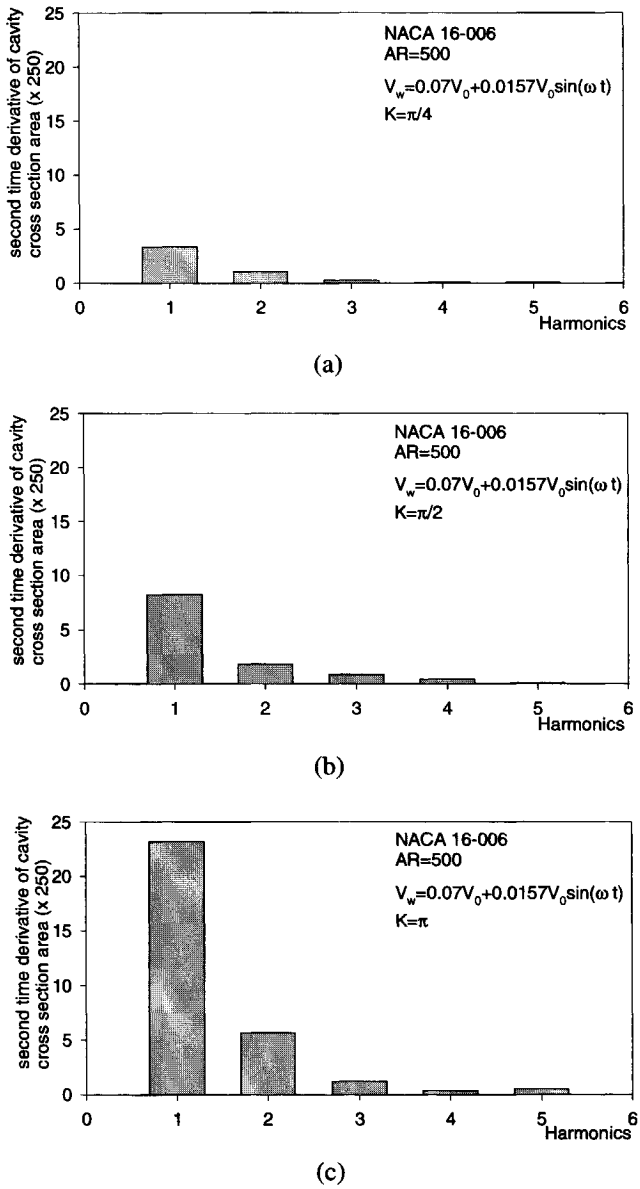

Figure 7.8: Spectrum of the second time derivative of the cavity cross-sectional area. (a) $K = \pi/4$; (b) $K = \pi/2$; (c) $K = \pi$. (NACA 16-006, AR=500, vertical gust $V_W = 0.07V_0 + 0.0157V_0 \sin(\omega t)$, $\sigma = 1.0$)

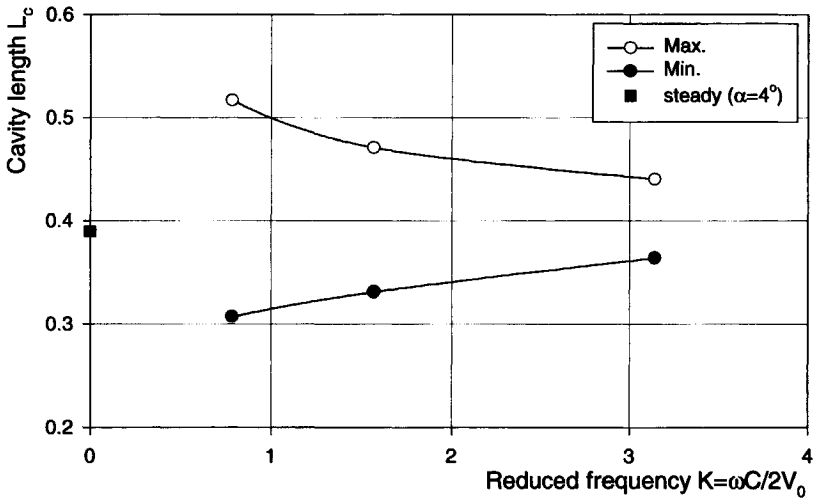

Figure 7.9: Influence of the reduced frequency on the cavity length. (NACA 16-006, AR=500, vertical gust $V_W = 0.07V_0 + 0.0157V_0 \sin(\omega t)$, $\sigma = 1.0$)

tion (7.8). But if detailed information of the cavity thickness variation is taken into account using equation (7.6), more contributions to the higher harmonic components of the pressure can be expected from the present unsteady cavity flow calculations.

With the same average vertical gust and the same amplitude of the gust variations as given in equation (7.10), the variations of the cavity extent are different at different reduced frequency K. The influence of the reduced frequency on the cavity extent variations are plotted in Figure 7.9, where the open circles represent the maximum cavity length while the solid circles represent the minimum cavity length. The steady flow result of the same section at an angle of attack of 4° from the two-dimensional calculations of Section 6.1.6 (or Table B.1), is plotted as the solid square, which is assumed to be the result at zero reduced frequency. This figure shows that the amplitude of the cavity extent variation reduces quickly as the reduced frequency increases. This has been observed by Shen & Peterson (1978) in their experiments with pitching hydrofoil as well, where they claimed that the cavity length observed for the stationary foil at the maximum angle of the oscillating foil is twice as long as the cavity length observed at a finite value of K (eg. K=1.2). The same results are also calculated by Van Houten (1983) in his numerical simulations.

Cavity flow in a sinusoidal pressure field

A situation specific for propeller cavitation is that the blades sections are traveling through a varying ambient pressure field due to the depth of water. An extreme example is when a huge propeller of 10 meters in diameter is rotating behind a ship in the sea. The variation of the static pressure at the tip of the propeller is roughly as large as one bar. So the effect of the ambient pressure variation on the cavity dynamics should also be investigated and will be carried out in the following.

We use the same hydrofoil as we used in the previous section with the same number of panels. The hydrofoil is set at an angle of attack of 4° and the ambient pressure variation is realized by the variation of the cavitation number in the onset flow. This variation is set to,

$$\sigma = 1.0 + 0.2 \sin \omega t. \tag{7.11}$$

As we expected, the response of the cavity length, cavity volume and cavity thickness variation to the sinusoidal pressure variation is non-linear. This is presented in Figure 7.10 and Figure 7.11. Two peaks of the second time derivatives of the cavity in one cycle are clearly seen in Figure 7.11. This results in a large second harmonic as shown in Figure 7.12, where the amplitude of the second harmonic is comparable to that of the first harmonic and the amplitude of the third harmonic is also considerable.

Cavity flow on different profiles

Because of their relatively flat pressure distribution at the suction side and their large cavitation buckets (Brockett (1966)), some of the NACA sections (e.g. NACA 16 and 6-series) have been extensively used for hydrofoils and propeller blades in the last decades. These NACA sections were originally designed for wing sections of airplanes and the design goals were either promoting laminar flow (NACA 6-series) or minimizing the compressibility bubble at high speed (NACA 16-series)(ITTC (1990)). No considerations have been given to delaying cavitation inception of these series when they were designed.

Since the introduction of Eppler's method for the design of sections for hydrofoils and propeller blades (Shen & Eppler (1981), Shen (1985)), new blade sections, considering cavitation inception and viscous effects, are continuously designed and applied for propeller blades (Kuiper & Jessup (1993), Yamaguchi *et al.* (1988), Dang *et al.* (1992), Stanier (1992)) in the last decades. Full-scale investigations showed that the new blade sections are quite promising in delaying both sheet cavitation and bubble cavitation (Kuiper & Jessup (1993)). Initially designed sections (such as YS9-series) have an extremely unloaded leading edge, which results in a leading edge with a larger leading edge radius and an almost symmetrically-shaped suction and pressure side. The chordwise

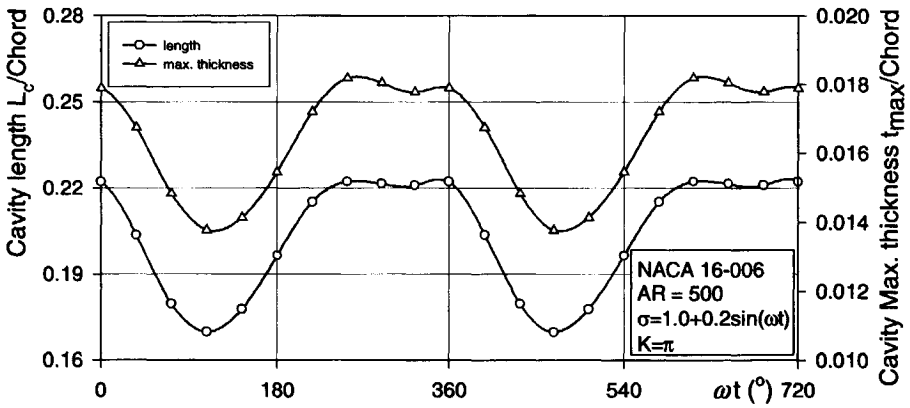

Figure 7.10: Cavity length and maximum thickness variation in time on a high aspect ratio hydrofoil in a sinusoidal pressure field. (Aspect ratio AR=500, NACA16-006 section, pressure field $\sigma = 1.0 + 0.2\sin(\omega t)$, reduced frequency $K = \pi$.)

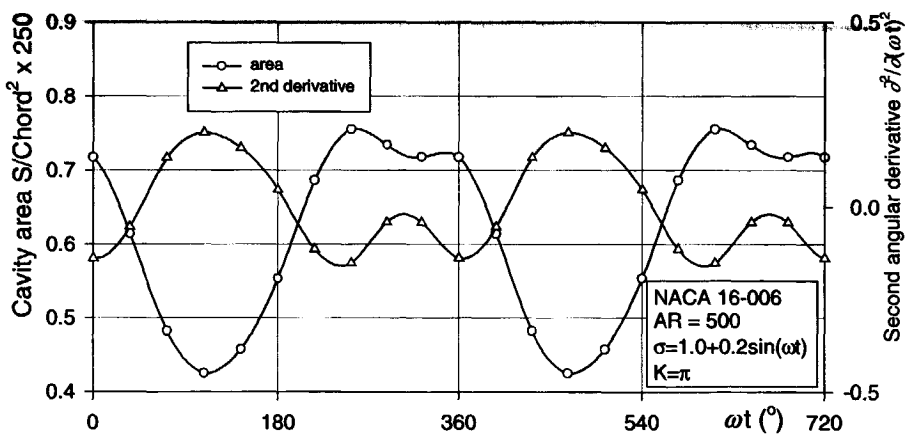

Figure 7.11: Cavity cross-sectional area and its second time derivative on a high aspect ratio hydrofoil in a sinusoidal pressure field. (Aspect ratio AR=500, NACA16-006 section, pressure field $\sigma = 1.0 + 0.2\sin(\omega t)$, reduced frequency $K = \pi$.)

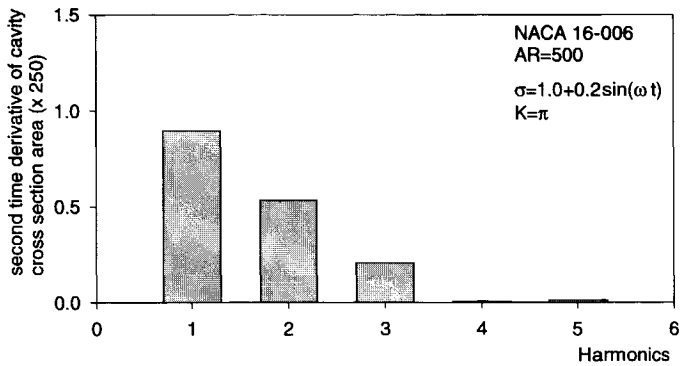

Figure 7.12: Spectrum of the second time derivative of the cavity cross-sectional area. (NACA 16-006, AR=500, pressure field $\sigma = 1.0 + 0.2\sin(\omega t)$, reduced frequency $K = \pi$.)

loading on the section is largely shifted towards the trailing edge, which results in a large positive camber in the aft end of the sections. But a design of a new section for a marine propeller shows a section that is totally different. It has a negative camber near the trailing edge (Kuiper & Jessup (1993)). It indicates that the new blade sections are no longer the sections like NACA section series, which have a definite thickness and camber distribution. On the contrary, it means any design that meets certain design requirements to fit specific inflow conditions.

But there is one question left for the new blade sections that have not yet been answered. Does the cavity vary more violently on a profile with a flat pressure distribution or on a profile with a more triangular pressure distribution? A part of the concern is that, when the pressure distribution is very flat, the cavity length becomes very sensitive to the pressure, which may lead to erosion.

We chose two extreme test cases. One is a NACA 66(MOD) section with a NACA $a = 0.8$ camber, which has a typical flat pressure distribution on the suction side. The other is a NACA 0006 section with a NACA $a = 0.0$ camber, which has an almost perfect triangular pressure distribution on the suction side. The thickness and the camber of both sections are set to 6% and 2%, respectively. The test is done in such a way that both sections generate the same lift with the same length of sheet cavity on the suction side. We chose the wetted lift for both sections as $C_L \approx 0.51$, where the angle of attack is 2.22° for the NACA 66(MOD) and 3° for NACA 0006. The cavitation numbers are set differently to make the cavity length more or less the same ($l/C \approx 0.5$).

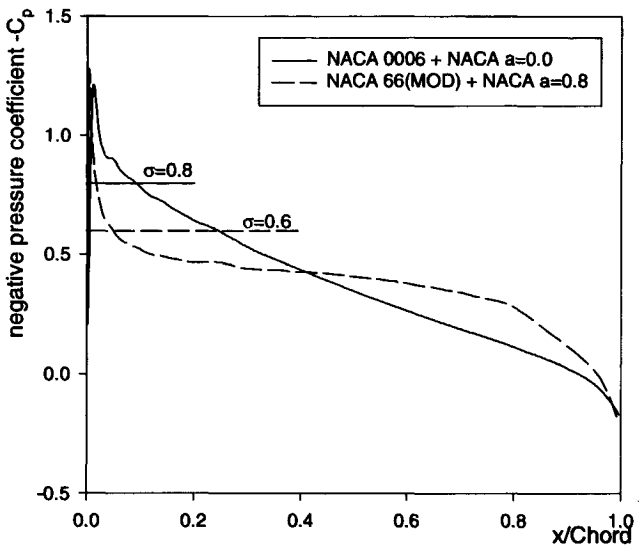

Figure 7.13: Comparison of the upper surface pressure distribution at fully wetted condition for NACA 0006 and NACA 66(MOD). ($t/C = 0.06; f/C = 0.02; \alpha_{NACA0006} = 3°; \alpha_{NACA66(MOD)} = 2.22°$)

The pressure distribution for the fully wetted flow is plotted in Figure 7.13. The cavity flow was calculated with the same panel arrangement as we used in the previous two subsections. The cavitation number σ is chosen to be 0.8 for NACA 0006 section and 0.6 for NACA 66(MOD). Both sections are placed in the vertical gust of the following form,

$$V_W = 0.0157 V_0 \sin(\omega t). \tag{7.12}$$

The comparison of the cavity length variation of the two sections is plotted in Figure 7.14. It is unexpected that the cavity length variation is even larger for the triangular pressure section than for the flat pressure section. But looking at the slope of the non-cavitating pressure distribution at the cavitation index, it can be seen that in this case the NACA 0006 was the flatter distribution and the NACA 66 was the steeper one. Since our investigation is limited as leading-edge partial cavity flow, the cavity thickness on the NACA 66 section with the flat pressure distribution is even larger than that on the triangular section. This brings the volume variation of both sections in the same range, as shown in Figure 7.15.

The comparison of the harmonics of the second time derivatives of both sections, up to the fifth order, is shown in Figure 7.16. It is surprising to find

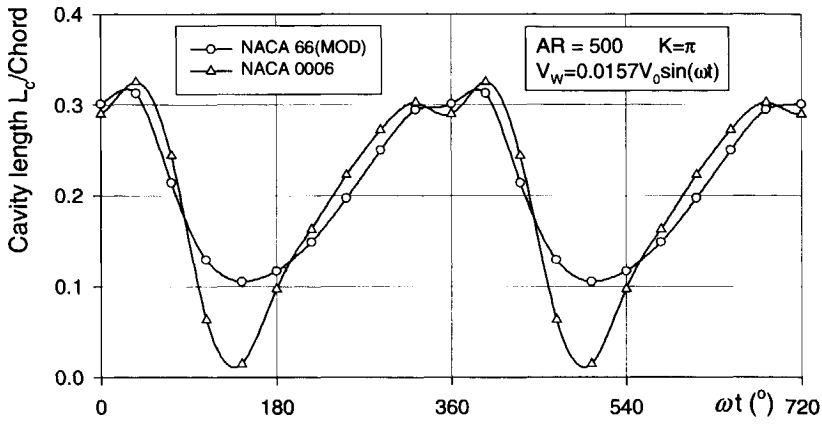

Figure 7.14: Comparison of the cavity length variations of NACA 0006 and NACA 66(MOD) in the sinusoidal gust.

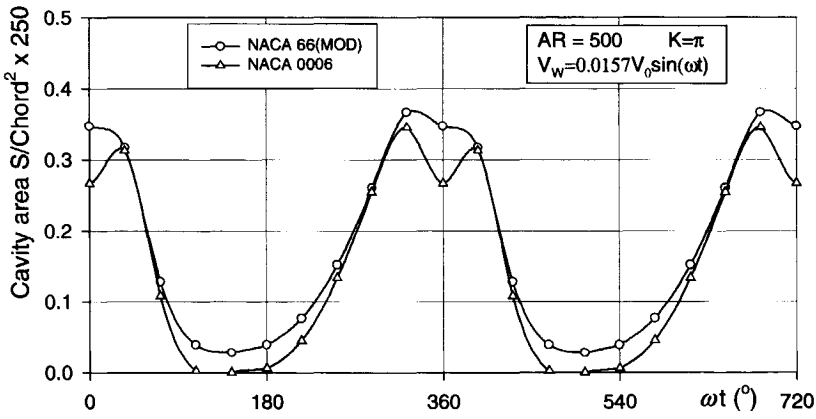

Figure 7.15: Comparison of the cavity volume variations of NACA 0006 and NACA 66(MOD) in the sinusoidal gust.

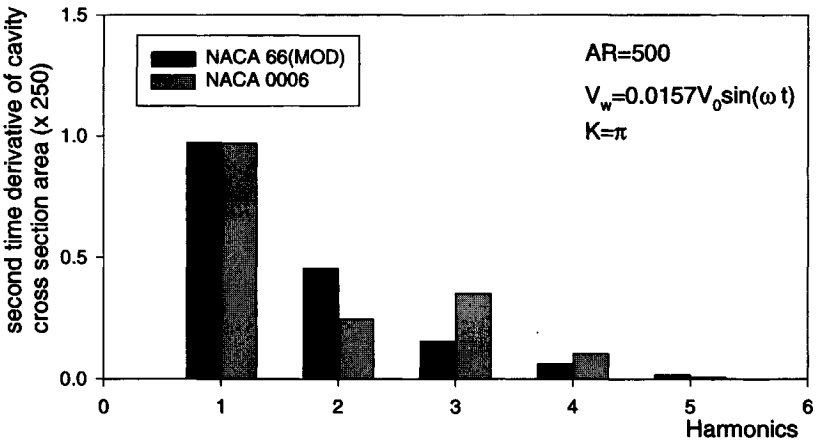

Figure 7.16: Comparison of the spectrums of the second time derivatives of the volume change for NACA 0006 and NACA 66(MOD) in the sinusoidal gust.

that the first harmonic is almost identical for both sections. There is a slight trend towards higher harmonics for the NACA 0006 with the more sensitive cavity length. It can be expected that the situation will be different when the cavitation index is closer to the value of the pressure coefficient in the flat pressure distribution. So it is not easy to generalize the effect of the pressure distribution on the higher harmonics.

7.1.2 Three-dimensional cavity flows

Using the same profile (NACA 16-006) as we used in the last section for the two dimensional investigation of the cavity flow simulation, we reduced the aspect ratio of the hydrofoil from 500 to 2. Then the flow becomes strongly three-dimensional. The results of the steady cavity flow calculation have been shown in Figure 6.28 of section 6.2.3. Here we chose $\sigma = 0.5$ for the present calculation.

The calculated cavity shape variation at the mid-span is shown in Figure 7.17. Compared to Figure 7.1, Figure 7.17 has almost the same cavity length but the cavity is thinner. This is due to the strong down-wash in this small aspect ratio hydrofoil, which reduces the effective angle of attack. The re-entrant jet at the cavity end is hardly predicted with the present number of panels. But the motion of the maximum thickness of the cavity can still clearly be seen.

The cavity extent variation during the gust at three different span locations

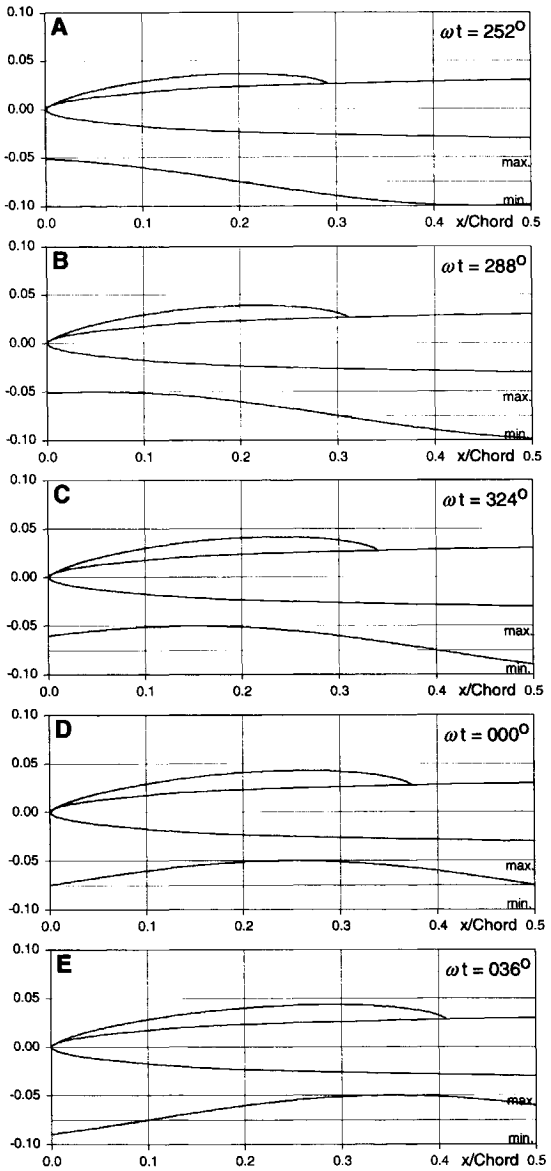

Figure 7.17: Motion of the cavity at the mid-span section of a rectangular hydrofoil in a sinusoidal vertical gust. (Aspect ratio AR=2, NACA16-006 section, vertical gust $V_W = 0.07V_0 + 0.0157V_0 \sin(\omega t)$, reduced frequency $K = \pi$, cavitation number $\sigma = 0.5$.)

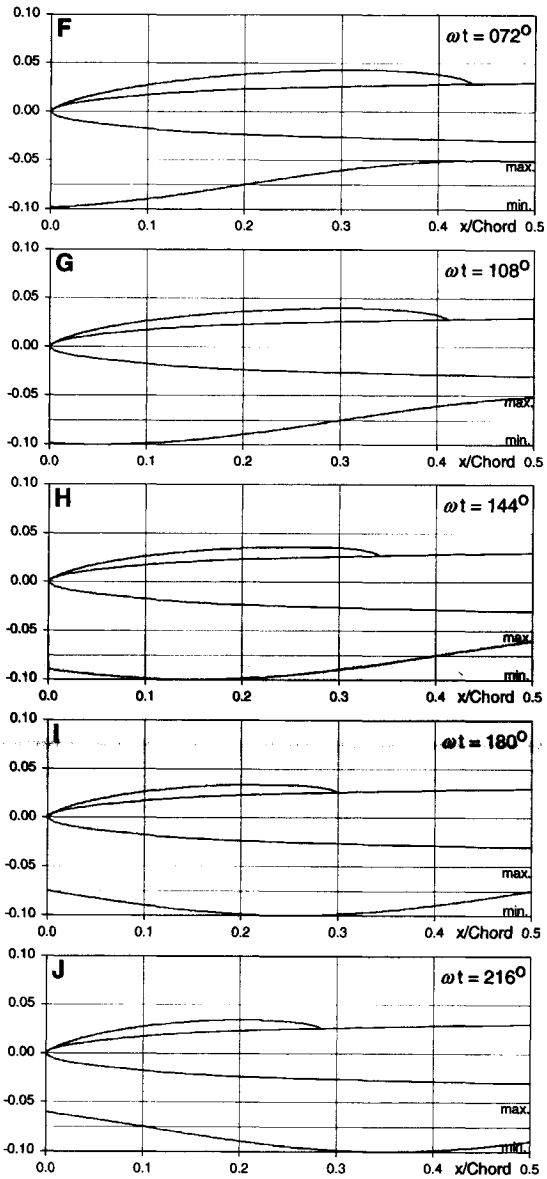

Figure 7.17: (continued) Motion of the cavity at the mid-span section of a rectangular hydrofoil in a sinusoidal vertical gust. (Aspect ratio AR=2, NACA16-006 section, vertical gust $V_W = 0.07V_0 + 0.0157V_0 \sin(\omega t)$, reduced frequency $K = \pi$, cavitation number $\sigma = 0.5$.)

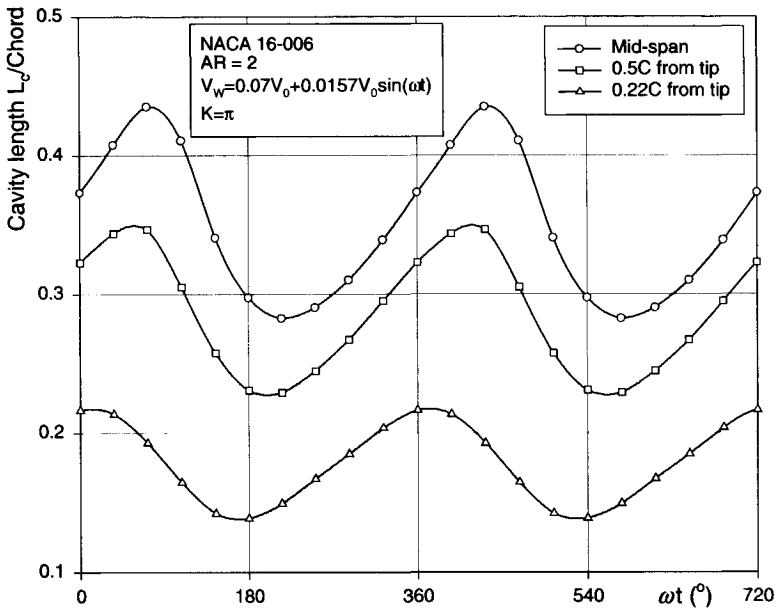

Figure 7.18: Cavity length variation in time on rectangular hydrofoil in a sinusoidal vertical gust. (Aspect ratio AR=2, NACA16-006 section, vertical gust $V_W = 0.07V_0 + 0.0157V_0 \sin(\omega t)$, reduced frequency $K = \pi$, cavitation number $\sigma = 0.5$.)

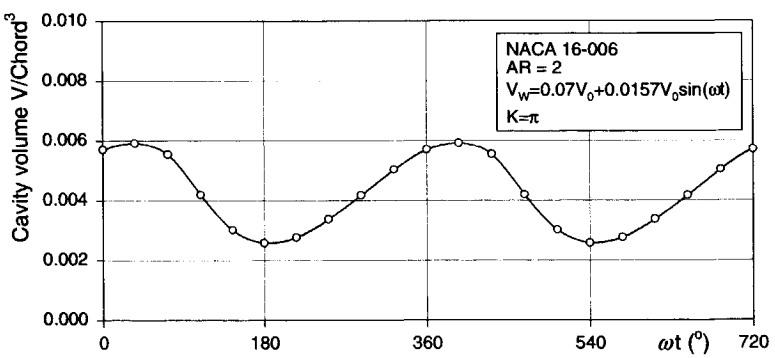

Figure 7.19: Cavity cross-sectional area variation in time on rectangular hydrofoil in a sinusoidal vertical gust. (Aspect ratio AR=2, NACA16-006 section, vertical gust $V_W = 0.07V_0 + 0.0157V_0 \sin(\omega t)$, reduced frequency $K = \pi$, cavitation number $\sigma = 0.5$.)

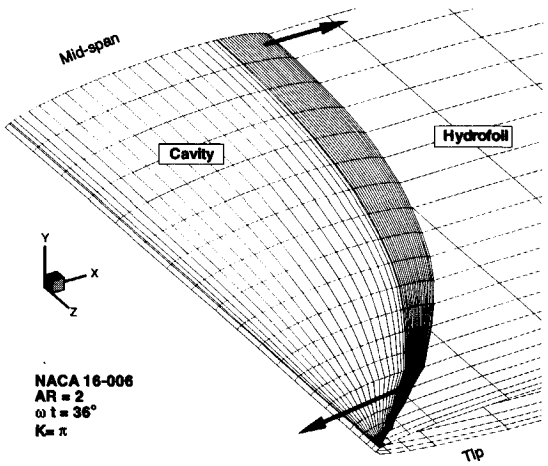

Figure 7.20: Predicted cavity motion on a rectangular hydrofoil in a sinusoidal vertical gust. (Aspect ratio AR=2, NACA16-006 section, vertical gust $V_W = 0.07V_0 + 0.0157V_0 \sin(\omega t)$, reduced frequency $K = \pi$, cavitation number $\sigma = 0.5$.)

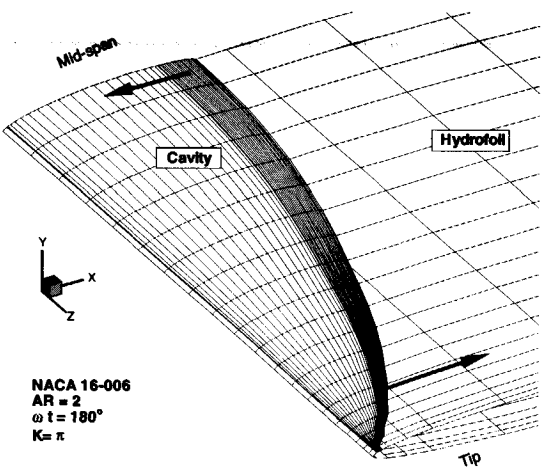

Figure 7.21: Predicted cavity motion on a rectangular hydrofoil in a sinusoidal vertical gust. (Aspect ratio AR=2, NACA16-006 section, vertical gust $V_W = 0.07V_0 + 0.0157V_0 \sin(\omega t)$, reduced frequency $K = \pi$, cavitation number $\sigma = 0.5$.)

is presented in Figure 7.18. It is quite clear that the cavity extent has a slow growth and a faster collapse. This feature is stronger at the mid-span section than for the section close to the tips. 60% of the time in a cycle is used for the growth of the cavity while 40% of a cycle is used for the collapse. This is also true for the cavity volume as shown in Figure 7.19.

Another interesting finding is that there is a phase shift for the cavities at different span positions (Figure 7.18). The cavity at the mid-span grows and collapses later than the cavity close to the tips. This phase difference is as large as 90°. This means that when the cavity at the mid-span is still growing up to the maximum cavity length, the cavity at the tip is already shrinking (as shown in Figure 7.20). In another extreme when the cavity at the mid-span is still shrinking towards the minimum length, the cavity at the tip is already growing (as shown in Figure 7.21).

As we have discussed at the beginning of this chapter, this kind of strong three-dimensional, out-of-phase motion is believed to generate higher values of the higher harmonic components.

7.2 Propeller flows

The present research should finally lead to the prediction of unsteady cavity flow on propeller blades and the prediction of the pressure fluctuations due to this cavitation on ship hulls. Extensive verification and validation has been carried out in the previous sections for steady and unsteady hydrofoil flows, and also for steady propeller cavity flows. The unsteady cavity flow on propeller blades is addressed in this section on the same propeller as we used in Section 6.3 — the *S Propeller*.

There are only few publications available on the validation of panel codes for propeller cavity flows, and almost no reliable experiments are available. A numerical verification was done by Kinnas & Fine (1992) for only a one-bladed pseudo-propeller in an artificial symmetric wake peak at 12'oclock position. The results show that the cavity volume variation gives a linear response to the wake field. No validation has been done in their paper for a real propeller in a non-uniform wake field. Kim & Lee (1996) validated their method by comparing their calculation with the experimental results from the HYKAT. The predicted extent of the cavity agrees reasonably well with the experiments.

As in the validation of the steady cavity flow calculation, we prefer to start the calculation from some fundamental case before we can apply the present method to a cavitating propeller in a real ship wake.

An ideal experimental result from Kuiper (1984), carried out in the cavitation tunnel at MARIN in the 80's, was chosen for our present validation. The wake peak was generated by mounting a foil with a chord of 30cm upstream of the propeller. By putting the propeller at two different downstream positions

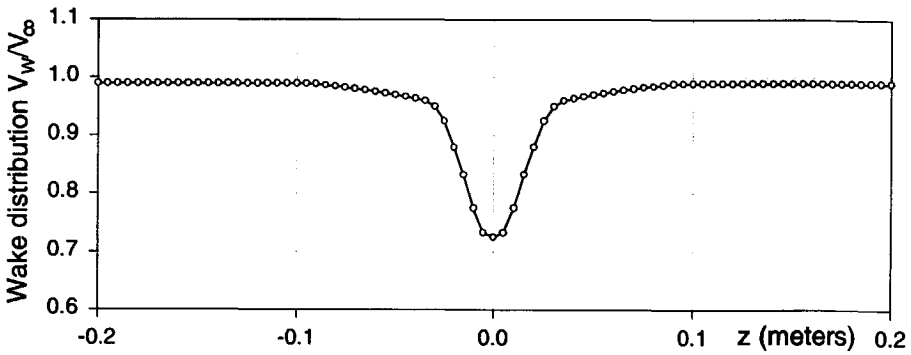

Figure 7.22: 27% peak wake.

and by using smooth and roughened surfaces for this foil, four different wake peaks were generated, 8%, 12%, 18% and 27% of the velocity reduction to the uniform inflow at the peak. The profile is a NACA 66-021 symmetric section.

The *S Propeller* is chosen to operate in this wake. The unsteady cavity flow tests were carried our at two different advance ratios, $J = 0.4$ and $J = 0.6$. The cavitation numbers σ_n are chosen to be 0.92, 3.00 and 0.92, 1.65, respectively. In total, 16 different combinations of the conditions are tested. From all of these tests, the test with $J = 0.6$ and $\sigma_n = 0.92$ was chosen for the present validation. The wake peak is chosen to be 27% as shown in Figure 7.22. At this condition, the cavity on the blade remains a partial cavity during the whole revolution, but varies violently when the blade is passing through the wake peak. The purpose of this validation focuses not on the details of the cavity shape, but mainly on whether the present method can capture the dynamic motion of the cavity in the wake.

The tunnel wall can be simulated simultaneously by the present panel method, but the following calculations are carried out in an unbounded flow field, for the sake of reducing the computational effort. From the experiments, the influence of the tunnel wall was found to have an effect of 5% increase on the advance ratio (Kuiper (1984)). Hence the calculation is carried out at an effective advance ratio of $J = 0.62$ to account for the wall effects.

In order to save computing time, except for the key blade, the other three blades are discretized with a relatively coarse grid ($N_c \times N_s = 12 \times 15$). On the key blade, we used $N_c \times N_s = 25 \times 30$ on one side of the blade. The cavitation is only calculated on the key blade. The other blades are treated as fully wetted. This simplification is assumed to have a minor effect on the cavity on the key blade.

When a 5° step in revolution is chosen for the calculation, 120 wake panels

in stream direction are generally needed to form a wake that is as long as two times the propeller diameter for this propeller at $J = 0.6$. This wake length has been found to be the minimum wake length for fully wetted and cavitating propeller flows for most cases.

The calculated variation in cavity extent, when the key blade is passing through the sharp wake peak at 12 o'clock position, is presented in Figure 7.23. It is concluded from this figure that:

1. When the blade is outside of the wake peak, as shown at $+30°$ position in this figure, the cavity is restricted to the mid span with a maximum length approximately 50% of the chord length.

2. When the leading edge of the blade enters the wake peak, as shown at $-30°$, the cavity grows both in radial direction toward the tip and slightly in the chord direction.

3. The cavity grows towards the tip of the blade from $-30°$ to $-5°$, where the cavity covers most of the mid-span and the tip region of the blade.

4. At $0°$ position, because the leading edge of the blade leaves the wake peak, the cavity suddenly collapses in the tip region. After this collapse, the cavity extent shrinks gradually to the extent outside the wake peak.

The details of the cavity extent at certain angular positions are drawn and compared in Figure 7.24 together with the experimental observations. Except for the cavity very close to the 12 o'clock position, where the cavity extent is predicted too large, the cavity extent outside of the peak agrees quite well with the experiment. The important feature of the cavity collapse, when the leading edge is leaving the peak at 12 o'clock, is predicted by the present simulation (from $-15°$ to $0°$). The cavity collapse in the tip region at $0°$ is not simulated, because the detachment of the cavity in the simulation is fixed at the leading edge. In the experiment, when the blade enters the wake peak (from $-60°$ to $-10°$), the cavity thickness is increasing dramatically but the maximum length is not. The calculation seems to have over-predicted the cavity length. When the blade leaves the wake peak (from $0°$ to $+30°$), the cavity at mid span becomes quite long and thick in the experiment. But the calculation under-predicts the cavity length.

The cavity volume change within one cycle is plotted in Figure 7.25. The predicted total cavity volume in the present case shows a very quick increase but a relatively slow decreasing, even when the cavity close to the tip shows an abrupt collapse. The reason is that the cavity close to the tip is very thin. So it has only a minor contribution to the total volume. The cavity at the mid-span is dominant in the cavity volume. The cavity thickness in the collapsing stage at mid-span becomes much thicker than the cavity at the growing stage (comparing the photo at $+15°$ to the photo at $-15°$).

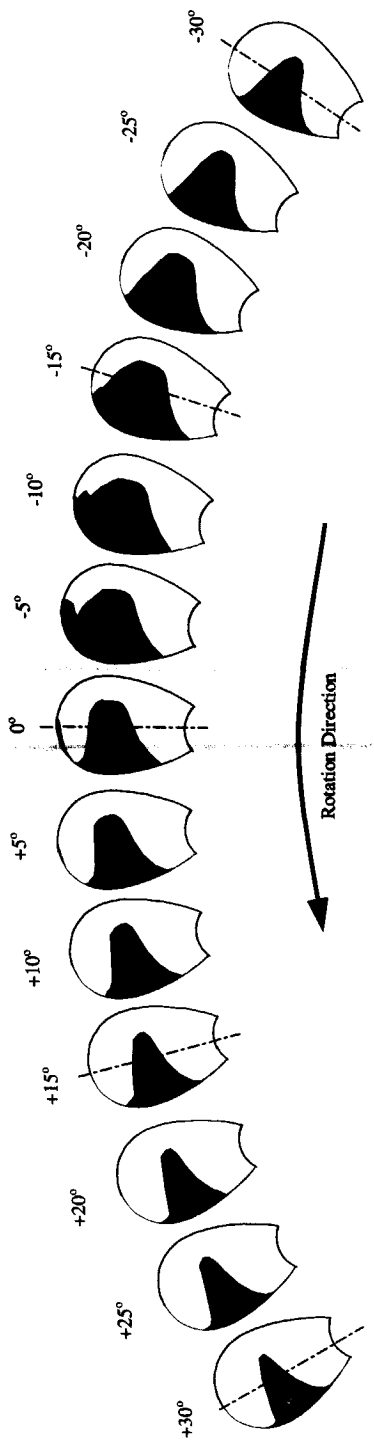

Figure 7.23: The predicted cavity extent variation when the key blade is passing through the sharp wake peak. (*S Propeller* Kuiper (1981) $J = 0.6$, $\sigma_n = 0.92$)

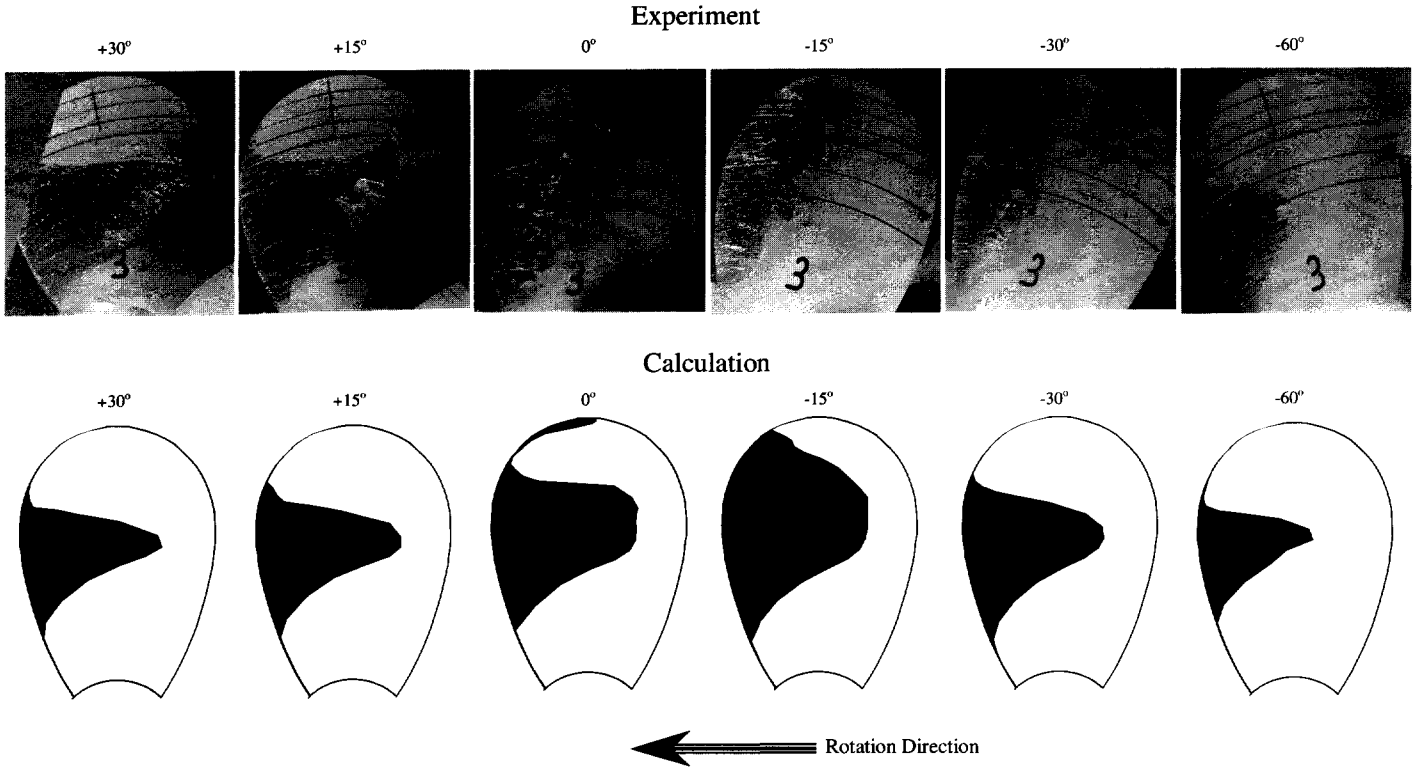

Figure 7.24: Comparison of the calculated cavity extents with the experimental observations (Kuiper (1981)) in the sharp wake peak. (*S Propeller* $J = 0.6$; $\sigma_n = 0.92$)

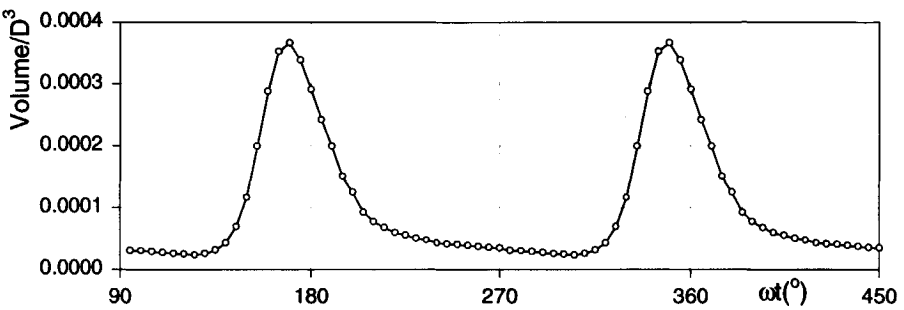

Figure 7.25: The cavity total volume change when the key blade passes through the sharp wake peak. ($J = 0.6$, $\sigma = 0.92$)

7.3 Conclusions

The present computational method has been successfully applied in this chapter to the simulation of the unsteady cavity flow both on hydrofoil surfaces and on propeller blades. The results show that the main dynamic features of the unsteady cavity flows are captured by present calculation method. Simple verification and validations are carried out, which show that the present method can be expected to predict unsteady cavity flow on the propeller blades effectively.

Two-dimensional unsteady cavity flow in a sinusoidal gust shows a nonlinear response of the cavity shape to the gust. The maximum thickness of the cavity moves towards the end of the cavity as the cavity is growing. This effect becomes stronger when the reduced frequency of the gust is increased. The reentrant jet can be clearly seen at the end of the cavity when the cavity length reaches the maximum length in a cycle and at the early stage when the cavity starts to shrink, but is not found for the rest of the cycle. This is in accordance with the observation in the experiments. The amplitude of the cavity length and cavity volume variation is found to decrease with the increase of the gust frequency.

A three-dimensional calculation of cavity flow on a hydrofoil with a small aspect ratio shows the basic features of slow growth and faster collapse of a cavity in terms of both cavity length and cavity volume. Phase angle differences for the cavities at different span positions are also found. For a rectangular hydrofoil at a reduced frequency up to $K = \pi$, the phase difference between the cavity length at the mid-span and the cavity length at the tip can be as large as 90°.

The prediction of the cavity flow on propeller blades in a sharp wake peak shows that the present method can capture the important feature of growth and collapse of the cavity, but the calculated cavity extent is generally longer than that of the observations. Further validation is needed in the future before this method can be practically used for the prediction of the characteristics of cavitating propellers.

Chapter 8

Experiment and Validation

A benchmark test is now being carried out in the cavitation tunnel of Technical University Delft on a twisted transparent hydrofoil. The test setups and the test procedure are described in the following. Some preliminary results are obtained and given in this chapter. Comparisons are made between the experimental results and the calculations. Good agreement is found.

It is necessary to validate the present numerical method with experiments before we are confident about the results of the calculations. The simple validations we have carried out in the previous chapters (in Section 6.1.6, Section 6.2.5 and Section 7.2) are not sufficient. The validation should consist of not only the cavity extent (contour in three-dimension), but also the cavity thickness distribution, and even, the re-entrant jet direction and the re-entrant jet thickness. Validation for unsteady cavity flows is even more important than for steady flows. To the knowledge of the author, there is still no reliable test result available even for steady cavity flows. Although some tests and measurements have been conducted and published in the previous decades, those tests were either performed for a two-dimensional profile (Shen & Dimotakis (1989*a*), Shen & Peterson (1978)), for a three-dimensional hydrofoil (Kinnas & Fine (1993)) or for a complicated propeller blade. Some measurements of the cavity length have even been carried out in an unsteady situation (Hsu & Shen (1988)). But all the results are not accurate enough to serve as a bench mark for the present validation. The two-dimensional steady cavity flow tests show unsteady results due to the impinging of the re-entrant jet on the cavity surface and the constant shedding of the cloud. The three-dimensional hydrofoil and propeller tests do not provide the basic structure that we can use to validate the present numerical simulation.

Moreover, due to the difficulties of the measurement of the cavity thickness,

only the cavity extents are always measured. The measuring techniques for cavity thickness are still developing. A pin-gauge method is widely used for two-dimensional cavity flows and also for propeller sheet cavitation. Some very preliminary trials have even been attempted for full-scale propellers in sea trials, but very limited data are available. The drawback of this method is quite obvious: the pins interfere with the flow and the cavity surface and hence change the flow itself. Furthermore, installing the pins on the surface is not easy and mostly they are lost during the test, or they catch drifting rubbish and frustrate the test completely. Other methods like stereo photography has been also developed for these measurements. Unless it can be automated, it takes too much time and labor to analyze the results. A method using laser beams has been tried recently for cavity flows as well. It is very promising and will be considered in the present experiments. The application of this method to the measurement of the cavity thickness on a propeller has been shown successfully by Ukon *et al.* (1991).

With the support of Maritime Research Institute Netherlands (MARIN), a bench mark test is being carried out in the cavitation tunnel of Technical University Delft. A twisted rectangular hydrofoil has been designed to generate a distinct and stationary cavity on most part of the hydrofoil. Plexiglas is used so that the profile is transparent and the re-entrant jet can be easily observed from the bottom of the hydrofoil. A laser beam will be used to measure the cavity thickness distribution along both the chord and the span. Unsteady cavity length and thickness measurements for this hydrofoil in a gust is planned. The gust will be generated by placing two small oscillating fins in front of the hydrofoil in the tunnel, as is presently being pursued at Chalmers University of Technology by Schöön (2000). Presently only some preliminary steady inflow observations are available for comparison.

8.1 Experiment Setups

8.1.1 The tunnel

The cavitation tunnel at Technical University Delft is a *Kempf und Remmers* closed re-circulation tunnel with a square test section of 0.3×0.3 square meters and 0.6 meters long as shown in Figure 8.1. The highest water speed in the test section is $7m/s$. The tunnel is driven by a 4-bladed axial impeller with *Ward Leonard* control. The power of the motor is up to $15Kw$ at a speed of revolution of $2920rpm$. The pressure at the test section is adjustable from 102 kPa (maximum) to 11 kPa (minimum), which suits most of the cavitation test on hydrofoils and propeller blades.

The velocity at the test section is measured by the pressure drop of the contraction, which is calibrated in advance. The water is deairated by running

Figure 8.1: The test section of the cavitation tunnel at Technical University Delft with the twisted transparent hydrofoil installed.

the water at low pressure with a free surface for half a day. The air content is measured by a *Van Slijke* apparatus and maintained at 0.85% during all of the runs.

The static pressure at the test section is adjusted by a vacuum pump and the pressure relative to the atmospheric pressure is measured by a U-shaped mercury tube. The cavitation number of the test is calculated by equation (1.1).

8.1.2 The twisted hydrofoil

In order to represent a typical propeller blade and to control the cavity and its re-entrant jet in a restricted area, a specific twisted hydrofoil has been designed for this test. The profile of the hydrofoil is chosen to be NACA four digits profile with a representative thickness to chord ratio of 9% (with zero camber). The hydrofoil is twisted in such a way that the loads at its two tips are zero, while the load is high at the mid-span with a sharp leading edge suction peak. This twisting is done by rotating the profile around its mid-chord point to a certain designed angle of attack. A relatively thick sheet cavity can be expected to start from the leading edge.

After an estimate of the cavity flow by the present numerical method, the angle of attack at the tips was set to $-1°$ and the angle of attack at the mid-span was set to $+7°$. The wall effect is fully taken into account by putting

panels on all the walls and on the inlet- and outlet-plane of the calculation domain. A third order-polynomial is used to obtain a smooth distribution of the twist,

$$\alpha = 7^\circ - 24^\circ|z/z_{max}|^2 + 16^\circ|z/z_{max}|^3, \tag{8.1}$$

where z is in span direction as shown in Figure 6.20 and z_{max} is the half of the span.

Due to this twisting, the cavity extent is expected to increase from zero at the tip to a certain length at mid-span at a given cavitation number. Due to this change of the cavity length over the span, the re-entrant jet is expected not to impinge on the cavity surface in the upstream but turns to a direction along the span. Finally it finds an exit at the mid-span section only. Except for the cavity at the mid-span, on most part of the hydrofoil the cavity can be expected to be stationary in most test cases.

The hydrofoil is made of Plexiglas. The size of the hydrofoil is $150mm$ in chord and $300mm$ in span. The surface is milled by the new computer controlled milling machine at MARIN and then polished by hand. The deformation of the hydrofoil under lifting force during the test has been estimated. Due to the twisting of the foil, the deformation is negligible when the water speed is less than $6m/s$. Because of its transparency property, the cavity on the hydrofoil can be observed on both sides of the foil. It makes the observation of the re-entrant jet much easier.

In order to reduce the scale effect as much as possible, roughness is applied at the leading edge of this hydrofoil. These are carborundum grains with a size of $60\mu m$. The roughness is glued on the back of the foil around the minimum pressure position of the foil with a width of $5mm$ which starts $3mm$ downstream of the leading edge at a place very close to the location of the minimum pressure point on the profile. This roughness makes the boundary layer turbulent all over the surface and prevents spot cavitation to occur. Hence we can have a nice sheet cavity on the suction side of the foil.

8.1.3 Procedure and Photographing

During the whole test, the static pressure at the test section of the tunnel was kept constant (−644mmHg) relative to the atmospheric pressure. The atmospheric pressure was measured during each run. The cavitation number is changed by changing the velocity of the water in the test section. The tests were done for five different angles of attack. All the test conditions are listed in Table 8.1. On average, six photos were taken for each condition.

A *Nikon F301* camera with an objective of *Sigma 90mm* was used for photographing during the test. Two stroboscopes were used for the illumination of the object from the top and the side. While taking the photos, the test

Table 8.1: The test conditions for the twisted transparent hydrofoil.

	Angle of attack at the tips α				
V (m/s)	-2°	-1°	0°	+1°	+2°
4.1				×	×
4.3	×	×	×	×	×
4.6	×	×	×	×	×
4.8		×	×	×	×
5.1	×	×	×	×	×
5.3		×	×	×	×
5.6	×	×	×		
5.8	×				
6.1	×				

× the photo was taken at this condition

section was covered with a simple black tent. The shutter was switched on first by hand-timer and then the light was triggered once to make the exposure of the film. Different positions of the lights have been tried and the best position was determined by the quality of the photos and maintained during all of the test runs.

8.2 Experimental Results

As we did expect, the scale effect was very strong when the roughness was not applied. Because of the twisting of the foil, the suction peak at the mid-span decreases towards the tip. When the peak is lower than a certain value at a certain span position, the laminar boundary layer no longer separates and hence no sheet cavity was observed at this position. The cavity sheet stops suddenly towards the tip and the cavity is restricted to the mid-span. Because of its special topology, some vortex systems were generated, which influence the formation of cloud cavitation in a specific way. This has been observed and analyzed extensively by Foeth (2000) in Ann Arbor, Michigan.

When the angle of attack is low (say $-1°$), this sheet cavity becomes a series of spot cavities at mid-span accompanied with bubble cavitation at both sides. When the angle of attack is very low (say $-2°$), only bubble cavitation was observed.

The scale effect can easily be reduced by applying roughness at the leading edge to promote sheet cavitation. The mechanism of the roughness (see Kuiper (1981)) will not be discussed here, but the basic idea is to generate sheet cavitation inception when the pressure is at the vapor pressure. When the roughness is sufficiently small and sufficiently widely distributed (Ligtelijn

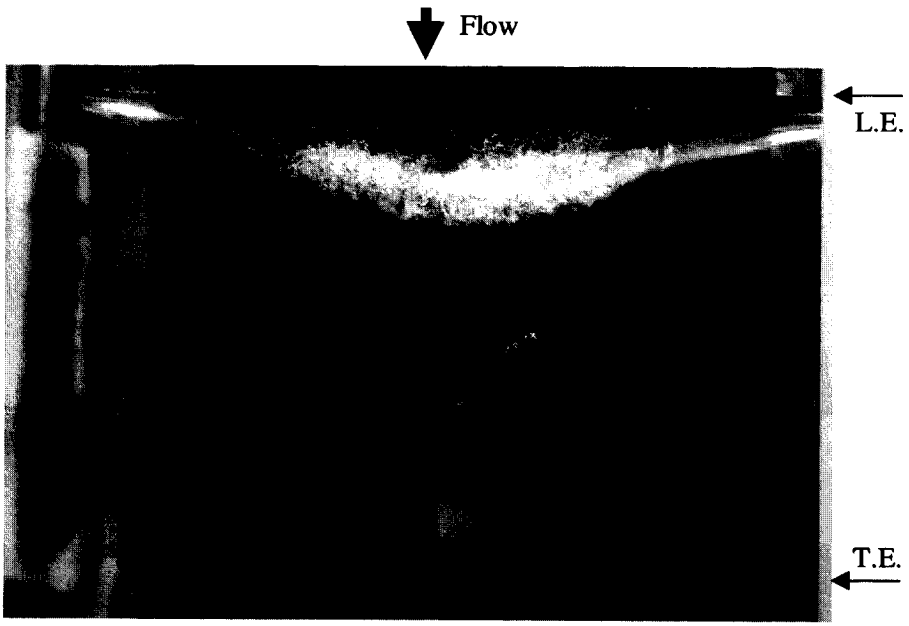

Figure 8.2: Observed cavity on the twisted hydrofoil in the cavitation tunnel. (angle of attack at the tips $\alpha_{tip} = -1°$; $V_0 = 5.1m/s$; cavitation number $\sigma = 0.979$)

& Kuiper (1983)), the pressure distribution should not be affected by the roughness. One of the typical photos of cavity flow with leading edge roughness is shown in Figure 8.2, which gives a top view of the cavity with the flow in the direction from the top of the page to the bottom of the page. The leading edge and trailing edge are indicated in this figure. A nice sheet cavity was formed in most part of the cavitating area, except very close to the sides of the sheet where spot cavities can be observed. This indicates that the roughness close to the right side of the hydrofoil is not sufficient. In this photo, the roughness on the left side has been applied better.

The experiments are still being performed and the measurement of the cavity thickness and the observation of the unsteady cavity flow in a gust have not yet been completed. Some selected results at the design condition ($\alpha = -1°$) are listed in Appendix C. The cavity length at different cavitation numbers are then measured from these photos and presents in a figure in the next section, where the calculations are compared with the experimental results.

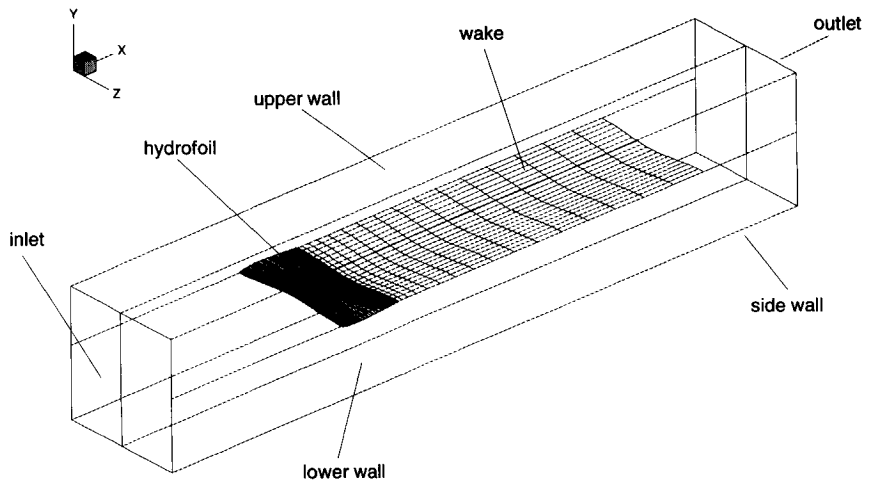

Figure 8.3: Schematics of the numerical cavitation tunnel and the discretization of the hydrofoil and its wake in the tunnel.

8.3 Comparisons

In order to include all the possible effects from the tunnel walls, the calculations were carried out in a numerical cavitation tunnel as sketched in Figure 8.3. The tunnel walls consist of three parts, the top wall, the bottom wall and the side wall. The side wall is split into two parts, the upper and lower wall, at the intersection of the foil and the wall. An inlet- and an outlet-plane are also introduced to guarantee a uniform inflow and a uniform out flow.

The twisted hydrofoil is placed at the center of the tunnel with two tips connected with the wall. The wake from the trailing edge of the foil is parallel to the top and bottom walls. The wake is cut off at a sufficiently long distance from the trailing edge before the outlet. This cutting-off is expected to have minor influence on the flow at the hydrofoil. And because of this, the flow at the outlet can be simply treated as a uniform flow. The discretization of the foil surface and the wake is shown in Figure 8.3.

The impenetrable condition of equation (2.24) is applied on all tunnel walls. To guarantee a uniform and constant axial flow at both the inlet and the outlet, the following condition was applied,

$$\frac{\partial \varphi}{\partial n} = 0. \tag{8.2}$$

The discretization of the tunnel walls and the inlet and outlet is shown in

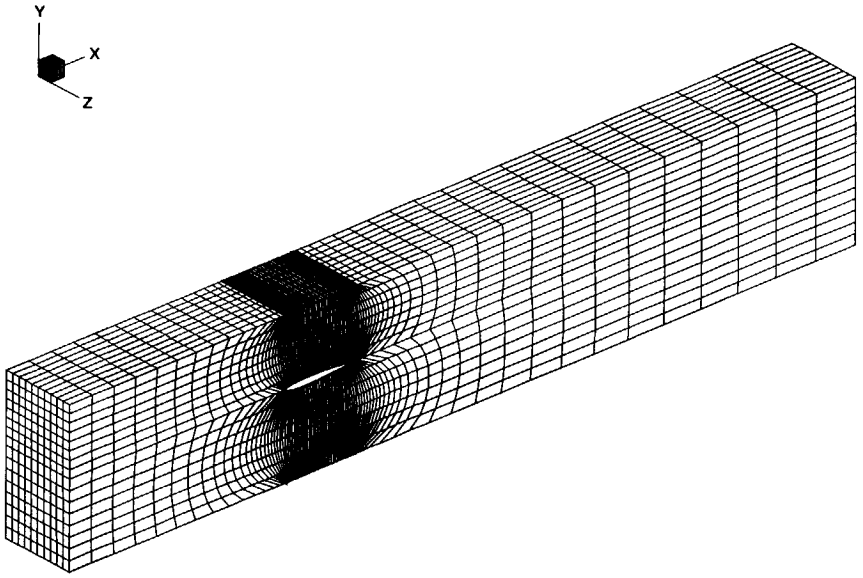

Figure 8.4: The discretization detail of half the tunnel walls and its inlet and outlet. (the example is given when the foil's angle of attack at the tip is 0°.)

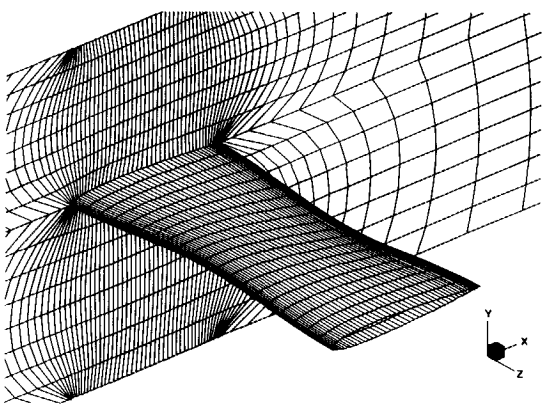

Figure 8.5: The discretization details of the intersetion of the foil and the tunnel side wall. (the example is given when the foil's angle of attack at the tip is 0°.)

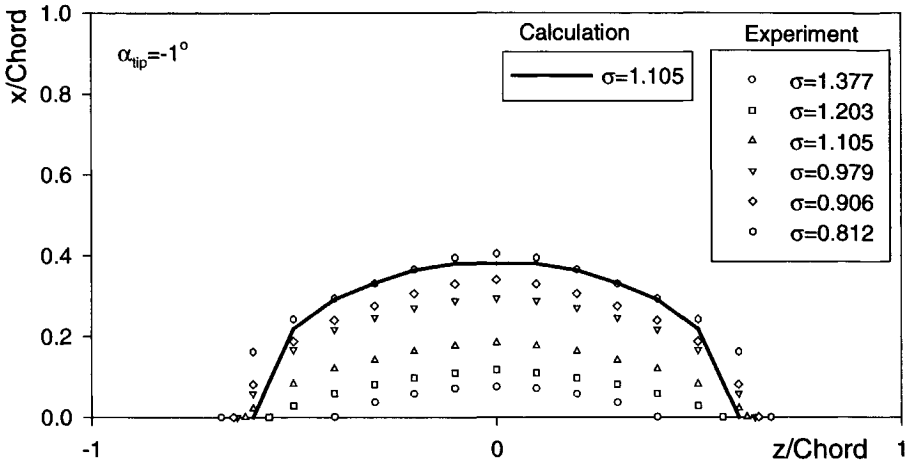

Figure 8.6: Comparison of the calculated cavity extent and the one measured in the cavitation tunnel. (the angle of attack $\alpha = -1°$)

Figure 8.4. The details of the intersection of the foil and the side wall are shown in Figure 8.5. Due to the symmetry of the flow, only half the system was taken into account for the numerical calculations.

In chord direction, 50 panels were used around the foil from the trailing edge on the face to the leading edge and from the leading edge to the trailing edge on the back. In steady flow, there is no need to use a very fine grid for the wake because the singularity distribution of the wake will remain constant on each strip. Seventeen panels were used in chord direction. On the cavity surface, 30 panels were used in chord direction. The number of panels in span direction has been kept the same at the foil, the wake and the cavity. Over half the span 10 panels have been used.

In order to take the wall effect accurately into account, a relatively fine grid was used close to the foil on the tunnel wall (Figure 8.4). On whole wall, 60 panels have been used in the flow direction and 10 or 16 panels in lateral direction. The panels on the inlet and outlet surface are matched with the panels on the side walls. In total, 2980 panels have been used in this computation.

The calculated cavity extent is compared with the experimental result in Figure 8.6, where the symbols are experimental results and the solid curve is the calculated. Only on of the calculated results is shown here since the others have the same deviation from the experiments. The result is for $\sigma = 1.105$,

at which a partial cavity with a length about 20% of the chord length was observed on the hydrofoil.

As we can see, the calculated cavity extent has generally the same shape as the observed ones, but it is longer than the observation. This is not unexpectated since the cavity closure in the experiment shows a strong turbulent closing at the cavity end (Figure C.3).

Chapter 9

Conclusions and Recommendations

After successful implementation of the present method and after extensive verification and validation for both two-dimensional and three-dimensional cavity flows, the main conclusions are drawn in this chapter. Problems are discussed and recommendations for further improvement are surveyed

Viscosity has been found to have a strong effect on cavitation inception. One of the reasons is that it changes the surface pressure distribution. But this effect is limited for fully developed cavity flows, like a sheet cavity. Mostly, the sheet cavity detaches from the leading edge of a lifting body and forms a transparent smooth cavity surface. The shear stress on the interface between the liquid and the vapor is so small that its effects can be neglected. Then a potentialv flow theory can be expected to give a sufficiently good prediction for this kind of flow, except at the detachment and the reattachment of the sheet.

Investigations on sheet cavity flows (Laberteaux (1998)) show a good correlation between the experiment and the prediction by potential flow theory when the cavity closure is a laminar closure. This is especially true for three-dimensional sheet cavity flows when the re-entrant jet turns in the span direction and the cavity is not locally shedding as cloud cavities. We are then encouraged to develop the present method that is based on the panel method, due to its simplicity and efficiency. It is even used for the simulation of the re-entrant jet.

The single-phase approach methods, which use an artificial equation of state together with a compressible the Euler or RANS code, predict sheet cavity flows in which the fluid in the cavity moves at supersonic speeds. But this is not observed in experiments. The surface-capturing methods based on Euler

or RANS codes treat the cavity surface as a free surface and the dynamic characteristics of the sheet cavity can then be predicted. With an improvement of the calculation efficiency, they are also quite promising too.

After deriving the formulation, the present method has been successfully implemented in a computer code that shows the method to be stable and accurate. Generally, two different kinds of boundary conditions are used, one is the Dirichlet boundary condition on the cavity surface which is derived from the dynamic boundary condition, and the other is the Neumann boundary condition that reflects the non-penetrating kinematic condition. The cavity surface is assumed at first on the body surface and the kinematic boundary condition on the cavity surface is used to iterate the cavity surface or to advance the cavity surface in time until a converged result is reached.

It has been found that this method is quite stable and accurate for steady cavity flow predictions, and also very promising for capturing the main features of the unsteady dynamic variation of the cavity. After extensive numerical verification and experimental validation, we formulate the following conclusions and recommendations.

9.1 Concluding remarks

Some of the remarks have been concluded in the previous chapters, some others will be drawn in the following. Both are listed below.

- A potential based higher-order panel method has been shown by De Koning Gans (1994) to be advantageous both in terms of efficiency and accuracy, especially for the flow around sharp edges like the leading edge of a profile. However care must be paid to the evaluation of the near field influence coefficients when the body-fitted curvilinear coordinates are used and when all the variables are expanded based on these coordinates. Special attention has to be paid to the triangular shaped panels at the tip of a hydrofoil or a propeller blade.

- Lagrangian methods for advancing the solution in time have been found to be not practical for cavity flow problems due to the high speed of the fluid at the cavity surface and the high curvature at the cavity end. Previous exercises with this method (De Koning Gans (1994), De Lange (1996)) do not show to be promising for solving cavity flow problem on lifting bodies with a complicated geometry like propeller blades. An Euler method has been found to be marginally stable under the present formulation, but wiggles can propagate from the edges to the central part of the cavity and quickly contaminate the whole cavity surface. Only the alternative Euler method has been found to be stable and hence has been used in the present simulation.

- The choice of the detachment position of the sheet cavity has been found to have a very strong effect on the calculated cavity shape (both for the length and for the thickness distribution). For the present potential flow theory, choosing the detachment point at the physical detachment point of the cavity may not seem to be right, because the surface tension, the *dead water* and the round nose of the cavity is not represented. However, taking into account the fact that the laminar boundary layer separation will move upstream to a position very close to the minimum pressure point after cavitation inception has occurred, setting the cavity detachment at the minimum pressure point may give a better prediction of the cavity shape.

- The Kutta condition, which enforces equal pressure at both sides of the trailing edge by changing the singularity strength on the first panel of the wake and keeping this strength for the other panels in the same strip (steady flow case) or shedding this strength to the next panel in the next time step (unsteady flow case), has been found to imply fundamental errors, because it violates Kelvin's circulation conservation law. In three-dimensional flow situations, when the trailing edge is not perpendicular to the local flow direction, the change of the singularity strength of the first wake panel can generate a very high artificial speed in a direction parallel to the trailing edge. Sometimes equal pressure can be achieved but a suction peak is formed at the trailing edge which is not realistic. Sometimes, equal pressures cannot be achieved. The influence of the pressure Kutta condition on the sheet cavity simulation depends highly on the pressure difference at the trailing edge when the Morino Kutta condition is used. No general conclusions can be drawn.

- In unsteady flow calculations, the shedding of the vorticity at the trailing edge has been found to have a strong effect on the pressure distribution and the loading, and hence on the cavity shape. It is found that a higher order formulation of the singularity in the first few panels in the wake is generally needed. But the wake shape has been found to have minor influence on the calculation, except when the propeller is highly loaded.

- The two-dimensional flow calculations for profiles with different thickness to chord ratio shows the trend that the cavity length decreases when the foil thickness increases. This is in accordance with the experimental observations. Linear methods show an opposite trend. The predicted cavity length exhibits a very good correlation with experimental results when the closure of the cavity is smooth. When the closure of the cavity is cloudy, the present method predicts a cavity length which includes the cloudy region.

- The re-entrant jet has been successfully predicted by the present method when many panels are used at the closure of the cavity. Without considering the boundary layer, the predicted re-entrant jet thickness thickness is always around 8 to 10% of the cavity maximum thickness. The re-entrant jet in the viscous flow is expected to be thicker than this value. The direction of the re-entrant jet is predicted to reflect at the cavity end in the three-dimensional flow case, which is found to have a strong influence on the formation of the cloud cavitation and eventually on the topology of the cavity. Unsteady flow calculations show the trend that the re-entrant jet forms when the cavity has grown to the maximum length and during the early stage of collapse.

- The dynamic motion of the cavity in the two-dimensional flow case shows an out-of-phase motion of the cavity thickness over the span. This out-of-phase motion is also found for the cavity extent at different span positions. The phase angle for a rectangular hydrofoil with an aspect ratio of 2 can be as large as 90°.The cavity maximum thickness is found to move downstream towards the cavity end when the cavity is in the growing stage.

- All the calculated results for a hydrofoil in a sinusoidal gust show a slow increase and a faster decrease of the cavity size. This is found for both the cavity extent and the cavity volume. In the case of the *S Propeller* passing through a sharp wake peak, the cavity length at most radii has the same characteristics, but the total volume of the cavity changes differently in the wake peak. It increases slowly and decreases faster. This is because of the phase difference for cavities at different radii.

- The preliminary results from the cavitation test on a transparent twisted hydrofoil in the cavitation tunnel show that this is a very promising method for a benchmark test on steady and unsteady cavity flows, including the measurement of the cavity thickness and the volume variation in a gust. The calculated cavity shapes agree with experiments.

9.2 Recommendations

The following recommendations are given for further development and improvement of the present method.

- The difference of the influence coefficients computed for a flat panel and that computed for a curved panel comes from the curvature of the panel. This difference is small in most cases, and can be evaluated by a higher-order panel method. Since this difference is subtle, the accuracy of the

evaluation has to be improved and addressed carefully, especially for triangular panels.

- The search for the intersection of the cavity surface and the body surface has a severe influence on the robustness of the present method. The present method is found to have a problem in three-dimensional flow calculations when the cavity is very thin so that the cavity surface is almost tangential to the foil surface. An error in the search for the intersection can generate a wiggle in the next iteration or time step, and this wiggle can result in a fatal failure in the following steps.

- The correct simulation of the dynamic motion of the cavity surface depends partly on the convergence of the $\frac{\partial \eta}{\partial t}$ term in equation (4.32) and the $\frac{\partial \varphi}{\partial t}$ term in equation (4.36). Convergence was observed in all the calculations, and very good convergence was obtained for the hydrofoil flows. However further investigations should be carried out in more detail and the convergence test should be quantified.

- Further validation of the present method should be done in the future. Emphasis should be put on the dynamic variation of the cavity shape and its volume. Since there are still no reliable experimental results for unsteady cavity flows, a good benchmark test for both steady and unsteady cavity flows should be carried out. Details of the cavity thickness distribution should be measured.

- At present, the code is fully vectorized for the supercomputer Cray C90 for the calculation of the influence coefficients. But since the cavity surface has to be re-paneled after each iteration step or time step, part of the influence coefficients must be re-evaluated. During the developing stage of the code, all the influence coefficients are simply re-evaluated for each step. An improvement in this respect can increase the efficiency of the code quite a lot.

Bibliography

ACOSTA, A. J. 1955 A note on partial cavitation of flat plate hydrofoils. *Technical Report No. E-19.9, California Institute of Technology* .

ARAKERI, V. H. 1975 Viscous effects on the position of cavitation separation from smooth bodies. *Journal of Fluid Mechanics* **68** (4), 779–799.

AVELLAN, F., DUPONT, P. & RYHMING, I. 1989 Generation mechanism and dynamics of cavitation vortices downstream of a fixed leading edge cavity. *Proceedings of 17th ONR* .

BIRKHOFF, G. & ZARANTONELLO, E. H. 1957 Jets, wakes and cavities. *Academic Press* .

BLAKE, F. G. J. 1949 The tensile strength of liquids: A review of literatures. *Harvard Acoustics Research Laboratory* **TM9**.

BOSE, N. 1994 Explicit kutta condition for an unsteady two-dimensional constant potential panel method. *AIAA Journal* **32** (5), 1078–1080.

BRESLIN, J. P. & ANDERSEN, P. 1994 Hydrodynamics of ship propellers. *Cambridge Ocean Technology Series 3* .

BROCKETT, T. 1966 Minimum pressure envelopes for modified naca-66 sections with naca a=0.8 camber and buships type i and type ii sections. *DTNSRDC Report 1780* (1780).

BURRILL, L. C. 1947 On propeller theory. *Institute of Engineering and Shipbuilding in SEOTH* .

CHEN, C. F. 1962 Second order suppercavitating hydrofoil theory. *Journal of Fluid Mechanics* **13**, 321–332.

CHEN, Y. & HEISTER, S. D. 1994 A numerical treatment of attached cavitation. *Journal of Fluid Engineering* **116**, 613–618.

CHENG, S. I. & LU, Y. L. 1986 An eulerian method for transient nonlinear free surface wave problems. *Journal of Computational Physics* **62**, 429–440.

COURANT, R. & HILBERT, D. 1962 Method of mathematical physics ii. *Interscience Publishers* **3** (6).

COX, A. D. & CLAYDEN, W. A. 1958 Cavitating flow about a wedge at incidence. *Journal of Fluid Mechanics* **3** (6).

CRIGHTON, D. G. 1985 The kutta condition in unsteady flow. *Annual Review of Fluid Mechanics* **17**, 411–445.

DANG, J., CHEN, J. D. & TANG, D. H. 1992 A design method of highly skewed propellers with new blade sections in circumferentially non-uniform ship wake. *Proceedings of the 2nd International Symposium on Propeller and Cavitation* pp. 7–17.

DANG, J. & KUIPER, G. 1998*a* Re-entrant jet medeling of partial cavity flow on three-dimensional hydrofoils. *Proceedings of ASME FEDSM'98* (4884).

DANG, J. & KUIPER, G. 1998*b* Re-entrant jet modeling of partial cavity flow on two-dimensional hydrofoils. *Proceedings of 3rd International Symposium on Cavitation* **2**, 233–242.

DAVI, G., MARRETTA, R. M. A. & MILAZZO, A. 1997 Explicit kutta condition for unsteady two-dimensional high-order potential boundary element method. *AIAA Journal* **35** (6), 1080–1081.

DELANNOY, Y. & KUENY, J. L. 1990 Two phase flow approach in unsteady cavitation modeling. *Proceedings of Cavitation and Multi-Phase Flow Forum, ASME FED* pp. 153–158.

DESHPANDE, M. D., FENG, J. & MERKLE, C. L. 1993 Navier-stokes analysis of 2-d cavity flows. *Proceedings of Cavitation and Multiphase Flow, ASME* **FED-VOL. 153**, 149–155.

DESHPANDE, M. D., FENG, J. & MERKLE, C. L. 1994 Cavity flow predictions based on the euler equation. *Transactions of the ASME* **116**, 36–44.

DUPONT, P. & AVELLAN, F. 1991 Numerical computation of a leading edge cavity. *Proceedings of cavitation'91, ASME FED* .

EFROS, A. G. 1946 Hydrodynamics theory of two-dimensional flow with cavitation. *Dokl. Akad. Nauk. SSSR* **51**, 267–270.

FABULA, A. G. 1962 Thin-airfoil theory applied to hydrofoils with single finite cavity and arbitrary freestream detachment. *Journal of Fluid Mechanics* **12**, 227–240.

FINE, N. E. & KINNAS, S. A. 1993 A boundary element method for the analysis of the flow around 3-d cavitating hydrofoils. *Journal of Ship Research* **37** (3), 213–224.

FLEETER, S. 1979 Trailing edge condition for unsteady flows at high reduced frequency. *AIAA paper 79-0152* .

FOETH, E. 2000 Observation of a three-dimensional sheet cavity on a hydrofoil. *M. Sc. thesis of Technical University Delft* .

FRANC, J. P. & MICHEL, J. M. 1985 Attached cavitation and the boundary layer: Experimental investigate and numerical treatment. *Journal of Fluid Mechanics* **154**, 63 90.

FURNESS, R. A. & HUTTON, S. P. 1975 Experimental and theoretical studies of two-dimensional fixed-type cavities. *Journal of Fluids Engineering* pp. 515–522.

FURUYA, O. 1975 Three-dimensional theory on supercavitating hydrofoils near a free surface. *Journal of Fluid Dynamics* **71** (2), 339–359.

GATES, E. M. 1977 The influence of freestream turbulence, freestream nuclei population and a drag-reducing polymer on cavitation inception on two axissymmetric bodies. *Report No. Eng. 183-2* .

VAN GENT, W. 1994 Pressure field analysis of a propeller with unsteady loading and sheet cavitation. *Proceedings of 20th ONR* pp. 355–367.

GEURST, J. A. 1959 Linearized theory for partially cavitated hydrofoils. *International Shipbuilding Progress* **6** (60), 369 384.

GEURST, J. A. 1960 Linearized theory for fully cavitated hydrofoils. *International Shipbuilding Progress* **7** (65).

GEURST, J. A. & VERBRUGH, P. J. 1959 A note on camber effects of a partially cavitated hydrofoil. *International Shipbuilding Progress* **6** (61).

GILBARG, D. & ROCK, H. H. 1946 On two theories of plane potential flow with finite cavities. *Naval Ordnance Laboratory* (NOLM 8718).

GOLDEN, D. W. 1975 A numerical method for two-dimensional, cavitating lifting flow. *Department of Ocean Engineering, MIT, Report No. 81512-1* .

GREELEY, D. S. & KERWIN, J. E. 1982 Numerical methods for propeller design and analysis in steady flow. *SNAME transaction* **90**, 415–453.

HESS, J. L. 1972 Calculation of potential flow about arbitrary bodies. *Douglas Aircraft Company* (MDC J5679-01).

HESS, J. L. 1979 A higher order panel method for three dimensional potential flow. *Report Number NADC 77166-30, Douglas Aircraft Company* .

HESS, J. L. 1990 Panel methods in computational fluid dynamics. *Annual Review to Fluid Mechanics* **22**, 255–274.

HESS, J. L. & VALAREZO, W. O. 1985 Calculation of steady flow about propeller using surface panel method. *AIAA Journal of Propulsion Power* .

HIRSCHI, R., DUPONT, P. & AVELLAN, F. 1997 Centrifugal pump performance drop due to leading edge cavitation: Numerical predictions compared with model tests. *FEDSM'97-3342* .

HIRSCHI, R., DUPONT, P. & AVELLAN, F. 1998 Partial sheet cavities prediction on a twisted elliptical planform hydrofoil using a fully 3-d approach. *Proceedings of the 3rd International Symposium on Cavitation* (1), 245–249.

HOEIJMAKERS, H. W. M. 1989 Computational aerodynamics of ordered vortex flow. *PhD Thesis of Technique University Delft* .

HOEIJMAKERS, H. W. M., JANSSENS, M. E. & KWAN, W. 1998 Numerical simulation of sheet cavitation. *Proceedings of the 3rd International Symposium on Cavitation* **2**, 257–262.

HOSHINO, T. 1989 Hydrodynamic analysis of propellers in steady flow using a surface panel method. *Journal of the Society of Naval architects of Japan* **165**, 55–70.

HOSHINO, T. 1991 A surface panel method with deformed wake model to analyze hydrodynamic characteristics of propeller in steady flow. *Mitsubushi Technical Bulletin* (195).

HOSHINO, T. 1994 Hydrodynamic analysis of propellers in unsteady flow using a surface panel method. *Journal of the Society of Naval architects of Japan* **174**, 71–87.

VAN HOUTEN, R. J. 1983 The numerical prediction of unsteady sheet cavitation on high aspect ratio hydrofoils. *Proceedings of 14th ONR* pp. 733–782.

HSU, C. C. & SHEN, Y. T. 1988 Unsteady partial cavity flow on foils. *Proceedings of 17th ONR* pp. 349–363.

DE ST ISAACSON, M. 1982 Nonlinear-wave effect on fixed and floating bodies. *Journal of Fluid Mechanics* **120**, 267–281.

ITTC 1990 Propulsor committee report, 19th ittc **1**.

ITTC 1999 Report of the special committee on computational method for propeller cavitation. *Proceedings of 22nd International Towing Tank Conference* **1**, 433–463.

JESSUP, S. D. 1989 An experimental investigation on viscous aspects of propeller blade flow. *Dissertation of The Catholic University of American* .

JIANG, C. W. & LEEHEY, P. 1977 A numerical method for determining forces and moments on supercavitating hydrofoils. *The Second International Conference on Numerical Ship Hydrodynamics* pp. 250–257.

JOHNSON, F. T. & RUBBERT, P. E. 1975 Advanced panel-type influence coefficient methods applied to subsonic flows. *AIAA paper 75-50* .

KERWIN, J., KINNAS, S. A., LEE, J. & SHIH, W. 1987 A surface panel method for the hydrodynamic analysis of ducted propellers. *SNAME Transaction* **95**, 93–122.

KERWIN, J. E., KINNAS, S. A., WILSON, M. B. & MCHUGE, J. 1986 Experimental and analytical techniques for the study of unsteady propeller cavitation. *Proceedings of the 16th Symposium on Naval Hydrodynamics* .

KERWIN, J. E. & LEE, C. S. 1978 Prediction of steady and unsteady marine propeller performance by numerical methods. *Transaction of SNAME* **86**.

KIM, Y. G. & LEE, C. S. 1996 Prediction of unsteady performance of marine propellers with cavitation using surface-panel method. *Proceedings of 21st Symposium on Naval Hydrodynamics* pp. 913–929.

KIM, Y. G., LEE, C. S. & SUH, J. C. 1994 Surface panel method for prediction of flow around a 3-d steady or unsteady cavitating hydrofoil. *Proceedings of the 2nd International Symposium on Cavitation* .

KINNAS, S. A. 1991 Leading edge correction to the linear theory of partially cavitating hydrofoils. *Journal of Ship Research* **35** (1), 15–27.

KINNAS, S. A. 1992 Leading edge correction to the linear theory of cavitating hydrofoil and propellers. *Proceedings of 2nd International Symposium on Propeller and Cavitation* .

KINNAS, S. A. 1998 The prediction of unsteady sheet cavitation. *Proceedings of the Third International Symposium on Cavitation* pp. 19–36.

KINNAS, S. A. & FINE, N. E. 1991 Non-linear analysis of flow around partially or supercavitating hydrofoils by a potential based panel method. *Proceedings of Boundary Integral Methods - Theory and Applications* pp. 289–300.

KINNAS, S. A. & FINE, N. E. 1992 A nonlinear boundary element method for the analysis of unsteady propeller sheet cavitation. *Proceedings of 19th ONR* .

KINNAS, S. A. & FINE, N. E. 1993 A numerical nonlinear analysis of the flow around two- and three-dimensional partial cavitating hydrofoils. *Journal of Fluid Mechanics* **254**, 151–181.

KINNAS, S. A. & HSIN, C. 1992 Boundary element method for the analysis of the unsteady flow around extreme propeller geometries. *AIAA Journal* **30** (3), 688–696.

KINNAS, S. A., MISHIMA, S. & BREWER, W. H. 1994 Non-linear analysis of viscous flow around cavitating hydrofoils. *Proceedings of 20th ONR* .

KINNAS, S. A. & PYO, S. 1997 Propeller wake alignment models in uniform and inclined inflow. *Proceedings of Propeller/Shafting'97* .

KNAPP, R. T., DAILY, J. W. & HAMMITT, F. G. 1970 Cavitation. *McGraw-Hill Book Company* .

DE KONING GANS, H. 1994 Numerical time dependent sheet cavitation simulations using a high order panel method. *Ph. D. Thesis, TU Delft* .

KUBOTA, A., KATO, H., YAMAGUCHI, H. & MAEDA, M. 1989 Unsteady structure measurement of cloud cavitation on a foil section using conditional sampling technique. *Transaction of the ASME* **111**, 204–210.

KUIPER, G. 1981 Cavitation inception on ship propeller models. *Netherlands Ship Model Basin* **Publication No. 655**.

KUIPER, G. 1984 Cavitation on propeller models in a sharp wake peak. *Maritime Research Institute Netherlands* **Internal Report No. 40020-2-SR**.

KUIPER, G. 1994 Cavitation and new blade sections. *FED, Cavitation and Gas-Liquid Flow in Fluid Machinery and Devices, ASME* **190**, 25–32.

KUIPER, G. & JESSUP, S. D. 1993 A propeller design method for unsteady conditions. *Proceedings of SNAME Annual Meeting* .

LABERTEAUX, K. R. 1998 Flow in the closure of partial attached cavitation. *Ph. D. Thesis, University of Michigan* .

LABERTEAUX, K. R. & CECCIO, S. 1997 Flow in the closure region of stable partial attached cavitation. *1997 ASME Fluids Engineering Division Summer Meeting* (FEDSM97-3248).

LAMB, S. H. 1945 Hydrodynamics (6th edition). *Dover Publications* .

DE LANGE, D. F. 1996 Observation and modeling of cloud formation behind a sheet cavity. *Ph. D. Thesis, Twente University* .

LE, Q., FRANC, J. P. & MICHEL, J. M. 1993 Partial cavities: Global behavior and mean pressure distribution. *Journal of Fluids Engineering* **115**, 243–248.

LEE, C. S. 1979 Prediction of steady and unsteady performance of marine propellers with and without cavitation by numerical lifting surface theory. *Ph. D. Thesis, Department of Ocean Engineering, MIT* .

LEE, C. S., KIM, Y. G. & SUH, J. C. 1994 A surface panel method for design of hydrofoils. *Journal of Ship Research* **38** (3), 175–181.

LEEHEY, P. 1971 Supercavitating hydrofoils of finite span. *Proceedings of IUTAM Symposium on Non-steady Flow of Water at High Speeds* .

LIGHTHILL, M. J. 1951 A new approach to thin aerofoil theory. *The Aeronautical Quarterly* **3** (2), 193–210.

LIGTELIJN, J. T. & KUIPER, G. 1983 Intentional cavitation as a propeller design parameter. *Proceedings of 2nd International Symposium on Practical Design in Shipbuilding* pp. 339–346.

MAITRE, T. A. & ROWE, A. R. 1991 Modelling of flow around a marine propeller using a potential-based method. *Journal of Ship Research* **35** (2), 114–126.

MANIAR, H. D. 1995 A three dimensional higher order panel method based on b-spline. *Ph D. Dissertation of MIT* .

MAZZI, B. 1999 Optimization of reference plane coefficients for higher order panel method. *MARIN Report, No. 15290-2-RD* .

MCCROSKEY, W. J. 1982 Unsteady airfoil. *Annual Review of Fluid Mechanics* **14**, 285–311.

MERKLE, C. L. 1998 Computational modeling of the dynamics of sheet cavitation. *Proceedings of the 3rd International Symposium on Cavitation* (2), 307–311.

VAN DER MEULEN, J. H. J. & WIJNANT, I. L. 1990 On the structure and intensity of sheet cavitation. *Proceedings of Cavitation and Multiphase Flow Forum - 1990* **FED-VOL. 98**, 101–105.

MORINO, L. & KUO, C. C. 1974 Subsonic potential aerodynamics for complex configurations: A general theory. *AIAA Journal* **12** (2), 191–197.

MOULIJN, J. C. & KUIPER, G. 1995 The influence of the wake model on induced velocities in the propeller plane. *An international Conference on Propeller Cavitation to celebrate 100 years of Propeller Cavitation Research - PROPCAV'95* .

OHASHI, H. & ISHIKAWA, N. 1972 Visualization study of flow near the trailing edge of an oscillating airfoil. *Bulletin JSME* (15), 840–847.

PEALLAT, J. M. & PELLONE, C. 1996 Experimental validation of two- and three-dimensional numerical analysis of partially cavitating hydrofoils. *Journal of Ship Research* **40** (3), 211–223.

PELLONE, C. & ROWE, A. 1981 Supercavitating hydrofoils in non-linear theory. *The Third International Conference on Numerical Ship Hydrodynamics* pp. 399–413.

PINKERTON, R. M. 1936 Calculated and measured pressure distributions over the midspan section of the naca 4412 airfoil. *NACA report No. 563* (563).

POLLING, D. R. & TELIONIS, D. P. 1986 The response of airfoils to periodic disturbances – the unsteady kutta condition. *AIAA Journal* **24** (2), 193–199.

PYO, S. 1995 Numerical modelling of propeller tip flows with wake sheet roll-up in three dimension. *Dissertation of MIT* .

RIABOUCHINSKY, D. 1921 On steady fluid motions with free surfaces. *Proceedings of London Mathematics Society* **19**, 206–215.

ROMATE, J. E. 1988 Local error analysis for 3-d panel method. *Journal of Engineering Mathematics* **22**, 123–142.

ROMATE, J. E. 1989 The numerical simulation of non-linear gravity waves in three dimensions using a higher order panel method. *Ph. D. Thesis, University Twente* .

RONALD, Y. F. 1989 Cavitation. *McGraw-Hill Book Company* .

ROWE, A. & BLOTTIAUX, O. 1993 Aspects of modeling partially cavitating flows. *Journal of Ship Research* **37** (1), 34–48.

SCHÖÖN, J. 2000 A method for the study of unsteady cavitation. *PhD Thesis of Chalmers University of Technology* .

SHEN, Y. T. 1985 Wing sections for hydrofoils -part3: Experimental verifications. *Journal of Ship Research* **29** (1), 39–50.

SHEN, Y. T. & DIMOTAKIS, P. E. 1989*a* The influence of surface cavitation on hydrodynamic forces. *Proceedings of 22nd ATTC* .

SHEN, Y. T. & DIMOTAKIS, P. E. 1989*b* Viscous and nuclei effects on hydrodynamic loadings and cavitation of a naca 66 (mod) foil section. *Journal of Fluids Engineering* **111**, 306–316.

SHEN, Y. T. & EPPLER, R. 1981 Wing sections for hydrofoils - part 2: Non-symmetrical profiles. *Journal of Ship Research* **25** (3), 191–200.

SHEN, Y. T. & PETERSON, F. B. 1978 Unsteady cavitation on an oscillating hydrofoil. *Proceedings of 12nd ONR* pp. 362–384.

SHEN, Y. T. & PETERSON, F. B. 1980 The influence of hydrofoil oscillation on boundary layer transition and cavitation noise. *Proceedings of 13th ONR* pp. 221–239.

SONG, S. C. & HE, J. 1998 Numerical simulation of cavitating flows by single-phase flow approach. *Proceedings of the 3rd International Symposium on Cavitation* **2**, 295–300.

STANIER, M. J. 1992 Propeller blade sections with improved cavitation inception. *Proceedings of I Mech E 92* pp. 205–216.

STERN, F. 1989 Comparison of computational and experimental unsteady cavitation on a pitching foil. *Journal of Fluids Engineering* **111**, 290–299.

STERN, F. & VORUS, W. S. 1983 A nonlinear method for predicting unsteady sheet cavitation on marine propellers. *Journal of Ship Research* **27** (1), 56–74.

TAKINACI, A. C. 1996 A wake rollup model for heavily loaded marine propellers. *International shipbuilding progress* **43** (435), 247–272.

TULIN, M. P. 1953 Steady two-dimensional cavity flows about slender bodies. *DTMB Technical Report N. 834* .

TULIN, M. P. 1964 Supercavitating flows — small perturbation theory. *Journal of Ship Research* **7**, 16–37.

TULIN, M. P. & HSU, C. C. 1980 New application of cavity flow theory. *Proceedings of 13th Symposium on Naval Hydrodynamics* .

UHLMAN, J. J. S. 1978 A partially cavitating hydrofoil of finite span. *Journal of Fluids Engineering* **100**, 353–354.

UHLMAN, J. J. S. 1987 The surface singularity method applied to partially cavitating hydrofoils. *Journal of Ship Research* **31** (2), 107–124.

UKON, Y., KUDO, T. & KUROBE, Y. 1991 Measurement of cavity thickness distribution on the blade of propeller models by laser-ccd method. *ASME FED-VOL 116, Cavitation'91* **116**, 99–104.

WADE, R. B. 1967 Linearized theory of a partially cavitating plano-convex hydrofoil including the effects of camber and thickness. *Journal of Ship Research* **11** (1), 20–27.

WU, T. Y. 1956 A note on the linear and nonlinear theories for fully cavitated hydrofoils. *CIT Technical Report No. 21-22* .

WU, T. Y. 1972 Cavity and wake flow. *Annual Review of Fluid Mechanics* **4**.

YAMAGUCHI, H., H., K., S., T. & M., M. 1988 Development of marine propellers with better cavitation performance - 2nd report: Effect of design lift coefficient for propellers with flat pressure distribution. *Journal of the Society of Naval Architects of Japan* **163**, 48–65.

YAMAGUCHI, H. & KATO, H. 1983 On application of nonlinear cavity flow theory to thick foil sections. *Proceedings of the 2nd International Conference on Cavitation* pp. 167–174.

Appendix A

Polynomial Coefficients

Consider a variable y to be an sufficiently differentiable function of x. The Taylor expansion of this function can be written as,

$$y = f(x) = \sum_{i=0}^{N} a_i \ x^i, \tag{A.1}$$

where, N is the order of expansion. If we know the discrete (x_{ip}, f_{ip}) pairs, we can construct the function by using a local polynomial spline. For point x_{ip}, we write the polynomial based on the relative coordinate,

$$\tilde{x} = x - x_{ip}, \tag{A.2}$$

as,

$$y = f(x) = a_0 + a_1\tilde{x} + a_2\tilde{x}^2 + a_3\tilde{x}^3 + a_4\tilde{x}^4 + ... \tag{A.3}$$

Then at the nodal points,

$$\tilde{x}_k = x_{ip+ir(k)} - x_{ip}, \tag{A.4}$$

where $ir(k)$ is the relative index function of k, and $k = 1, 2, ..., K$. K is the number of nodes. When this polynomial passes through all the selected nodal points, we obtain the following linear equations,

$$\begin{pmatrix} \tilde{f}_0 \\ \tilde{f}_1 \\ \tilde{f}_2 \\ \tilde{f}_3 \\ \tilde{f}_4 \\ \cdots \end{pmatrix} = \begin{bmatrix} 1 & 0 & 0 & 0 & 0 & \cdots \\ 1 & \tilde{x}_1 & \tilde{x}_1^2 & \tilde{x}_1^3 & \tilde{x}_1^4 & \cdots \\ 1 & \tilde{x}_2 & \tilde{x}_2^2 & \tilde{x}_2^3 & \tilde{x}_2^4 & \cdots \\ 1 & \tilde{x}_3 & \tilde{x}_3^2 & \tilde{x}_3^3 & \tilde{x}_3^4 & \cdots \\ 1 & \tilde{x}_4 & \tilde{x}_4^2 & \tilde{x}_4^3 & \tilde{x}_4^4 & \cdots \\ \cdots & \cdots & \cdots & \cdots & \cdots & \cdots \end{bmatrix} \begin{pmatrix} a_0 \\ a_1 \\ a_2 \\ a_3 \\ a_4 \\ \cdots \end{pmatrix} = \mathbf{A} \begin{pmatrix} a_0 \\ a_1 \\ a_2 \\ a_3 \\ a_4 \\ \cdots \end{pmatrix}, \tag{A.5}$$

Solving this system of linear equations, the coefficients can then be expressed as a function of the spline supports $\tilde{f}_0, \tilde{f}_1, \cdots$ as,

$$\begin{pmatrix} a_0 \\ a_1 \\ a_2 \\ a_3 \\ a_4 \\ \cdots \end{pmatrix} = \mathbf{A}^{-1} \begin{pmatrix} \tilde{f}_0 \\ \tilde{f}_1 \\ \tilde{f}_2 \\ \tilde{f}_3 \\ \tilde{f}_4 \\ \cdots \end{pmatrix} = \mathbf{C} \begin{pmatrix} f_{ip+ir(0)} \\ f_{ip+ir(1)} \\ f_{ip+ir(2)} \\ f_{ip+ir(3)} \\ f_{ip+ir(4)} \\ \cdots \end{pmatrix}. \tag{A.6}$$

where $\mathbf{C} = \mathbf{A}^{-1}$. Once the matrix $\mathbf{A}^{-1}$ is calculated, the coefficients are determined. The coefficients for the first three orders are listed in the following,

1. 0^{th}-order approach

$$\mathbf{C} = [1]. \tag{A.7}$$

2. 1^{st}-order approach

$$\mathbf{C} = \begin{bmatrix} 1 & 0 & 0 \\ 0 & \frac{-1}{\tilde{x}_2 - \tilde{x}_1} & \frac{1}{\tilde{x}_2 - \tilde{x}_1} \end{bmatrix}. \tag{A.8}$$

3. 2^{nd}-order approach

$$\mathbf{C} = \begin{bmatrix} 1 & 0 & 0 \\ \frac{-\tilde{x}_1 - \tilde{x}_2}{\tilde{x}_1 \tilde{x}_2} & \frac{-\tilde{x}_2}{\tilde{x}_1(\tilde{x}_1 - \tilde{x}_2)} & \frac{-\tilde{x}_1}{\tilde{x}_2(\tilde{x}_2 - \tilde{x}_1)} \\ \frac{1}{\tilde{x}_1 \tilde{x}_2} & \frac{1}{\tilde{x}_1(\tilde{x}_1 - \tilde{x}_2)} & \frac{1}{\tilde{x}_2(\tilde{x}_2 - \tilde{x}_1)} \end{bmatrix}. \tag{A.9}$$

4. 3^{rd}-order approach

$$\mathbf{C} = \begin{bmatrix} 1 & 0 & 0 & 0 \\ \frac{-(\tilde{x}_2\tilde{x}_3 + \tilde{x}_1\tilde{x}_2 + \tilde{x}_3\tilde{x}_1)}{\tilde{x}_1\tilde{x}_2\tilde{x}_3} & \frac{\tilde{x}_2\tilde{x}_3}{(\tilde{x}_2\tilde{x}_3 - \tilde{x}_1\tilde{x}_2 + \tilde{x}_1^2 - \tilde{x}_1\tilde{x}_3)\tilde{x}_1} & \frac{\tilde{x}_1\tilde{x}_3}{(-\tilde{x}_2\tilde{x}_3 + \tilde{x}_3\tilde{x}_1 + \tilde{x}_2^2 - \tilde{x}_1\tilde{x}_2)\tilde{x}_2} & \frac{\tilde{x}_2\tilde{x}_1}{(-\tilde{x}_2\tilde{x}_3 + \tilde{x}_2\tilde{x}_1 + \tilde{x}_3^2 - \tilde{x}_1\tilde{x}_3)\tilde{x}_3} \\ \frac{\tilde{x}_1 + \tilde{x}_2 + \tilde{x}_3}{\tilde{x}_1\tilde{x}_2\tilde{x}_3} & \frac{-(\tilde{x}_2 + \tilde{x}_3)}{(\tilde{x}_2\tilde{x}_3 - \tilde{x}_1\tilde{x}_2 + \tilde{x}_1^2 - \tilde{x}_1\tilde{x}_3)\tilde{x}_1} & \frac{-(\tilde{x}_1 + \tilde{x}_3)}{(-\tilde{x}_2\tilde{x}_3 + \tilde{x}_3\tilde{x}_1 + \tilde{x}_2^2 - \tilde{x}_1\tilde{x}_2)\tilde{x}_2} & \frac{-(\tilde{x}_2 + \tilde{x}_1)}{(-\tilde{x}_2\tilde{x}_3 + \tilde{x}_2\tilde{x}_1 + \tilde{x}_3^2 - \tilde{x}_1\tilde{x}_3)\tilde{x}_3} \\ \frac{-1}{\tilde{x}_1\tilde{x}_2\tilde{x}_3} & \frac{1}{(\tilde{x}_2\tilde{x}_3 - \tilde{x}_1\tilde{x}_2 + \tilde{x}_1^2 - \tilde{x}_1\tilde{x}_3)\tilde{x}_1} & \frac{1}{(-\tilde{x}_2\tilde{x}_3 + \tilde{x}_3\tilde{x}_1 + \tilde{x}_2^2 - \tilde{x}_1\tilde{x}_2)\tilde{x}_2} & \frac{1}{(-\tilde{x}_2\tilde{x}_3 + \tilde{x}_2\tilde{x}_1 + \tilde{x}_3^2 - \tilde{x}_1\tilde{x}_3)\tilde{x}_3} \end{bmatrix}. \tag{A.10}$$

Appendix B

Two-dimensional Results

For future reference and comparison, all of the calculated results for NACA 16 series are listed in the following tables.

Table B.1: Calculated results for NACA 16-006 at $\alpha = 4°$

σ	l/C	t_{max}/C	x_{tmax}/C	Cv	h/C	C_L	C_D
0.83	0.7324	0.06272	0.4452	0.03496	0.00549	0.6252	0.0270
0.85	0.6624	0.05737	0.3897	0.02888	0.00448	0.5920	0.0241
0.87513	0.5928	0.05197	0.3464	0.02338	0.00424	0.5614	0.0220
0.90	0.5355	0.04767	0.3124	0.01936	0.00384	0.5383	0.0206
1.00	0.3917	0.03721	0.2379	0.01106	0.00300	0.4940	0.0179
1.10	0.3066	0.03082	0.1866	0.00717	0.00275	0.4752	0.0164
1.20	0.2460	0.02607	0.1487	0.00487	0.00234	0.4635	0.0153
1.30	0.2070	0.02318	0.1220	0.00365	0.00225	0.4562	0.0142
1.40	0.1724	0.02011	0.1014	0.00264	0.00207	0.4498	0.0133
1.50	0.1454	0.01757	0.0853	0.00195	0.00185	0.4445	0.0125
1.60	0.1241	0.01549	0.0727	0.00147	0.00165	0.4412	0.0118
1.70	0.1073	0.01378	0.0628	0.00113	0.00154	0.4384	0.0112

Table B.2: Calculated results for NACA 16-009 at $\alpha = 4°$

σ	l/C	t_{max}/C	x_{tmax}/C	Cv	h/C	C_L	C_D
0.81	0.6998	0.04799	0.4212	0.02516	0.00339	0.5581	0.0160
0.90	0.4748	0.03407	0.2841	0.01202	0.00244	0.4957	0.0117
1.00	0.3376	0.02593	0.2088	0.00650	0.00180	0.4622	0.0094
1.10	0.2629	0.02117	0.1613	0.00412	0.00173	0.4606	0.0087
1.20	0.2019	0.01683	0.1234	0.00251	0.00136	0.4522	0.0076
1.30	0.1579	0.01367	0.0970	0.00159	0.00118	0.4368	0.0057
1.40	0.1271	0.01122	0.0778	0.00105	0.00103	0.4361	0.0050
1.50	0.1029	0.00915	0.0640	0.00069	0.00088	0.4349	0.0044

Table B.3: Calculated results for NACA 16-012 at $\alpha = 4°$

σ	l/C	t_{max}/C	x_{tmax}/C	Cv	h/C	C_L	C_D
0.80	0.6544	0.03373	0.3982	0.01606	0.00226	0.5037	0.0076
0.90	0.4261	0.02348	0.2608	0.00719	0.00148	0.4714	0.0051
1.00	0.2843	0.01595	0.1823	0.00321	0.00100	0.4575	0.0040
1.10	0.1821	0.00994	0.1195	0.00125	0.00082	0.4260	0.0015
1.20	0.1258	0.00652	0.0082	0.00054	0.00048	0.4260	0.0008

Appendix C

Experimental Results

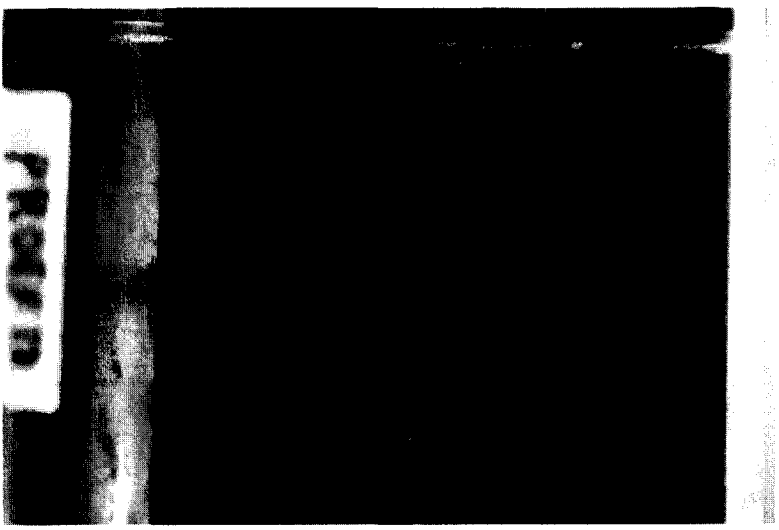

Figure C.1: Observed cavity extent. ($\alpha_{tip} = -1°$, $V_0 = 4.3m/s$, cavitation number $\sigma = 1.377$, with leading edge roughness)

Figure C.2: Observed cavity extent. ($\alpha_{tip} = -1°$, $V_0 = 4.6m/s$, cavitation number $\sigma = 1.203$, with leading edge roughness)

Figure C.3: Observed cavity extent. ($\alpha_{tip} = -1°$, $V_0 = 4.8m/s$, cavitation number $\sigma = 1.105$, with leading edge roughness)

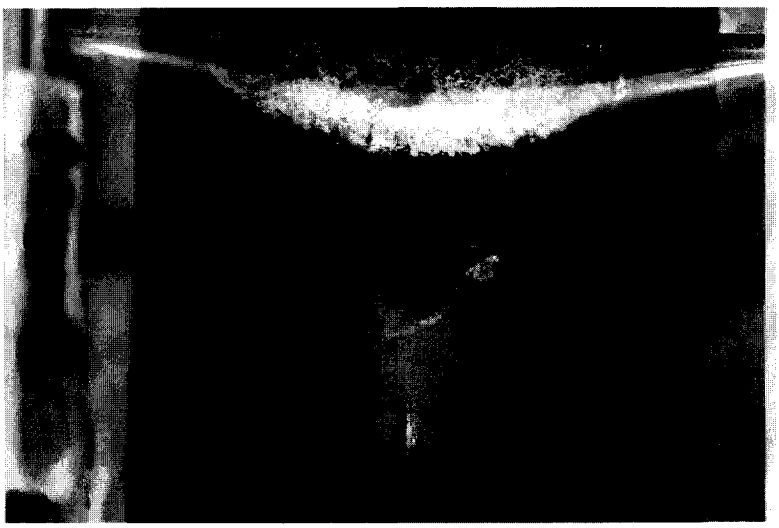

Figure C.4: Observed cavity extent. ($\alpha_{tip} = -1°$, $V_0 = 5.1m/s$, cavitation number $\sigma = 0.979$, with leading edge roughness)

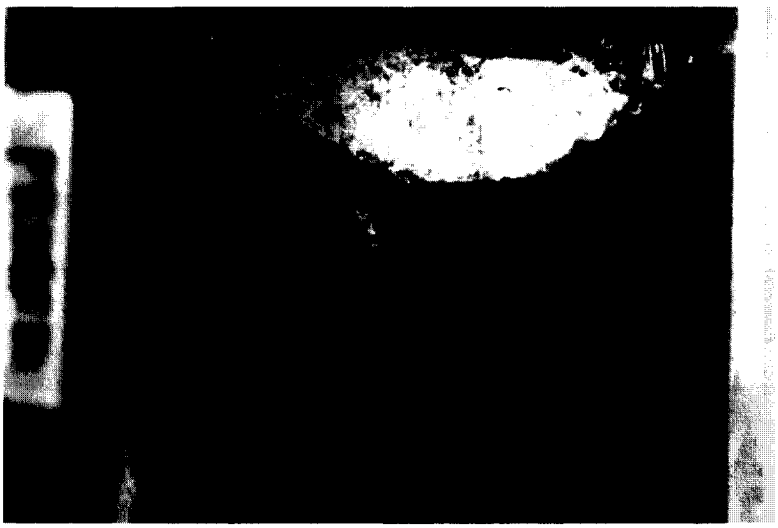

Figure C.5: Observed cavity extent. ($\alpha_{tip} = -1°$, $V_0 = 5.3m/s$, cavitation number $\sigma = 0.906$, with leading edge roughness)

Figure C.6: Observed cavity extent. ($\alpha_{tip} = -1°$, $V_0 = 5.6m/s$, cavitation number $\sigma = 0.812$, with leading edge roughness)

List of Figures

1.1 Schematics of the various cavitation on propeller blade. 3
1.2 a) (left) Convex shape of the closure line in case of a local break-off sequence: NACA 16-009, $\alpha = 3°$, $\sigma = 1.39$, $U = 6.9m/s$. b) (right) Top view of the 3-dimensional cavity and jet layer on the swept wing. The black arrows sketch the direction of the re-entrant jet. De Lange (1996). 5
1.3 Cavitation Observation in the Cavitation Tunnel on Propeller S at $J = 0.4$. ($Re_n = 1.78 \times 10^6$, $\sigma_n = 1.3$, without tunnel wall correction), Kuiper (1981). 6

2.1 Schematics of the general problem by a hydrofoil system. . . . 16
2.2 Schematics of the possible topology for reattachment for 2-dimensional steady cavity flow. a) tangential with body surface but travels upstream; b) tangential with body surface but travels downstream. 26

3.1 Schematics of the topological triangular or close to triangular panel and its flat reference panel. 49
3.2 Flat reference plane for a propeller blade-liked circular disk at the tip. 50

4.1 The wiggles of the disturbance potential on the cavity surface by using an implicit iterative algorithm. (NACA 16-006, AR=500, vertical gust $V_W = 0.07V_0 + 0.0157V_0 \sin \omega t$), time step $\Delta(\omega t) = 0.2\pi$. 61
4.2 The wiggles in the normal derivative of the potential on the cavity surface by using implicit iterative algorithm. (NACA 16-006, AR=500, vertical gust $V_W = 0.07V_0 + 0.0157V_0 \sin \omega t$), time step $\Delta(\omega t) = 0.2\pi$. 61

5.1 Planform searching procedure on a rectangular hydrofoil. (NACA 16-006, aspect ratio AR=2, angle of attack $\alpha = 4^o$, cavitation number $\sigma = 0.5$). 74

5.2 The cavity end thickness on a rectangular hydrofoil. (NACA 16-006, aspect ratio AR=500, angle of attack $\alpha = 4^o$, cavitation number $\sigma = 1.0$). 75
5.3 Comparison of the cavity shapes with and without jet section. . 76
5.4 Schematics of the intersection between cavity surface and the solid body surface. 77
5.5 Schematics of the intersection between cavity surface and the solid body surface. 78
5.6 Schematics of the separation point of the cavity on a smooth solid body. 80
5.7 Influence of the detachment position on the cavity length. (NACA 16 series, $\alpha = 4^o$, $\sigma = 0.87513$) 81
5.8 Pressure distribution at the nose of NACA 16 series. 82
5.9 Detachment of the cavity from the foil surface at different positions. (NACA 16 series, $\sigma = 0.87513$, $\alpha = 4°$) 83
5.10 Euler method (A) and prediction-correction method (B) for the wake alignment in the circular moving flow. 86
5.11 Schematics of the effective wake rolling-up procedure, downstream of a lifting body. 87
5.12 **Wake alignment procedure for Propeller 4119 at design point $J = 0.833$. 30×50 panels are used on the blade surface, 30×120 are used on the wake. (Only one of the three wake sheets is shown.)** 90
5.13 Top view (from the tip to the root) of blade sections and their aligned wake at selected radius for Propeller 4119 at $J = 0.833$. 91
5.14 Schematics of the Morino's Kutta condition. 93
5.15 Schematic illustration of Kelvin's theorem. 96
5.16 A hydrofoil travelling in a sinusoidal vertical gust with a constant speed. 97
5.17 Influence of the unsteady wake on the lift force. (rectangular foil with aspect ratio of 2, NACA16-006 section, in sinusoidal gust with reduced frequency $K = \pi$) 98
5.18 Schematics of the wake dipole strength and wake shedding (left: linear; right: quadratic). 99
5.19 Comparison of calculated cavity extent on S-propeller (Kuiper (1981)) using Morino and pressure Kutta conditions. ($J = 0.4$, $\sigma_n = 1.7$) 100
5.20 Influence of partial time derivative of the potential $\frac{\partial \varphi}{\partial t}$ on the unsteady lift with Morino's Kutta condition. (rectangular foil with aspect ratio of 2, NACA16-006 section, in sinusoidal gust with reduced frequency $K = \pi$) 102

5.21 Influence of partial time derivative of the potential $\frac{\partial \varphi}{\partial t}$ on the unsteady lift with pressure Kutta condition. (rectangular foil with aspect ratio of 2, NACA16-006 section, in sinusoidal gust with reduced frequency $K = \pi$) 102

6.1 Schematics of the cavity-hydrofoil system in two-dimensional flow. 105
6.2 Surface paneling around the re-entrant jet surface and the cavity end. (NACA16-006 section at an angle of attack 4°, and cavitation number 0.87513) 111
6.3 Variation of the cavity length with number of panels. (NACA16-006 section at an angle of attack 4°, and cavitation number 0.87513) 112
6.4 Variation of the jet thickness with number of panels. (NACA16-006 section at an angle of attack 4°, and cavitation number 0.87513) 113
6.5 Changes of the cavity shape with iteration steps. (NACA 16-006 $\alpha = 4°$, $\sigma = 0.87513$, $l_{initial}/C = 0.37550$, converged $l/C = 0.59279$). 113
6.6 Changes of the cavity shape with iteration steps. (NACA 16-006, $\alpha = 4°$, $\sigma = 1.4$). 113
6.7 Pressure distribution on the cavity and foil surface. (NACA 16-006, $\alpha = 4°$, $\sigma = 0.87513$, re-entrant jet cavity model) 114
6.8 Pressure distribution on the cavity and foil surface. (NACA 16-006, $\alpha = 4°$, $\sigma = 0.87513$, termination wall cavity model) . . 115
6.9 Comparison of the cavity shapes for these two different cavity models. (NACA 16-006, $\alpha = 4°$, cavitation number $\sigma = 1.3$). . 116
6.10 Comparison of the cavity shapes for these two different cavity models. (NACA 16-006, $\alpha = 4°$, cavitation number $\sigma = 0.87513$). 116
6.11 Cavity re-entrant jet thickness h/C versus cavitation number σ. (the angle of attack α is 4°) 117
6.12 The re-entrant jet thickness as fraction of the cavity maximum thickness versus the cavity length. (NACA 16 series, angle of attack $\alpha = 4°$) 118
6.13 The maximum cavity thickness position as fraction of the cavity length. (NACA 16 series, angle of attack $\alpha = 4°$) 118
6.14 Comparison of results of the present method and those of the non-linear method of Uhlman (1987) for NACA 16 series. . . . 120
6.15 Comparison of results of the present method and the results from the linear method provided by Uhlman (1987). (NACA 16 series) 121
6.16 Comparison of cavity volume obtained from different methods. ($C_v = volume/C^2$, NACA 16 series). 121

6.17 Comparison of the pressure distribution for an angle of attack of 4°. (NACA 66(MOD) thickness + NACA a=0.8 camber, the experimental data are from Shen & Dimotakis (1989*a*)) 123
6.18 Comparison of the cavity shape for the de-cambered and the original section. (NACA 66(MOD) thickness + NACA a=0.8 camber, angle of attack $\alpha = 4°$) 124
6.19 Comparison of pressure distribution on the modified Joukowsky profile. (angle of attack $\alpha = 3.25°$, experimental data are from Shen & Peterson (1978)) 125
6.20 Schematics of the 3-D cavity flow of a hydrofoil in uniform oncoming flow. 128
6.21 The side view of the cavity on a NACA 16-006 rectangular hydrofoil (aspect ratio = 500, angle of attack $\alpha = 4°$ and cavitation number $\sigma = 1.0$). 129
6.22 Cavity volume as a function of the number of chordwise panels on the cavity surface (NACA 16-006, aspect ratio = 500, angle of attack $\alpha = 4°$ and cavitation number $\sigma = 1.0$). 130
6.23 Cavity length as a function of the number of chordwise panels on the cavity surface (NACA 16-006, aspect ratio = 500, angle of attack $\alpha = 4°$ and cavitation number $\sigma = 1.0$). 131
6.24 Cavity volume as a function of the number of iteration steps (NACA 16-006, aspect ratio = 500, angle of attack $\alpha = 4°$ and cavitation number $\sigma = 1.0$). 131
6.25 Comparison of 2-D flow cavity length with 3-D flow results at midspan (NACA 16-006, aspect ratio = 500, angle of attack $\alpha = 4°$ and cavitation number $\sigma = 1.0$). 132
6.26 Comparison of cavity volume at midspan in 3-D cavity flow calculation with 2-D cavity flow results (NACA 16-006, aspect ratio = 500, angle of attack $\alpha = 4°$ and cavitation number $\sigma = 1.0$). 133
6.27 Comparison of the cavity shape at midspan (NACA 16-006, aspect ratio = 500, angle of attack $\alpha = 4°$ and cavitation number $\sigma = 1.0$). 133
6.28 The calculated 3-D cavity-hydrofoil system (NACA 16-006, aspect ratio = 2, angle of attack $\alpha = 4°$ and cavitation number $\sigma = 0.5$). 134
6.29 The calculated cavity planform for different cavitation numbers (NACA 16-006, aspect ratio = 2, angle of attack $\alpha = 4°$). . . . 135
6.30 The cavity volume at different cavitation numbers (NACA 16-006, aspect ratio = 2, angle of attack $\alpha = 4°$) 135
6.31 Pressure distribution and streamline on the cavity-foil surface(NACA 16-006, aspect ratio = 2, angle of attack $\alpha = 4°$, cavitation number $\sigma = 0.5$). 137

6.32 The flow 'reflects' at the end of the cavity(NACA 16-006, aspect ratio = 2, angle of attack $\alpha = 4°$, cavitation number $\sigma = 0.5$). 137
6.33 Comparison of calculated cavity length with experimental data. (Kinnas & Fine (1993), angle of attack $\alpha = 6.5°$) 138
6.34 Cavity shapes at different spanwise positions. (for the hydrofoil of Kinnas & Fine (1993), angle of attack $\alpha = 6.5°$) 139
6.35 Comparison of cavity shape on *S Propeller* at $J = 0.4$, $\sigma_n = 2.2$ and 2.0. Experiments were carried out in the depressurized towing tank with roughness (Kuiper (1981)). 142
6.36 Comparison of cavity shape on *S Propeller* at $J = 0.4$, $\sigma_n = 1.7$ and 1.5. Experiments were carried out in the depressurized towing tank with roughness (Kuiper (1981)). 143
6.37 Comparison of cavity shape on *S Propeller* at $J = 0.6$, $\sigma_n = 1.2$ and 1.0. Experiments were carried out in the depressurized towing tank with roughness (Kuiper (1981)). 144

7.1 Unsteady motion of the cavity on a high aspect ratio hydrofoil travelling in a sinusoidal vertical gust. (Aspect ratio AR=500, NACA16-006 section, vertical gust $V_W = 0.07V_0 + 0.0157V_0 \sin(\omega t)$, reduced frequency $K = \pi$, $\sigma = 1.0$.) 153
7.1 (continued) Unsteady motion of the cavity on a high aspect ratio hydrofoil travelling in a sinusoidal vertical gust. (Aspect ratio AR=500, NACA16-006 section, vertical gust $V_W = 0.07V_0 + 0.0157V_0 \sin(\omega t)$, reduced frequency $K = \pi$, $\sigma = 1.0$.) 154
7.2 Cavity length and maximum thickness variation in time for a high aspect ratio hydrofoil in a sinusoidal vertical gust. (Aspect ratio AR=500, NACA16-006 section, vertical gust $V_W = 0.07V_0 + 0.0157V_0 \sin(\omega t)$, reduced frequency $K = \pi/4$, $\sigma = 1.0$.) 156
7.3 Cavity cross-sectional area and its second derivative in time for a high-aspect-ratio hydrofoil in a sinusoidal vertical gust. (Aspect ratio AR=500, NACA16-006 section, vertical gust $V_W = 0.07V_0 + 0.0157V_0 \sin(\omega t)$, reduced frequency $K = \pi/4$, $\sigma = 1.0$.) 156
7.4 Cavity length and maximum thickness variation in time for a high-aspect-ratio hydrofoil in a sinusoidal vertical gust. (Aspect ratio AR=500, NACA16-006 section, vertical gust $V_W = 0.07V_0 + 0.0157V_0 \sin(\omega t)$, reduced frequency $K = \pi/2$, $\sigma = 1.0$.) 157
7.5 Cavity cross-sectional area and its second derivative variation in time for a high-aspect-ratio hydrofoil in a sinusoidal vertical gust. (Aspect ratio AR=500, NACA16-006 section, vertical gust $V_W = 0.07V_0 + 0.0157V_0 \sin(\omega t)$, reduced frequency $K = \pi/2$, $\sigma = 1.0$.) 157

7.6 Cavity length and maximum thickness variation in time for a high-aspect-ratio hydrofoil in a sinusoidal vertical gust. (Aspect ratio AR=500, NACA16-006 section, vertical gust $V_W = 0.07V_0 + 0.0157V_0 \sin(\omega t)$, reduced frequency $K = \pi$, $\sigma = 1.0$.) 158

7.7 Cavity cross-sectional area and its second derivative variation in time for a high-aspect-ratio hydrofoil in a sinusoidal vertical gust. (Aspect ratio AR=500, NACA16-006 section, vertical gust $V_W = 0.07V_0 + 0.0157V_0 \sin(\omega t)$, reduced frequency $K = \pi$, $\sigma = 1.0$.) 158

7.8 Spectrum of the second time derivative of the cavity cross-sectional area. (a) $K = \pi/4$; (b) $K = \pi/2$; (c) $K = \pi$. (NACA 16-006, AR=500, vertical gust $V_W = 0.07V_0 + 0.0157V_0 \sin(\omega t)$, $\sigma = 1.0$) 159

7.9 Influence of the reduced frequency on the cavity length. (NACA 16-006, AR=500, vertical gust $V_W = 0.07V_0 + 0.0157V_0 \sin(\omega t)$, $\sigma = 1.0$) 160

7.10 Cavity length and maximum thickness variation in time on a high aspect ratio hydrofoil in a sinusoidal pressure field. (Aspect ratio AR=500, NACA16-006 section, pressure field $\sigma = 1.0 + 0.2\sin(\omega t)$, reduced frequency $K = \pi$.) 162

7.11 Cavity cross-sectional area and its second time derivative on a high aspect ratio hydrofoil in a sinusoidal pressure field. (Aspect ratio AR=500, NACA16-006 section, pressure field $\sigma = 1.0 + 0.2\sin(\omega t)$, reduced frequency $K = \pi$.) 162

7.12 Spectrum of the second time derivative of the cavity cross-sectional area. (NACA 16-006, AR=500, pressure field $\sigma = 1.0 + 0.2\sin(\omega t)$, reduced frequency $K = \pi$.) 163

7.13 Comparison of the upper surface pressure distribution at fully wetted condition for NACA 0006 and NACA 66(MOD). ($t/C = 0.06$; $f/C = 0.02$; $\alpha_{NACA0006} = 3°$; $\alpha_{NACA66(MOD)} = 2.22°$) . . 164

7.14 Comparison of the cavity length variations of NACA 0006 and NACA 66(MOD) in the sinusoidal gust. 165

7.15 Comparison of the cavity volume variations of NACA 0006 and NACA 66(MOD) in the sinusoidal gust. 165

7.16 Comparison of the spectrums of the second time derivatives of the volume change for NACA 0006 and NACA 66(MOD) in the sinusoidal gust. 166

7.17 Motion of the cavity at the mid-span section of a rectangular hydrofoil in a sinusoidal vertical gust. (Aspect ratio AR=2, NACA16-006 section, vertical gust $V_W = 0.07V_0 + 0.0157V_0 \sin(\omega t)$, reduced frequency $K = \pi$, cavitation number $\sigma = 0.5$.) 167

7.17 (continued) Motion of the cavity at the mid-span section of a rectangular hydrofoil in a sinusoidal vertical gust. (Aspect ratio AR=2, NACA16-006 section, vertical gust $V_W = 0.07V_0 + 0.0157V_0 \sin(\omega t)$, reduced frequency $K = \pi$, cavitation number $\sigma = 0.5$.) 168
7.18 Cavity length variation in time on rectangular hydrofoil in a sinusoidal vertical gust. (Aspect ratio AR=2, NACA16-006 section, vertical gust $V_W = 0.07V_0 + 0.0157V_0 \sin(\omega t)$, reduced frequency $K = \pi$, cavitation number $\sigma = 0.5$.) 169
7.19 Cavity cross-sectional area variation in time on rectangular hydrofoil in a sinusoidal vertical gust. (Aspect ratio AR=2, NACA16-006 section, vertical gust $V_W = 0.07V_0 + 0.0157V_0 \sin(\omega t)$, reduced frequency $K = \pi$, cavitation number $\sigma = 0.5$.) 169
7.20 Predicted cavity motion on a rectangular hydrofoil in a sinusoidal vertical gust. (Aspect ratio AR=2, NACA16-006 section, vertical gust $V_W = 0.07V_0 + 0.0157V_0 \sin(\omega t)$, reduced frequency $K = \pi$, cavitation number $\sigma = 0.5$.) 170
7.21 Predicted cavity motion on a rectangular hydrofoil in a sinusoidal vertical gust. (Aspect ratio AR=2, NACA16-006 section, vertical gust $V_W = 0.07V_0 + 0.0157V_0 \sin(\omega t)$, reduced frequency $K = \pi$, cavitation number $\sigma = 0.5$.) 170
7.22 27% peak wake. 172
7.25 The cavity total volume change when the key blade passes through the sharp wake peak. ($J = 0.6$, $\sigma = 0.92$) 176

8.1 The test section of the cavitation tunnel at Technical University Delft with the twisted transparent hydrofoil installed. 181
8.2 Observed cavity on the twisted hydrofoil in the cavitation tunnel. (angle of attack at the tips $\alpha_{tip} = -1°$; $V_0 = 5.1m/s$; cavitation number $\sigma = 0.979$) 184
8.3 Schematics of the numerical cavitation tunnel and the discretization of the hydrofoil and its wake in the tunnel. 185
8.4 The discretization detail of half the tunnel walls and its inlet and outlet. (the example is given when the foil's angle of attack at the tip is 0°.) 186
8.5 The discretization details of the intersection of the foil and the tunnel side wall. (the example is given when the foil's angle of attack at the tip is 0°.) 186
8.6 Comparison of the calculated cavity extent and the one measured in the cavitation tunnel. (the angle of attack $\alpha = -1°$) 187

C.1 Observed cavity extent. ($\alpha_{tip} = -1°$, $V_0 = 4.3m/s$, cavitation number $\sigma = 1.377$, with leading edge roughness) 210

C.2 Observed cavity extent. ($\alpha_{tip} = -1°$, $V_0 = 4.6m/s$, cavitation number $\sigma = 1.203$, with leading edge roughness) 210
C.3 Observed cavity extent. ($\alpha_{tip} = -1°$, $V_0 = 4.8m/s$, cavitation number $\sigma = 1.105$, with leading edge roughness) 211
C.4 Observed cavity extent. ($\alpha_{tip} = -1°$, $V_0 = 5.1m/s$, cavitation number $\sigma = 0.979$, with leading edge roughness) 211
C.5 Observed cavity extent. ($\alpha_{tip} = -1°$, $V_0 = 5.3m/s$, cavitation number $\sigma = 0.906$, with leading edge roughness) 212
C.6 Observed cavity extent. ($\alpha_{tip} = -1°$, $V_0 = 5.6m/s$, cavitation number $\sigma = 0.812$, with leading edge roughness) 212

List of Tables

3.1 Consistence requirement for potential based higher-order panel method. 48
3.2 Series expansion coefficients of equation (3.43). 48

6.1 Comparison of different approaches for the same cavity termination wall model. 119
6.2 Comparison of the cavity length and the lift coefficient. (NACA 66(MOD) thickness + NACA a=0.8 camber, angle of attack α = 4°) 123
6.3 Comparison of cavity length calculations with experiments. (Modified Joukowsky foil, Shen & Peterson (1978)) 124
6.4 The calculated cavity volume for the three dimensional hydrofoil used by Kinnas & Fine (1993). (cavitation number σ = 1.084 and 1.148, angle of attack $\alpha = 6.5°$) 138

8.1 The test conditions for the twisted transparent hydrofoil. . . . 183

B.1 Calculated results for NACA 16-006 at $\alpha = 4°$ 207
B.2 Calculated results for NACA 16-009 at $\alpha = 4°$ 208
B.3 Calculated results for NACA 16-012 at $\alpha = 4°$ 208

Summary

This thesis deals with the theory and the numerical simulation of sheet cavity flows on arbitrary lifting bodies like hydrofoils and propeller blades. The objective of this research is the accurate prediction of the cavity volume and the volume variations in time when these lifting bodies travel in a gust or are subject to an ambient pressure change. This volume change plays an important role in the pressure excitation on neighboring structures like hull of a ship and in the radiation of underwater noise.

The physical phenomenon of sheet cavitation on lifting bodies is described according to experimental observations at the beginning of this thesis. The specific features of sheet cavitation, different from bubble and cloud cavitation, are addressed. The basic cavity flow theory within the frame of the potential theory is described and all the boundary conditions are discussed in order to obtain the solution of the problem. For predicting the dynamics of the cavity, numerical methods to find the solution in time are studied.

All the numerical algorithms for solving the problem are discussed in detail and checked extensively by numerical tests. A higher order panel method is described and evaluated. Emphasis is given to the problems of the analytical calculation of the influence coefficients. The system of equations of the fully wetted and cavitated flows are established under different Kutta conditions. The detachment condition and its influence on the cavity flow are studied. Cavity planform searching, grid updating and cavity-body intersection are described. Other highly-related numerical methods for panel methods and cavity flows, like the Kutta condition and wake alignment, are investigated and checked by numerical tests. Specific attention is paid to the influence of these numerical algorithms on the calculated results.

The present method for predicting steady sheet cavity flows on two-dimensional and three-dimensional hydrofoils and on propeller blades is used extensively and validated by experimental results in this thesis. Good agreement between the calculations and the experiments is achieved. The dynamics of sheet cavitation is predicted by the present method for a hydrofoil moving into a sinusoidal gust and for a propeller rotating in a sharp wake peak. The present method demonstrates the ability of capturing the dynamic movement of the sheet cavitation.

At the end of the thesis, the conclusion is drawn that the present method has the potential to predict the cavity topology and the cavity dynamics. After improvement of some numerical algorithms, the efficiency of the method can be enhanced to such a level that it can be applied in the early stage of ship propeller design in order to prevent excessive cavitation and vibrations.

Samenvatting

In dit proefschrift wordt ingegaan op de theorie en de numerieke simulatie van vliescavitatie op dragende lichamen, zoals vleugels en schroefbladen. Het doel van dit onderzoek is om het volume van de caviteit en de verandering daarin in de tijd nauwkeurig te voorspellen wanneer de invalshoek in de tijd varieert of wanneer de omgevingsdruk varieert. Deze volumeveranderingen spelen een belangrijke rol bij de opwekking van drukfluctuaties op naburige lichamen zoals de huid van een schip. Ook de hoeveelheid lawaai die een schroef onder water maakt wordt in belangrijke mate bepaald door deze volumeveranderingen.

In het begin van dit proefschrift wordt aan de hand van experimentele observaties de fysica van vliescavitatie op dragende lichamen beschreven. De specifieke eigenschappen van deze vorm van cavitatie verschillen van die van bellen- of wolken-cavitatie. Vervolgens wordt stroming met caviteiten beschreven met behulp van potentiaaltheorie samen met alle randvoorwaarden die nodig zijn om het probleem op te lossen. Ook wordt een methode gegeven om het instationaire gedrag van de caviteit te beschrijven.

Alle algorithmen voor de oplossing van het probleem worden tot in detail beschreven en worden grondig getest met behulp van numerieke experimenten. De nadruk wordt gelegd op het uitrekenen van de invloedscoefficienten van de hogere orde panelen methode die is gebruikt. Het systeem van vergelijkingen voor het oplossen van stromingen met en zonder cavitatie wordt gegeven voor verschillende Kutta condities. Het effect van de plaats waar de caviteit start en de richting waaronder dit gebeurt op de berekening van de caviteit wordt besproken. Ook wordt de iteratie van de cavitatievorm en de aanpassing van het rekenrooster aan de veranderende geometrie in de tijd beschreven. Andere daarmee samenhangende numerieke problemen voor de beschrijving van een stroming met cavitatie door middel van een panelenmethode, zoals de toepassing van de Kutta conditie en de vorm van het volgstroomveld, worden onderzocht met numerieke experimenten. Speciale zorg is besteed aan de invloed van deze numerieke algorithmen op de berekening van cavitatie.

De gepresenteerde methode voor de beschrijving van twee en drie dimensionale stationaire stromingen met cavitatie op een watervleugel en voor een stroming met cavitatie op een schroef wordt uitvoerig gevalideerd aan de hand van experimentele resultaten. Goede overeenstemming tussen de berekende en gemeten resultaten wordt gevonden. Met behulp van de opgestelde rekenmodellen is de dynamica van vliescavitatie voor twee gevallen voorspeld. Als eerste is het gedrag van een cavitarende vleugel in een sinusoidaal varierende aanstroming voorspeld en vervolgens is een schroef werkend in een scherpe volgstroom piek berekend. Deze resultaten zijn vergeleken met het in experimenten gevonden gedrag van vliescavitatie.

Geconcludeerd kan worden dat de in dit proefschrift gepresenteerde methode mogelijkheden biedt voor het voorspellen van de vorm en het gedrag van

cavitatie in instationaire aanstroming. Na verbetering van een aantal algorithmen kan de effectiviteit van de methode dusdanig worden verbeterd dat deze in een vroeg stadium in het schroefontwerp gebruikt kan worden, zodat excessieve cavitatie en trillingen kunnen worden voorkomen.

摘 要

本论文论述了任意有升力物体，如水翼和螺旋桨叶片上片状空泡流的理论和数值计算方法。本研究的目标在于精确地预报空泡的体积和它随时间的变化率。这种体积的变化发生在当有升力体穿过不均匀的阵风或者当环境压力发生变化时。它在船舶结构振动和水下噪声问题上起着重要的作用。

根据试验观察的结果，本论文一开始对升力物体上片状空化的物理现象进行了描述，强调了片状空化不同于泡状和云雾状空泡的主要特性，然后建立了势流理论基础上的空泡流理论，详细讨论和推导了解决该问题的边值条件。为获得非定常解和空泡的动力学运动，本论文讨论了解的时间推进的方法。

本文详细讨论并通过数值试验验证了所有该方法中使用的数值算法。描述了一种高阶面元法和其中用解析方法计算诱导系数时可能遇到的问题。讨论了不同库塔条件下系统方程的建立。研究了片状空泡分离点和分离点位置对解的影响、以及空泡区域的寻找、空泡表面网格的更新、和空泡与物面交线的计算。其它与面元法和空泡流相关的数值问题。如库塔条件和尾涡迭代也在本文中进行了详细的讨论和数值验算。这些研究的重点都放在该数值方法对空泡流结果的影响上。

本论文通过对二维、三维水翼和螺旋桨叶片上空泡流的大量计算，验证了本方法。通过与试验结果的比较，本方法得到了证实。比较的结果在相关的章节中进行了描述。结果表明计算结果和试验吻合较好。本方法成功地预报了当水翼在正弦阵风中运动和当螺旋桨叶片通过尖锐的尾流峰值时空泡的不定常的动力运动。显示了该方法在捕捉空泡动力学运动中的能力。

最后，本文给出了该研究的结论：该方法可用于预报定常片状空化的几何结构并可用于预报非定常片状空化的动力学运动。通过进一步的数值算法的优化，该方法的计算效率可大幅提高，从而可将该方法用于螺旋桨初期设计时的计算，和激振、噪声的预报和控制上。

Curriculum Vitae

The author was born on October 7, 1962 in Huangshi, Hubei Province, central China. In the early 70's of the last century, he moved to the southwest part of China and started his education as a primary school pupil in 1970 in Dukou (Panzhihua), Sichuan Province. In 1975, he entered the secondary school in the same city and graduated from high school in 1979. Afterwards he was enrolled to Huazhong Institute of Technology (HIT) (which is now called Huazhong University of Science and Technology (HUST)) in Wuhan, China, majored in Shipbuilding and Ocean Engineering and got a bachelor degree of engineering. In 1983, he entered the graduate school at China Ship Scientific Research Center (CSSRC) in Wuxi, China and completed a Master's study on Ship Hydrodynamics in 1986. He was employed in the same year by CSSRC and worked as a research engineer, a graduate school teacher and later on, a senior research engineer on ship hydrodynamics in the Propulsion Division. During his stay in CSSRC, he worked on numerical and experimental research on ship propellers and new blade section design for hydrofoils and propeller blades. In January 1997, under the support of Maritime Research Institute Netherlands (MARIN), he came to the Netherlands to pursue a doctoral program in the Naval Architecture Department of the Technical University Delft under the supervision of Professor dr. ir. Gert Kuiper. This thesis contains the research he did in this four-year PhD program.

Since January 1, 2001, he is employed by Lips Propeller Works in the Netherlands.

Note

Note

Note